Cranfield University

Xavier Tonnellier

Precision Grinding for Rapid Manufacturing of Large Optics

School of Applied Sciences

PhD Thesis

Cranfield University

School of Applied Sciences

PhD THESIS

Academic Year 2008 - 2009

Xavier Tonnellier

Precision Grinding for Rapid Manufacturing of Large Optics

Supervisors: Prof. P.Shore and Prof. D.J.Stephenson

May 2009

This thesis is submitted in partial fulfilment of the requirements
for the degree of Doctor of Philosophy

ABSTRACT

Large scale nuclear fusion and astronomy scientific programmes have increased the demand for large freeform mirrors and lenses. Thousands of one metre class, high quality aspherical optical components are required within the next five to ten years. Current manufacturing process chains production time need to be reduced from hundred hours to ten hours.

As part of a new process chain for making large optics, an efficient low damage precision grinding process has been proposed. This grinding process aims to shorten the subsequent manufacturing operations. The BoX® grinding machine, built by Cranfield University, provides a rapid and economic solution for grinding large off-axis aspherical and free-form optical components.

This thesis reports the development of a precision grinding process for rapid manufacturing of large optics using this grinding mode. Grinding process targets were; form accuracy of 1 μm over 1 metre, surface roughness 150 nm (R_a) and subsurface damage below 5 μm. Process time target aims to remove 1 mm thickness of material over a metre in ten hours.

Grinding experiments were conducted on a 5 axes Edgetek high speed grinding machine and BoX® grinding machine. The surface characteristics obtained on optical materials (ULE, SiC and Zerodur) are investigated. Grinding machine influence on surface roughness, surface profile, subsurface damage, grinding forces and grinding power are discussed.

This precision grinding process was validated on large spherical parts, 400 mm ULE and SiC parts and a 1 m Zerodur hexagonal part. A process time of ten hours was achieved using maximum removal rate of 187.5 mm^3/s on ULE and Zerodur and 112.5 mm^3/s on SiC.

The subsurface damage distribution is shown to be "process" related and "machine dynamics" related. The research proves that a stiffer grinding machine, BoX, induces low subsurface damage depth in glass and glass ceramic.

ACKNOWLEDGEMENTS

I would like to thank my supervisors at Cranfield University, Professor Paul Shore, Ultra Precision Engineering Centre and Professor David Stephenson, Advanced Material department.

A special thanks goes to Mr. Andrew Baldwin who was there at any time throughout this project when I needed help. I would also like to thank Mr. Paul Morantz who helped me with the work carried out on the BoX grinding machine. Ms. Lynne Allgood also helped greatly my work at Cranfield with her support.

I would also like to acknowledge the help of the following persons: Dr. Isidro Durazo-Cardenas, Dr. Xichun Luo, Dr. Andrew Dyer, Mr. Roger Collins, Mr. Roger Read and the team in UPS lab, North Wales.

Finally, I would like to thank my current employer, Mr. Sean Amos, for his support during the writing of my thesis.

This work was funded by the McKeown Precision Engineering and Nanotechnology Foundation at Cranfield and project funding through the UK's Joint Research Councils' - Basic Technologies programme and EPSRC funded Integrated Knowledge Centre (IKC) for Ultra Precision and Structured Surfaces (UPS^2).

TABLE OF CONTENTS

LIST OF FIGURES

LIST OF TABLES

LIST OF PUBLICATIONS

Tonnellier, X. et al. (2007), "Subsurface damage in precision ground ULE and Zerodur surfaces", Optics Express 15(19), 12197-12205.
Tonnellier, X. et al. (2007), "Subsurface damage caused during rapid grinding of Zerodur", Key Engineering Materials Advances in abrasive technology X, CD-ROM, paper N°72.

Tonnellier, X. et al. (2006), Diamond resin bond wheel wear in precision grinding of optical, in "Proceedings of ICMR", pp. 205-210.
Tonnellier, X. et al. (2006), High performance grinding studies on optical materials suitable for large optics, in "Proceedings of 2nd CIRP conference on High Performance Cutting", CD-ROM, paper N°28.
Tonnellier, X. et al. (2006), Wheel wear and surface/subsurface qualities when precision grinding optical materials, in "Proceedings of the SPIE", Vol. 6273, pp. 627308-627308-9.
Tonnellier, X. et al. (2006), Wheel wear investigations when precision grinding of optical materials using the BoX grinding mode, in "Proceedings of 5th International Conference on High Speed Machining", pp. 177-187.
Tonnellier, X. et al. (2007), Rapid grinding of ceramic and glass mirror materials for Extra Large Telescopes, in "Proceedings of CIRP STC-G - Technical Contribution", Paris.
Tonnellier, X. et al. (2007), Comparison of the subsurface damage induced when precision grinding ULE and Zerodur surfaces, in "Proceedings of Lamdamap", pp. 279-288.
Tonnellier, X. et al. (2008), Development of an ultra precision grinding capability for large optics, in "Proceedings of CMC", CD-ROM, paper N°91.
Tonnellier, X. et al. (2008), Surface quality of a 1m Zerodur part using an effective grinding mode, in "Proceedings of the SPIE", Vol. 7102, pp. 71020B-71020B-9.
Tonnellier, X. et al. (2008), Sub-surface damage issues for effective fabrication of large optics, in "Proceedings of the SPIE", Vol. 7018, pp. 70180F.1-70180F.10.
Tonnellier, X. et al. (2008), Subsurface damage evaluation in grinding of large optics, in "Proceedings of ASPE", pp. 84-87.

NOTATIONS

a	[μm]	Depth of largest surface flaw
a_e	[mm]	Depth of cut
a_{eG}	[μm]	Grit cutting depth
a_m	[mm^{-2}]	Average cross sectional area of chips
a_s	[μm]	Actual depth of cut of grinding wheel
a_t	[μm]	Set depth of cut of grinding wheel
b	[mm]	Plastic zone depth
b_b	[mm]	Width of the active grinding wheel profile
b_s	[mm]	Width of grinding wheel
b_w	[mm]	Grinding wheel contact width
B	[$m^{-1/2}$]	Brittleness
c_h	[μm]	Hertzian crack depth
c_l	[μm]	Lateral crack length
c_m	[μm]	Median crack depth
c_n	[-]	Constant (Grinding force)
c_p	[J/(Kg.K)]	Specific heat
c_r	[μm]	Radial crack depth
c_s	[N.s/m]	Damping coefficient
c^*_s	[-]	Constant (Grinding force)
c_t	[-]	Constant (Grinding force)
C_a	[N/μm]	Constant determined by grinding conditions
C_i, N	[mm^{-2}]	Number of active grits per unit area
C_p	[-]	Preston coefficient
C*	[μm]	Initial penetration depth
d	[mm]	Nozzle outlet height (round nozzle)
d_g	[μm]	Diameter of diamond grain
d_s	[mm]	Diameter of grinding wheel
d_w	[mm]	Diameter of workpiece
D	[mm]	Inlet diameter
e, u	[J/mm^3]	Specific grinding energy
E	[Pa]	Modulus of elasticity
E_s, E_1	[Pa]	Modulus of elasticity of the grinding wheel
E_w, E_2	[Pa]	Modulus of elasticity of the workpiece
f	[-]	Constant (number of active diamond)
f_{gn}	[N]	Normal grinding force per grit

f_r	[mm/step]	Feed per step
	[mm/rev]	Feed per revolution
F_1	[N/mm]	Initial specific tangential grinding force
F_0	[N]	Break-in force
F_{eG}	[N]	Tangential force per grit
F_n	[N]	Normal grinding force
F_{nG}	[N]	Normal force per grit
F_t	[N]	Tangential grinding force
F_z	[N]	"Actual" normal grinding force
F'_n	[N/mm]	Specific normal grinding force
F'_t	[N/mm]	Specific tangential grinding force
F*	[N]	Critical load per grit
G	[-]	Grinding ratio
h	[μm]	Lateral crack depth
h_{eq}	[μm]	Equivalent chip thickness
h_{max}	[μm]	Maximum undeformed chip thickness
h_s	[μm]	Surface scallop height
h_{slot}, h	[mm]	Nozzle slot thickness
H	[Pa]	Micro hardness
H_v	[Pa]	Vickers hardness of workpiece material
k	[W/(m.K)]	Thermal Conductivity
k_f	[-]	Dimensionless constant
k_r	[N/μm]	Proportionate factor
k_s	[N/μm]	Static stiffness of machine tool structure
K_{Ic}, K_c, T	[MPa.m$^{1/2}$]	Fracture toughness
K_s	[1/Pa]	Grinding wheel elastic coefficient
K_w	[1/Pa]	Workpiece elastic coefficient
l_c	[mm]	Real contact length
l_f	[mm]	Contact length due to applied force
l_g	[mm]	Contact length due to depth of cut
l_k	[mm]	Contact length (Chip formation/ploughing/sliding)
l_n	[mm]	Evaluation length (Roughness)
l_r	[mm]	Sampling length (Roughness)
L	[μm]	Abrasive grain size
m	[-]	Constant (SSD)
M	[#]	Mesh size
N_p	[rpm]	Part speed
N_w	[rpm]	Grinding wheel speed

P	[N]	Applied load
P_c	[W]	Grinding power / Cutting power
P_i	[W]	Power without coolant (idle grinding)
P_m	[W]	Net grinding power
P_t	[μm]	Surface profile
P_{tot}	[W]	Total power
P_v	[W]	Power with coolant
P'	[N]	Sliding applied load
P'_e	[W/mm]	Working power per unit wheel width
P''_c	[W/mm^2]	Specific grinding power
P*	[N]	Minimum initial applied load
q_d	[-]	Speed ratio forming
Q_w	[mm^3/s]	Material removal rate
Q'_w	[mm^2/s]	Specific material removal rate
r	[-]	Chip width to thickness ratio
r_g	[mm]	Diamond grain radius
R	[mm]	Radius of track
R_a	[μm]	Arithmetic surface roughness
R_c	[mm]	Grinding wheel cutting radius
R_e	[-]	Reynolds number
R_t	[μm]	Total height of profile roughness
R_z	[μm]	Maximum height of profile roughness
RSm	[mm]	Spacing Distance
s_d	[μm]	Subsurface damage
sd_{max}	[μm]	Single last fracture depth
$sd_{process}$	[μm]	Subsurface damage (Process related)
S_z	[μm]	Static deflection of grinding system
t_w	[μm]	Workpiece thickness
U_1	[-]	Material removal constant 1
U_2	[-]	Material removal constant 2
U_3	[-]	Material removal constant 3
v_c (v_s)	[mm/s]	Grinding wheel velocity (cutting speed)
v_{cd}	[m/s]	Grinding wheel speed - forming
v_{fad}	[mm/s]	Feed speed
v_{frd}	[mm/rev]	Infeed speed (forming)
v_{rd}	[m/s]	Profile roll/form disc speed (forming)
v_{slot}	[m/s]	Coolant velocity
v_w	[mm/s]	Workpiece surface speed

V_w	[cm^3]	Volume of material removed
w	[mm]	Average distance between active cutting edges
z, d	[μm]	Penetration depth
z_c	[μm]	Controlled depth
z_T	[-]	Grinding wheel direction
α	[10^{-6}/K]	Coefficient of thermal expansion
α_h	[°]	Favourable tilt angle (Hertzian)
α_k	[-]	Constant (SSD)
α_l	[-]	Constant (Lateral)
α_r	[-]	Constant (Radial)
β	[°]	Angle between workpiece and grinding wheel
$\beta_{1,2,3}$	[-]	Constant (Wheel topography)
β_s	[N]	Holding strength
Δ_{vs}	[mm^3]	Volume of wheel wear
Δ_{vw}	[mm^3]	Volume of material removed
η	[Pa.s]	Dynamic viscosity of the fluid
θ	[°]	Semi incl. angle for undeformed chip cross section
λ	[$m^{1/2}$]	Constant (SSD)
μ	[-]	Friction coefficient
ξ	[μm]	Penetration depth of subsurface cracks
ρ	[g/cm^3]	Density
υ	[-]	Volume fraction - Diamond grain
υ_s	[-]	Grinding wheel Poisson's ratio
υ_w	[-]	Workpiece Poisson's ratio
ϕ	[°]	Angle between grinding wheel and workpiece
χ	[-]	Constant (SSD)
ψ	[°]	Indentation angle
Ω	[μm]	Crack length

ABBREVIATIONS

AEGM	Arc Envelope Grinding Method
ANSI	American National Standards Institute
BoX	Big OptiX
CELT	California Extremely Large Telescope
CMM	Coordinate Measuring Machine
CNC	Computer Numerical Control
CTE	Coefficient of Thermal Expansion
CVD	Chemical Vapour Deposition
CVC	Chemical Vapour Composites
DoE	Design of Experiments
ELT	Extremely Large Telescope
E-ELT	European Extremely Large Telescope
ELID	Electrolytic in-process Dressing
EUVL	Extreme UltraViolet Lithography
FAG/LAG	Fixed/Loose Abrasive Grinding
FEPA	Federation Europeenne des fabricants de Produits Abrasifs
GSMT	Giant Segmented Mirror Telescope
GTC	Gran Telescopio Canarias
HCl	Hydrochloric
HF	Hydrofluoric
IBF	Ion Beam Figuring
IKC	Integrated Knowledge Centre
IRIS	IR Imaging Surveyor
ISO	International Organization for Standardization
LBT	Large Binocular Telescope
LIL	Ligne d'Integration Laser
LLNL	Lawrence Livermore National Laboratory
LMJ	Laser Mega-Joule
LODTM	Large Optics Diamond Turning Machine
LOG	Large Optics Generator
LVDT	Linear Variable Differential Transformer
MRF	Magnetorheological Finishing
Nd:YAG	Neodymium-doped Yttrium Aluminium Garnet
NIF	National Ignition Facility
OAGM	Off Axis Generating Machine

OWL	OverWhelmingly Large telescope
RAP	Reactive Atom Plasma
RMS	Root Mean Square
SEM	Scanning Electron Microscope
SiC	Silicon Carbide
SPDT	Single Point Diamond Turning
SR	Surface Roughness
SSD	Sub-Surface Damage
SSiC	Sintered Silicon Carbide
TEM	Transmission Electron Microscopy
TMT	Thirty Meter Telescope
ULE	Ultra Low Expansion
UPS^2	Ultra Precision and Structured Surfaces
UPS	Ultra Precision Surfaces
VLOT	Very Large Optical Telescope
VLT	Very Large Telescope

1. INTRODUCTION

The number of major science and high technology engineering projects that demand numerous large optics is increasing. Astronomy instruments, inertia nuclear fusion studies, lithography and earth observation are the main projects. For example, the Moore's Law (Moore, 1965) states that the number of transistors per chip will double every two years. For this to be true, the key enabling lithography technology has to continuously evolve. Large quantities of high quality large optics at a lower cost are required (Meiling et al., 2004). A similar large demand for large optics has arisen from large segmented primary mirror telescope projects (Shore and Parr-Burman, 2003).

1.1 Process chain for large optics

1.1.1 Current manufacturing process

The manufacturing process concept reported by Sagem or Kodak, to make a 1 metre hexagonal mirror, remains basically the same (Geyl and Cayrel, 1999, Pileri and Krabbendam, 1995). First, a blank piece, in glass or in ceramic, is machined or moulded to a flat or already curved shape. Then, the blank is first machined by successive grinding to reach the desired shape. The mirror is subsequently lapped and polished to get the right geometry dimensions and to remove the subsurface damage induced by earlier machining processes. Finally, a final process such as ion beam figuring (IBF) is used to achieve the necessary form accuracy typically 10-20 nm RMS for 1-2 m mirror segments (Shore and May-Miller, 2003).

1.1.2 Manufacturing process estimated costs

Different working groups have estimated the cost per metre square to polish those large optics. For example, one study estimated the polishing cost to be 80,000 \$/m^2 for a non light-weighted Zerodur blank to 100,000 \$/m^2 for a light-weighted SiC blank (Roberts, 2001). Another study estimated the polishing cost at 13,000 €/m^2 for spherical Zerodur segments up to 60,000 €/m^2 for aspheric Zerodur segments. The estimation was based on the cost reported for the 36 segments for the GTC primary mirror (Enard et al., 2006).

1.1.3 Process development - Ultra Precision Surfaces project

This PhD project is part of the Ultra Precision Surfaces (UPS) project funded by the UK's Joint Research Councils - Basic Technologies programme, which will establish a new UK laboratory based in North Wales at the OptiC Technium Centre. The laboratory will have grinding, polishing, measurement and energy beam machines. From a blank entering the facility, a hexagonal freeform optic will be delivered, ready to be coated (Figure 1.1).

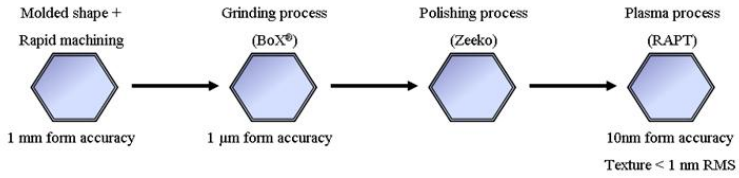

Figure 1.1: UPS process chain

To achieve that goal, a new ultra precision large optics grinder, BoX® (Figure 1.2), has been developed at Cranfield University (Shore et al., 2005). Compared with other free-form surface grinders, the BoX® grinding machine pursues a novel 3 axes approach by using two linear motions and one rotary motion. This design offers a high dynamic stiffness, a compact structural design and an in situ measurement system.

Figure 1.2: BoX® grinding machine (Shore et al., 2005)

1.2 Research objectives

The previous "state of the art", reported in the literature, in grinding large components are the Kodak Off Axis Generating Machine (OAGM) for the quality achieved (P-V < 3 μm)

and the Large Optics Generator (LOG) in Arizona for the fast process (28 mm^3/s) (Leadbeater et al., 1989, Parks et al., 1985).
The aim of this project is the rapid precision machining of large freeform optics using the BoX® grinding machine. Its objectives are a surface form quality of P_t under 1 μm, a surface roughness (R_a) of 50-150 nm and subsurface damage less than 5 μm. The grinding process will be optimized to have a material removal rate of 200 mm^3/s which is about ten times faster than the current capability.
This process will be applied to large optical blanks with a diameter up to 1 metre with off axis and freeform surfaces. The materials of interest are a glass (ULE®), a glass-ceramic (Zerodur®) and a ceramic (SiC). These materials are potential candidates for the European Extremely Large Telescope (E-ELT) segments (Dierickx et al., 2004).

1.3 Research hypothesis

The hypothesis behind this research is that the levels of subsurface damage are highly associated with the machine tool stiffness and the motion dynamics. This thesis studies the optimisation of the grinding process to obtain an efficient material removal rate of 200 mm^3/s. This research validates the levels of induced subsurface damage to minimize the amount of material to be subsequently polished.

1.4 Thesis structure

This thesis is structured as followed:

- The literature review chapter points out the important variables and research previously carried relating to the precision grinding of large optical components.
- The experimental equipment and procedures employed for characterisation are detailed in Chapter 3.
- Chapter 4 details and compares the characterisation of the experimental equipment results.
- Results of trials carried out using an established Edgetek grinding machine are given in Chapter 5. Whereas, results of trials carried out using the developed BoX® grinding machine are given in Chapter 6. Additional experiments were carried out on larger samples to prove the process scalability and the machining of more complex parts such as freeform optics.
- Comparisons of the grinding process results using the Edgetek and BoX® grinding machines are presented in Chapter 7.

- Chapter 8 details subsurface damage results on Zerodur® and ULE® . The influence of the Edgetek and BoX® grinding machine stiffnesses on the subsurface damage is also covered.

- The detailed discussion of the thesis results is presented in Chapter 9.

- Finally, Chapter 10 highlights the contribution to knowledge of this research and suggests future work that should be carried out.

2. LITERATURE REVIEW

2.1 Astronomy instruments

2.1.1 Large monolithic primary mirror telescopes

From the earliest history, natural scientists have been studying the stars and planets. Astronomy's history has flourished through instruments developed to look further into space. In recent history, telescopes were built up for that purpose and used by famous scientists such as Kepler, Huygens, Galileo and Newton (Court and Von Rohr, 1929). In the last century, the development of larger telescopes has increased dramatically. Different assembly and mechanical concepts were implemented such as the "Cassegrain" telescope design. However, they remained based on the use of a large monolithic primary mirror.

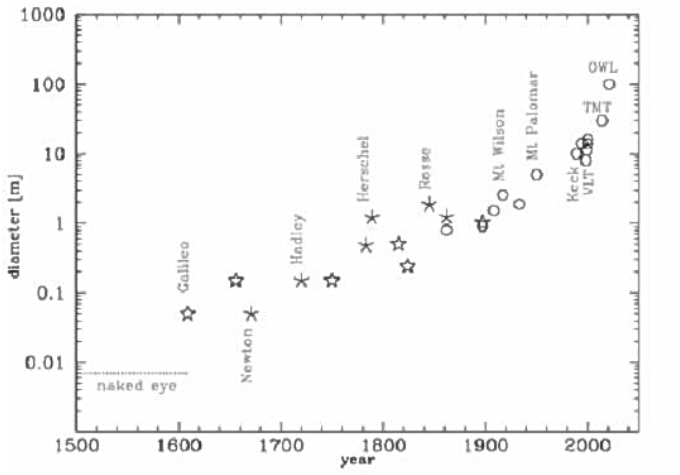

Figure 2-3 Brief history of the telescope. Stars are refractors, asterisks are speculum reflectors and circles are glass reflectors. Some specific telescopes are named.

Figure 2.1: Brief history of the telescope (Gilmozzi and Dierickx, 2000)

In the last decade, Figure 2.1 some very large monolithic type telescopes have been manufactured (Gilmozzi and Dierickx, 2000, Ealcy, 2003). The maximum size was reached by the 8.4 m primary mirror for the Large Binocular Telescope (LBT) (Hill and Salinari, 1998). It was manufactured in the Steward Observatory Mirror Lab, University of Arizona (Martin et al., 2003). Two other challenging projects were done by Sagem-Reosc (Geyl and Cayrel, 1999) in Paris, France: the Very Large Telescope (VLT) project

with its four 8 m primary mirrors and the Gemini project with two 8.2 m primary mirrors (Enard and Swings, 1983, Mountain et al., 1994).

A new interest by the astronomy community is to resolve "earth-like" planets near far away stars. Looking for extraterrestrial life will only be possible by building the new generation of extra large ground based telescopes. By increasing the primary mirror diameter, a better resolution can be achieved (Figure 2.2).

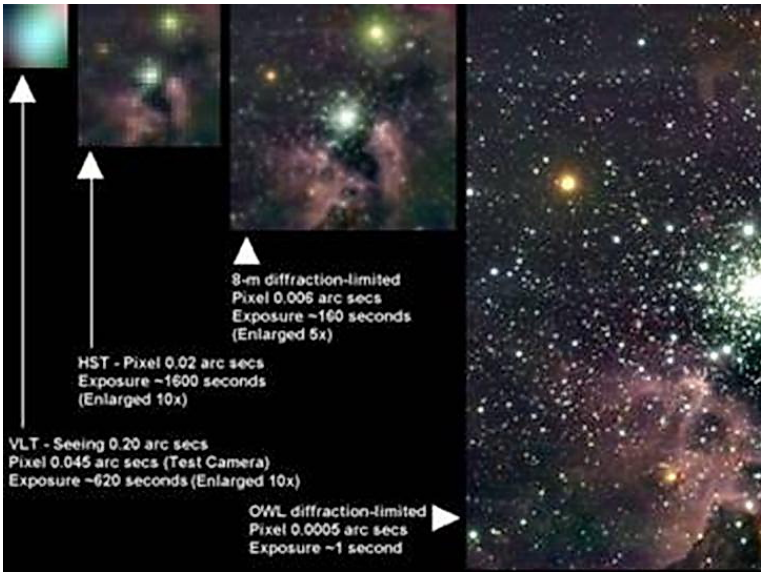

Figure 2.2: Examples of improved resolution importance (Gilmozzi and Dierickx, 2000)

For this purpose, the OverWhelmingly Large (OWL) telescope design concept (Gilmozzi and Dierickx, 2000) was developed to reach an extreme dimension for the primary mirror of 100 m diameter. Some of the best sites to use the ground based telescopes are at high altitudes, where atmospheric conditions are stable, such as the Paranal observatory in Chile or Mauna Kea in Hawaii. These geographically remote sites make the shipment of very large monolithic mirrors a real challenge.

2.1.2 Large segmented primary mirror telescopes

A relatively new design approach to build large primary telescope mirrors has been introduced. Instead of building the primary mirror in one piece, hexagonal segmented parts were assembled to create the primary mirror of the Keck Telescope in Hawaii (Nelson, 2000). A new generation of extra large telescope (ELT) designs have emerged based on Keck's primary mirror segmented approach. These include: The California Extremely Large telescope (CELT) (Nelson, 2000), the Giant Segmented Mirror Telescope (GSMT) (Strom et al., 2003), the Very Large Optical Telescope (VLOT) (Crabtree et al.,

2003), the Thirty Meter Telescope (TMT) (Stepp and Strom, 2004), the Euro50 (Andersen et al., 2003) and the Overwhelmingly Large telescope (OWL) (Gilmozzi and Dierickx, 2000).

The ELT designs range between 30 and 100 metres in diameter. This will break the traditional laws of the art of telescope making: the cost law, the cost is usually proportional to the diameter $D^{2.6}$ and the growth law, the size of the next generation telescope is twice as large as the previous one (Gilmozzi, 2004). The size growth will be a factor of 3 to 10, depending on the project (Figure 2.3).

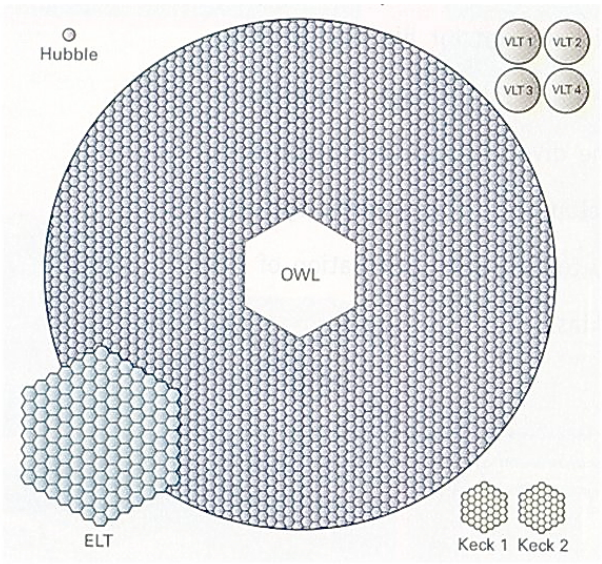

Figure 2.3: Size comparison of different telescope primary mirrors (Szeged, 2007)

The cost range of these projects is 600 to 1000 million Euros (Gilmozzi, 2004). The cost is expected to be much lower with a large scale segment production. The number of pieces to manufacture in 5 years is about 500 to 2000 segments. Some studies indicate that, with the actual manufacturing techniques, these will be a great challenge (Shore and May-Miller, 2003).

The proposed ELTs segments will be based on either a spherical or off axis parabolic design. Spherical segments will be manufactured at lower cost than off axis parabolic ones. However, off axis parabolic segments have previously been used for the Keck project and should lead to an "easier" optical conception. The last important difference is that the spherical segments will be interchangeable but not the parabolic ones (Dierickx, 2000).

At the end of 2006, two concepts, Euro50 and OWL, were merged by the European community into a new project, the European Extremely Large Telescope (E-ELT) (Gilmozzi

and Spyromilio, 2007). This telescope (Figure 2.4) will have a "smaller" 42m primary mirror to reduce the risk of the whole project.

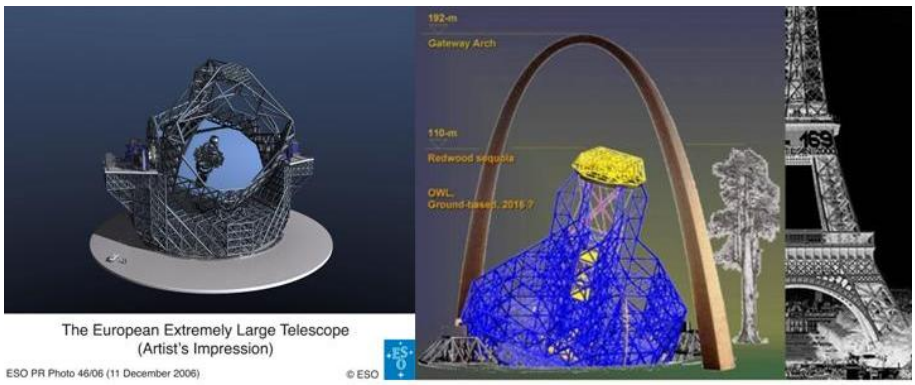

Figure 2.4: European Extremely Large Telescope (Gilmozzi and Dierickx, 2000)

Two different designs for this E-ELT project are being studied. At the moment, the preference goes to a five mirrors design ahead of a Gregorian design. Each design uses an aspheric primary mirror with a 42 m diameter. This mirror is made of 900 hexagonal segments of 1.45 m peak to peak each (Gilmozzi and Spyromilio, 2007). The time-scale for the construction of the chosen design is seven years starting after the final three years design study that should be achieved during 2009-2010 (Gilmozzi and Spyromilio, 2007).

2.2 Other large optics demand

The development of a number of major science projects and advanced manufacturing technologies have increased the demand for large size optics. For example, lithography machines require large optics to manufacture integrated circuits. Laser confined nuclear fusion projects such as the National Ignition Facility in US and its equivalent in France, the Laser Mega Joule will use large mirrors. Those projects demand a continuous replacement of large quantities of optics. This continuous demand requires an increase of manufacturing capabilities of large optics. The industry sector, from the material manufacturer to the machining plants, has to migrate from rather small to large optimised production lines. Large quantities need to be produced quicker than the current manufacturing time.

2.2.1 Inertia fusion studies

Two large projects are under development, the National Ignition Facility (NIF) in US and the Laser Mega-Joule (LMJ) in France. Due to their large demands of optics in a short timescale, these projects have driven the improvement of optical manufacturing and measurements.

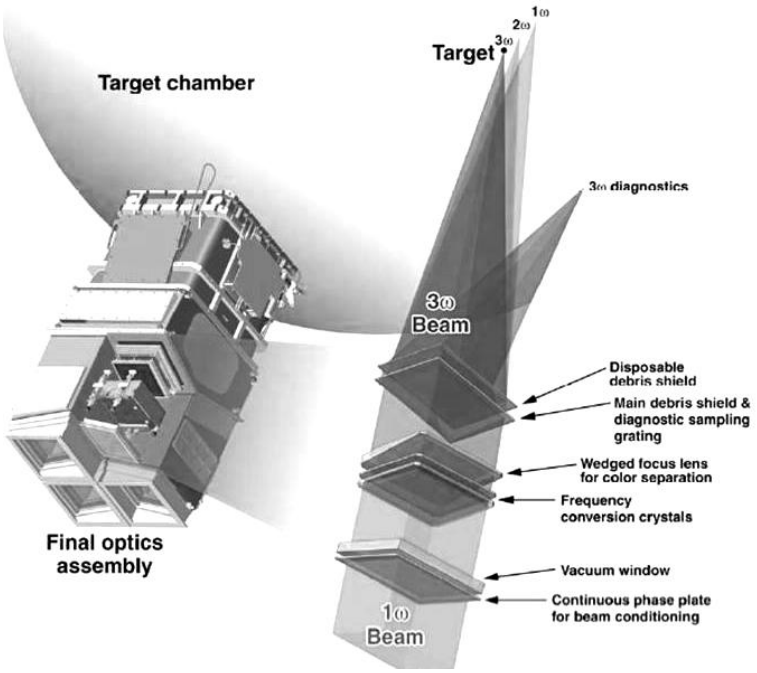

Figure 2.5: NIF - Final optics assembly (Bibeau et al., 2006)

The NIF required 7360 optics between 500 mm to 1000 mm diameter in materials such as BK7 and SiO_2. This corresponds to a production rate of about one hundred large optics per month (Campbell et al., 2004).

The LMJ project also needs a large amount of optics. The testing facility for that technology called "Ligne Intégration Laser" (LIL), used 135 m^2 of polished glass. The full scale project, LMJ, will required 4000 m^2 of polished glass. Development of improved manufacturing processes will be necessary to produce its 4200 glass laser plates with a dimension of 810 mm x 460 mm (CEA, 2007).

2.2.2 Lithography

Optical lithography systems are employed to manufacture integrated circuits since the late 1970s. The need of smaller features sizes has required an improvement in the technology and the optics (Stulen, 1999). Some of the main companies involved in lithography are Nikon, Canon, Zeiss and ASML. It evolved through stepper technology, scanner technology and finally Extreme Ultraviolet Lithography, EUVL (Fay, 2002, Ronse, 2006).

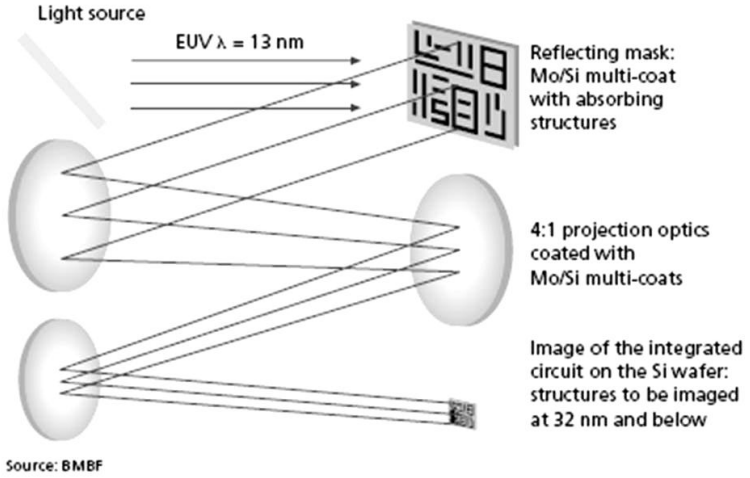

Figure 2.6: EUV lithography optic system (Löfken, 2008)

A recent lithography technique, Extreme Ultraviolet Lithography EUVL, has imaging beams reflected by mirrors instead of refracted by lenses (Löfken, 2008). It requires projection optics with a figure accuracy of 0.25 nm rms. The roughness levels are 0.20 nm rms mid-spatial frequency roughness and high spatial frequency roughness of 0.10 nm rms. These optics needs to be aspherics (Taylor et al., 1998).
The lithography masks are made of low CTE optics materials such as Zerodur, BK7 and ULE. The peak to valley accuracy needs to be better than 50 nm. Low defects concentration is also required (Kemp and Wurm, 2006, Paret et al., 2002).

2.2.3 Earth observation

A number of new projects, such as Earth observation cameras, demand large lightweight optics.

Figure 2.7: Lightweight IRIS CVD SiC mirror (Onaka et al., 1999)

By 2030, for example, NASA roadmap on precise optics shows demands for a decrease in areal density and cost by two and ten times respectively.
Cryogenic missions will require over 400 mirrors, in the range of 2 m class optics, with an areal density < 30 kg/m^2 with a figure accuracy > 10 nm RMS.
Other missions will require precise optics. For example, over 40 mirrors, in the range of 2 m class optics, will require an areal density < 40 kg/m^2, with a figure accuracy < 10-15 nm RMS. The aim is to produce 25000 m^2 of optics at < $2000 per m^2 (Feinberg, 2005, Stahl and Feinberg, 2007).

2.3 Mirror substrate materials

This thesis concentrates on substrate materials for large segmented telescope primary mirrors. The main optical materials, that have been considered, for making large telescope segments are: Glass (ULE®), Glass ceramic (Zerodur® , Clearceram®), Ceramics (SiC, CVD SiC) and some others materials such as Beryllium (Matson, 2003, Shore and May-Miller, 2003, Ohara, 2008).
For example, Keck and GTC telescopes have been made out of zero expansion glass ceramics. Silicon carbide is also a potential material (Dierickx et al., 2004). It is stiffer than Zerodur. The support structure, therefore the whole telescope, can be made lighter (Dierickx, 2000). Beryllium will not be investigated. While it has been demonstrated that 1 m components can be made, there are several issues. For example, the raw material cost and its dimensional stability compared to glass-ceramics through time are major concerns (Dierickx, 2000).

Mechanical and thermal properties for main optical materials are shown in Table 2.1.

Material	Density ρ (g/cm^3)	Elastic modulus E (GPa)	Knoop hardness H (GPa)	Fracture toughness K_{Ic} (MPa.m$^{1/2}$)	Thermal conductivity k (W/(m.K)	CTE α (10^{-6}/K)
Zerodur	2.52	91	6.2	0.9	1.63	0.05
Clearceram	2.55	90	6.4	-	1.52	0.04
ULE	2.2	70	4.6	1.8	1.35	0.025
Fused Silica	2.2	72.5	4.8	0.74	1.30	0.57
SSiC	3.15	420	27.4	3.5	190	2.1
CVC SiC	3.18	456	28.5	3.39	140	2.33

Table 2.1: Optical material properties

The comparison of the potential materials can be done by using different ratios of mechanical and thermal properties (AMEC Dynamic Structures Ltd., 2002). These ratios highlight the behaviour of each material to machining. For example, the specific stiffness (ρ/E) relates to the flexion of the component under high pressure. The steady state thermal distortion (α/k) corresponds to the thermal expansion under high grinding temperature (Matson, 2003, Dierickx, 2000).

2.3.1 Glass

Corning 7971, best known as ULE® , is an ultra low-expansion glass (Hamilton et al., 2004). It is a hard and brittle material. It is an amorphous glass made of fused silica (92.5 % SiO_2) doped with Titanium (7.5 % TiO_2). There are no crystalline phases. It is manufactured by Corning in US. Its coefficient of thermal expansion (CTE) at room temperature is twenty times lower than pure fused silica (Materials, 2007, VanBrocklin et al., 2004).

2.3.2 Glass ceramics

Zerodur® is a glass-ceramic composite manufactured by Schott in Germany (Pannhorst, 2002). Its linear thermal expansion coefficient is almost zero in the temperature range 20 °C to 300 °C. Zerodur has a completely non-directional structure, and a non-porous surface (Viens, 1990). The crystalline and glass phases have chemical characteristics and hardness values similar to those of optical glass. It is 25 % vitreous phase and 75 % crystalline phase. Zerodur is processed using the same machines and tools as optical and technical glasses (Walker et al., 2002).

2.3.3 Ceramics

Silicon carbide (SiC) is a non oxide ceramic. It is isotropic and homogeneous. It is dimensionally stable when subjected to repeated temperature variations (Walker et al., 2002). There are several different manufacturing processes for producing SiC (AMEC Dynamic Structures Ltd., 2002, Foss, 2005, Krodel, 2006).
For example, sintered silicon carbide (SSiC) is produced in France by Boostec. The SSiC (98.5 % SiC and 1 % boron as sintering additive) shows a polycrystalline structure with highly isotropic physical properties (Bougoin and Deny, 2004). A residual porosity is due to the sintering process as illustrated in Figure 2.8.

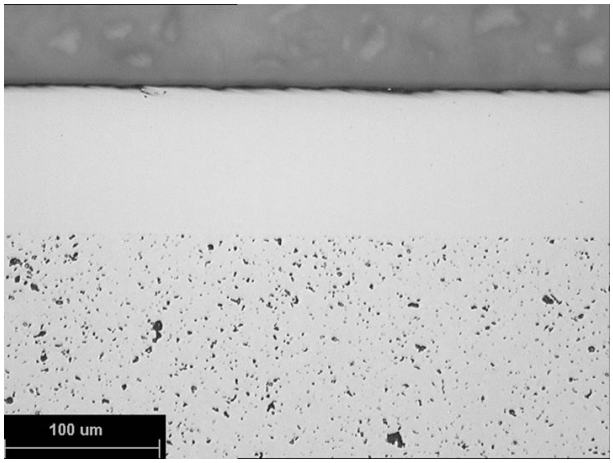

Figure 2.8: CVD SSiC cross section micrograph - Boostec (Shore and Parr-Burman, 2003)

To remove the surface porosity, a CVD SiC coating around 100 μm thick, is deposited before final grinding and polishing (Bougoin and Deny, 2004).

2.4 Optical fabrication technologies

The machining accuracy achievable, using different technologies over more than sixty years, is represented in Figure 2.9. This shows that each process expectation and perception continue to improve with time. The same processes are continuously developed to be more efficient while achieving better surface quality output.

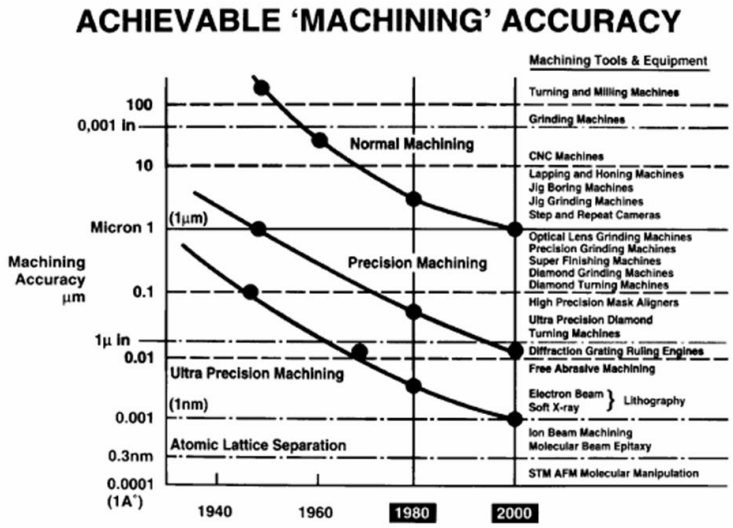

Figure 2.9: Development of achievable "machining" accuracy [From McKeown... after Taniguchi (Corbett et al., 2000)]

To achieve our project peak to valley form accuracy of 1 μm, the machining operation employed can be classified as precision machining. Many different types of precision machining technologies, such as grinding, have been reported to achieve this form accuracy (Stowers et al., 1998). This form accuracy needs to be combined with high removal rate. Many of these precision machining technologies do not offer a material removal rate over 10 mm^3/s.

Figure 2.10 shows different machining processes with their respective achievable surface roughness (RMS) and material removal rate.

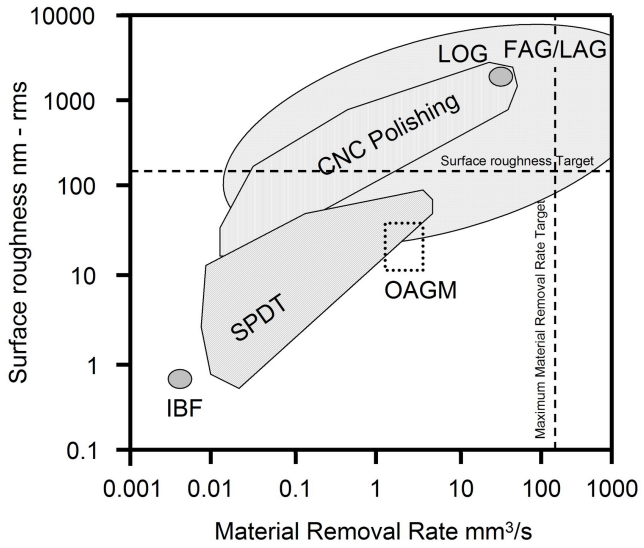

Figure 2.10: Different precision machining processes - Surface roughness rms versus removal rate (After (Stowers et al., 1998) and (Shore and Parr-Burman, 2003))

The different machining processes mentioned are single point diamond turning (SPDT), conventional fixed or loose abrasive grinding (FAG/LAG), computer numerical control polishing (CNC) and non-contact machining (Ion Beam Figuring - IBF) (Stowers et al., 1998). Each machining process achieves the surface roughness targeted of 150 nm. The project maximum material removal rate of 200 mm^3/s is achievable using a fixed abrasive grinding process. To achieve 1 μm peak to valley form accuracy over one metre, a precise and repeatable controlled process is necessary. The quality of the grinding process is function of the grinding machine input errors. A precise grinding machine with a dedicated grinding mode is required.

2.4.1 Material removal mechanisms

Material removal of brittle materials can be achieved through brittle, semi-ductile or ductile mode grinding.

Ductile grinding mode has been reported to achieve minimal subsurface damage (Bifano et al., 1991) in brittle materials. For such materials, this "ductile" mode is limited in regards of removal rate as it is only achievable with very low critical depth of cut. For example, this depth of cut is 50 nm for Zerodur (Shore et al., 1995).

Wills-Moren (Wills-Moren et al., 1990) showed ductile grinding is reached with high static stiffness, over 220 N/μm, and high dynamic stiffness between the grinding wheel and the workpiece for BK7 and Zerodur. The depth of cut was controlled within 10 nm

with high resolution accurate motion. A rigid bond grinding wheel was trued within 10 nm. A continuous dressing technique was employed to keep cutting efficiency. Ball et al. (1991) and Shore (1995) also showed that ability to machine glasses in a ductile mode was considered to be machine tool dependent. A dynamically stiff machine induces high quality surface finishes with minimum subsurface damage and relative high material removal rate.

Micro brittle fracture (Inasaki, 1987) grinding supports higher manufacturing rates. This mode leaves surface and subsurface damage on brittle materials ground surfaces. An efficient grinding process will require the optimization of the grinding parameters to reduce the amount of subsurface damage. The micro fracture mechanisms that lead to sub-surface damage have been extensively investigated by Lawn (Lawn and Wilshaw, 1975).

2.5 Grinding machines

Few large grinding machines have been purposely built for grinding large optics.
In 1985, the Large Optics Generator (LOG) was built by the Optical Science centre in Arizona University. It is a large bridge-type vertical spindle grinder that machines single mirror glass blanks up to 8 m in diameter. A spherical cup shaped grinding wheel with a tilt angle is used (Parks, 2004). Its grinding removal rate is 28 mm^3/s for a final form error of 4 μm and a surface roughness about 2 μm-rms (Parks et al., 1985).

In 1989, a high performance grinding machine, Cranfield Precision OAGM2500 (Figure 2.11), has been developed for Eastman Kodak .

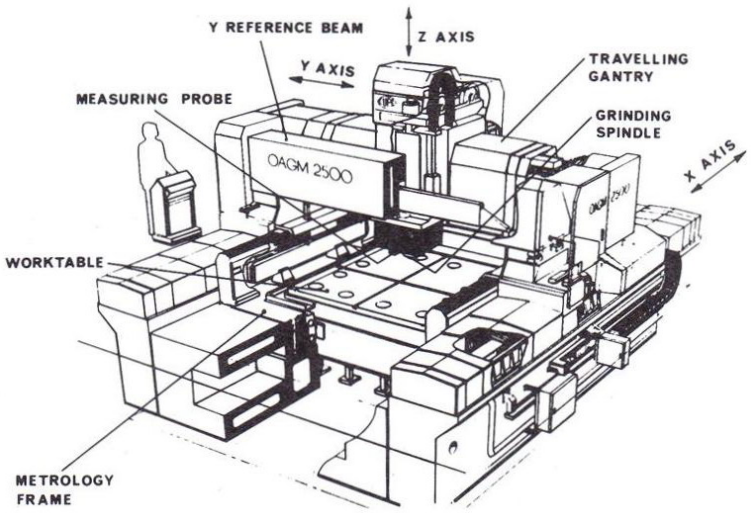

Figure 2.11: Kodak OAGM 2500 (Leadbeater et al., 1989)

This machine has a "low damage" grinding mode. It has a material removal rate of 1-5 mm^3/s with a surface roughness R_a of 10-50 nm and a form accuracy P_t of 2-5 μm per metre. The associate subsurface damage is less than 10 μm for optical components of 2.5 metres dimension (Leadbeater et al., 1989, Shore and Walker, 2004).

In 2005, another grinding machine, BoX® , was built by Cranfield Precision based on a design concept from Cranfield University Precision Engineering Centre (Shore et al., 2005). The maximum material removal rate target was 200 mm^3/s with a surface roughness of 50-150 nm RMS and a form accuracy P_t of 1 μm per metre.

Those dedicated high precision grinding machines are built following design principles found in diamond turning machines. This is necessary to obtain high form accuracy and process repeatability over one metre. The amount of heat generated is minimized. The hydrostatic grinding spindle is specified to achieve only required maximum material removal rate targeted to minimize unnecessary generated heat. Thermal control loops are implemented for every component that generates heat. The heat fluctuation during the grinding process is reduced to a minimum. A separate metrology frame enables in situ measurement of the ground part and error compensation for repeatable grinding machine and grinding process errors.

2.6 Machine tool errors: Design, reduction and compensation

The assessment of machine tools errors have extensively been reported and discussed over the years (Hocken et al., 1977, Bryan, 1979, Eman et al., 1987, Belforte et al., 1987, Hale, 1999). The identification of those errors is important to obtain high precision grinding machines. The machine tool errors can be described using an error budget of each specific motion (Donaldson, 1980, Donmez et al., 1986, Thompson, 1988). Those machine tool errors can be separated into geometric/kinematic errors, thermal error, fixture dependent error and cutting force induced errors (Thompson and McKeown, 1989, Ramesh et al., 2000).

Two different approaches are used in assessment of random errors in machine tools. The deterministic approach considers that "random" errors are random only because they have not been understood and measured yet (Bryan, 1984). Another view is that "random" errors are defined as "those which under apparently equal conditions at a given point do not always have the same value and can only be expressed statistically" (Bryan, 1984). This statement was first published in 1978 in a report from the metrology committee of CIRP (CIRP, 1978).

An example of grinding machine that follows the deterministic approach is the BoX grinding machine. Its design follows "eleven principles and techniques" in precision engineering employed at Cranfield University (Cranfield Precision Engineering Centre, 2005). Different precision engineering groups have described and combined those design principles differently (Schellekens et al., 1998, Slocum, 1992).

The following sections describe the source of errors, which influences the precision grinding process. An important factor to control is the distance between the grinding wheel and the workpiece over extended grinding operations time. Geometric errors, thermal errors, grinding machine stiffness and grinding wheel wear errors are discussed. Error compensation strategies, applied on highly repeatable errors, are identified.

2.6.1 Machine performance errors

Three important definitions in machine performance errors are accuracy, repeatability and resolution. Figure 2.12 illustrates those definitions' differences.

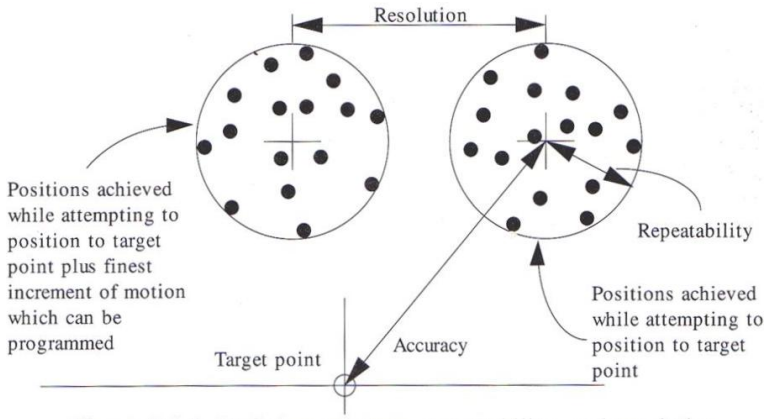

Figure 2.1.1 Defining accuracy, repeatability, and resolution.

Figure 2.12: Accuracy, repeatability & resolution definitions (Slocum, 1992)

Accuracy is "the maximum translational or rotational error between any two points in the machine's work volume". Repeatability is "the error between a number of successive attempts to move the machine to the same position". Resolution is "the larger of the smallest programmable step or the smallest mechanical step the machine can make during point-to-point motion" (Slocum, 1992). Those errors are quasi static and dynamic generated.

The types of geometric errors encountered are positioning, straightness, angular squareness and parallelism (Ferreira and Liu, 1986, Sartori and Zhang, 1995). Those errors are due to the machine tool design and the components quality used.

The evaluation of the dynamic characteristic of the machine structure and the individual elements is required in precision machining (Franse et al., 1991). The machine modes generate excitations that result in geometric error on the machine part (Schultschik, 1981). This can limit the operational grinding speed or axis acceleration and movements. This dynamic response can be estimated theoretically during the design stage (Shore et al., 2005). Vibrations are induced by the grinding spindle and table spindle rotations and friction in the axis motions. For example, the use of counterweight for the Z axis generates geometric errors that can be reduced by designing damping systems (Lin et al., 2008).

2.6.2 Thermal errors

Two types of heat sources have been identified: external such as workshop temperature and internal generated by spindles, motors and machining process (Bryan, 1990, Weck et al., 1995). Those heat sources induce thermo-elastic deformations. The installation of the machine tool in a temperature controlled room reduces the error due to an external heat source. During the machine tool design, the internal heat sources can be reduced and insulated. The use of a counterweight for the Z axis can reduce the motors uses and therefore heat consumption (Weck et al., 1995). Models simulating thermal drifts are used during the design stage (Weck et al., 1995). The accuracy of the model boundary conditions is essential and studies have investigated the importance of joint contacts (Gashi and Shore, 2006).
Another important technique is the cooling and control of any oil, water cooling and coolant fluid in the system. This can be done using cooling water system with temperature sensors and monitoring temperature loops (Leadbeater et al., 1989).
The critical components of the machine tool can also be cooled to maintain a relative constant working operational temperature (Saito et al., 1994). The use of oil showers over the machine tool is also efficient (Weck et al., 1995).

As a structural loop, the thermal loop is "a path across an assembly of mechanical components, which determines the relative position between specified objects under changing temperatures" (Schellekens et al., 1998).
For example, some NIF optics required a constant monitoring of the thermal deflection of the part and the fixture. They were made of phosphate which is a high thermal expansion material. Kaman's eddy current gauges were employed to record the movement of the optic assembly with time (Boland, 1999).
Another example is the design of a spindle in low thermal expansion glass-ceramic to reduce the influence of thermal effects. This spindle was installed in a precise grinder with hydrostatic oil bearings. The grinding results show 5 nm P-V on NbFl optical glass and sub micron flatness on various glasses (Namba et al., 1989).

The remaining thermal errors can be reduced by error compensation techniques.

2.6.3 Grinding machine loop stiffness

Grinding machine tool static and dynamic stiffnesses are important in precision grinding operations (Wills-Moren et al., 1982, 1990, Franse et al., 1991, Shore, 1995, Nakao and Hatamura, 1996, Zhang et al., 1999). The grinding machine needs to be designed with those concepts in mind. A structural machine stiffness can be identified following a closed loop (Koenigsberger and Tlusty, 1971, Schlesinger, 1978, Slocum, 1992). An example of grinding machine "closed" loop stiffness (Holroyd Edgetek machine) is shown in Figure 2.13.

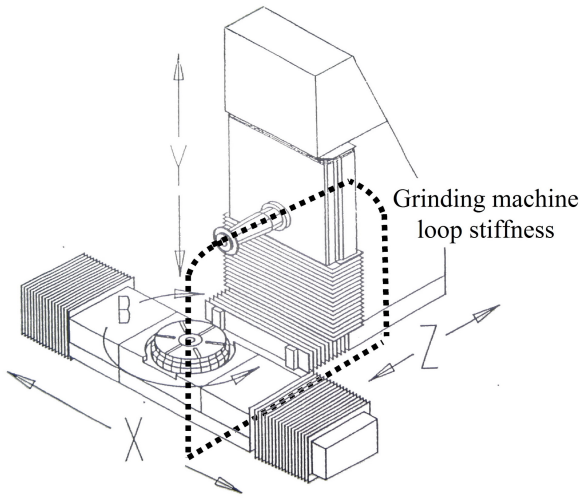

Figure 2.13: Grinding machine loop stiffness - Holroyd Edgetek machine

Each individual machine element stiffness, such as bearings, linear slides, rotary table, contribute to final machine structural loop stiffness. Other important contributors to the grinding loop stiffness are the grinding wheel, workpiece and holding fixture (Corbett et al., 2002). It is necessary to evaluate the interaction between the grinding wheel and the workpiece.

The grinding machine dynamic response during grinding is more difficult to identify. The use of specific materials for the machine tool bed and main structure is important to improve machine dynamic response (McKeown and Morgan, 1979, Schellekens et al., 1998).

The interaction between the grinding wheel and holding fixture is an important part of the grinding loop stiffness. It defines the amount of material that is actually removed compared to the programmed depth of cut. The grinding wheel needs to be designed in

such a way that the core body deflection is minimized.
Figure 2.14 illustrates the interaction between grinding wheel and workpiece/holder (Yang et al., 2001).

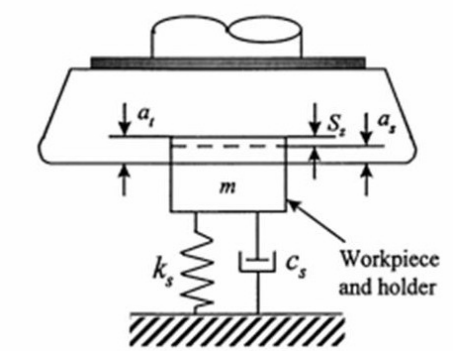

Figure 2.14: Static model grinding wheel-workpiece/holder interaction (Yang et al., 2001)

The influence of a core aluminium body was described in grinding silicon carbide. The maximum chip thickness equation was adjusted taking into account the ratio between grinding wheel body and workpiece elastic modulus (Gopal and Rao, 2004).

In a micro level, the abrasive layer compression under grinding pressure has to be taken into consideration. In fact, the elastic modulus of the wheel body and abrasive layer are different. Smaller deflections were observed using a harder wheel grade (Saini, 1990). The influence of the workpiece hardness was seen as a contribution due to the increase of normal grinding forces for similar grinding parameters (Wager and Saini, 1986, Saini and Wager, 1985).

2.6.4 Grinding wheel wear error

A grinding wheel is subject to wear during grinding process. The abrasive layer as well as the diamond grits wear out. The grinding wheel working life is governed by its cutting efficiency and its form accuracy. To evaluate the grinding wheel wear, the G ratio (Malkin, 1968, Lindsay, 1983, Malkin, 1989) can be used. This factor relates the ratio between the volume of material removed (Δv_w) and the volume of wheel wear (Δv_s).

$$G = \frac{\Delta v_w}{\Delta v_s} \tag{2.6.1}$$

The grinding ratio decreases with lower concentrations and smaller grit (Inasaki, 1987). The grinding wheel wear behaviour described in Figure 2.15, is similar to other wear processes (Jackson, 2004).

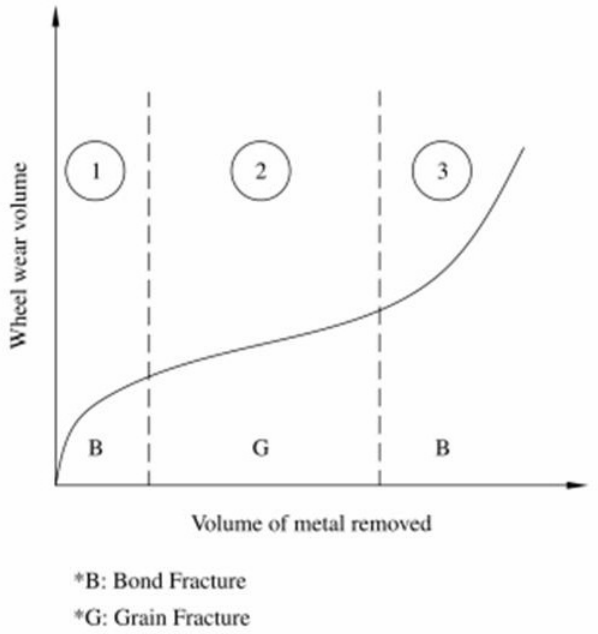

Figure 2.15: Wheel wear curve (Jackson, 2004)

Three successive phases have been identified. The grinding wheel wear is initially high due to bond fracture (1). This is followed by a steady state wear due to grain fracture (2). The final phase is a dramatic wear acceleration (3). This leads to dressing of the grinding wheel to regain cutting efficiency. If the abrasive layer geometry is lost, the grinding wheel needs to be trued. This curve can be plotted by conducting repeated grinding tests. Those tests have to be repeated for each grinding wheel and grinding conditions combination.

Different in-process methods to measure grinding wheel wear have been developed (Hassui et al., 1998, Fan et al., 2002, Furutani et al., 2003). For example, a measurement technique is based on an "imprint technique" (Li et al., 2004). After a set amount of material removed, the grinding wheel form is recorded by plunging the grinding wheel into a test block. The grinding wheel form and wear magnitude is measured using a profilometer.

2.6.5 Error compensation techniques

The careful design of a machine tool with high static and dynamic stiffness and thermal controlled loops reduces significantly the amount of residual errors (Wu and Ni, 1989). A subsequent possible improvement of the machine tool accuracy is error compensation of geometry errors, grinding wheel wear, and thermal errors (Ferreira and Liu, 1986, Weck et al., 1995, Sartori and Zhang, 1995). For example, thermal drift can be reduced by up to 90% through error compensation (Weck et al., 1995).

Those errors compensation methods are efficient when high repeatability is achieved and following deterministic measurement principles (Schellekens et al., 1998).
There are two approaches to error compensations named "pre-calibrated error compensation" and "active error compensation" (Ramesh et al., 2000). The "pre-calibrated error compensation" is based on highly repeatable processes. The finite element analysis and developed models are trying to remove specific errors before grinding. Errors measured for a specific grinding process can be compensated during subsequent grinding operations. For example, using an independent metrology frame removes combined errors that are measurable on the workpiece after grinding.

Precision grinding can be achieved by the use of a separate metrology frame (Estler, 1985) included in the grinding machine (Wills-Moren and Wilson, 1989, Donaldson and Patterson, 1983). This enables the in-situ measurement of the ground part. The ground profile is measured using the in-situ metrology frame. This measurement is subtracted from the theoretical part profile and the residual error obtained is included in the CNC programme. Therefore, the machining path programmed will grind the reverse shape error. This technique relies on the repeatability of the error generated and the accuracy of the measurement taken.

Figure 2.16 shows an example of such a metrology frame on the OAGM grinder.

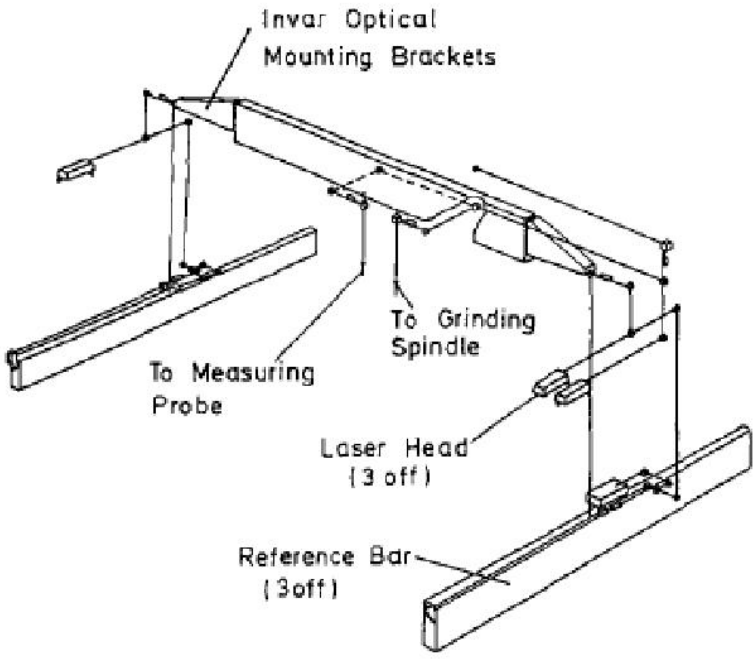

Figure 2.16: OAGM laser interferometer system (Wills-Moren and Wilson, 1989)

The frame has a reference bar kinematically mounted and is separated from the grinding loop. An air bearing vertical probe is used to measure the ground part. This measurement is compared to the straightedge through a retroreflector (Wills-Moren and Wilson, 1989). Other examples of machines that used metrology frames are the Large High Precision CNC Diamond Turning Machine (Wills-Moren et al., 1982), the Large Optics Diamond Turning Machine (LODTM) (Donaldson and Patterson, 1983) and the BoX grinding machine (Shore et al., 2005).

"Active error compensation" is based on monitoring the grinding process and applying error compensation during that same process. Error compensation of the grinding process can be done using force, power or acoustic emission sensors. Grinding machine thermal and geometric distortions can be monitored and compensated on-line.

2.7 Precision grinding process

2.7.1 Grinding modes for optical grinding

Different grinding modes have been described to machine aspherical surfaces. Some modes are based on using dedicated grinding machines designed for specific optical components geometry and dimensions. Other grinding modes are applicable on "generic" built grinding machines.

Figure 2.17 illustrates the parallel grinding and cross grinding methods.

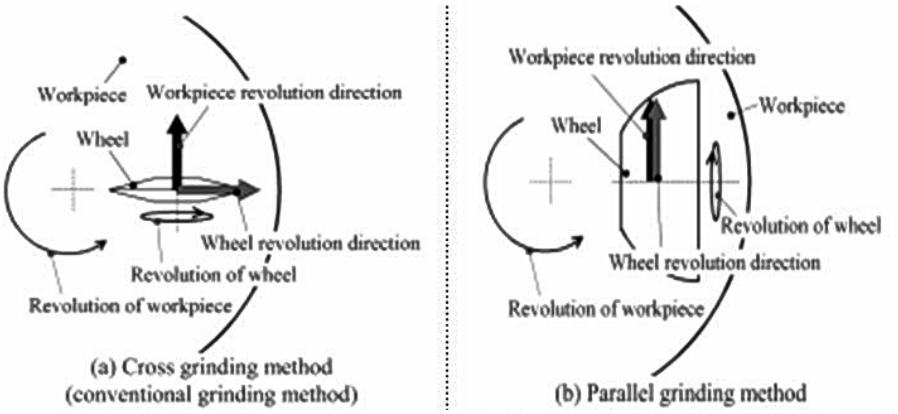

Figure 2.17: Different grinding modes for aspherical optics (Yoshihara et al., 2004)

In the cross grinding method (a), the grinding wheel revolution direction is perpendicular to the workpiece revolution direction. As its name suggests, in parallel grinding (b), the workpiece and grinding wheel revolution directions are parallel (Yoshihara et al., 2004). Those grinding methods were compared on BK7 glass (Sun et al., 2006). The results

show that ductile regimes enable higher removal rate in parallel grinding than in cross grinding. Different primary and secondary wheel wear zones were also identified.
Variation of the grinding mode is achieved by tilting the grinding spindle at an angle with a spherical cup grinding wheel (Parks et al., 1985).

The Kodak OAGM machine was built to grind large off axis optical components. This grinding machine has 3 linear axes. Its grinding mode is illustrated in Figure 2.18.

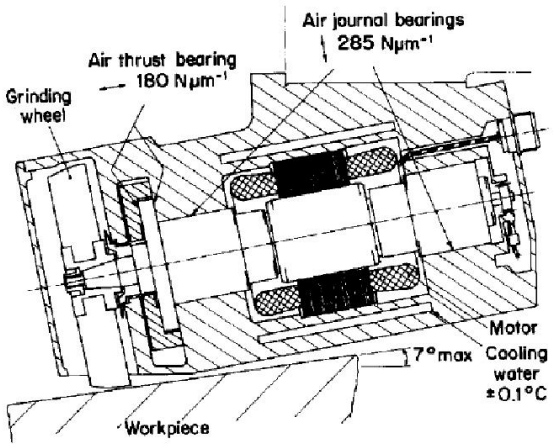

Figure 2.18: OAGM grinding mode (Leadbeater et al., 1989)

This grinding machine used a fixed workpiece. This workpiece is inclined to minimize the angle and maximum sagitta seen by the grinding tool. The Z axis is moved above the part to generate the optic shape. The grinding spindle is inclined at 10°, limiting the maximum optic slope to 7°. The grinding wheel used is spherical (Leadbeater et al., 1989).

Other grinding modes can be employed to shape concave optics. Figure 2.19 describes different grinding modes for toroidal optics.

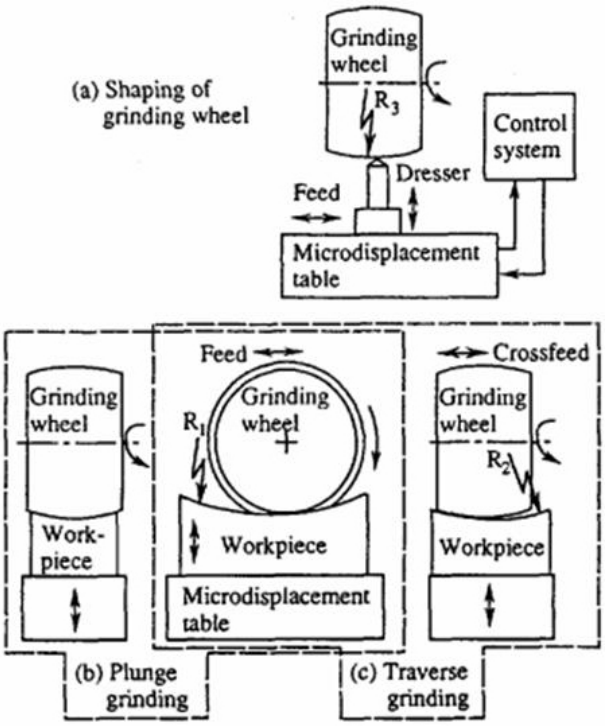

Figure 2.19: Different grinding modes for toroidal optics (Zhong and Nakayama, 1992)

The grinding wheel is precisely ground to the right shape using a dresser (a) placed on a microdisplacement table. In the case of plunge grinding (b), the grinding wheel is shaped to the same radius of curvature as the final optic width. The grinding wheel is made larger than the workpiece. A microdisplacement table is used to slow feed the workpiece into the grinding wheel. By truing differently the grinding wheel, this grinding process can be used to grind toroidal or cylindrical shapes. In the case of traverse grinding (c), the grinding wheel is smaller than the workpiece. A crossfeed is used along with the feed to shape the workpiece (Zhong and Nakayama, 1992).

For aspherical optics, another grinding mode uses a cup grinding wheel. Figure 2.20 shows two ways of setting up the workpiece and the grinding wheel.

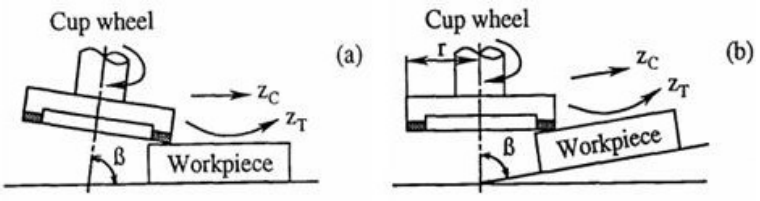

Figure 2.20: Different grinding modes for aspherical optics (Zhong and Nakagawa, 1996)

The cup wheel is fixed at a defined angle β in method (a). The workpiece is kept flat. The grinding wheel is controlled along the z_c direction. The depth is controlled along

z_t to generate the required shape. In method (b), this time, it is the workpiece that is set at an angle β. The grinding wheel is moved along z_c and z_t to generate the desired shape (Zhong and Nakagawa, 1996).
Namba et al. (1997) used grinding method (a), in Figure 2.20, with a resin bonded cup diamond wheel. The results showed a super smooth optical glass surface obtained without polishing through ductile grinding mode.

Another grinding mode called "Arc Envelope Grinding Method" (AEGM) was developed (Kuriyagawa et al., 1996). This grinding mode is compared to a conventional one in Figure 2.21.

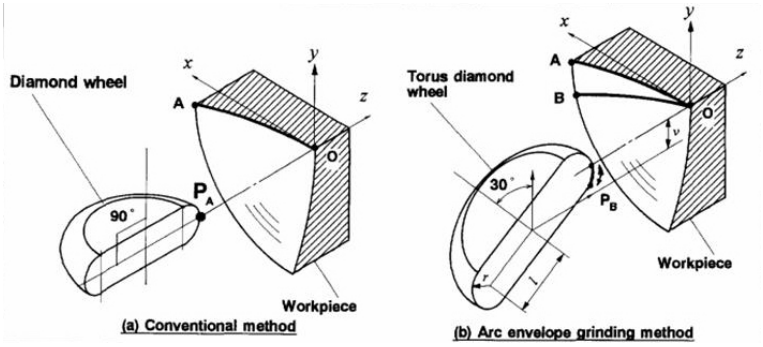

Figure 2.21: "Arc Envelope Grinding Method" (AEGM) (Kuriyagawa et al., 1996)

The conventional grinding wheel is kept perpendicular to the ground shape at all time. The grinding zone in contact remains the same. The grinding wheel wear is concentrated in that region. The AEGM approach (b) uses a toric wheel at a fixed angle. In this example, the angle is fixed at 30°. The grinding zone changes during the grinding. The full width of the grinding wheel is employed. The grinding wheel has a constant spread wear.

2.7.2 Grinding wheels type

The choice of grinding wheel is important. Many parameters have to be chosen. Its shape type, bond type and abrasive type are some examples. Each of those parameters follows an ISO standard. Each grinding wheel can be bespoke to suit specific grinding configurations. The grinding wheel can be defined with the supplier to suit the type of ground materials and grinding conditions defined (Meyer and Klocke, 2000).

- Shape cup wheel

The grinding wheel shape is described following designation in ISO 6104 ((ISO 6104:2005, 2005)). The grinding wheel reference corresponds to combination of core shape and superabrasive section shape as illustrated in Figure 2.22.

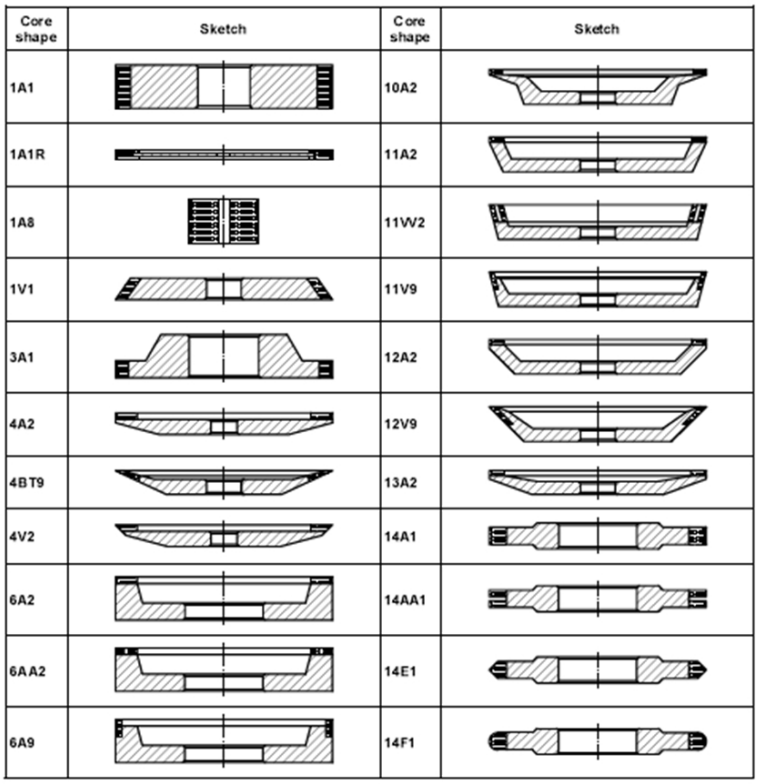

Figure 2.22: Grinding wheel shapes - ISO 6104:2005

For example, the reference 12A2 corresponds to a core shape, number 12 and a superabrasive section, A2. The core shape is a taper cup grinding wheel. The superabrasive section is one side and flat.

- Bond materials

The superabrasives grinding wheel abrasive layer can be made in different bond materials such as metal, plated, vitrified, resin, and polyimide (Bryant, 1998, Galen, 2001, Webster and Tricard, 2004). The bond material is chosen to fit the material ground.

For grinding optical components, a metal bonded grinding wheel needs a slow grinding process to avoid cracks due to the high pressure and hard bond (Zhang and Howes, 1995). The vitrified bond wheel loses its form quickly and is subject to damage under medium pressure. The resin bond wheel induces less damage to the grinding surface (Inasaki, 1987, Mayer Jr. and Fang, 1994). It is made usually of phenolic resins with a dedicated structure depending on its applications. This grinding wheel type wears quite fast but it can be dressed and trued easily to keep its form. It can not stand high temperatures. The polyimide bond wheel is similar to a resin bond wheel. However, a polyimide resin can be used with additives that improve the heat or wear resistance.

- Abrasives

Two main grits size standard designations are employed. The American National Standards Institute (ANSI) uses "mesh size". It corresponds to the number of wires per inch on the diamond-sizing screen. The Fédération Européenne des Fabricants de Produits Abrasifs (FEPA) and ISO uses "standard grain size". It is the size of the opening in the calibrated control sieves. This designation corresponds to grains between a maximum and minimum grain diameters described in ISO 6106 (ISO 6106:2005, 2005).
Table 2.2 shows examples of the relation between grit size and mesh size.

ISO grit designation	Equivalent mesh size (US) (#)	Sieve through which 99,9 % must pass (μm)	0,5 % max. through (μm)
D251	60/70	384	151
D181	80/100	271	107
D126	120/140	197	75
D91	170/200	139	57
D76	200/230	116	49
D46	325/400	75	32
D25$*$	800$*$	29$*$	25$*$
D16$*$	1200$*$	18$*$	12$*$
D10$*$	1800$*$	12$*$	8$*$
D6.3$*$	3000$*$	8$*$	4$*$
$*$	not same standard		

Table 2.2: Diamond grain sizes (ISO 6106:2005, 2005)

The wheel concentration is the amount of diamond mixed within the grinding wheel bond. For example, a concentration of 100 equals to 25 % of the matrix volume. This corresponds to 4.4 carat per cm^3 in one cm^3 of abrasive coating (Bryant, 1998).
Table 2.3 shows some more values.

Designation	Quantity (% by volume)	Weight (carat/cm^3)	Weight (g/cm^3)
C150	37.5	6.6	1.32
C100	25.0	4.4	0.88
C75	18.75	3.3	0.66
C50	12.5	2.2	0.44

Table 2.3: Diamond grain concentrations and weights

2.7.3 *Forming techniques*

The grinding wheel form is obtained by forming the abrasive layer. Different forming techniques are employed to generate the desired shape. This truing operation is subsequently repeated at regular interval to retain the correct grinding wheel form. The truing operation has to be carefully done. A comparison for very fine diamond grinding wheels was done to grind optical fibres. The results show that loose abrasive truing pull out less diamonds and left more active grits on the grinding wheel (Chen et al., 2005).

The forming wheel can shape different forms onto the grinding wheel. Inasaki (1989) mentioned the use of a truing wheel on a brake truing system as a standard truing system for resin bonded grinding wheel. The truing silicon carbide wheel used has a width of 25 mm. The parameters used were a traverse speed of 33 mm/s, a down feed 20 μm per pass. The ratio of grinding to truing wheel surface speeds is 0.6 with the grinding wheel speed at 23 m/s.

A swing arc truer with a green silicon carbide cup wheel was successfully used for truing and dressing fine grit resin bonded diamond wheels (Kuriyagawa et al., 1993). The form accuracy achieved was 0.8 μm over 15 mm and a radius error of 0.16 mm for a 30mm radius.

Different forming techniques examples are shown in Figure 2.23 (Derkx et al., 2008).

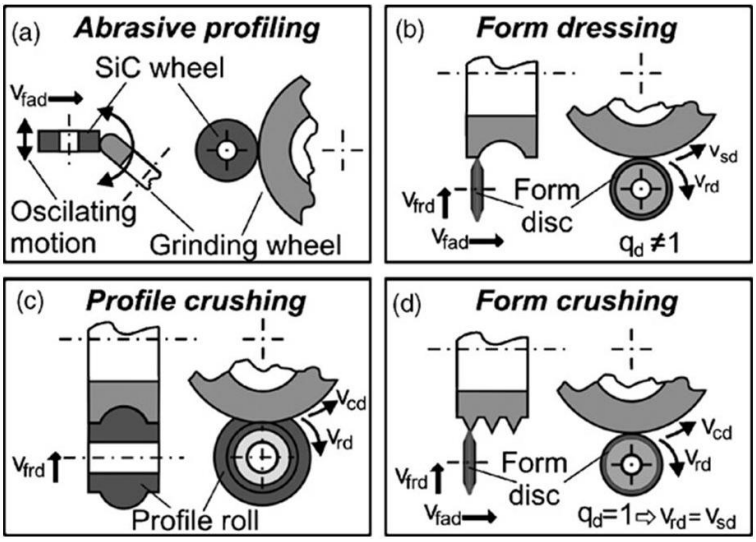

Figure 2.23: Different forming techniques (Derkx et al., 2008)

The truing operation can be done by abrasive profiling (a) which uses a "soft" forming wheel such as vitrified silicon carbide (Derkx et al., 2008), to grind the grinding wheel

profile. Form dressing (b) is similar but the forming wheel is made of hard bond and large diamond particles such as electroplated nickel wheel. The speed ratio (q_d) between the truing wheel speed (v_{rd}) and grinding wheel speed (v_{cd}) varies from 0.7 up to 0.9 (Derkx et al., 2008). Profile crushing (c) is employed for grinding wheels with brittle bonds. The forming roller is shaped to the negative of the grinding wheel. The in-feed speed (v_{frd}) is of one per rotation of the grinding wheel. This wheel rotates at very low speed around 2 m/s. The speed ratio is kept to one to avoid tangential forces (Derkx et al., 2008). Form crushing (d) uses a form disc which feeds (v_{fad}) across the grinding wheel.

Single point diamond "dressing" is another forming technique. As its name implies, a single point diamond is run across the grinding to true it. The accuracy of the shape profile is set at the traverse speed of the diamond. It is close to the forming technique (Figure 2.23b). The radius of the diamond leaves small cusping on the grinding tool (Chen and Rowe, 1996).

2.7.4 Dressing techniques

After the forming operation, the grits are at the same level as the bond. The dressing operation is necessary to "open" the grinding wheel. The dressing operation exposes the abrasive grits by removing carefully the bond around the diamonds that creates a sharp layer of abrasives. The dressing needs to be made carefully to get a good grinding efficiency because this can lead to lack of grits exposed or grits pull-out. The dressing operation needs to be done often to keep the grits exposed as the grinding process intends to fracture and pull out the grits. A high load on the grinding wheel has to be avoided to keep the grinding wheel integrity. As the truing and dressing of the grinding wheel influenced directly the grinding efficiency, experiments have been conducted to get a better understanding of the best speed ratio, truing and dressing time and processes (Inasaki, 1989).

- Dressing sticks

Inasaki (1989) discussed dressing of resin bonded diamond wheels. The dressing sticks used were silicon carbide sticks, C220G8V. Alumina oxide dressing sticks were also used successfully on resin bonded grinding wheels (Mayer Jr. and Fang, 1994, Hwang and Malkin, 1999).

- Electrolytic in-process dressing

Electrolytic in-process dressing (ELID) is a technique that continuously dresses the grinding wheel. Ohmori and Nakagawa (1995) have developed this technique successfully on metal bonded grinding wheels. Figure 2.24 shows the ELID dressing method (Ohmori et al., 2001).

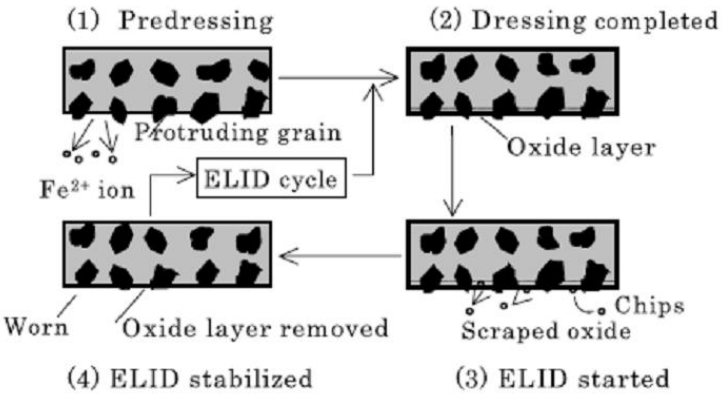

Figure 2.24: ELID dressing technique (Ohmori et al., 2001)

The ELID set up is composed of a direct current power source, an electrode and metal bond wheel. When the grinding coolant is fed, an electrolysis occurs between the grinding wheel and the electrode (1). An oxide layer is generated (2) and is removed during the grinding (3). Once this oxide layer is gone, the electrolysis is repeated (4). This continuous dressing of the grinding wheel enable use of fine grit size grinding wheels.

For example, ELID dressing with bronze bonded grinding wheels was tested and monitored for phosphate optics for the NIF project (Boland, 1999). Ductile grinding of BK7 and SF10 optical glasses with low damage was achieved with cast iron grinding wheels with very fine grit sizes (3-6 μm) (Ball et al., 1991). Other surface roughnesses (R_a) reported using a cast iron # 4000 grinding wheel are 9 nm, 15 nm, 11 nm for CVD SiC, SSiC and Zerodur respectively. The depth of cut was 0.7 μm, traverse pitch was 0.5 mm and surface speed 125 mm/s (Dai et al., 2004).

A limitation of this technique is the need of a conductive abrasive layer. A resinoid bonded grinding wheel with mixed carbon was developed. In 2004, ELID dressing using this wheel was reported (Itoh et al., 2004). The surface roughness quality achieved on silicon using a # 8000 grinding wheel was 185 nm-PV without ELID and 30 nm-PV with ELID. The surface roughness was better with the metal free grinding wheel than the equivalent cast iron bonded wheel. However, the cutting quality was poor with higher wheel axial load.

Another important limitation of ELID is that the grinding wheel form changes with time. Researches have been looking at controlling the ELID process and compensate for wheel

wear (Sazedur Rahman et al., 2008).

After error compensation, a Schmidt plate in Fused Silica was produced using a 0.5 μm depth of cut and a feed rate of 0.3 mm/s. Over 200 mm x 300 mm, a 2.5 μm form accuracy and 180 nm roughness was achieved with # 1200 cast iron grinding wheel (Shaohui et al., 2005).

- Laser dressing

Laser dressing is an alternative technique. Successful demonstrations were carried out with pulsed Nd:YAG lasers on bronze bonded (Hosokawa et al., 2006), vitrified bonded (Jackson et al., 2007) and resin bonded (Xie et al., 2004) grinding wheels. No thermal damage was observed. As a non contact dressing operation, the laser dressing for resin bonded wheel is more suitable than a mechanical dressing with a corundum (aluminium oxide) block (Xie et al., 2004).

2.7.5 Nozzle and coolant selection

The choice of nozzle design and coolant type is important as it can influence grinding wheel wear and surface roughness (Brinksmeier et al., 1999).

- Nozzle designs

The adequate application of coolant is the grinding contact zone is difficult. The use of a coherent and laminar flow is necessary. A laminar flow is obtained for Reynolds number below 2300 (Webster et al., 1995). The Reynolds number, R_e is calculated using equation 2.7.1 for a slot nozzle (Marinescu et al., 2004*a*).

$$R_e = \frac{\rho \times v_{slot} \times h_{slot}}{\eta} \tag{2.7.1}$$

with η is the dynamic viscosity of the fluid (water = 0.001 Pa·s) and ρ is the density of the fluid (water = 1000 kg/m^3). For a slot nozzle, the coolant velocity is v_{slot} and slot thickness is h_{slot}.

The use of designed nozzles helps to reach those conditions (Webster et al., 1995). Figure 2.25 shows a round nozzle (a) and a traditional nozzle (b).

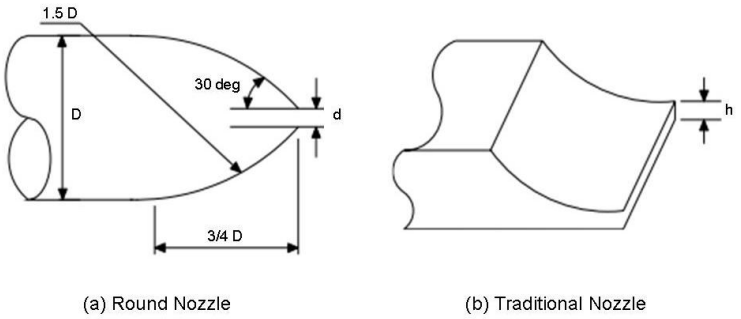

Figure 2.25: Different grinding nozzle designs (Irani et al., 2005)

The nozzle outlet height is called d and h for round and traditional nozzles respectively. The round nozzle shape is proportional to its inlet diameter D. The use of a coherent flow helps to have a cooling efficiency that works at different distances to the grinding zone. Matching as close as possible the grinding wheel speed and the coolant velocity will reduce the friction effect on the grinding wheel (Brinksmeier et al., 1999, Ramesh, Yeo, Zhong and Sim, 2001). It also helps to breach the air barrier generated around the grinding wheel (Irani et al., 2005).

- Coolants

The grinding coolant reduces friction between the grinding wheel and the workpiece. It removes swarfs from the contact zone and reduces the risk of loading the grinding wheel. The grinding contact zone and the grinding wheel need to be cooled down to avoid burn (Irani et al., 2005). Coolants are divided into oil based and water based (Brinksmeier et al., 1999). The water based emulsion coolant is a mix of water with low oil percentage. Water based emulsions are successfully used to grind ceramics (Inasaki, 1987, Evans et al., 1997). Additives are used to improve chemical and physical coolant characteristics. Other additives are anti-corrosion and anti-oxidants substances (Brinksmeier et al., 1999).

2.8 Grinding process characterisation

The grinding process parameters for a parallel grinding process are illustrated in Figure 2.26

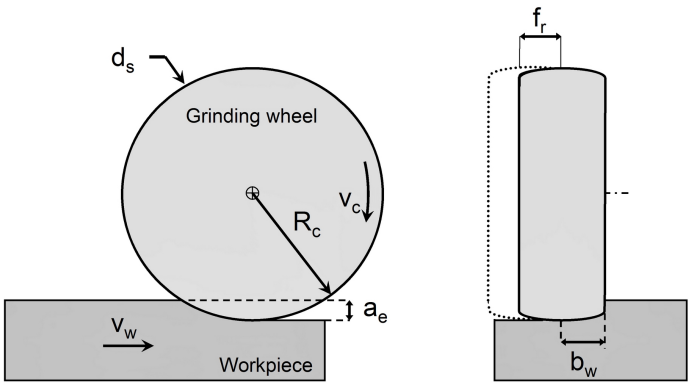

Figure 2.26: Grinding process parameters

The material removal rate (Q_w) is calculated using equation 2.8.1.

$$Q_w = a_e \times f_r \times v_w \tag{2.8.1}$$

with a_e depth of cut, f_r feed per revolution or feed per step and v_w workpiece surface speed. The specific material removal rate (Q'_w) is the material removal rate divided by the grinding wheel contact width (b_w). It is calculated using equation 2.8.2.

$$Q'_w = \frac{a_e \times f_r \times v_w}{b_w} \tag{2.8.2}$$

2.8.1 Contact length

In grinding, the ideal contact length is proportional to the depth of cut and the wheel diameter. Figure 2.27 illustrates the real contact length.

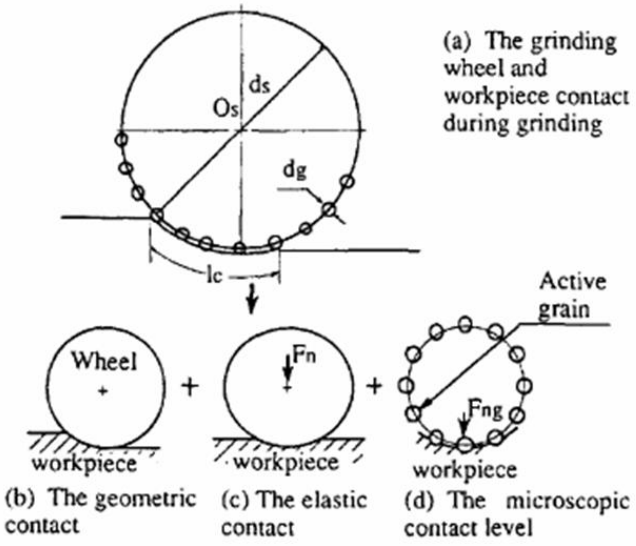

Figure 2.27: Real contact length (Rowe et al., 1993)

The real contact length, l_c, is influenced by the contact pressure between the workpiece and the grinding wheel and the depth of cut. The contact length obtained for a given applied force (F_n) is l_f. For a given depth of cut, the contact length is l_g.

Rowe et al. (1993) summarised different published equations to calculate the actual contact length. Using Hertz contact theory, the calculated contact length is described in equation 2.8.3.

$$l_c = [8 \times F'_n(K_s + K_w)d_s + a_e d_s]^{0.5} = (l_f^2 + l_g^2)^{0.5} \tag{2.8.3}$$

with F'_n the specific normal grinding force, K_s the grinding wheel elastic coefficient, K_w the workpiece elastic coefficient and d_s the grinding wheel diameter.

$$K_s = (1 - \upsilon_s^2)/(\pi E_s) \tag{2.8.4}$$

$$K_w = (1 - \upsilon_w^2)/(\pi E_w) \tag{2.8.5}$$

with E_w the workpiece modulus of elasticity, E_s the grinding wheel modulus of elasticity, υ_s the workpiece Poisson's ratio and υ_w the grinding wheel Poisson's ratio. The specific normal grinding force is used instead of the pressure as the tangential force contribution to Hertz contact is considered negligible. Therefore, the contact length l_c is equal to l_g when the specific normal grinding force is very small and equal to l_f when the depth of cut is very small.

2.8.2 Number of active grits per unit area

Different equations can be used to calculated the number of active grits per unit area such as equation 2.8.6 (Xu et al., 1997), equations 2.8.7 and 2.8.8 (Li and Liao, 1997). The grinding wheel specifications such as diamond grit size and concentration are employed.

$$C_1 = \frac{4f}{d_g^2(4\pi/3\upsilon)^{2/3}} \tag{2.8.6}$$

With grit diameter d_g = 15.2 M^{-1}, υ is volume fraction, M mesh size and constant f = 0.5 for half of diamonds active (Agarwal and Venkateswara Rao, 2008).

$$C_2 = \beta_s \times \frac{6\upsilon}{\pi d_g^2} \tag{2.8.7}$$

$$C_3 = (\frac{6\upsilon}{\pi d_g^3})^{2/3} \tag{2.8.8}$$

With β_s, holding strength of the abrasive grits in the wheel, varying between 0 and 1 (Li and Liao, 1997). For each of those equations, the diamond grits geometry was assumed to

be spheres of diameter d_g. The calculated values overestimate the grit concentrations for small grit sizes (Mayer Jr. and Fang, 1994, Xu et al., 1997, Agarwal and Venkateswara Rao, 2008).
Another possibility has been to count the number of grits per area using optical microscope or three dimensional profilometer (Tamaki and Kitagawa, 1995, Li and Liao, 1997).

2.8.3 Maximum undeformed chip thickness

The maximum undeformed chip thickness (h_{max}) is used to compare different grinding processes (Malkin, 1989). The influence of different grinding parameters, on the specific grinding energy, surface quality or grinding forces, are studied using the maximum undeformed chip thickness (Hwang and Malkin, 1999, Hwang et al., 1999, Huang et al., 2003). The maximum undeformed chip thickness is determined using equation 2.8.10 (Huang et al., 2003) or equation 2.8.9 (Malkin, 1989).

$$h_{max} = \sqrt{\frac{3}{C \times r} \times \frac{v_w}{v_c} \times \sqrt{\frac{a_e}{d_s}}} \tag{2.8.9}$$

$$h_{max} = \sqrt{\frac{3}{C \times tan(\theta)} \times \frac{v_w}{v_c} \times \sqrt{\frac{a_e}{d_s}}} \tag{2.8.10}$$

These equations include the wheel topography with the number of active grits per unit area (C) and grit geometry. The chip width-to-thickness ratio (r) or semi-included angle for the undeformed chip cross-section (θ) are used. These values are difficult to determine experimentally. A value of 10 was chosen for r (Mayer Jr. and Fang, 1994). The θ values are reported (Huang et al., 2003) to be around 75° for a sharp grit and 50° for a worn or dull grit. The grit geometry is assumed to be triangular. The influence of grinding wheel wear on the grinding process can be studied. A limitation is the possibility to measure the grit geometry at different stages of the grinding process.

Mayer Jr. and Fang (1994) compared those two different ways to calculate h_{max}. It was concluded that C and r have to be measured. To measure the wheel grit depth of cut, equation 2.8.10 is the most adequate equation.

In 2004, a modified equation was developed based on grinding experiments on silicon carbide. This model includes the grinding wheel elastic modulus and the workpiece elastic modulus in addition to the previous known models (Gopal and Rao, 2004).

$$h_{max2} = \left[\frac{E_1}{E_2}\right]^{0.548} \times h_{max} \tag{2.8.11}$$

The modulus of elasticity E_1 of the diamond grinding wheel is the grinding wheel core material modulus of elasticity. This assumption was made as the abrasive layer thickness

was 4 mm. E_2 is the modulus of elasticity of the workpiece. E_1, E_2 and the equation factor need to be redefined for thicker abrasive layers or different workpiece materials.

2.8.4 *Equivalent chip thickness*

The equivalent chip thickness (h_{eq}) is used to compare grinding processes (Snoeys et al., 1974). It is defined as the material layer thickness removed at a cutting velocity (Rowe and Chen, 1997).

$$h_{eq} = \frac{Q'_w}{v_c} \tag{2.8.12}$$

Using h_{eq}, grinding parameters influence on grinding forces and grinding energy, for a given grinding wheel, can be compared. A size effect is observed as the specific grinding energy value increases with a decrease in h_{eq} value (Kompella et al., 2001). In comparison with the maximum undeformed chip thickness, fewer variables have to be measured. For example, no grinding wheel measurement is required. The equivalent chip thickness is influenced by the wear of the grinding wheel radius of curvature. A limitation is that the influence of grit wear on the grinding forces is not taken into consideration.

The equivalent chip thickness can relate to specific tangential grinding force (F'_t) using equation 2.8.13 (Marinescu et al., 2004*b*).

$$F'_t = F_1 h_{eq}^f \tag{2.8.13}$$

with a constant f between 0.7 and 1.0 and F_1, an initial specific tangential grinding force. The ratio h_{eq}/l_g is the dimensionless theoretical chip cross section, as shown in equation 2.8.14 (Roth and Tonshoff, 1993).

$$\frac{h_{eq}}{l_g} = \frac{v_w}{v_c}\sqrt{\frac{a_e}{d_w}} \tag{2.8.14}$$

with d_w the workpiece diameter. This was used to characterise grinding conditions as the maximum chip thickness, h_{max}. The values employed are easier to obtain than for h_{max}. This ratio can only compare the same grinding wheel with the same dressing technique. The assumption is made that the spacing between cutting edges remains constant for a given grinding wheel (Roth and Tonshoff, 1993).

2.8.5 *Grinding forces*

Grinding force models have been developed extensively as shown in the review made by Tönshoff et al. (1992).
Liang (Liang and Devereux, 1993) described the normal grinding forces as the penetration loads applied on the grits. The tangential grinding forces are due to friction between the

grits and the workpiece as well as a coolant viscous effect. The grinding forces models are described in equations 2.8.15 and 2.8.16.

$$F_n = c_n \times v_w \times a_e \tag{2.8.15}$$

$$F_t = c_t \times v_w \times a_e \tag{2.8.16}$$

with c_n and c_t constants. The normal and tangential forces are proportional to the product of workpiece velocity and depth of cut. The normal and tangential grinding forces are proportional to a friction coefficient, μ, shown in equation 2.8.17.

$$F_t = \mu \times F_n \tag{2.8.17}$$

The specific normal grinding force (F'$_n$) is calculated using equation 2.8.18. Equation 2.8.19 corresponds to the specific tangential grinding force.

$$F'_n = \frac{F_n}{b_w} \tag{2.8.18}$$

$$F'_t = \frac{F_t}{b_w} \tag{2.8.19}$$

A model was evaluated to determine the dominant material removal mechanism in ceramics, brittle fracture or micro cutting. Equations 2.8.20 and 2.8.21 correspond to a micro cutting mode and a grain dislodgement removal mechanism respectively (Huang and Liu, 2003). The specific normal grinding force is also influenced by the ground material characteristics as shown in equation 2.8.22 (Yin et al., 2005).

$$F_n = \beta_1 \times H \times \left(\frac{v_w}{v_s}\right) \times a_e \tag{2.8.20}$$

$$F_n = \beta_2 \times \left(\frac{K_c^{1/2} H}{E^{2/5}}\right) \times \left(\frac{v_w}{v_s}\right)^{3/4} \times a_e \tag{2.8.21}$$

$$F'_n = \beta_3 \times \left(\frac{K_c^{1/2} H^{9/10}}{E^{2/5}}\right) \times \left(\frac{v_w}{v_s}\right)^{3/4} \times a_e^{11/12} \times d_s^{1/12} \tag{2.8.22}$$

with β_1, β_2 and β_3 constants representing grinding wheel topography. The normal grinding force is proportional to both grinding wheel and workpiece speeds.

Different studies showed that the total normal grinding force is a combination of a cutting force and a coolant induced force. This coolant induced force is due to the hydrodynamic pressure generated between the grinding wheel and the workpiece and increases with the grinding wheel speed. This force has the same magnitude as the cutting force and sometimes even higher (Brinksmeier et al., 1999). Yin et al. (2005) recorded coolant induced forces up to six times higher than the cutting normal grinding force on ceramics. Klocke et al. (2000) recommended the use of a shoe nozzle to reduce the total normal grinding

forces. Its design reduces the demand of coolant flow needed to reach the grinding gap. For "low" grinding wheel speed of 30 m/s, the coolant induced force is reduced significantly.

Yang et al. (2001) studied the influence of the machine tool stiffness on the normal grinding force. This leads to a modified grinding force (F_z) taking into account the actual depth of cut (a_t) and machine static stiffness (k_s).

$$F_z = F_0 + C_a a_s = \frac{F_0 + C_a a_t}{1 + C_a/k_s} \tag{2.8.23}$$

with F_0 the break-in force, C_a a constant and a_s the set depth of cut of grinding wheel. The normal grinding force per grit (f_{gn}) is used in a number of models such as indentation theory for subsurface damage investigations (Yang et al., 2001).

$$f_{gn} = \frac{k_f F_z}{N} = \frac{2k_f F_z}{\pi R C b_w} \tag{2.8.24}$$

with k_f a constant, R wheel edge radius and N number of active cutting points.

Matsuo et al. (1989) studied the influence of the grain shape and sharpness on grinding forces in steels using a single grit test. A dull grain leads to higher normal grinding forces. A different grain shape showed different tangential grinding forces but similar normal grinding forces.

2.8.6 Grinding power

The total power (P_{tot}) is divided into grinding power (P_c), coolant power and general power loss. The grinding power is a fraction of the actual total grinding spindle power employed as shown in Figure 2.28 (Brinksmeier et al., 1999).

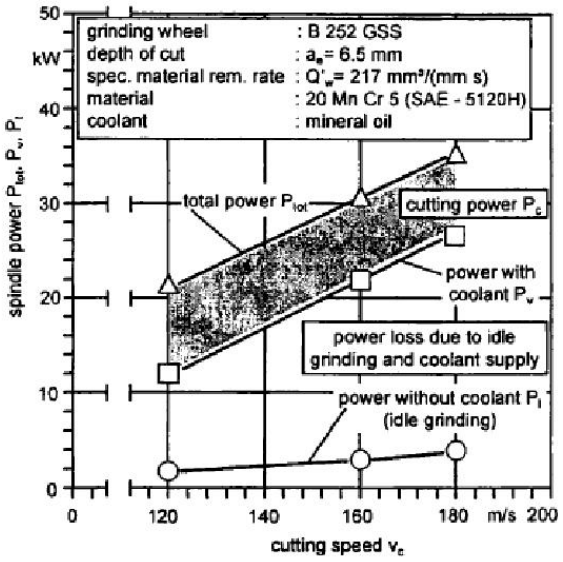

Figure 2.28: Total power (Brinksmeier et al., 1999)

General power loss (P_v) is due to coolant power loss and idle grinding power (P_i) necessary to rotate the grinding wheel. The coolant power loss is due to the hydrodynamics effects increasing the tangential force. The acceleration of the coolant velocity and the drag effect into the grinding contact zone are two other factors (Brinksmeier and Minke, 1993). The grinding coolant velocity is usually lower than the grinding wheel velocity. The power loss, due to the power coolant and "no load" power, can reach 80% of the total power. Figure 2.28 shows that coolant power loss is significantly reducing with a decrease of grinding wheel speed (Brinksmeier et al., 1999). For "low" grinding wheel speed of 30 m/s, the coolant power loss is anticipated to be reduced significantly.

The grinding power can be calculated using the tangential grinding force (Malkin, 1989).

$$P_c = F_t \times (v_s \pm v_w) = F_t \times v_s \tag{2.8.25}$$

The equation is simplified as the workpiece surface speed v_w is much smaller than the grinding wheel speed v_s.

2.8.7 Grinding energy

During grinding, the energy necessary to create a chip is transformed into different forms. Figure 2.29 shows the three grinding process steps.

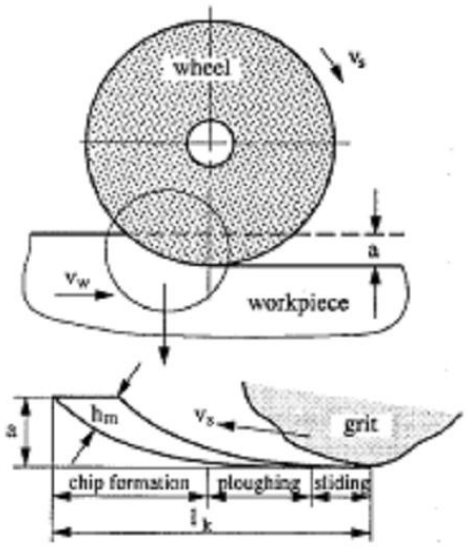

Figure 2.29: Grinding process steps (Rowe and Chen, 1997)

The grinding process is separated into sliding, ploughing and chip formation. The grinding power has been divided in a similar way (Malkin, 1989). When the grain depth of cut decreases, the sliding and ploughing powers proportions are more important. It leads to an increase in grinding energy (Rowe and Chen, 1997). The main amount dissipates through thermal energy while a small amount generates residual stresses in the ground part (Inasaki, 1987, Tönshoff et al., 1992). The specific grinding energy required to grind a material for particular machining conditions is calculated using equation 2.8.26 (Liang and Devereux, 1993, Malkin, 1989, Hwang et al., 1999).

$$e = \frac{F_t \times v_c}{Q_w} = \frac{P_c}{Q_w} \tag{2.8.26}$$

Figure 2.30 shows examples of specific grinding energy (u) versus maximum undeformed chip thickness (h_m) on ceramic (SiC) and glass (soda-lime).

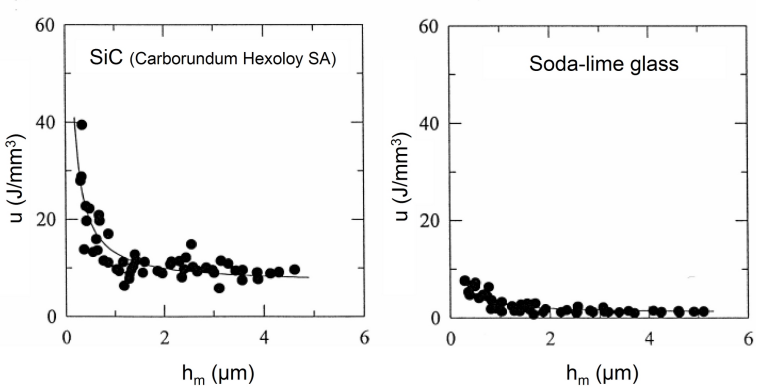

Figure 2.30: Specific grinding energy versus maximum undeformed chip thickness - Examples (Hwang and Malkin, 1999)

Those specific grinding energies are generated using a resin bonded diamond grinding wheel with # 180 grit size. The maximum undeformed chip thickness was calculated using equation 2.8.10. The specific energy is much lower in glass than SiC for a given maximum chip thickness. The specific grinding energy is influenced by the maximum chip thickness. This relation is showed in other studies (Inasaki, 1987, Huang and Liu, 2003). From a high h_{max} value to a critical h_{max} value, the specific energy stays quasi constant. The removal mode is mainly fracture mode. From that given value, the specific grinding energy has a rapid increase. The removal mode changed from fracture to ductile mode at higher specific energy.

Inasaki and Nakayama (1986) used equation 2.8.27 to show a close relation with the specific grinding energy in ceramics.

$$a_m = w^2 \frac{v_w}{v_c} \sqrt{\frac{a_e}{d_w}} \tag{2.8.27}$$

with w the average distance between the active cutting edges and a_m, average cross-sectional area of the effective cutting edges.
The specific grinding energy increases with decreasing of a_m. This effect was confirmed in another study (Kitajima et al., 1992) to compare three different ceramics. A larger a_m value leads to a low grinding energy used. This shows that the grinding energy needed for a rough cut is less than for a fine cut (Kitajima et al., 1992).

The specific grinding energy can be calculated using the equivalent chip thickness (Marinescu et al., 2004*b*). This relationship is described by equation 2.8.28.

$$e = \frac{F_t}{b_w h_{eq}} \tag{2.8.28}$$

By combining equations 2.8.28 and 2.8.13, the specific grinding energy is equal to equation 2.8.29.

$$e = F_1 h_{eq}^{f-1} \tag{2.8.29}$$

2.8.8 Preston coefficient

The Preston coefficient C_p has been developed by Preston (Preston, 1927) and used in lapping and polishing processes. The Preston coefficient equation is:

$$C_p = \frac{Q_w}{F_N \times v_c} \tag{2.8.30}$$

It can be related to the specific energy with using the coefficient of friction between the workpiece and the tool (Tong et al., 2006):

$$C_p = \frac{Q_w}{\mu \times F_t \times v_c} = \frac{1}{\mu \times e} \tag{2.8.31}$$

The normal grinding force instead of the tangential grinding force is used in the equation. This is particularly interesting when the grinding forces are really low as in the grinding of glass. For example, it was used in investigating grinding of BK7 glass with a 2-4 μm resin bonded grinding wheel (Tong et al., 2006).

2.9 Surface texture and form

A grinding mode is characterized using the surface roughness, peak to valley profile and surface patterns. The measurement of the surface roughness and surface profile are recommended by ISO (ISO 4288:1998, 1998). Figure 2.31 gives the recommended sampling lengths and evaluation lengths to use for a 2D measurement taken from ISO 4288-1998 (ISO 4288:1998, 1998).

Ra µm	**Roughness sampling length** lr mm	**Roughness evaluation length** ln mm
(0,006) < $Ra \leqslant$ 0,02	0,08	0,4
(0,02) < $Ra \leqslant$ 0,1	0,25	1,25
0,1 < $Ra \leqslant$ 2	0,8	4
2 < $Ra \leqslant$ 10	2,5	12,5
10 < $Ra \leqslant$ 80	8	40

Rz[a] $Rz1\text{max.}$[b] µm	**Roughness sampling length** lr mm	**Roughness evaluation length** ln mm
(0,025) < Rz, $Rz1\text{max.} \leqslant$ 0,1	0,08	0,4
0,1 < Rz, $Rz1\text{max.} \leqslant$ 0,5	0,25	1,25
0,5 < Rz, $Rz1\text{max.} \leqslant$ 10	0,8	4
10 < Rz, $Rz1\text{max.} \leqslant$ 50	2,5	12,5
50 < Rz, $Rz1\text{max.} \leqslant$ 200	8	40

[a] Rz is used when measuring Rz, Rv, Rp, Rc and Rt.
[b] $Rz1\text{max.}$ is used only when measuring $Rz1\text{max.}$, $Rv1\text{max.}$, $Rp1\text{max.}$ and $Rc1\text{max.}$

Figure 2.31: Recommended sampling length - ISO 4288-1998

The choice of sampling length (l_r) is done in two steps. The expected achieved surface roughness defines the sampling length and evaluation length (l_n) to be used. The first measurement is analysed. The sampling length is changed until the expected surface roughness matches the actual surface roughness.

2.9.1 Surface Roughness

The arithmetic surface roughness, R_a is defined by ISO 4287:2000 (2000) as "the arithmetic average of the absolute values of the deviations of the surface profile height from the mean line within the sampling length, l_r". The total peak to valley surface roughness, R_t and maximum peak to valley surface roughness, R_z (after ISO 4287:1984) are defined as the "sum of the height of the largest peak height and the largest profile valley height within" the evaluation length, l_n and sampling length, l_r respectively.

For grinding, a rough approximation of the arithmetic roughness can be made by us-

ing the relation $R_t = 4 \times R_a$ (Malkin, 1989). Other approximations have been developed based on experimentation. For grinding of a glass mould (Meneghello et al., 2006), the relation became $R_z = 5.81 \times R_a^{0.86}$.

Hed et al. (1988) stated that surface roughness is inversely proportional to the Young modulus. Zhao (Zhao et al., 2007) showed that the surface roughness decreases with higher material fracture toughness using same grinding conditions.

Maximum undeformed chip thickness and chip cross sectional area are proportional to the surface roughness values (Mayer Jr. and Fang, 1995). Different equations, to obtain the surface roughness, have been developed based on grinding parameters and grinding wheel. An example is the surface scallop height, h_s, based on the grinding parameters and wheel estimated topography (Mayer Jr. and Fang, 1995).

$$h_s = \frac{v_w^2}{4 \times v_c^2 \times d_s \times C} \tag{2.9.1}$$

This equation showed some correlation with the surface roughness, R_a. Another parameter proportional to surface roughness is the theoretical cutting edge spacing, $w = C^{-1/2}$ (Mayer Jr. and Fang, 1995).

Other equations have been developed to obtain more precise estimation. Zhou and Xi (2002) studied the influence of wheel wear. However, many assumptions are still needed such as the wheel topography. Statistical approach (Ali and Zhang, 1999) has been reported but are based on important assumptions, such as that a groove generated by a grain is a circle (Agarwal and Venkateswara Rao, 2005).

Some variations in surface roughness need to be taken into account. Assumption is made that the surface roughness remains the same in every direction of the ground surface. Different surface patterns are generated using specific grinding modes as described in details in section 2.9.3. The surface roughness measured along and across cutting direction are reported to be different (Lodha et al., 1998).

2.9.2 Peak to valley profile

The theoretical surface profile generated using the chosen grinding mode for this research is illustrated in Figure 2.32.

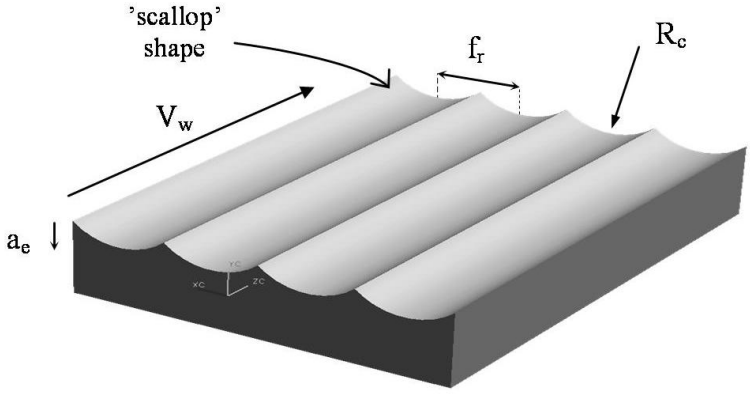

Figure 2.32: Peak-to-Valley profile example

The "scallop" shape generated by this grinding mode can be related to the shape left by a diamond turning tool. The surface profile generated can be estimated using an equation developed for diamond turning (Cheung and Lee, 2000) replacing the diamond tool radius by grinding wheel abrasive layer cutting radius.

$$P_t = R_c - \sqrt{R_c^2 - \frac{f_r^2}{4}} = R_c \left[1 - \sqrt{1 - \frac{f_r^2}{4 \times R_c^2}}\right] \tag{2.9.2}$$

with f_r the feedrate per revolution and R_c the wheel cutting radius.
This equation can be simplified based on the wheel radius been much larger than the feedrate per revolution. The final equation is equation 2.9.3 (Franse, 1990, Cheung and Lee, 2000).

$$P_t = \frac{f_r^2}{8 \times R_c} \tag{2.9.3}$$

From this equation, it can be deduced that for a given grinding wheel cutting radius, the feedrate per revolution is the only grinding parameter influencing the surface profile. This equation does not take into account any process error.

The depth of cut can be affected by vibrations, grinding wheel wear, temperature growth of the grinding spindle and grinding machine thermal errors (Takasu et al., 1985, Sata et al., 1985, Franse, 1991). An example of variations of cusp positions due to tool vibrations in diamond turning is illustrated in Figure 2.33.

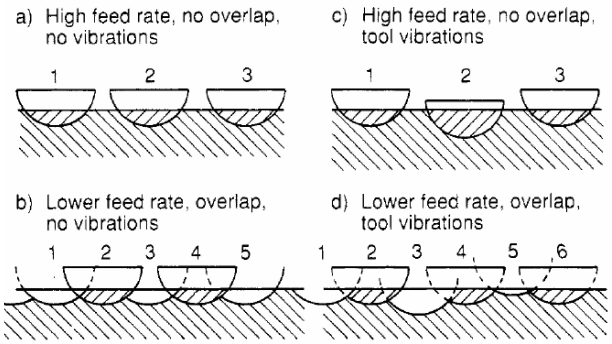

Figure 2.33: Surface profile - successive tool overlap (Franse, 1990)

During the grinding process, a similar effect is expected for any change in depth of cut between each revolution of the workpiece. The surface profile is expected to be different than the calculated surface profile using equation 2.9.3.

2.9.3 Surface patterns

Surface patterns are generated on the ground surface due to the grinding mode used. Different grinding modes generate different defined grinding patterns. Figure 2.34 shows examples of surface patterns induced using grinding modes described in Figure 2.17 in section 2.7.

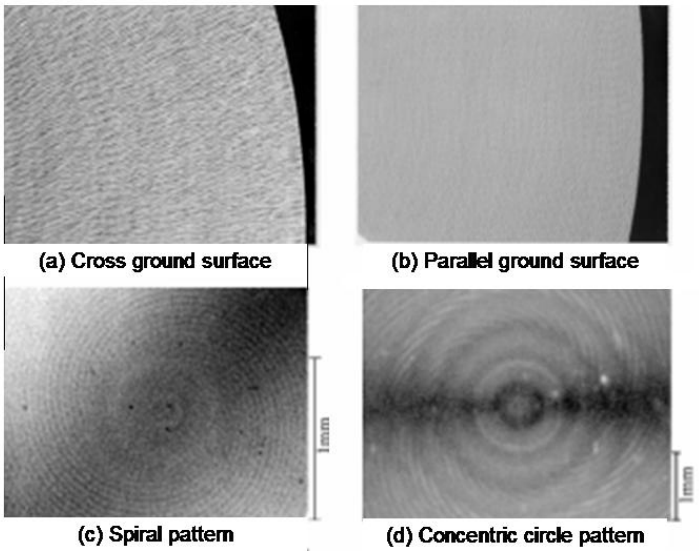

Figure 2.34: Different surface patterns (Yoshihara et al., 2004)

The cross ground surface (a) has higher surface pattern roughness than the parallel grinding surface (b). Using the parallel grinding mode, the surface shows a distinctive spiral pattern (c) or a concentric circle pattern (d). Based on simulations of grinding processes,

the results show that the spiral pattern corresponds to a steady grinding condition. The concentric circle pattern is generated by fluctuating grinding conditions. The fluctuation simulated is a vibration of the grinding wheel spindle along the vertical axis. A waviness as the contact point changes is generated (Yoshihara et al., 2004).

Franse (1991) simulated the grinding pattern by looking at a single point cutting. The simulation showed the importance of the ratio between the workpiece and the grinding wheel. The same approach was employed to simulate the grinding process with multi grits. The surface roughness pattern is modified once grinding wheel wear occurs as grits become blunt leading to different number of active grains.

Heinzel et al. (2006) modelled based on similar observation the surface generated by contour grinding. Similar patterns were observed and simulated. The results showed that a small fluctuation in the ratio between the grinding wheel and workpiece speeds modifies the generated pattern.

2.10 Subsurface damage

Fracture mechanics has been used to study the subsurface damage induced in ground surfaces. Different types of cracks depending of the type of indentation have been described. In order to measure the extent of subsurface cracks depth, different techniques have been developed. They can be categorized into non destructive and destructive measurements methods. Different analytical techniques were also developed based on the measured surface roughness to estimate the subsurface damage depth.

2.10.1 Fracture mechanics

As described in section 2.4.1, material removal of brittle materials can be achieved through brittle, semi-ductile or ductile mode grinding. The initiation and propagation of median and lateral cracks in brittle materials, described by Lawn (Lawn and Wilshaw, 1975), are shown in Figure 2.35.

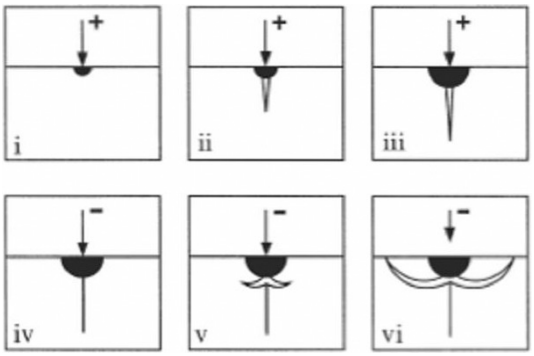

Figure 2.35: A model of crack initiation (Lawn and Wilshaw, 1975)

An indentation load is applied (i). This leads to a small median crack (ii) creation. This crack increases with the load (iii). With the unloading, the median crack starts to close (iv). A lateral crack (v) appears which grows toward the surface (vi) (Lawn and Wilshaw, 1975). This model is in two dimensions and corresponds to a static load applied using a sharp indenter.

Cook and Pharr (1990) illustrated that the formation of radial cracks occurred at different stage of the loading and unloading cycle for glasses and ceramics. For crystalline materials and densifying glass (ie. fused silica), the radial crack formation occurs during loading. For other glasses (ie. borosilicate, soda lime), the unloading cycle generates cracks.

Argon (1959) observed that the distribution of number of cracks per unit area per crack depth versus crack depth on 7740 Pyrex glass follows a power law function.
In Fused silica, the crack distribution is explained in three fracture zones. A rubble zone is followed by shallow fractures. After that point, heavy fracture network disappears. Fracture pattern and length are observed and characterise the process used. Those split finally into radial fracture of set length before no damage is seen (Menapace et al., 2005*b*).

An example of a three dimensions representation of cracks generated by a diamond grit along a grinding track is shown in Figure 2.36.

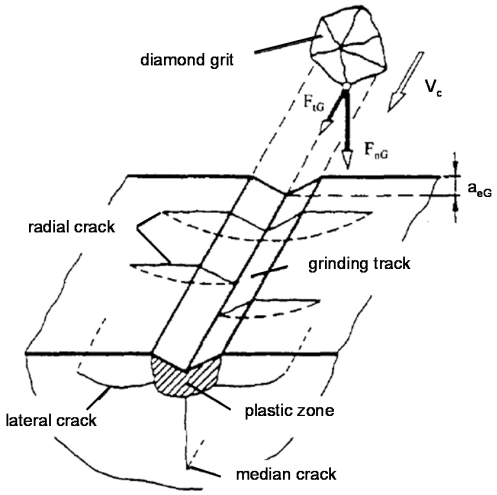

Figure 2.36: Cracks initiation along grinding track (Li and Liao, 1996)

For a grit cutting depth, a_{eG}, the normal and tangential grit forces are F_{tG} and F_{nG} respectively. These fracture mechanisms result in surface and subsurface defects. Below the grinding track generated by the diamond grit, a plastic zone is present. Lateral, median and radial cracks propagate from this plastic zone. Those different cracks are described in Figure 2.37. The parameters in the indentation using a blunt indenter and a sharp indenter have been described in details by Lawn (Lawn et al., 1975, 1976).

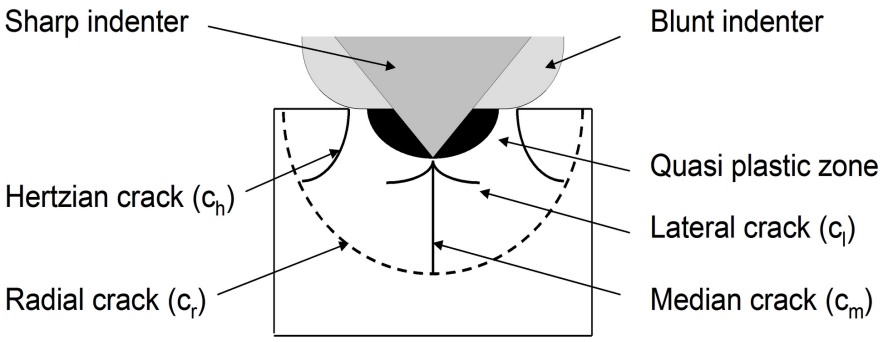

Figure 2.37: Subsurface damage cracks [after (Lawn et al., 1975, 1976, Lawn, 1985)]

Under a given load, a quasi plastic zone is generated. For a sharp indenter, median/radial cracks (c_m/c_r) commence and propagate with increase of indentation load. With indentation unloading, the median cracks close and lateral cracks (c_l) grow towards the surface. A blunt indenter induces Hertzian cracks (c_h) instead of median cracks. The dimensions, width and depth, for each cracks type induced under an applied load are shown in Figure 2.38.

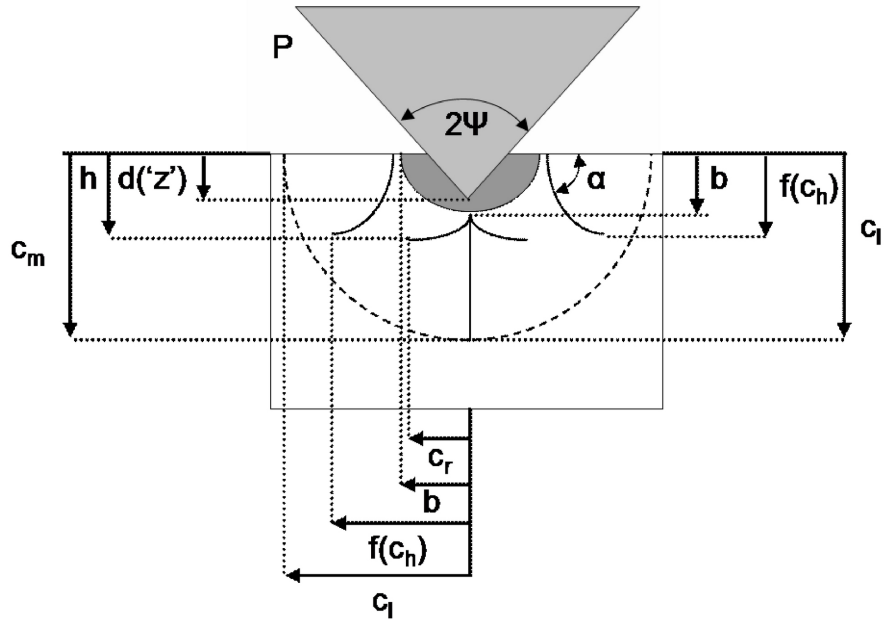

Figure 2.38: Subsurface damage cracks depths [after (Lawn et al., 1975, 1980, Marshall et al., 1982)]

The sharp indenter has an indentation angle ψ. The applied load (P) induces a penetration (d or z) into the surface. The Hertzian crack is generated along α_h favourable tilt angle (ie. 22° for glass) (Lawn et al., 1975). The depth of plastic zone is b. Below a plastic zone, the cracks present in the surface are lateral cracks, median/radial cracks and Hertzian cracks (Lawn et al., 1975). The thickness of material above the lateral crack plane is h. The indentation depth (d) of a sharp indenter is calculated using equation 2.10.1 (Lawn et al., 1980).

$$d = cos(\psi) \tag{2.10.1}$$

Marshall et al. (1982) estimated that the lateral cracks occur at the end of the plastic zone (b). Therefore, h (= b) is calculated using equation 2.10.2 (Marshall et al., 1982).

$$b \approx h \approx (\frac{E}{H})^{1/2}(cos\psi)^{1/3}(\frac{P}{H})^{1/2} \tag{2.10.2}$$

The radial and median cracks are similar. Lawn et al. (1980) proposed to use the term "median" for cracks that are turned into subsurface damage. "Radial" is used for strength test cracks for example. The median crack depth is calculated using equation 2.10.3.

$$c_m = \left(\frac{\alpha_m P}{K_c}\right)^{2/3} \tag{2.10.3}$$

In ceramics, the median crack depth (l_{mc}) is calculated using equation 2.10.4 (Lawn et al., 1980).

$$l_{mc} = c_m = \left(\frac{0.034(cot\psi)^{2/3}E^{1/2}F}{H^{1/2}K_c}\right)^{2/3} \tag{2.10.4}$$

Inasaki (Inasaki, 1988) showed that average sectional area of active cutting edges (a_m see equation 2.8.27) are proportional to the estimated median crack depth (c_m) for silicon nitride and silicon carbide. For a minimum a_m value, a plastic flow zone is achievable which corresponds to a theoretical critical load per grain reached, F^* (Lawn and Evans, 1977).

With a blunt indenter, a Hertzian crack is generated into the surface. The angle α_h varies with the type of material. The Hertzian depth below the surface is calculated by equation 2.10.5 (Lawn et al., 1975).

$$c_h = \left(\frac{\alpha_h P}{K_c}\right)^{2/3} \tag{2.10.5}$$

A similar form as for median cracks is adopted for Hertzian cracks. The single last fracture depth corresponds to one or the other type of cracks. This depends, for example, on the grit diamond sharpness.

As the indentation is dynamic, the sliding effect was investigated. The friction coefficient μ was employed. The sliding load P' was calculated using equation 2.10.6 (Lawn et al., 1984).

$$P' = P(1 + \mu^2)^{1/2} \tag{2.10.6}$$

This sliding load P' replaces P in radial and Hertzian equations. A trailing depth is obtained that is deeper than static depth. For a static load, μ = 0 and P = P'.

Subsurface damage initiation and penetration depth are influenced by materials characteristics of ground substrates. An important parameter to calculate is the material brittleness (B). It corresponds to the micro hardness (H) divided by the fracture toughness (K_c) for a given material.
Lawn and Evans (1977) showed that an initial load has to be applied to develop an initial penetration crack depth. The minimum initial load applied is P^* as calculated using equation 2.10.7 (Lawn and Evans, 1977).

$$P^* \approx [(54.47\alpha)/(\eta^2\theta^4)] \times (K_c/H)^3 K_c \tag{2.10.7}$$

with dimensionless factors, η = 1, $\alpha = 2/\pi$ and θ = 0.2
The initial penetration depth is c^* and is calculated using equation 2.10.8 (Lawn and Evans, 1977).

$$c^* \approx (1.767/\theta^2) \times (K_c/H)^2 \tag{2.10.8}$$

The values obtained from those two parameters are approximated within an order of magnitude (Lawn and Evans, 1977). Zhang and Howes (1995) used those parameters to compare different materials to a reference material, silicon nitride.

The brittleness, P*and c* for different materials are shown in Table 2.4.

Material	Micro Hardness H (GPa)	Fracture toughness K_c (MPa.m$^{1/2}$)	Brittleness B H/K_c (1/m$^{1/2}$)	Initial applied load P* (N)	Initial penetration depth c* (μm)
Fused silica	4.8	0.74	6490	0.06	1.05
ULE	4.6	1.8	2560	2.37	6.74
Zerodur	6.2	0.9	6890	0.06	0.93
SiC	27.4	3.5	7830	0.16	0.72

Table 2.4: Initial applied loads and penetration depths examples

Of the materials investigated, the initial applied load to create subsurface damage is the highest for ULE. Fused silica and Zerodur have the same threshold which is forty times lower than ULE. Similar trend is shown for the initial penetration depth. ULE has the deepest crack depth while Zerodur is seven times shallower. Fused silica has deeper damage depth for a similar initial applied load required. Interestingly, the initial load necessary to generate subsurface damage is the highest in ULE but once reached the deepest damage is to be anticipated.
Observations made for P* and c* can be described using material brittleness parameter. A lower material brittleness value leads to a higher initial load required to generate subsurface damage. Once the subsurface damage starts, the fracture toughness is the main controlling factor (Lawn and Evans, 1977).

2.10.2 Non destructive measurement techniques

Non destructive measurement techniques have been developed to measure subsurface damage depth in optical components. Measurements on the actual component, while preserving its optical integrity, is valuable. A limitation is the depth resolution of the technique employed. The level of subsurface damage is shallow in precision grinding and polishing.

Brinksmeier (1989) made a review of different non destructive techniques used to observe subsurface damage. Raman spectroscopy, ultrasound and X-ray techniques are few examples of techniques discussed. Some non destructive subsurface inspection techniques such

as the ultrasonic Rayleigh wave measurement have proved successful for information and qualification of significant and deep cracks. Those methods limitation is the measurement resolution in respect of the depth.

Cross sectional transmission electron microscopy (TEM) analysis has proved to be extremely informative for detection of sub-micron scale defects in glasses and crystals (Puttick et al., 1992). This TEM process is however time consuming and less appropriate for large defects in multi-phase advanced ceramics.

Pfeiffer and Hollstein (1997) showed that the X-ray diffraction method can be used to measure residual stresses and microplastic deformation. Another review of different techniques in particular for ceramics and glasses have been done by Lucca et al. (1998).

Goch et al. (1999) reviewed new techniques and amelioration in existing techniques. The demand of methods to study small film thickness and coatings helped in the progress of techniques that can be applied to subsurface damage assessment. However, the conclusions were that more work was still required.

In measurement of laser damage in fused silica, a modified commercial optical coherence tomography system was used to detect large subsurface damage regions (400 μm) with a depth of 300 μm on polished surfaces (Guss et al., 2008).

2.10.3 Destructive measurement techniques

Destructive measurement techniques have proved successful for detecting micron and sub-micron scale fractures. A wide range of techniques have been described depending on the subsurface damage depth and the ground material type. These techniques are used based on the assumption that each particular assessment does not induce subsequent cracks or extend the existing ones. A limitation is the lack of measurement on the actual manufactured parts. This relies on a careful choice of representative experiments and the repeatability of the grinding process evaluated.

Polishing techniques are widely used. Repetitive polishing, etching and optical microscopy observations have been employed to observe subsurface damage in ground glasses (Hed et al., 1988, Ball et al., 1991, Wuttig et al., 1999, Menapace et al., 2005*b*). After polishing, acid etching is necessary to remove the redeposited layer of hydrated glass (Menapace et al., 2005*a*). A variant of this repetitive polish and etch method is a taper polishing approach. This taper or "wedge" was obtained using different polishing techniques such as metallography laboratory polishing equipment (Sun et al., 2006) and

CNC polishing machines for an automatic controlled process (Suratwala et al., 2006). Menapace et al. (2005*a*) used a magnetorheological finishing (MRF) wedge polishing technique shown in Figure 2.39.

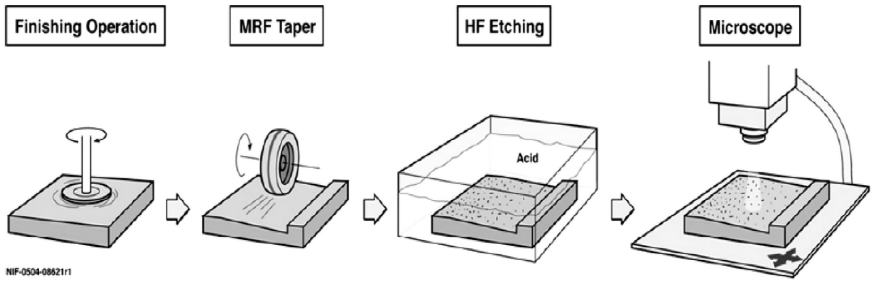

Figure 2.39: MRF wedge polishing technique (Suratwala et al., 2006)

Large areas in different optical materials can be assessed. After etching, the cracks were observed with a microscope. In order to automate the measurement process, the picture obscuration at different depth beneath the ground surface was measured. This gave a plot of the obscuration due to cracks in the surface versus the depth under the ground surface. Tonnellier et al. (2007) used a wedge polishing technique with a deterministic polishing process. After the etching, using an optical microscope for observation, the number of cracks per mm^2 was counted manually. Those measurements were used to obtain a graph of number of cracks per mm^2 versus depth beneath the ground surface (Argon, 1959, Shore, 1995).

Zhao et al. (2006) generated a taper by cross sectioning the sample with a diamond saw at angle of 135°. The samples were mapped, polished and etched before observation to expose the cracks. Scanning electron microscopy (SEM) observations were done after the samples were gold coated. The assessment length and therefore the depth resolution was lower than the taper polishing technique.

Dimple techniques, such as COM ball method and MRF spot technique were used as shown in Figure 2.40.

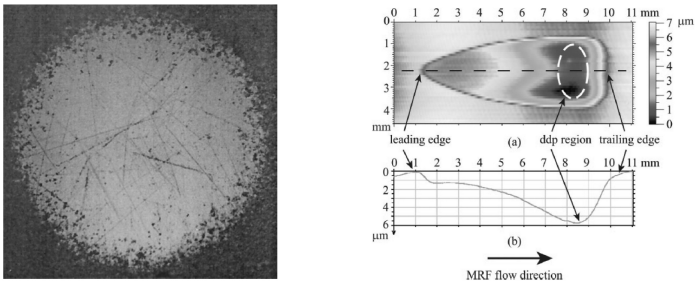

(a) COM ball method (Randi et al., 2005)

(b) MRF spot technique (Shafrir et al., 2007)

Figure 2.40: COM ball method and MRF spot technique

Zhou et al. (1994) revealed subsurface damage after a dimple polishing and etching on fused silica and BK7. Observations made using both a SEM and a conventional optical microscopy gave similar depth observation. The COM ball method (Arrasmith et al., 2001) is an alternative dimple technique using a precision stainless steel ball and diamond paste. A MRF spot technique (Shafrir et al., 2007) was also used on CVD SiC. With a white light interferometer, the surface roughness was measured until reaching a constant value. This value defined the subsurface damage depth due to the grinding process. Those tests showed that MRF leaves a signature but no subsequent subsurface damage. Randi et al. (2005) compared the COM ball method and the MRF spot technique. Using MRF spot technique no damage was left, while COM ball method had damage to be removed from measurements (Figure 2.40(a)). For harder material, the material removal rate is better using the MRF technique. Menapace et al. (2005*a*) highlighted a general disadvantage for the polishing technique described above which was the relatively small assessment area compare to the full optic surface area. The use of an automatic MRF wedge polishing with etching using obscuration as a observation method over 6 x 6 cm was recommended.

Xu and Jahanmir (1994) described another assessment technique. A sample is sliced into two parts. Each face is ground and polished. The two parts are glued back together with a very fine layer of adhesive. A clamping force is applied to maintain a constant glue thickness < 1 μm. The sample is ground. After removing the glue, the two parts are cleaned with acetone in an ultrasonic bath and gold coated. The observation is done with a Nomarski optical microscope. Agarwal and Venkateswara Rao (2008) used the same slicing technique to observe SiC ground subsurface damage using a SEM for observation.

Preston (1922) used chemical etching technique to measure the subsurface damage depth in glass. This technique relies on a consistency in etching rate for a particular surface quality and contact area with the etchant used. Higher etching rate is obtained for a surface with cracks. When the etching rate, measured by weighing the part at regular intervals,

becomes stable, the surface has no cracks.
This technique is easier and cheaper than the polishing techniques. It does not rely on the experience of the operator for subsurface damage observation (Hed et al., 1988).
For material with high chemical resistance at room temperature such as SiC, plasma etching was successfully used to reveal subsurface cracks (Kanematsu, 2006).

Fracture mechanics using a three support balls fracture test with a ball load applied is described by Hed et al. (1988). Using linear elastic behaviour of samples, flaw depth is calculated. Due to several value assumptions, the results show lower values than other techniques (Hed et al., 1988). Maksoud et al. (1999) used a three-point bending test on ground silicon nitride. Cracks were observed using a SEM observation with a thin layer of gold plated. Other fracture test configurations have also been employed.

Twyman effect was used for assessing subsurface damage depth (Preston, 1922). A bending effect is observed in thin samples induced by machining residual stresses (Lambropoulos et al., 1996). Using damage free removal processes such as polishing (Arrasmith et al., 2001) or RAP processing (Verma et al., 2006), the stressed surface is progressively removed. The depth of material removed to obtain a stress free sample is the amount of subsurface damage depth induced by the previous machining process.

2.10.4 Analytical techniques

Different analytical methods have been developed based on experiments to estimate the subsurface damage depth.
Lambropoulos (2000) advocated a correlation between sub-surface damage and abrasive grain size (L). An average subsurface damage (SSD) is 1.07 x $L^{3/4}$ and the interval for any grinding parameter is 0.3 x $L^{0.68}$ < SSD (μm) < 2 x $L^{0.85}$.

The definition of subsurface damage depth as a function of surface roughness has been proposed (Hed and Edwards, 1987*a*). The values of ratio k of 4.4 $\pm$0.9 (cluster depth) and 6.4 $\pm$1.3 (single last fracture depth) are reported. Hed et al. (1988) proposed that R_t is equal to 5 - 7 times the subsurface damage depth for bond abrasive in glass if the grinding mechanism is dominated by fracture and not plastic scratching. Lambropoulos et al. (1999) found the minimum of subsurface damage to be removed by polishing can be estimated by SSD = R_t or SSD = 2 x R_t. In microgrinding of optical glasses, such as BK7 and fused silica, using metal bonded diamond ring tool, 2-4 μm and 10-20 μm, an upper limit was found to be SSD = 0.38 x R_t (LLE, 1997). Randi et al. (2005) found that SSD < 1.4 x R_t is higher limit for single crystal micro grinding.

Based on the ratio values found between the surface roughness (SR) and subsurface damage depth (SSD), few equations have been proposed based on Lawn's fracture mechanics (Lawn et al., 1975). Lambropoulos et al. (1999) defined the surface roughness to be equal to the plastic zone b and the subsurface damage to be equal to the radial crack depth, c_r as shown in equation 2.10.9.

$$\frac{SSD}{SR} = \frac{c_r}{b} = 2.326 \times \alpha_K^{2/3} \times \left(\frac{E}{H}\right)^{\frac{2-5m}{3}} \times \frac{(cot\psi)^{1/9}}{(sin\psi)^{1/2}} \times \left(\frac{H^3}{K_c^4}\right)^{1/6} \times P^{1/6} \quad (2.10.9)$$

with $\alpha_K \approx$ 0.03 - 0.04 and m $\approx$ 0.33 - 0.50. The relation obtained is proportional to the indentation load, $P^{1/6}$ and the indentation angle. The subsurface damage depth varies also with a different material.

Miller et al. (2005) redefines the ratio between surface roughness and subsurface damage using different assumptions as shown in equation 2.10.10. The surface roughness is defined as proportional to the lateral crack depth, c_l. The grit geometry used in lapping and grinding processes is assumed to correspond to a blunt indenter and not a sharp indenter. The Hertzian crack is believed to be the deepest type of cracks generated. The subsurface damage depth is equal to c_h.

$$\frac{SSD}{SR} = \frac{c_h}{c_l} = \left(\frac{\alpha_h^{2/3}}{\alpha_l}\right) \times \left(\frac{H}{K_c}\right)^{2/3} \times \left(\frac{H^{7/30}}{E^{2/5}}\right) \times P^{1/6} \quad (2.10.10)$$

The ratio SSD/SR is proportional to $P^{1/6}$ and the material parameters as for equation 2.10.9.

Li et al. (2008) modified equation 2.10.9 by raising SR to power 4/3 as shown in equation 2.10.11.

$$\frac{SSD}{(SR)^{4/3}} = \frac{c}{b^{4/3}} \quad (2.10.11)$$

This operation removes the indentation load P from the final equation 2.10.11. This modification is justified based on the difficulty to calculate experimentally P as the number of active grains is approximated (Li et al., 2008).

$$SSD = 3.08 \times \alpha_K^{2/3} \times \frac{1}{(sin\psi)^{2/3}} \times \frac{H^{2m}}{E^{(2m-2/3)} K_c^{2/3}} \times SR^{4/3} \quad (2.10.12)$$

The relation obtained between the subsurface damage and the corresponding surface roughness is SSD = χ x $SR^{4/3}$. The subsurface damage depth increases with larger surface roughness but is stable for any grinding forces applied for a given ground material.

Other models have been developed defining the subsurface damage depth function of the

grinding process parameters in ceramics. Zhang and Howes (1995) defined an analytical model that predicts the subsurface damage induced by grinding in ceramics.

$$\delta = (200 h_{max})^{1/log(\lambda(H/K_c))} \tag{2.10.13}$$

with $\lambda = 10^{-2}$ $m^{0.5}$.
This model is function of the maximum chip thickness and the material parameters H and K_c. All the other important parameters are included in the constant value λ.

These proposed relationships have, to a significant extent, been contradicted through the identification of the importance of grinding machine performance (Franse, 1991, Shore, 1995). Equation 2.10.14 defines the penetration depth of subsurface cracks having the following form (Lawn et al., 1980, Malkin and Hwang, 1996, Yang et al., 2001).

$$\xi = \left(\frac{4\pi}{r_g}\right)^{-4/9} \times \chi^{2/3} \times \left(\frac{K_c H^{5/6}}{\sqrt{E}}\right)^{-2/3} \times f_{gn}^{8/9} \tag{2.10.14}$$

The influence of the static machine stiffness was included into equation 2.10.14 by replacing the grinding force per grit (Yang et al., 2001) by relation shown in equation 2.10.15.

$$f_{gn} = \frac{2k_f}{\pi k_r C b_w} \times \frac{F_0 + C_a a_t}{1 + C_a/k_s} \times \left(\frac{a_t - F_0/k_s}{1 + C_a/k_s}\right)^{h-t} \tag{2.10.15}$$

This equation predicts that the subsurface damage decreases with decreasing the machine static stiffness. The relation, substituting the grinding force per grit in equation 2.10.14, is a function of the depth of cut. The actual depth of cut reduces with a decrease in machine stiffness. If the static stiffness decreases below a limit value the dynamic stiffness of the machine becomes the main contribution for subsurface damage as the process is unstable (Yang et al., 2001).

2.11 Summary

The literature review showed that a precision grinding process can theoretically achieve a form accuracy (P_t) of 1 μm and a surface roughness (R_a) of 150 nm on large optical components. This grinding process is required to be controlled, repeatable, accurate and stable. A precise grinding machine built following the design principles reported is preferable. Accuracy, repeatability and resolution of each axis are targeted. The external and internal heat sources are controlled and the main identified internal heat sources are limited. This can be achieved by specifying the grinding spindle power on the grinding process requirements. The load on the motors can be reduced using counterbalance system on Z axis and low moving masses. A high static stiffness is achievable by minimizing grinding loop stiffness path and using high stiffness bearings. A high dynamic machine

stiffness can be achieved using a low moving mass and carefully selecting materials for the main structural frame and the machine bed.

The repeatable grinding machine and process errors can be error compensated. The use of in-situ separate metrology frame was shown to be important especially for large components. The BoX grinding machine was designed following those concepts and was used in this project.

The grinding wheel parameters have a significant influence on the surface quality and the subsurface damage depth. Low subsurface damage depths were achieved with resin bonded grinding wheels on glass, glass ceramics and ceramics. A reduction in diamond grit sizes was identified to be another contributor to low subsurface surface damage depths. High material removal rates in ceramics were reported. This leads to a grinding wheel wear inducing form errors, a process instability and requires an efficient grinding coolant delivery system. The monitoring of the grinding ratio G was recommended to identify reshaping and dressing requirements. Resin bonded diamond grinding wheels with different grit sizes were used in this project to validate the effect for our grinding mode. Grinding wheel G ratios were investigated. A dressing using sticks was preferred to an ELID dressing as the control and the repeatability of the grinding wheel form needed to be maintained.

The grinding mode selected leads to the different grinding process parameters. The main parameters identified are the depth of cut, the grinding wheel speed, the workpiece speed and the feed per revolution. The estimated surface profile for our grinding mode is governed by the grinding wheel shape and the feed per revolution. The grinding process responses are the grinding forces and the grinding power. The normal grinding force and grinding stiffness control the form accuracy. The grinding power monitors the grinding process in relation with the maximum available spindle power. Different models have been developed to combine those responses into other parameters such as the equivalent chip thickness, the maximum undeformed chip thickness and the specific grinding energy. Those values were used to compare different grinding processes and grinding wheels. Those parameters were identified to be important for this project as two grinding machines were employed. Each parameter was recorded or calculated and compared to the literature.

The targeted material removal rate requires material removal through micro brittle fracture. The ductile mode leads to low material removal rate. The subsurface damage is proportional to the indentation load and is function of the material fracture toughness and brittleness. The grinding machine static stiffness is recognized to be an important factor.

Some researches highlighted that the surface roughness is proportional to the subsurface damage depth. The subsurface damage depth is investigated with a destructive method, the wedge polishing technique.

A grinding machine with high static and dynamic stabilities is necessary to obtain rapid and precise grinding of large optics with low levels of subsurface damage. Process optimisation needs repeatability of the grinding process as well as subsurface damage investigations. The aim of this research is the significant advance in precision grinding of large freeform optics by optimizing the machining process. The objectives are:

1. A surface quality of $P_t < 1$ μm and $R_a < 150$ nm,
2. A subsurface damage depth less than 5 μm,
3. An optimized grinding process for a one metre part that reduces grinding time from 100 hours to 10 hours,
4. The grinding of a large blank diameter up to one metre,
5. The grinding of a spherical, off-axis or freeform surface,
6. A grinding process suitable for glass (ULE), glass ceramics (Zerodur) and ceramics (SiC).

3. EXPERIMENTAL EQUIPMENT AND PROCEDURES

The experimental equipment is described in section 3.1. Details of the grinding, Edgetek and BoX machines, and the holding fixtures that have been used are provided. The grinding and metrology tools used are described in section 3.2. Details of the experimental procedures are explained in section 3.3. The experimental design sequences adopted are described. Preliminary parameter screening experiments were carried out, followed by Edgetek and BoX based test programmes. The approach applied to demonstrate the proposed grinding process is described and the assessment procedures are justified in section 3.4. The surface quality, subsurface damage, grinding wheel wear and grit concentration evaluation methods have been also explained.

3.1 Experimental equipment

Two grinding machine tools have been used for the experiment: the Holroyd Edgetek grinding machine, which is commercially available and a grinding machine specifically designed by Cranfield University called BoX.

3.1.1 Edgetek grinding machine specifications

The initial process development of the experiments were carried out on a Holroyd 5 axis SAM Edgetek grinding machine, which is commercially available and shown in Figure 3.1.

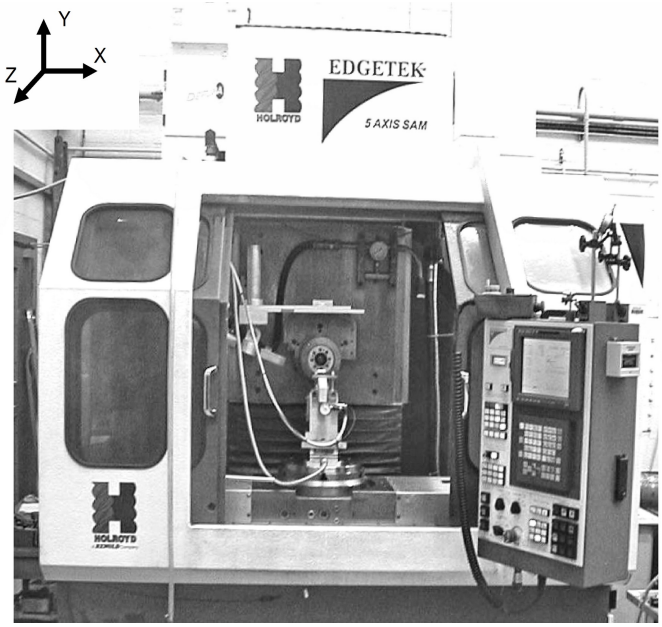

Figure 3.1: Edgetek - Superabrasive grinding machine

The Holroyd Edgetek grinding machine specifications are described in Table 3.1. This machine was used for grinding BK7 (Sun et al., 2006) and subsurface damage investigations.

X axis travel *mm*	Y axis travel *mm*	Z axis travel *mm*	Spindle Power *kW*	Spindle speed *rpm*	Feed Rate *mm/s*	Rapid Traverse *mm/s*
472	350	305	27	14000	0 to 66	0 to 126

Table 3.1: Edgetek - Superabrasive machine specifications

This grinding machine has three linear motions and two rotary motions. For the grinding experiments, the three linear axes have been employed and a designed test sample holding fixture (see section 3.1.4) has been used to emulate the BoX grinding mode.

- **Motions specifications**

The Edgetek grinding machine uses linear roller bearing ways. Those linear systems and their respective positioning, repeatability and resolution accuracies are listed in Table 3.2.

Way system	Position Feedback	Slide Ways Accuracy		
		Positioning	Repeatability	Resolution
Schneeberger Hi-precision Linear Roller Bearing Ways	Heidenhain Linear Scales on X, Y, Z Axes	± 0.005 mm per 300 mm	0.005 mm per 300 mm	0.001 mm

Table 3.2: Edgetek - Linear axes (X, Y and Z) specifications

- **Control system**

The Edgetek grinding machine is equipped with a CNC FANUC controller. The model used is a series, 16i-M Control.

3.1.2 BoX grinding machine specifications

The BoX, Big OptiX, has been developed at Cranfield University as part of the Basic Technology project. It was built by Cranfield Precision Ltd, designed and commissioned by Cranfield Precision Engineering Centre. I was involved in the development of the BoX grinding machine, whose fabrication started in November 2004; it then became available for process development in August 2007.
This grinding machine is shown in Figure 3.2.

Figure 3.2: BoX - Precision grinding machine

The BoX grinding machine was designed for grinding large optics with a high removal rate (200 mm^3/s) having a form accuracy of 1 μm over 1 metre and low subsurface damage (< 5 μm). The concept of the BoX machine design is to employ high stiffness and

high density subsystem layout; its design was made into a highly symmetrical machine. Therefore, a low moving Z axis mass and a high Z axis stiffness were key elements of the design. The combined Z and X axis carriage has a low moving mass below 750 kg. The use of high specification linear motors mounted on either side near the moving mass achieves a high frequency of 100 Hz (Shore et al., 2005).
The grinding machine axis specifications are given in Table 3.3.

X Axis		Z Axis		C Spindle		Spindle	
Travel	Speed	Travel	Speed	Torque	Speed	Power	Speed
mm	*mm/s*	*mm*	*mm/s*	*Nm*	*rpm*	*kW*	*rpm*
1350	0 to 50	120	0 to 20	878 (Max)	0 to 25	10	100 to 2600

Table 3.3: BoX - Precision grinding machine specifications

The grinding machine has three axes: X axis which is a horizontal linear axis, the rotary table, C, which can be controlled as an axis and the Z axis containing the grinding spindle. This spindle is inclined to a fixed 20° angle.

- **Motions specifications**

The BoX grinding machine uses hydrostatic bearings: the X horizontal linear axis parameters are described in Table 3.4.

Way system	Position Feedback	Accuracy Straightness	Accuracy Repeatability	Resolution
Hydrostatic bearings with two linear motors	Two Zerodur based gratings	5 μm over travel	0.1 μm	10 nm

Table 3.4: BoX - Horizontal linear axis (X) specifications

The X axis straightness was specified at 5 μm over 1350 mm with a repeatability of 100 nm and resolution of 10 nm using Zerodur gratings. Due to metrology most of the straightness error can be compensated. Compensation assures that one micron form accuracy is attainable.

Z vertical axis parameters are described in Table 3.5

Way system	Position Feedback	Accuracy Straightness	Repeatability	Resolution
Hydrostatic bearings with two linear motors	Two linear encoders	2 μm over travel	0.05 μm	10 nm

Table 3.5: BoX - Vertical linear axis (Z) specifications

The hydrostatic bearings were specified to give high static stiffness over 100 N/μm. The vertical axis repeatability was specified at 50 nm.

The C axis specifications are shown in Table 3.6.

Way system	Position Feedback	Error motion Axial	Radial	Accuracy Repeatability	Resolution
Hydrostatic spindle with a shaft mounted DC torque motor	In-line rotary grating system	$\leq$ 0.2 μm (centre), $\leq$ 0.5 μm (500mm radius)	$\leq$ 0.5 μm at 150mm	$\leq \pm$ 1 arc second from table surface	< 0.5 arc second

Table 3.6: BoX - Rotary axis (C) specifications

The Hembrug rotary table, C, is controlled as a rotary axis. A DC torque motor drives a hydrostatic spindle. The rotary table has an error motion specified at different positions from its centre. The table stiffness changes for different radius from the centre. The measured stiffness at the centre is 1600 N/μm and 420 N/μm at 500 mm radius (Morantz et al., 2006).

- **Control system**

The BoX grinding machine is equipped with a CNC FANUC controller and the model used a 300i control, which was chosen for its capability of NURBS programming. The NURBS programming reduces the quantity of NC codes necessary to generate a complex free form curve. Moreover, NURBS curve can smooth the grinding machine motions and generate a smooth ground surface (Shore et al., 2005).

- **Thermal stability control system**

The freeform surfaces require a fast response of the Z axis motion along with a repeatable repositioning. High power density subsystems were temperature controlled to limit the temperature generation. To reduce the power demands on the Z axis motors, an air cylinder was fitted. This limits the thermal heat dissipation into the Z carriage.

In order to obtain an adequate stability of the grinding process over 10 hours, a thermal control loop has been implemented. The C axis, X axis, Z axis and grinding spindle motors are cooled with chilled water. The services including the hydraulics and the grinding coolant are thermally controlled. Thermal sensors monitor the temperature fluctuation in the different parts and circuits of the machine. A controlled loop system was implemented to use this monitoring by 3DEvolution. Therefore, the grinding machine is kept stable over long grinding runs.

- **Metrology frame**

The BoX grinding machine is capable of measuring the ground part in-situ. An in-situ separate metrology frame is employed. The details of this metrology frame are highlighted in Figure 3.3.

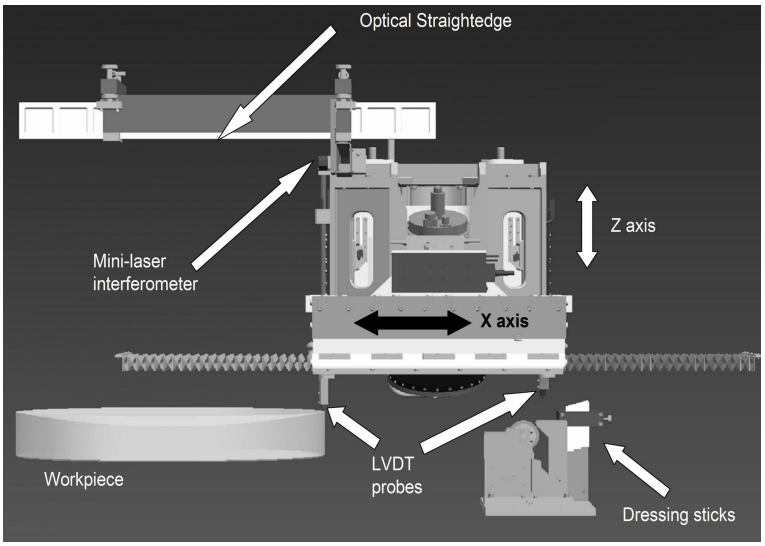

Figure 3.3: BoX - Metrology frame (Morantz et al., 2006)

The metrology system uses the grinding motions. Its reference optical straight-edge is mounted on a "non-stressed" frame. This reduces vibration and temperature errors. The metrology loop has different components. A LVDT contact probe is connected to an invar rod. A short path laser interferometer is mounted at the rod extremity. The reference for the measurement is a Zerodur straight edge held on a kinematic mounting. This probe measures the ground part without moving the holding fixture and the part. If needed, a form compensation can be done on the grinding process before unloading the part. A second LVDT probe is mounted on the Z axis. This probe is aligned with the centre line of the dressing sticks. It is used to measure the imprint of the grinding wheel as imprinted in dressing sticks. The profile can be correlated for the dressing stick geometry.

3.1.3 Comparison of grinding machines specifications

The BoX machine was designed to grind large freeform optical surfaces with a high material removal rate. The maximum grinding spindle power available gives the possibility of using a large depth of cut on glass and ceramics. The Edgetek machines maximum grinding spindle power and speed are higher than those of the BoX grinding machine. The maximum feed rate and rapid traverse speed are higher too. This provided the possibility to develop a comparable process. The maximum material removal rate achievable is higher than the targeted 200 mm^3/s.

In order to achieve good accuracy, stiffness and low friction, each axis of the BoX machine, uses hydrostatic bearings. Cranfield Precision has designed the X and Z axis hydrostatic bearings; the C axis was manufactured by Hembrug and the BoX was designed and specified to be more accurate than the Edgetek grinding machine. The sample dimensions used were 100 mm x 100 mm. Therefore, for the Edgetek grinding machine, the positioning accuracy for each axis was 10 μm and the repeatability was 5 μm. For the BoX grinding machine, the specified positioning accuracy was 5 μm and 2 μm for X and Z axes respectively. The specified repeatability was 0.1 μm and 0.05 μm for X and Z axes respectively.

The BoX grinding machine Z axis has a stroke of 120 mm that governs the maximum achievable slope. Its grinding spindle, tilted to a fix 20° angle and its grinding wheel specific geometry allow grinding of small radius of curvature. The grinding wheels important geometries were kept similar on both Edgetek and BoX grinding machines. The Edgetek maximum axis travels defined both the grinding wheel and holding fixture dimensions. The holding fixture on Edgetek grinding machine replicated the BoX grinding holding fixture.

3.1.4 Test sample holding fixtures

As previously explained, the Edgetek and BoX grinding machines have different motions. A test sample holding fixture was designed on the BoX grinding machine and in order to develop the grinding process on the Edgetek grinding machine, a specific holding fixture was designed. This holding fixture design replicates the BoX holding fixture. The correlation between the BoX and Edgetek grinding motions is illustrated in Figure 3.4.

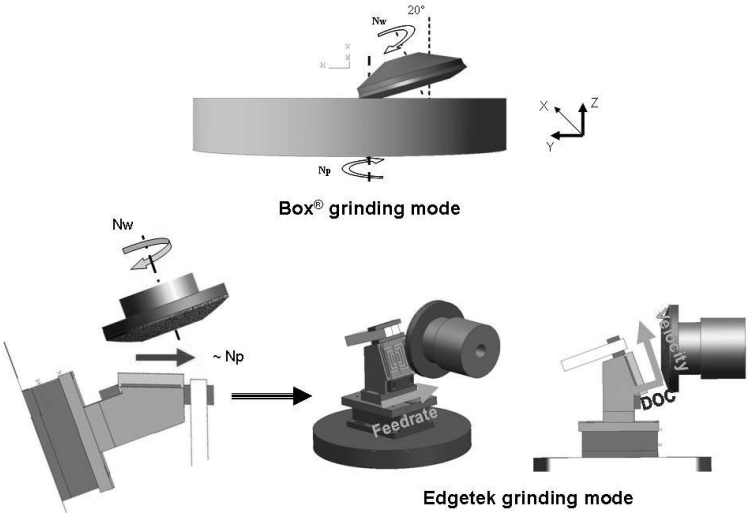

Figure 3.4: Correlation between the BoX and Edgetek grinding motions

The grinding mode on the Edgetek and BoX grinding machines is significantly similar. The part on the Edgetek grinding machine was tilted by 70° as the BoX grinding spindle was tilted at a fixed 20°. The rotary table motion on BoX grinding machine was generated using a linear motion on Edgetek grinding machine. The cusps were generated by moving the Y axis per cut by the same amount as the step per revolution on BoX grinding machine. This is a valid approximation if the ground part is placed on a rotary table with an "infinite" radius. The grinding experiments on BoX grinding machine were carried out at a radius of 450 mm from the centre of C axis.

- **Edgetek test sample holding fixture**

As previously described, a specific test sample holding fixture has been designed on the Edgetek grinding machine. This holding fixture was clamped on the Edgetek table as shown in Figure 3.5.

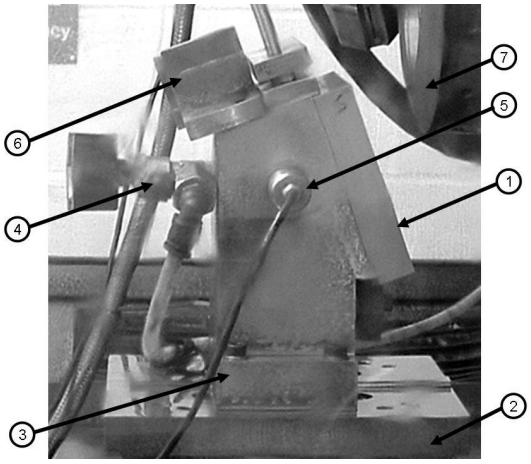

Figure 3.5: Edgetek test sample holding fixture

The blank samples were provided with an "as sawn" condition. Consequently the poor surface quality of the samples were prepared with a fine grind operation on one side. The achieved flat and smooth ground surface allowed the use of a vacuum clamping method. The angle between the sample and the grinding wheel (7) was set at 20°. The samples (1) were held at 70° to the horizontal. Grooves were machined for vacuum system on the holding fixture face. The vacuum pressure was set at 0.8 bar. A gauge (4) was bolted at the outlet of the holding fixture to continuously check the pressure during the grinding. The vacuum clamping approach eased the sample fitting and exchange. The Kistler platform (2) was bolted to a steel ground plate. This was needed as the machine holes were in imperial dimensions and the Kistler plate in metric. The holding fixture (3) was mounted on the Kistler platform. The dressing sticks and graphite blocks were clamped by two brackets (6). The acoustic emission (AE) sensor (5) was bolted to the side of the holding fixture close to the grinding zone.

- **BoX test sample holding fixture**

The test sample holding fixture used for BoX grinding machine is shown in Figure 3.6.

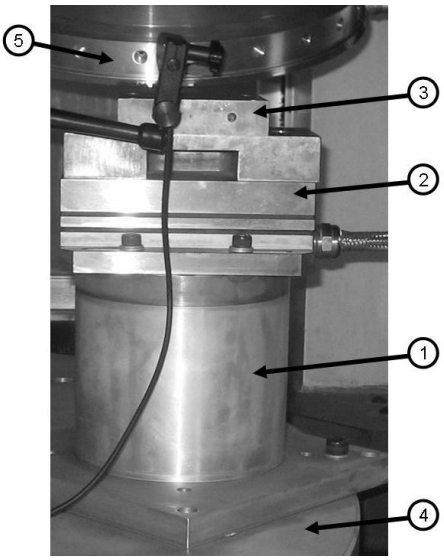

Figure 3.6: BoX test sample holding fixture

The holding fixture (1) used on the BoX grinding machine was mounted on a thick wall steel cylinder . This spacer was necessary to position the sample in the range of the Z axis and the grinding wheel strokes (5). The assembly was positioned on the outer diameter of the BoX rotary C axis table at a radius of 480mm (4). The Kistler dynamometer platform (2) was bolted on top of the spacer. Finally, the steel plate (3) was used to hold the ground sample.

The C rotary table has no hole through its centre. Therefore, a vacuum holding technique could not be employed. The samples were waxed on steel ground plates. The difference of clamping technique used was considered not to be critical. However, the holding system was designed to be stable and have high stiffness.

3.2 Grinding equipment

3.2.1 Grinding wheels

The grinding wheels used on Edgetek and BoX grinding machines have ostensibly the same specifications.

- **Edgetek grinding wheels specifications**

On the Edgetek grinding machine, four FEPA 6V5 "toric" shaped resin bonded diamond cup grinding wheels have been used. An example of the grinding wheel used is shown in Figure 3.7a.

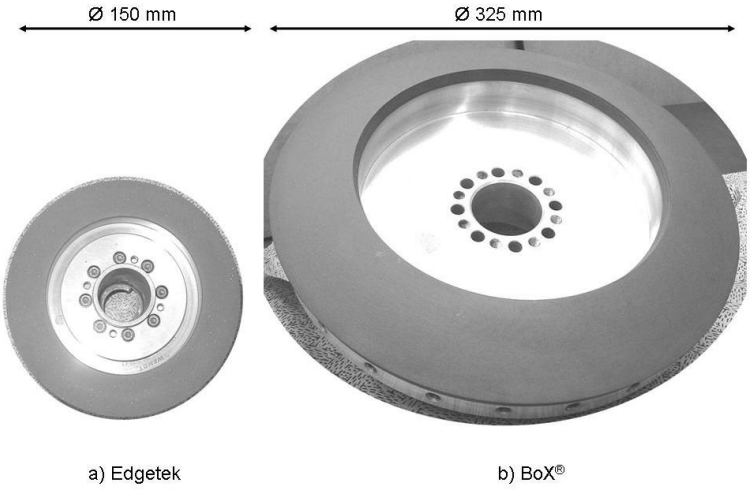

Figure 3.7: Resin bonded diamond cup grinding wheels

Two grinding wheels were manufactured by Wendt Boart and two were made by Cranden Diamond Products. The grinding wheel bodies are made of steel for Wendt Boart and aluminium for Cranden. The grinding wheel specifications are shown in Table 3.7.

Manufacturer	Grit size μm	Grit Concentration %	Wheel diameter *mm*	Abrasive layer width *mm*	Cutting radius R_c *mm*
Cranden	25	50	150	25	183
Wendt Boart / Cranden	46	50	150	25	183
Wendt Boart	76	75	200	35	242

Table 3.7: Grinding wheels specifications - Edgetek grinding machine

For each grinding wheel, the abrasive layer width was calculated to suit the maximum depth of cut to be taken. The difference in abrasive layer width induced different grinding wheel diameters. A 200 mm diameter grinding wheel with 76 μm diamond grit size was chosen for the rough cuts. A 150 mm diameter grinding wheel with 46 μm and 25 μm grit size was used for the semi finish and finish cuts. The chosen concentrations were, 75 for the D76 grinding wheel and 50 for the D46 and D25 grinding wheels. The shape of the grinding wheel was chosen to replicate the geometry that would be used on the BoX grinding machine. However, this was limited by the size of the Edgetek grinding machine. This means that the actual grinding cutting radius shapes are 242 mm for the D76 grinding wheel and 183 mm for the D46 and D25 grinding wheels, compared to a 300 mm radius of curvature for the BoX grinding machine.

The choice of grinding wheels bond material was resin. This decision was made in consideration of the low subsurface damage target. Metal bond grinding wheels were known to be efficient for grinding optics but ruled out because of the subsurface damage project target. Zhang and Howes (1995) obtained subsurface damage depth of 13 μm on SiC with a depth of cut of 15 μm using a metal bonded grinding wheel with 40 μm grit size. Furthermore, due to their brittleness at high material removal rate, vitrified grinding wheels were not considered.

The abrasive grit size was selected to ensure the roughness and the subsurface damage targeted (see section 2.11) would be achievable. Inasaki (1987) achieved a surface roughness, R_a, below 200 nm in SiC using 56 μm grit size with 100 concentration. The surface roughness and subsurface damage depth increase with coarser grit sizes in ceramics and glasses (Inasaki, 1987, Namba and Abe, 1993, Mayer Jr. and Fang, 1994, Zhang and Howes, 1995).

Larger grit size to achieve the maximum material removal rate targeted (see section 2.11) reduces normal grinding forces (Inasaki, 1987, Zhang and Howes, 1995).
Abrasive concentration values were recommended by the grinding wheel manufacturer

and supported by different grinding works on SiC (Inasaki, 1987, Mayer Jr. and Fang, 1994, Zhang and Howes, 1995, Hwang and Malkin, 1999).

- **BoX grinding wheels specifications**

On the BoX grinding machine, three "toric" cup grinding wheels (Figure 3.7b) were manufactured by Cranden Diamond Product. The grinding wheel specifications are shown in Table 3.8.

Manufacturer	Grit size μm	Grit Concentration %	Wheel diameter *mm*	Abrasive layer width *mm*	Cutting radius R_c *mm*
Cranden	25	50	325	60	300
	46	50	325	60	300
	76	75	325	60	300

Table 3.8: Grinding wheels specifications - BoX grinding machine

The "toric" shape grinding wheels have a diameter of 325 mm and a cross section radius of 300 mm. The diamond grit size chosen were 76 μm, 46 μm and 25 μm. The concentration employed were, 75 for the D76 grinding wheel and 50 for the D46 and D25 grinding wheels.
The abrasive layer width was defined large enough to accommodate the moving cutting point along the abrasive region. A width of 60 mm afforded the maximum depth of cut of 500 μm and a 3 m radius of curvature on the workpiece.
Based on the grinding wheel supplier machining capability, the grinding wheel body was made of a combination of aluminium and steel. In order to get a close fitting between the arbour and grinding wheel, a steel bore was ground and fitted to an aluminium body. This limited the likelihood of damaging the bore when the grinding wheels were fitted and removed.

- **Balancing**

Grinding wheels were balanced in-situ using a Schenck dynamic balancing system. The grinding wheels incorporated tapped holes around their periphery. For balancing, some of these holes were filled with "grub" screws. The balancing was performed at the grinding speed. This corresponded to 2865 rpm and 3820 rpm on the Edgetek grinding machine and 2129 rpm on the BoX grinding machine. The balancing quality achieved was better than 0.1 μm.

3.2.2 *Forming tools and dressing sticks*

The grinding wheels have a 300 mm radius cross sectional profile. Each grinding wheel was trued in situ before balancing. The forming tools also have a 300 mm radius cross sectional profile. This profile was concave as opposed to the convex profile of the grinding wheel. The two forming tools are shown in Figure 3.8.

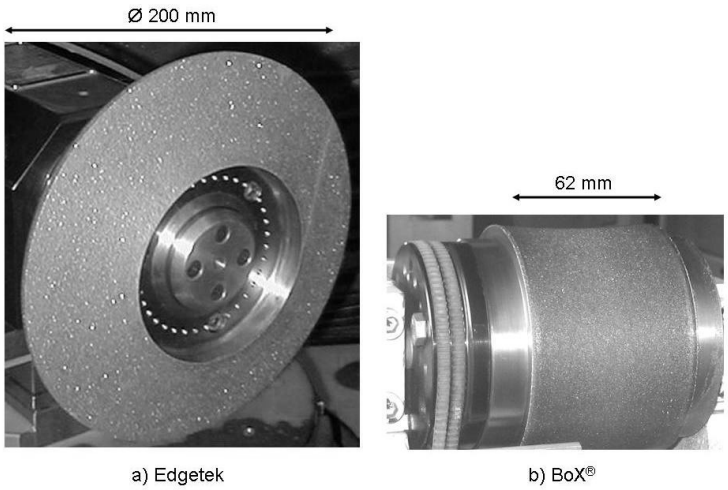

Figure 3.8: Nickel electroplated diamond truing wheel & roller

A truing wheel (Figure 3.8a) was used on Edgetek grinding machine. A truing roller (Figure 3.8b) was employed on BoX grinding machine.

- **Edgetek truing wheel specifications**

On the Edgetek grinding machine, a nickel electroplated diamond wheel was used. The truing wheel is shown in Figure 3.8a and its specifications are described in Table 3.9.

Manufacturer	Grit size μm	Wheel diameter mm	Abrasive layer width mm	Cutting radius R_c mm
Wendt Boart	181	200	50	300

Table 3.9: Truing wheel specifications - Edgetek grinding machine

The truing spindle was clamped on the grinding table. The forming/truing operation is shown in Figure 3.9.

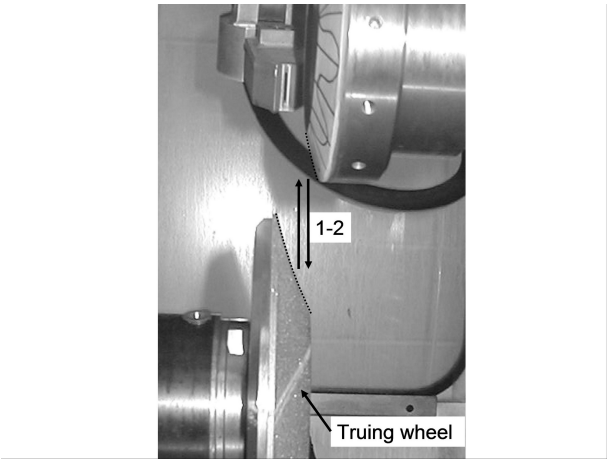

Figure 3.9: Edgetek forming/truing operation

An opposite rotation direction for the grinding and truing wheels were employed during the truing operation. The truing wheel was set at 5000 rpm clockwise while the grinding wheel speed was 800 rpm. The grinding wheel was plunging with an in-feed of 1 mm/min and a dwell time of 2 seconds. This operation (1-2) was repeated until the full grinding wheel abrasive layer was formed.

- **BoX truing roller specifications**

On the BoX grinding machine, a nickel electroplated diamond roller was used to perform the forming operation. The truing roller is shown in Figure 3.8b and its specifications are described in Table 3.10.

Manufacturer	Grit size μm	Wheel diameter mm	Abrasive layer width mm	Cutting radius R_c mm
Cranden	181	90	62	300
	256	90	62	300

Table 3.10: Truing roller specifications - BoX grinding machine

A modified Lidköping Machine Tools AB dressing unit was used. The Likoping truing spindle rotary speed is controlled with the oil pressure. This unit is at a fixed position inside the grinding machine. The forming/truing operation is shown in Figure 3.10.

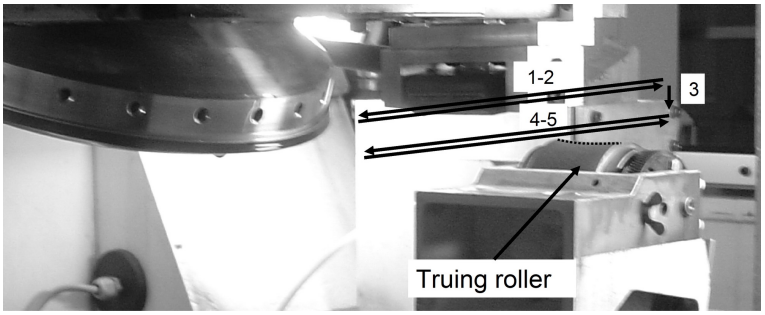

Figure 3.10: BoX forming/truing operation

The truing wheel was driven by slipping belts which lead to a low available torque when feeding the grinding wheel into the truing wheel (Form crushing). Therefore, the forming/truing operation was made by running traverse across the grinding wheel (1-2). The truing roller was set at 4000 rpm clockwise while the grinding wheel speed was 300 rpm. After each reciprocating passes (4-5), the Z axis was moved down by 0.5 μm (3). This operation was repeated to remove any grinding wheel run out and true the grinding wheel to the correct shape.

- **Dressing "sticks"**

After truing and between grinding cuts, the grinding wheels were dressed using dressing "sticks". This operation removes the resin bond between the diamonds to reveal sharp grits. Some dressing "stick" material used for dressing resin bonded diamond wheels are made of aluminum oxide (Mayer Jr. and Fang, 1994, Hwang and Malkin, 1999) and silicon carbide (Inasaki, 1989). Different dressing 'sticks' (Table 3.11) were recommended by each grinding wheel supplier.

Type	Reference code	Thickness	Width	Length
		mm	*mm*	*mm*
Green stick	WA220	25	25	150
White stick	XGC220/EBZ	25	25	150

Table 3.11: Dressing "sticks" specifications - Edgetek and BoX grinding machines

The Wendt Boart grinding wheels were dressed using a soft alumina white "stick". A green carborundum "stick" was used to dress the Cranden grinding wheels. The Edgetek and BoX dressing operations are shown in Figure 3.11.

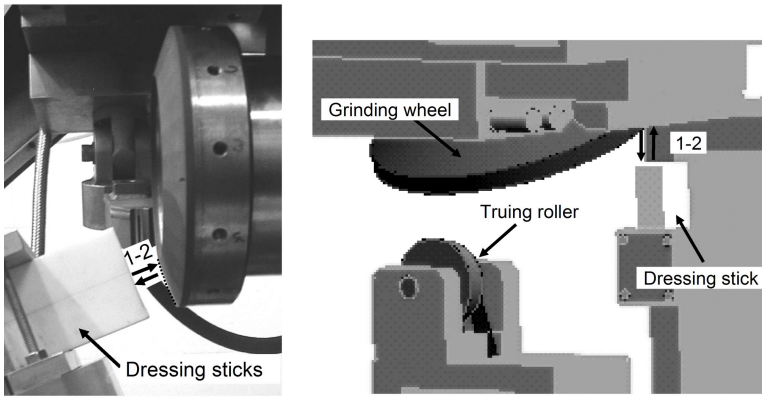

Figure 3.11: Edgetek and BoX dressing operations

On both grinding machine, the grinding wheel was gradually plunged into the "sticks" using a speed of 1 mm/min (1-2). The quantity removed from the "stick" during each dressing operation was 2 mm.

3.2.3 Grinding nozzles and coolant

As described in Chapter 2, slot type coolant nozzles were used as shown in Figure 3.12.

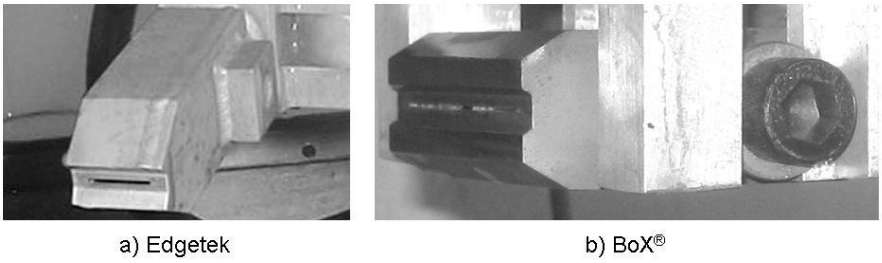

Figure 3.12: Grinding nozzles

- **Edgetek coolant nozzle**

The slot nozzle used on Edgetek grinding machine, Figure 3.12a, was manufactured by Cool-Grind Technologies. The slot has a 30 mm width and 0.6 mm height. A consistent coolant flow across the whole contact region between the specimen and the wheel is necessary (Webster et al., 1995). In order to achieve a visual laminar flow with the specific nozzle opening, the pressure was set at 2 bars.

- **BoX coolant nozzle**

A slot nozzle, Figure 3.12b, was used on the BoX grinding machine. The grinding wheel abrasive layer width, 60 mm, is larger than the nozzle slot width used on the Edgetek

grinding machine. A new nozzle with a wider opening was designed and manufactured. The new nozzle has a slot of 60 mm width and 0.6 mm height.

This nozzle was made following the design described in section 2.7.5. A laminar flow rate was targeted (R_e = 2000). The targeted coolant velocity was 30 m/s to match the grinding wheel speed. The coolant was assumed to be water as the percentage of grinding coolant was 2% in water as described in details below. Using equation 2.7.1 in section 2.7.5, to obtain a laminar flow with a Reynold Number, the slot height is 0.66 mm.

The flowrate, Q_f and pressure at nozzle, p_p are calculated using equation 3.2.1 and equation 3.2.2 respectively (Marinescu et al., 2004*a*).

$$Q_f = v_{slot} \times h_{slot} \times w_{slot} \tag{3.2.1}$$

$$p_p = \frac{12\eta \times l_{slot} \times v_{slot}}{h_{slot}^2} + \frac{\rho \times v_{slot}^2}{2} \tag{3.2.2}$$

The slot length and width are l_{slot} and w_{slot} respectively. The slot width was set at 60 mm to match the grinding wheel abrasive layer width. The calculated flowrate at nozzle is 64.8 l/min and calculated pressure at nozzle is 5.7 bar.

Compared to the Edgetek grinding machine, due to a limited space for a pressure gauge, the pressure was modified at the pump to keep a visual laminar flow. The pressure obtained at pump is 5-6 bars. No burning of the abrasive resin layer was observed.

- **Grinding coolant**

A water based grinding cooling fluid was chosen. Water based coolant were successfully used on ceramics and glasses (Inasaki, 1987, Evans et al., 1997, Hwang and Malkin, 1999). The coolant used was Dowel diluted at 2% in water. Dowel was recommended internally based on previous successful work on silicon carbide. The same coolant was used for Zerodur, ULE and Fused silica. This decision was based on reducing the down time between grinding experiments and the cleaning time required to switch between grinding coolant to avoid any cross contamination. No wheel burning occurred on Edgetek grinding wheels and rust was avoided. Therefore, no additional investigation was made to optimized the coolant type or concentration. The same grinding coolant and concentration was used on BoX grinding machine. No burning of the grinding wheels were observed when the coolant flow was kept constant in the contact zone.

3.2.4 *In-Process measurement equipment*

- **Grinding forces monitoring**

The grinding forces were monitored using a Kistler dynamometer table. It was calibrated using set of calibrated weights.
Grinding forces were monitored for each experiment on Edgetek and BoX grinding machines. This was important in order to assess the amount of deflection based on the machine tool respective stiffness. A Kistler 3 component dynamometer table, reference 9257BA, was used. This table is able to monitor the forces in 3 directions (F_X, F_Y and F_Z). A built-in charge amplifier (5233A) along with a software, DynoWare, allowed to record the signal. This software was used to analyse the grinding forces.

- **Spindle power monitoring**

On the Edgetek grinding machine, the spindle power was monitored during each grinding experiments. The machine is equipped with built-in monitoring system. The signal is linked to a computer with a data acquisition system. A NI Labview based programme was previously developed to process this signal (Walton, 2008).
On the BoX grinding machine, the tangential forces were used to calculate the grinding power based on equation that relates the tangential grinding force with grinding wheel speed.

3.2.5 *Metrology techniques*

- **Profilometer (Surface roughness and form)**

Figure 3.13: Taylor-Hobson Form Talysurf 120L profilometer

The parameters used to characterise the ground surface included surface roughness R_a and surface profile P_t. A Taylor-Hobson Form Talysurf 120L profilometer was used to

make these measurements. It has a resolution of 10 nm with an accuracy of 2 μm over 50 mm and 4 μm over 120 mm (Taylor-Hobson, 2009). The stylus tip employed was a 2 μm radius conisphere diamond.
From the raw profile, the Taylor-Hobson software filters calculate the surface parameters following the ISO standard 4287. This profilometer is a 2D tool capable of measuring in the range of ground surfaces, 2 nm to 1 μm R_a. Other tools such as white light interferometer were considered and tested but did not give usable results.

- **Profilometer (Large scale surface form)**

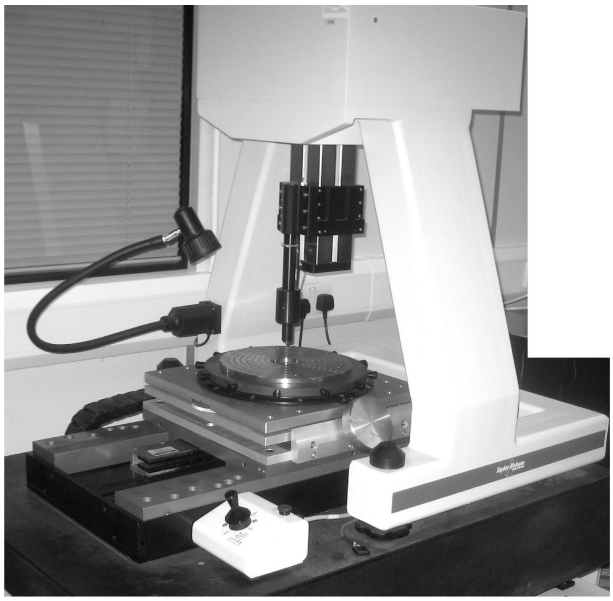

Figure 3.14: Taylor-Hobson Talyseries Form profilometer

A Taylor-Hobson Talyseries Form profilometer was employed to measure the surface profile of the 400 mm square ULE part and the 400 mm across corners hexagonal SiC part. Its maximum scanning length is 310 mm with a travel of 400 mm. The data spacing between collected points is 2.64 μm and the form accuracy, for best fit circular arc, is 1 μm over 300 mm. The stylus tip employed was a 1 mm diameter ruby ball.

- **Coordinate measuring machine (Large scale surface form)**

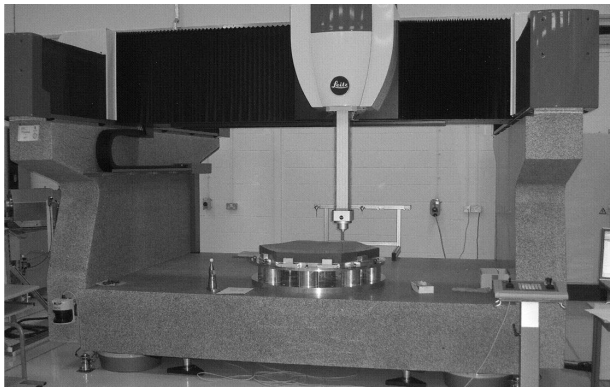

Figure 3.15: Leitz PMM-F co-ordinate measuring machine

A Leitz PMM-F co-ordinate measuring machine was used to measure the surface profile of the 400 mm across corners hexagonal SiC part and the 1 m across corners hexagonal Zerodur part. This CMM is located in the Hexagon Loxham Precision Laboratory at Cranfield University. A sapphire analogue probe of 5 mm diameter was employed. Continuous scanning with a sampling every 0.1 mm and 2 mm was used on the Zerodur and SiC parts respectively.

- **Microscope (Subsurface damage and grinding wheel topography)**

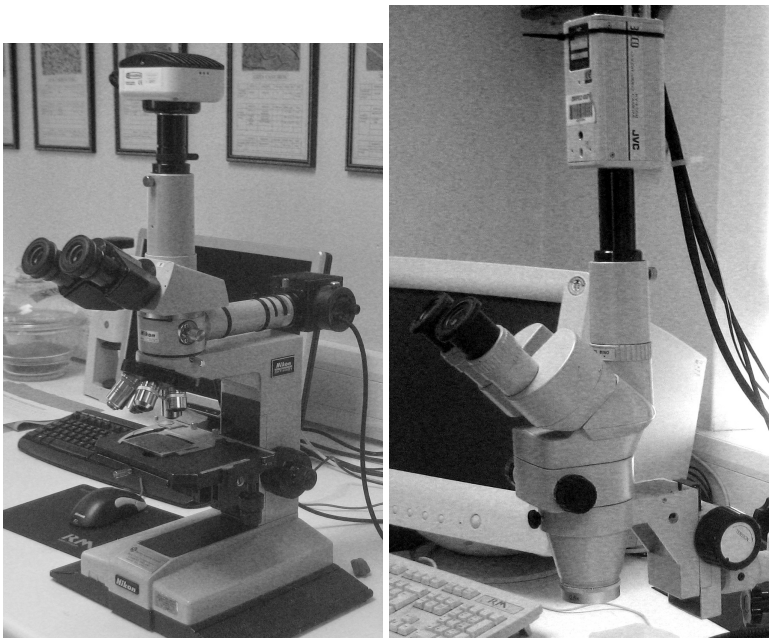

(a) Nikon Optishot microscope (b) Nikon 10x zoom microscope

Figure 3.16: Nikon optical microscopes

A Nikon Optishot optical microscope (Figure 3.16(a)) with a mounted digital live camera was used to inspect the subsurface defects. The principal lens used was a Nikon MPlan

40X, 0.65. The sample sizes were 100 mm x 100 mm x 20 mm. A microscope observation was preferred to a SEM image due to the size limitation for the SEM chamber.
A 10x zoom Nikon optical microscope (Figure 3.16(b)) with a mounted digital live camera was used to inspect grinding wheels. The grinding wheel grit concentration, number of grit per mm^2, were measured.

- **Grinding stiffness measurement**

The grinding stiffness of each grinding machine was investigated. These measurements were carried out using the same approach on both grinding machines.

A universal tension/compression load cell was used to measure the force applied. The model used was a Thames Side-Maywood Series U4000, Figure 3.17 with a load range up to 100kgf.

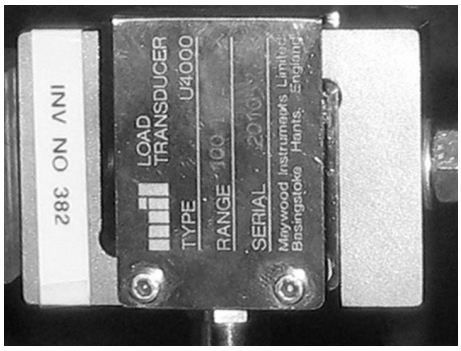

Figure 3.17: Universal tension/compression load cell

The load cell was calibrated (see Appendix A) using a compression bench. The procedure followed to measure the machine stiffness using the holding fixture is explained below.

The holding assembly fixture used during grinding was mounted and clamped in position. The load cell was placed at the same position as the ground sample. The grinding wheels were pushed into the load cell gradually. The deflection of the grinding wheel, the holding fixture and the machine tool stiffness were measured.
This way the grinding stiffness was measured and not only machine stiffness. All the results are described in details in sections 4.2 and 4.3.

3.3 Experimental design

At the start of this research, November 2004, the BoX grinding machine was under construction. It was commissioned in May 2007 and became available for process development in August 2007. Therefore, the research trials started using the Edgetek grinding

machine. The different grinding parameters and grinding wheels were tested. Confirmation research trials were repeated on the BoX grinding machine to control the dynamic influence on the process optimized parameters.

The methodology, using different grinding machines and different part dimensions, is described in Figure 3.18.

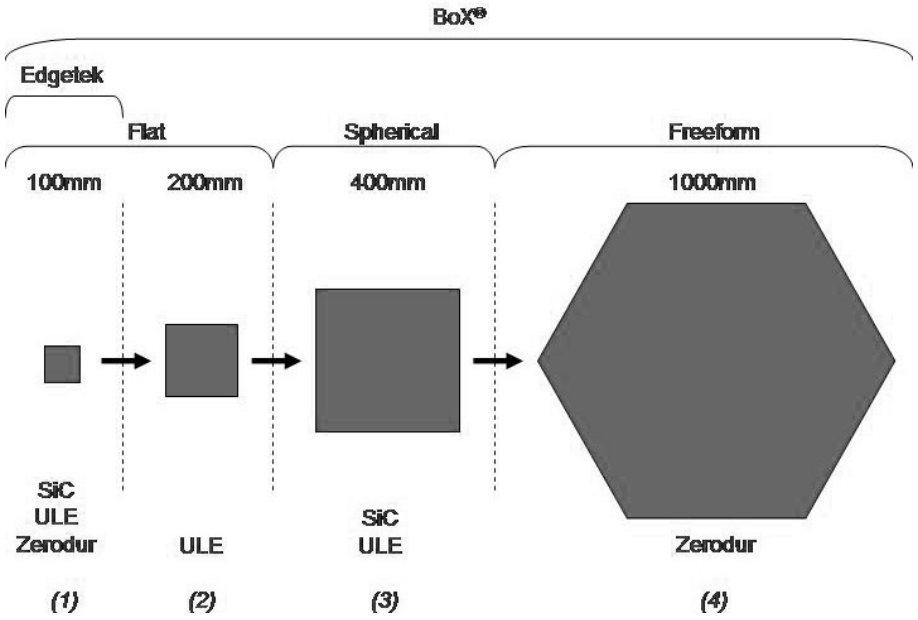

Figure 3.18: Process development methodology

The influence of grinding parameters were investigated using 100 mm square samples. On the Edgetek grinding machine, parameter screening experiments were carried out to investigate grinding parameter influences on Zerodur. Later, Edgetek based test programme (1) was done on Zerodur, ULE and sintered silicon carbide (SiC). Subsequent BoX based test programme was made to validate experiments (1). The total grinding process was validated on three large parts: the first part was a 400 mm square ULE sample (3), the second part was a 400 mm across corner SiC hexagonal part (3) and the third part was a 1 m across corner Zerodur hexagonal part (4).

3.3.1 Parameter screening

Parameter screening was defined using a design of experiment (DoE) approach. A Taguchi L9 array was chosen as an adequate DoE experiment. In nine experiments, four parameters with three levels were evaluated. The full factorial experiment required 81 runs.

Based on the literature review, four grinding parameters were recognised to significantly influence the grinding process of optics. Depth of cut, feedrate, work speed and cutting speed were highlighted to influence surface roughness, subsurface damage and surface profile. All four parameters were varied to three levels. Two other important parameters, the grinding wheel and the ground material, were kept constant. The experiments were carried out using the D46 grinding wheel. Zerodur parts were used with a dimension of 100 mm x 100 mm x 20 mm. The four parameters and three levels are described in Table 3.12.

	Factors			
	Depth of cut	Feedrate	Work speed	Cutting speed
	a_e	f_r	v_w	v_c
Trial N°	μm	$mm/step$	mm/s	m/s
1	50	1	5	25
2	50	5	10	30
3	50	10	15	35
4	100	1	10	35
5	100	5	15	25
6	100	10	5	30
7	250	1	15	30
8	250	5	5	35
9	250	10	10	25

Table 3.12: Design of experiments: Grinding parameters

The depth of cut levels chosen were 50 μm, 100 μm and 250 μm. The two higher levels were selected to investigate the high removal rate achievable for a given grinding wheel geometry. The lowest level was tested to evaluate minimum subsurface damage depth for a given grinding process. The number of stages required in the grinding process to achieved the maximum removal rate and subsurface damage depth were evaluated.

The feedrates were 1 mm/step, 5 mm/step and 10 mm/step. The two coarse levels were selected to achieve efficient material removal rate. The 1 mm/step was chosen based on diamond turned equation 3.3.1.

$$P_t = \frac{f_r^2}{8 \times R_c} \tag{3.3.1}$$

For a grinding wheel cutting radius of 300 mm, final output was lower than 1 μm cusp profile targeted.

The work speed levels were 5 mm/s, 10 mm/s and 15 mm/s. Those levels were chosen to achieve the targeted 10 hours process time.

Cutting speed levels were 25 m/s, 30 m/s and 35 m/s. The cutting speed was changed to evaluated Edgetek grinding machine resonance frequency. The cutting frequencies were 53 Hz, 63.6 Hz and 74 Hz. Those cutting speeds levels correspond to published values between 10 m/s and 40 m/s on grinding ceramics and glasses (Inasaki, 1987, Hwang and Malkin, 1999).

The process responses recorded were: grinding power and normal grinding forces. The surface responses measured were: surface roughness, surface profile and subsurface damage. The grinding visual quality responses observed were: surface cracks and edges chipping. The assessment procedures are described in section 3.4. The values targeted for those responses are compiled in Table 3.13.

Responses		Values targeted
Total process time	hours	10 (to remove 1 mm material thickness)
Material removal rate	mm^3/s	200 maximum (contact width 15 mm)
Normal grinding Forces	N	< 100 for finish cut
Grinding Power	W	< 6000
Surface profile (P_t)	μm	< 1
Surface roughness (R_a)	nm	< 150
Subsurface damage	μm	< 5
Edge damage		None
Cracks surface		None

Table 3.13: Design of experiments: Grinding responses

Project targets in respect of; surface profile, surface roughness and subsurface damage were fixed as input quality demands for the subsequent polishing process. A 10 hour total process time to remove 1 mm of material of ULE, SiC and Zerodur was defined as another demand. To achieve the necessary maximum material removal rate using the BoX grinding machine, a power request needed to be calculated.
Reported specific energy for SiC were approximately 30 J/mm^3 (Inasaki, 1987, Hwang and Malkin, 1999) using resin bonded diamond grinding wheels with 56 μm and 84 μm grit size. The specific grinding energy, for soda lime using the same grinding process, was lower than 10 J/mm^3. Using equation 2.8.26 in section 2.8.7, the maximum material removal rate calculated was 200 mm^3/s. The amount of grinding power available required

was 6000 W. The loss due idle power and cooling were estimated to be 3000 W and 1000 W respectively. The BoX grinding spindle maximum power was specified to be 10 000 W.

BoX stiffness was designed to 100 N/μm so to obtained a form accuracy below 1 μm, the maximum normal grinding force needed to stay lower than 100 N.
The grinding responses of those parameter screening experiments were used to define the second set of experiments.

3.3.2 Edgetek based test programme

The parameters defined for the Edgetek based test programme were chosen based on the results of the screening experiment. The proposed grinding process steps are shown in Figure 3.19 in term of depth of cuts.

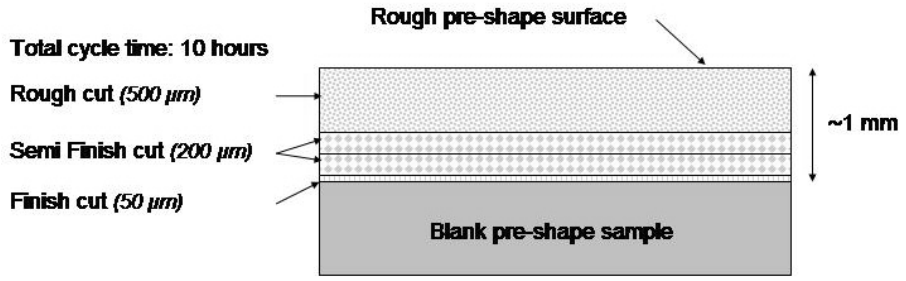

Figure 3.19: Grinding process steps (1/2)

The supplied blanks are generally lapped with a significant form error and "assumed" deep subsurface damage. Three grinding steps were proposed to achieve the surface quality demand within a process time of 10 hours. Each process step was carried out on a different sample for analysis purposes. Three materials, Zerodur, ULE and SiC were tested. The grinding parameters and levels are shown in Table 3.14.

Grinding Conditions	Grit size μm	Depth of cut a_e μm	Feedrate f_r *mm/step*	Work speed v_w *mm/s*	Cutting speed v_c *m/s*
Rough cut	76	500	15	25	30
Semi Finish cut	76	200	10	20	30
Semi Finish cut	46	200	10	20	30
Finish cut	76	50	1.5	25	30
Finish cut	46	50	1.5	25	30
Finish cut	25	50	1.5	25	30

Table 3.14: Process evaluation: Grinding parameters - Edgetek

For the three grinding conditions, three parameters were changed: depth of cut, feedrate and work speed. The cutting speed was kept constant at 30 m/s. The grit size was changed for semi finish cut and finish cut. The three grinding steps, in terms of expected form accuracy (P_t) and subsurface damage levels, are illustrated in Figure 3.20.

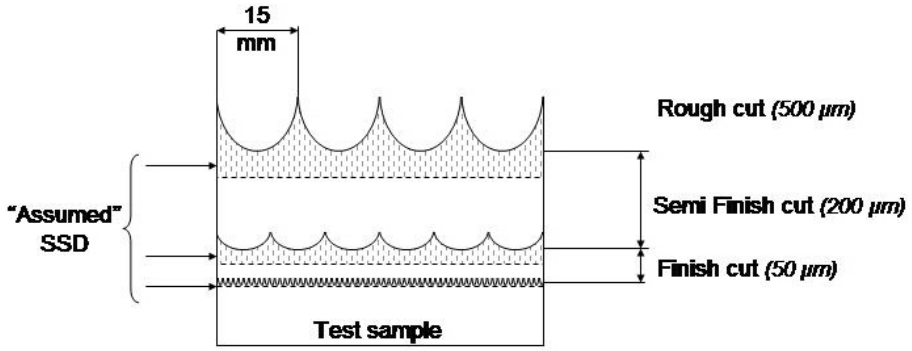

Figure 3.20: Grinding process steps (2/2)

The rough cut removes a large quantity of material, a 500 μm depth, with a high material removal rate of 187.5 mm^3/s. The screening experiments showed that such a high removal rate with a D46 grinding wheel was inappropriate due to high forces. The D76 grinding wheel was expected to be more efficient for the rough cut and reduce the high grinding force levels (Inasaki, 1987, Zhang and Howes, 1995).

The semi finish cut eliminates the rough cut surface error (estimated 94 μm) and subsurface damage layer. The parameters chosen were less aggressive in order to reduce the grinding forces, subsurface damage level and surface form error. The screening experiment results showed that a D46 grinding wheel was relevant to meet those targets.

The finish cut removes the surface form error (estimated 42 μm) and the subsurface damage induced by the semi finish cut. The parameters were again chosen based on the screening experiment results which achieved the final surface quality targets. A D25 grinding wheel was expected to reduce surface roughness along with subsurface damage (Inasaki, 1987, Namba and Abe, 1993, Mayer Jr. and Fang, 1994).

The process responses recorded were; grinding forces, grinding power and wheel wear. The surface qualities measured were surface roughness, surface profile and subsurface damage.

3.3.3 BoX based test programme

The process and surface responses obtained from the Edgetek based test programme demonstrated the possibility of an efficient grinding process. The BoX based test programme replicates the Edgetek based test programme as shown in Table 3.15.

Grinding Conditions	Grit size μm	Depth of cut a_e μm	Feedrate f_r *mm/step*	Work speed v_w *mm/s*	Cutting speed v_c *m/s*
Rough cut	76	500	15	25	30
Semi Finish cut	76	200	10	20	30
Semi Finish cut	46	200	10	20	30
Semi Finish cut	25	200	10	20	30
Finish cut	76	50	1.5	25	30
Finish cut	46	50	1.5	25	30
Finish cut	25	50	1.5	25	30

Table 3.15: Process evaluation: Grinding parameters - BoX

The D25 grinding wheel was also used for the semi finish experiments to assess the subsurface damage depth induced by the three different grit sizes. For a similar reason, the D76 grinding wheel was employed for finish experiments. Each grinding condition was tested on Zerodur and ULE materials.

Based on the Edgetek based test programme process responses, the D25 grinding wheel was employed on SiC with the finish cut levels. The calculated grinding power of BoX (6000 W) limited the depth of cut when grinding SiC. The maximum depth of cut used was 300 μm with a material removal rate of 112.5 mm^3/s.

The process responses recorded were grinding forces. The surface qualities measured were surface roughness, surface profile and subsurface damage.

3.3.4 BoX large scale surface experiments

Large scale grinding trials were carried out using the BoX grinding machine and the proposed three levels grinding process. The process conditions/targets are shown in Figure 3.21.

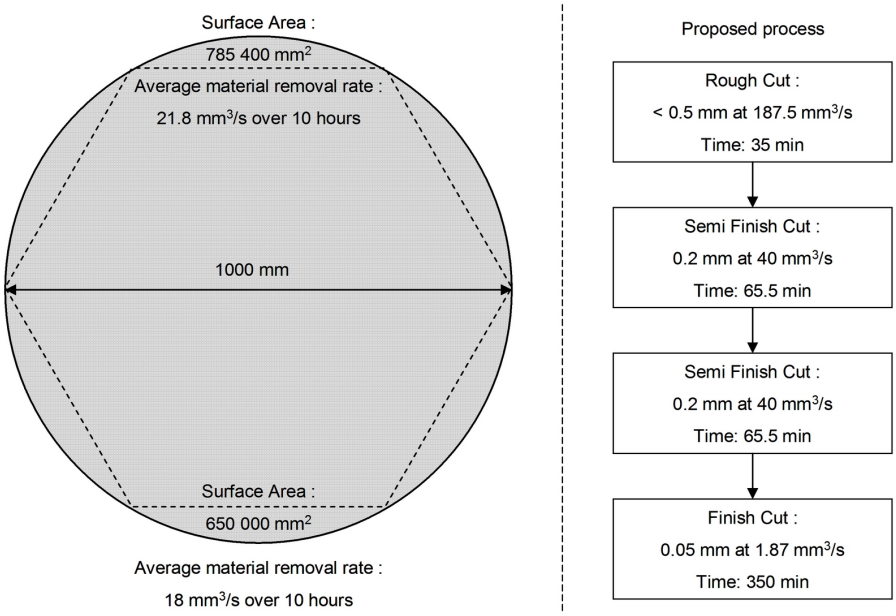

Figure 3.21: Process responses targets

The BoX large scale surface experiments were performed on three parts to validate the process development. A ULE plate, 400 mm x 400 mm x 25 mm was ground to 3000 mm radius of curvature. The surface roughness, profile and form accuracies were measured using the Talysurf profilometer.
The second part machined was a SiC plate, 400 mm across corner hexagonal part. This part was ground to 3180 mm radius of curvature. The surface profile and form were measured using the Talysurf profilometer and the Leitz CMM.
The third part was a 1 metre across corner hexagonal Zerodur segment. It was ground to a 3000 mm radius of curvature sphere. After grinding, a Leitz CMM was employed to measure the surface form.

3.3.5 Grinding wheel wear experiments

The grinding wheels employed were of a resin bonded diamond type. The resin bond was chosen to limit subsurface damage but potentially induces significant grinding wheel wear (Inasaki, 1987). Since the grinding wheel shape influences the final form accuracy (Li et al., 2004), wheel wear tests were carried out. Figure 3.21 illustrated the amount of material removed on a one metre part. The amount of grinding wheel wear was evaluated for each grinding condition. Three machining conditions were tested for each material. These experiments and the amount of material removed are shown in Table 3.16.

Wheel type	Q_w *mm^3/s*	a_e *μm*	f_r *mm/step*	v_w *mm/s*	v_c *m/s*	V_w for half scale tests *cm^3*
D76	187.5	500	15	25	30	125
D46	40	200	10	20	30	40
D46	1.87	50	1.5	25	30	10

Table 3.16: Grinding conditions for grinding wheel wear experiments

These grinding experiments were carried with no intermediate dressing. Material volumes of 125 cm^3, 40 cm^3 and 10 cm^3 were removed using rough, semi finish and finish grinding cuts respectively. These volumes correspond to the equivalent amount of material removed for a 500 mm diameter optic. These "half" scale experiments provide realistic information about the grinding of larger parts using the BoX grinding machine.

The ground sample thicknesses were measured at regular intervals. This gave a good assessment of the actual material volume removed compared to the programmed levels. An imprint of the grinding wheel shape was made. This is detailed in Chapter 3.4.3. The final value obtained is the material removed from the grinding wheel between each recorded run. The data collected was plotted to obtain a graph of grinding wheel wear versus material removed. This relation was made for each grinding condition on each material type. The final value determined is the G ratio for the overall process.

For example, Inasaki and Nakayama (1986) reported a G ratio of 71 using a D56 wheel in ceramic grinding with a depth of cut of 1 mm. In grinding SiC with a resin bonded wheels, G ratios of 259 and 130 for 126 μm and 64 μm grit sizes with 100 concentration were obtained. G ratios of 142 and 86 for 126 μm and 64 μm grit sizes with 75 concentration were reported (Inasaki, 1987).

3.4 Assessment procedures

3.4.1 Surface quality

The project targets are surface roughness R_a = 50-150 nm and surface profile P_t < 1 μm. The surface roughness and surface profile measurements directions are shown in Figure 3.22.

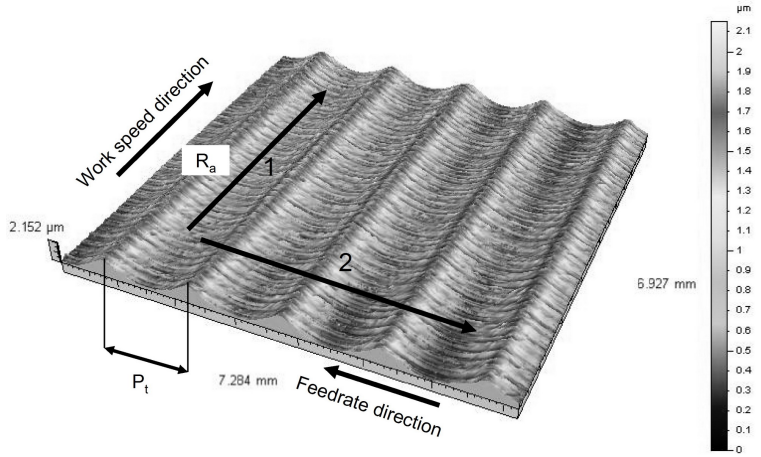

Figure 3.22: Roughness & Profile measurement directions

The work speed direction (1) and feedrate direction (2) are shown in Figure 3.22 respectively.

- **Surface roughness**

For each ground sample, the surface roughness, R_a, was measured using a Talysurf 120L profilometer (Chapter 3.2.5). The measurements were made following the ISO standard (Chapter 2.9) requirements. Table 3.17 shows the filter parameters used.

Sampling length l_r *(mm)*	Minimum Evaluation length l_n *(mm)*	Filter used
0.8	4	Gaussian G300

Table 3.17: Filter parameters used

These parameters were chosen based on the expected roughness values ($<$ 500 nm R_a). The roughness measurements were taken in the work speed direction (1). A measurement was also made across the ground sample cusps along the feedrate direction (2) for comparison.

- **Ground surface profile**

The peak to valley profile, P_t, generated by the particular grinding condition was measured using the Talysurf 120L profilometer. The parameters employed are shown in Table 3.17. The profile measurement was made across the work speed direction (2). These measurements were used to characterise the grinding mode output.

- **Form accuracy**

Form accuracy measurements were carried out on 400 mm and 1 metre ground samples using a Leitz CMM and a Talyseries form profilometer.

3.4.2 Subsurface damage assessment

Different destructive assessment techniques are described in section 2.10.3. The selected technique for subsurface damage assessment is taper ("wedge") CNC polishing with subsequent rapid acid etching. This technique permits examination of numerous depth zones in one operation. Examination of different depths in a single location would require a protracted iterative polish-etch cycle. This technique is believed to be comparable to the widely successfully used MRF wedge technique (Suratwala et al., 2006).

- **Taper polishing**

The subsurface damage levels were observed on ULE and on Zerodur. An example is shown in Figure 3.23.

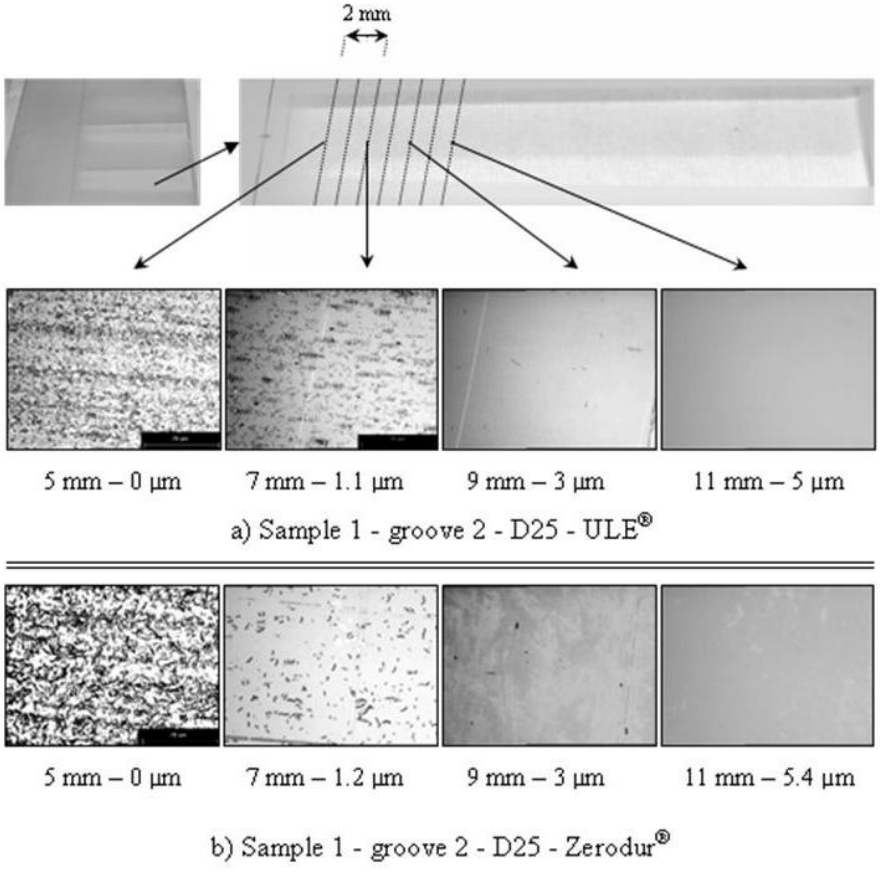

Figure 3.23: Subsurface damage depth measurement example - ULE and Zerodur - Finish cut (D25) - Edgetek

A Zeeko IRP polishing machine was employed to polish the tapered grooves. Grooves were polished in line with the grinding direction and corresponded to the bottom of the scallop where the ground surface is at its lowest point as shown in Figure 3.24.

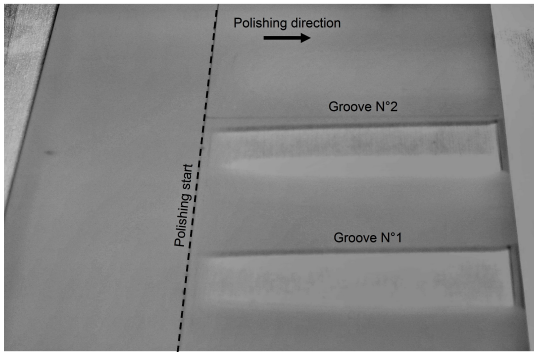

Figure 3.24: Polished grooves

Two grooves were polished on each sample in order to confirm repeatability of the measured value of the subsurface damage. The polished tapered grooves were etched using HF and HCl acids on Zerodur and ULE respectively.

- **Etching solution**

The material manufacturers were contacted to obtain details of a suitable etching fluid. The recommended etching fluids and techniques are described in Table 3.18.

Material	Etching fluid	Etching time calculated to remove $< 1\mu$m
Fused Silica	30% HF, 70% H_2O dist	2 minutes
ULE	143 g of Amonium bifluoride, 357g H_2O dist	30 seconds
Zerodur	2 vol. HF 40% 1 vol. HCl 32% 1.5 vol. H_2O dist	12 seconds

Table 3.18: Etching solution

The etching rate was assessed using the recommended etching solutions. Each of the etched areas were measured with a profilometer to evaluate the etching depth. The etching time versus etching depth was plotted (See Appendix B.1).
The etching time employed for subsurface damage analyses was selected to ensure a removal layer less than 1 μm from the polished surface.

- **Crack measurement**

After etching, the number of cracks were counted manually using an optical microscope fitted with a digital camera (See section 3.2.5). The evaluation area was 150 μm x 200 μm. An example is shown in Figure 3.25.

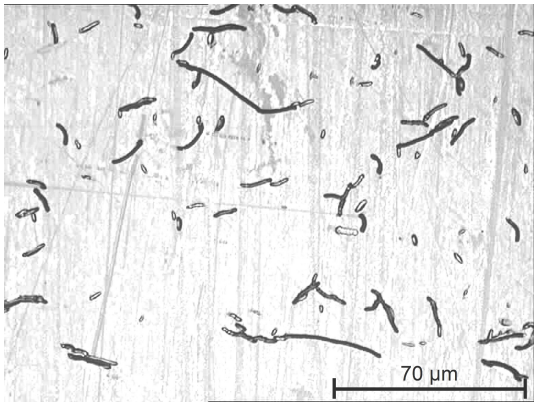

Figure 3.25: Evaluation area example - Zerodur - Semi finish cut (D76) - Edgetek

The number of cracks counted was multiplied by 33 in order to get a number of cracks per mm^2. Identification of defects for counting was based on human judgement. Where the degree of interconnect crack made individual counting difficult, the results were omitted from the analysis. Such results represented only very shallow damaged regions.

3.4.3 Grinding wheel wear evaluation

The grinding wheel wear was evaluated using an imprint technique. All grinding wheel wear experiments were carried out using the Edgetek grinding machine. Grinding wheel wear studies were undertaken on ULE, SiC and Zerodur. Grinding wheel wear was established by making graphite imprint. Imprints within the graphite blocks were band sawn into smaller blocks to allow profiles to be measured. A graphite imprint example is shown in Figure 3.26.

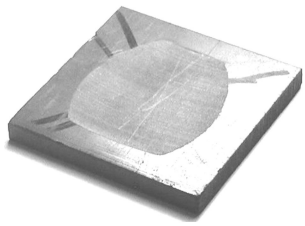

Figure 3.26: Graphite imprint example

Each block was measured using a profilometer to get the abrasive layer shape. These profiles were exported as raw data in a Microsoft Excel spreadsheet. This data was manipulated to align, as close as possible, for each imprint profile. Alignment was made using the none wear region between each run as shown in Figure 3.27.

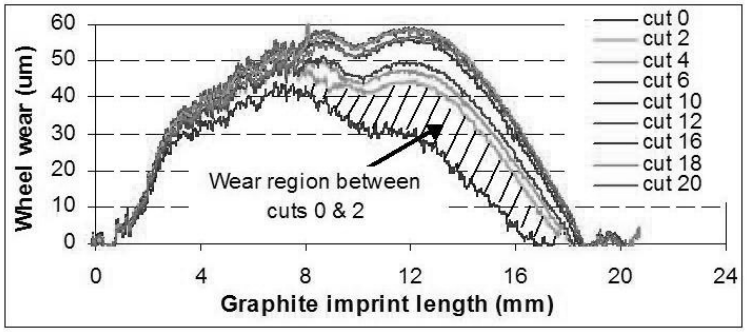

Figure 3.27: Wheel wear measurement example

3.4.4 Grit concentration measurement

A direct measurement of the grinding wheel was carried out using a Nikon optical microscope (See section 3.2.5). The grit concentration was calculated on each Edgetek grinding wheel. An observation example is shown in Figure 3.28.

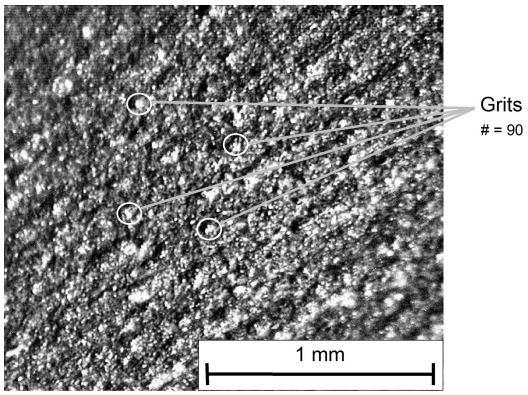

Figure 3.28: Grit concentration observation example - D46 grinding wheel - Wendt Boart

Each grinding wheel was assessed by counting the number of grits in a specific area. The number of grits per mm^2 was obtained. On each grinding wheel, measurement was repeated at four different places to obtain an average grit concentration.

4. CHARACTERISATION OF EXPERIMENTAL EQUIPMENT

In this chapter, the experimental equipment characterisation is detailed. This includes the grinding wheel grit concentration evaluation and Edgetek and BoX grinding stiffness evaluations. A comparison of grinding machine stiffness is presented.

4.1 Grinding wheels - grit concentration evaluation

Using an optical microscope, the grit concentration was measured for each Edgetek grinding wheel. The BoX grinding wheels have the same characteristics so the same values were assumed. The measured grit concentrations are shown in Table 4.1.

Grinding wheel grit size *(μm)*	Concentration	Volume fraction (υ) *(% by volume)*	Measured concentration *(#/mm^2)*
25	50	12.5	90
46	50	12.5	42
76	75	18.75	24

Table 4.1: Measured grit concentrations

The measurement procedure is described in details in section 3.4.4. The measured grit concentration is an average value based on four measurements. The values obtained are 90, 42 and 24 grits per mm^2 for the D25, D46 and D76 grinding wheels respectively. Those values are of similar magnitude as previously reported (Mayer Jr. and Fang, 1994, Zhang and Howes, 1995). The concentration varies with the grinding wheel wear, dressing conditions and the assessment technique employed.

The number of active grits per unit area were calculated for each grinding wheel using equations 2.8.6, 2.8.7 and 2.8.8 in section 2.8.5. The calculated number of active grits per unit area are shown in Table 4.2.

Grinding wheel designations	Equivalent US mesh size *(#)*	Number of active grits per unit area C_1 *(#/mm^2)*	C_2 *(#/mm^2)*	C_3 *(#/mm^2)*
D25 C50	800	533	191	616
D46 C50	325/400	88/133	56	182
D76 C75	200/230	44/58	24	87

Table 4.2: Calculated grit concentrations

The closest values to the measured concentrations are obtained for C_2 (equation 2.8.7). The calculated values overestimate the grit concentrations for small grit sizes (Mayer Jr. and Fang, 1994, Xu et al., 1997, Agarwal and Venkateswara Rao, 2008).

4.2 Grinding stiffness evaluation - Edgetek grinding machine

4.2.1 Test set up

The Edgetek grinding machine static stiffness was assessed with the D46 and D76 resin bonded grinding wheels. The D46 and D76 grinding wheels had different diameters, 150 mm and 200 mm respectively. The test set up used to measure the Edgetek grinding stiffness is shown in Figure 4.1.

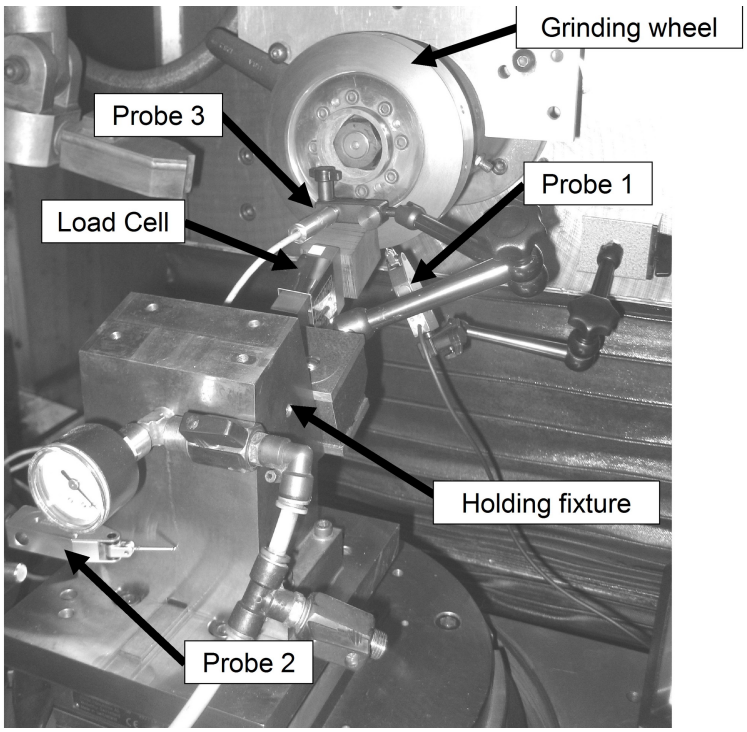

Figure 4.1: Grinding stiffness test set up - Edgetek grinding machine

The grinding wheel deflection was measured with a LVDT probe (1). It was placed at the back of the grinding wheel body. The holding fixture deflection was measured with a second LVDT probe (2). It was placed on the back of the holding fixture, opposite to the load cell. The load cell was positioned against the holding fixture face used to hold the ground sample. A third LVDT probe (3) was placed against the front of the grinding wheel and mounted on the holding fixture. For the D46 grinding wheel, measurements were taken at the top and bottom of the holding fixture. A graphite block was placed between the load cell and the grinding wheel. This block acted as an intermediate part that transferred force across the curved grinding wheel face. A second graphite block was placed between the load cell and the holding fixture. This set up is shown in Figure 4.2.

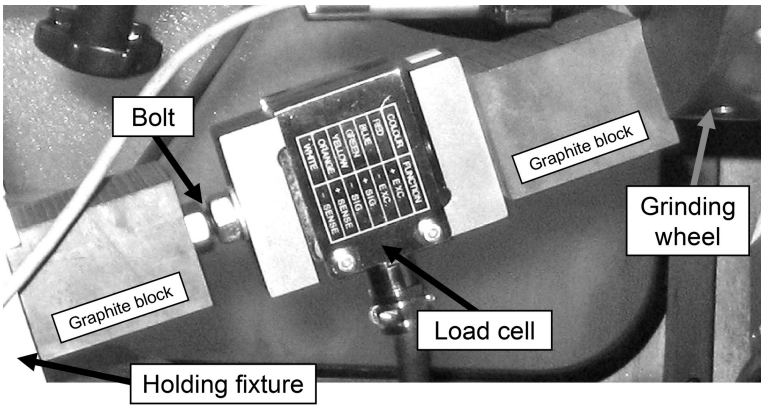

Figure 4.2: Load cell set up - Edgetek grinding machine

Graphite was selected for its high stiffness in compression. It is normally used for compression moulds. A graphite block was ground for each grinding wheel. This maintained the correct angle for the load applied between the grinding wheel and the load cell.
The load was applied by extending a bolt linked to the load cell. This testing approach was preferred to moving the grinding machine axis using the CNC control. The right angled motion would have been difficult to generate. The applied force was measured through voltage output from the calibrated load cell. The deflection between the grinding wheel and the holding fixture was obtained by adding the measurements of LVDT probes 1 and 2. This displacement was recorded under different load levels. This probe measuring set up ignored the deflections of the main slideways and the machine base. These systems were considered not to be major sources of the static deflection.

4.2.2 Results

The measurements results, for the D46 grinding wheel, with the load cell placed on the holding fixture top position are shown in Figure 4.3.

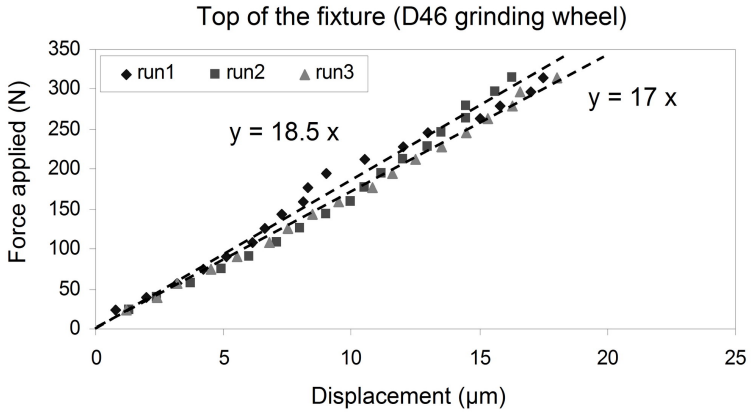

Figure 4.3: Grinding stiffness (a) results - Edgetek grinding machine - D46 top fixture

Three measurements runs were repeated. The grinding stiffness is 17-18.5 N/μm. Each run shows stable results once the applied load is over 90 N.

The measurements results, using the D46 grinding wheel, on the holding fixture bottom position are shown in Figure 4.4

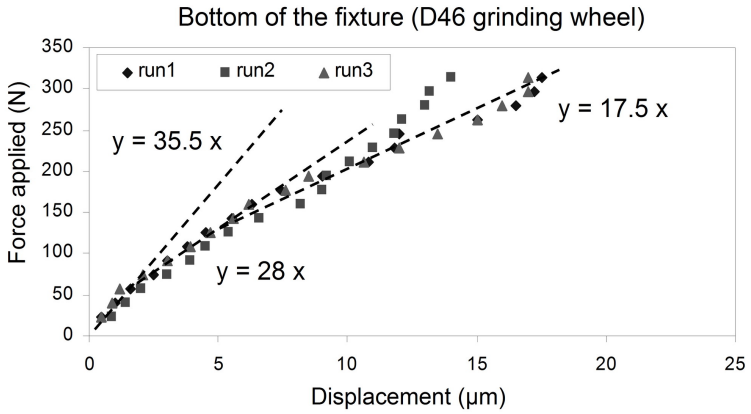

Figure 4.4: Grinding stiffness (b) results - Edgetek grinding machine - D46 bottom fixture

The measurement runs were carried out three times. These measurement results can be divided in three portions. The grinding stiffness starts at 35.5 N/μm until an applied force of 108 N is reached. It reduces to 28 N/μm between 108 N and 142 N. For a load over 142 N, the grinding stiffness stabilises at 17.5 N/μm which is similar to the grinding stiffness measured at the top of the holding fixture.
The holding fixture has a significant influence on the grinding stiffness under low grinding forces. As expected, the results show that the stiffness varies with the position of the force applied on the holding fixture. The holding fixture is stiffer at the bottom where the cantilever is minimized and the material is thicker.

The measurements results, for the D76 grinding wheel, are shown in Figure 4.5. The load cell was placed on the holding fixture top position.

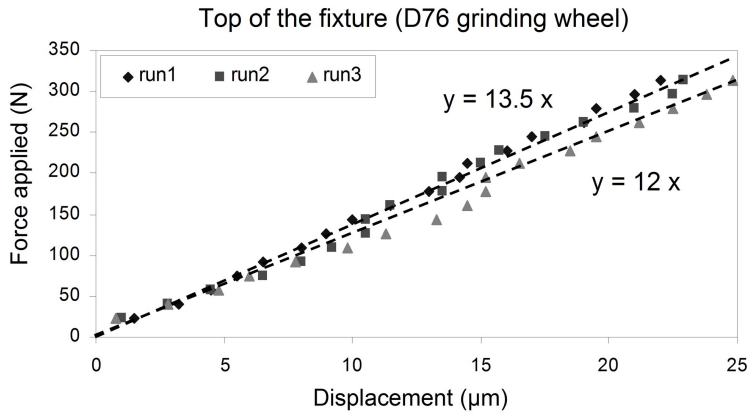

Figure 4.5: Grinding stiffness (c) results - Edgetek grinding machine - D76 top fixture

The measurement runs were repeated three times. The grinding stiffness is 12-13.5 N/μm. A different grinding stiffness is observed between the two grinding wheels. The use of a larger grinding wheel diameter induces a reduction of 5 N/μm on the grinding stiffness.

4.3 Grinding stiffness evaluation - BoX grinding machine

4.3.1 Test set up

The BoX grinding stiffness evaluation was done only using the D46 grinding wheel. A single test was done as the D25, D46 and D76 grinding wheels have the same dimensions. The test set up used to measure the BoX grinding stiffness is shown in Figure 4.6.

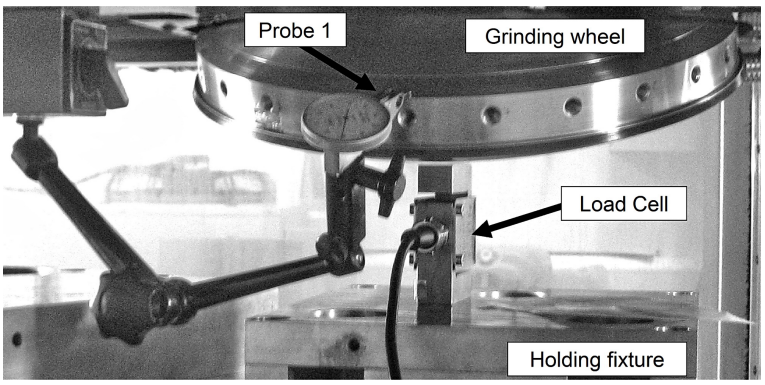

Figure 4.6: Grinding stiffness test set up - BoX grinding machine

A dial gauge was placed at the back of the grinding wheel. The load cell was positioned between the grinding wheel and the holding fixture.

The load was made by moving the Z axis with the CNC controller. Applying the load by extending a bolt linked to the load cell was tried. The torque applied was too important leading to a movement of the load cell. The deflection of the grinding wheel was measured. The load applied was recorded. This probe measuring set up ignores the deflections of the main slideways and the machine base. These systems were considered not to be major sources of the static deflection. The measured tilt stiffness of the C axis at 500 mm radius was 420 N/μm (Morantz et al., 2006).

4.3.2 Results

The measurements results are shown in Figure 4.7.

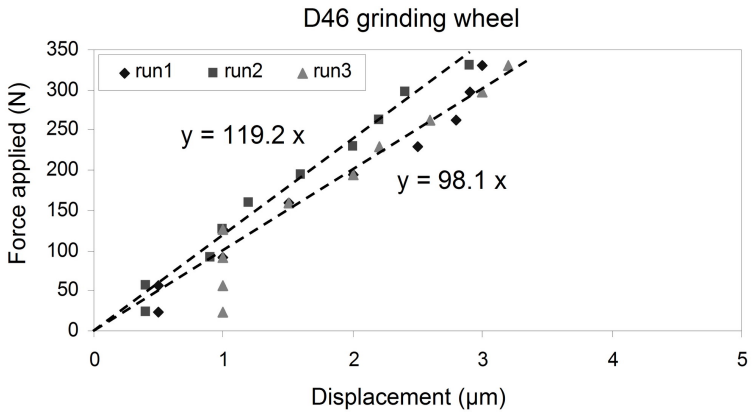

Figure 4.7: Grinding stiffness results - BoX grinding machine

Three repeated measurements runs were done. This grinding stiffness increases linearly with the load applied. The grinding stiffness measured is 98-119.5 N/μm.

4.4 Comparison

The comparison of the displacement versus applied loads over 100 N on Edgetek and BoX grinding machines is shown in Figure 4.8.

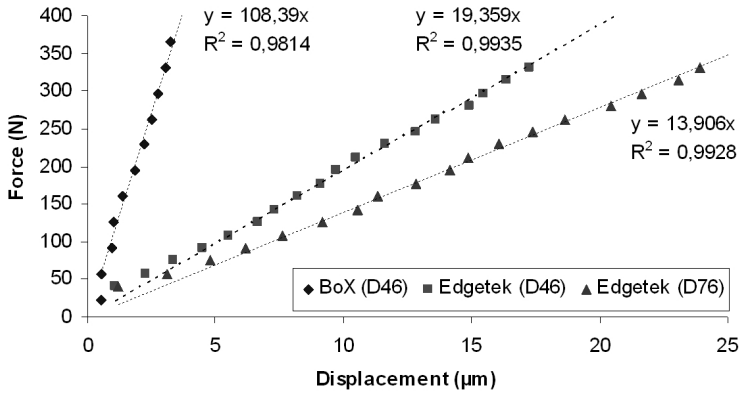

Figure 4.8: Comparison displacement versus applied loads over 100 N

A linear function trend is highlighted for both grinding machines. The BoX grinding machine is 5.6 to 7.8 times stiffer than the Edgetek grinding machine. Under 330 N, the measured deflections are 3 μm and 17-23 μm for BoX and Edgetek grinding machines respectively.

The comparison of the displacement versus applied loads below 100 N on Edgetek and BoX grinding machines is shown in Figure 4.9.

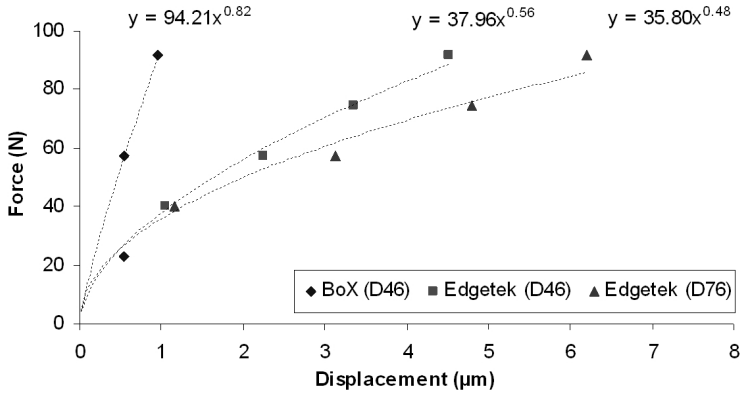

Figure 4.9: Comparison displacement versus applied loads below 100 N

A power function trend is obtained. The static grinding stiffness of both grinding machine changes with the load level applied. On the Edgetek grinding machine, a stable value is reached over 60 N and 90 N for the D46 and D76 grinding wheel respectively. On the BoX grinding machine, a load of 120 N is necessary. Each grinding machine has the grinding stiffness evolving differently. For the Edgetek grinding machine, the grinding stiffness decreases down to 18 N/μm for the D46 grinding wheel and 12-15 N/μm for the D76 grinding wheel. For the BoX grinding machine, the grinding stiffness increases up to 95-120 N/μm.

A displacement of 1 μm occurs under 36-38 N and 94 N for Edgetek and BoX grinding machines respectively. For 100 N, those estimated displacements are 1.1 μm and 5.6-8.5 μm.

5. EDGETEK BASED EXPERIMENTAL RESULTS

In this chapter, the grinding results using the Edgetek grinding machine are presented. Three specific sets of experiments are detailed: parameter screening, Edgetek based tests programme and grinding wheel wear experiments. The experimental responses evaluated were: surface roughness (R_a), surface profile (P_t), subsurface damage, grinding powers, grinding forces and specific grinding energy.

5.1 Parameter screening

5.1.1 Surfaces responses

A 3D surface measurement of a Zerodur sample is shown in Figure 5.1. A Taylor Hobson CCI interferometer was employed to obtain this measurement.

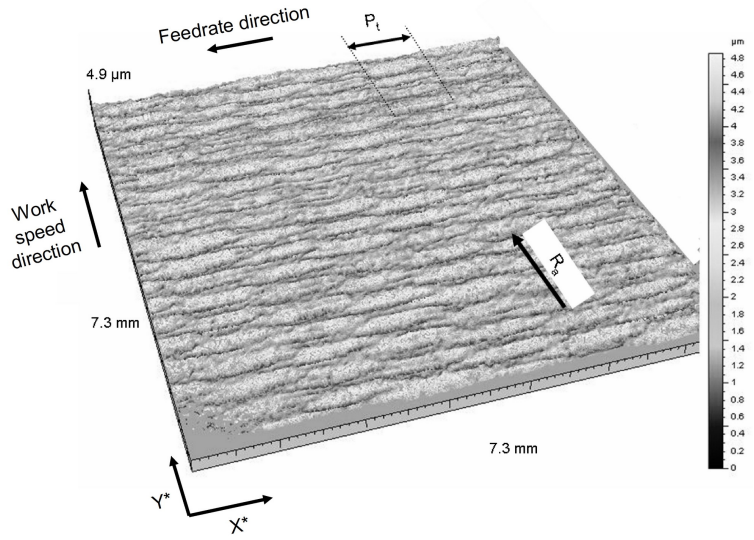

Figure 5.1: Surface measurement example (CCI (2.5X lens) - Zerodur - Trial N°1 - a_e = 50 μm, f_r = 1 mm/rev, v_w = 5 mm/s, v_c = 25 mm/s)

This measurement shows surface responses for Trial N°1, detailed in Table 5.1. The formation is an apparent "tessalated" surface based on the combination of the grinding wheel radius of curvature (300 mm), the feedrate per workpiece step (in the X* direction) and

the feedrate per wheel revolution per feedrate (in the Y* direction) (See Figure 5.1). The surface profile (P_t) "cusping" is parallel to the feedrate direction. Two surface assessments are the surface roughness (R_a) along Y* direction and the surface roughness along X* direction.

The parameter screening experiments factors and levels are compiled in Table 5.1.

	Factors				Responses	
	Depth of cut	Feedrate	Work speed	Cutting speed	Surface Profile	Surface Roughness
	a_e	f_r	v_w	v_c	P_t	R_a
Trials N°	μm	$mm/step$	mm/s	m/s	μm	nm
1	50	1	5	25	2,1	416
2	50	5	10	30	15,7	557
3	50	10	15	35	51,9	428
4	100	1	10	35	3,6	520
5	100	5	15	25	16,3	404
6	100	10	5	30	63,1	463
7	250	1	15	30	2,9	393
8	250	5	5	35	15,5	338
9	250	10	10	25	63,1	584

Table 5.1: Parameter screening - Surfaces responses - Zerodur

The justification of levels chosen for each factor is detailed in section 3.3.1. The Zerodur samples measured surface profile and surface roughness responses are recorded. Those results are discussed below.

The ratio between the surface profile P_t measured and theoretical is calculated in Table 5.2. The surface profile was estimated theoretically using equation 2.9.3, described in section 2.9.2.

Trials N°	Feedrate f_r $mm/step$	Surface profile (P_t) Measured μm	Theoretical μm	Ratio Meas./Theo.
1	1	2,1	0,7	3,1
2	5	15,7	17,1	0,9
3	10	51,9	68,3	0,8
4	1	3,6	0,7	5,3
5	5	16,3	17,1	1,0
6	10	63,1	68,3	0,9
7	1	2,9	0,7	4,3
8	5	15,5	17,1	0,9
9	10	63,1	68,3	0,9

Table 5.2: Parameter screening: Comparison surface profile measured and calculated - Zerodur

These results validate that equation 2.9.3 developed for diamond turning, is adequate to estimate surface profile P_t values. The surface profile is not only controlled by the grinding wheel radius of curvature. The grinding machine dynamics errors have to be taken into account. The measured and theoretical profiles differ over an amplitude of 8.1 μm. Trial N°3 is treated separately.

For a particular feedrate level, the measured surface profile varies. For a feedrate of 1 mm/step, the surface profile value fluctuates between 2.1 μm and 3.6 μm. This corresponds to a difference of three to five times from the theoretical value. The error is between 1.4 μm and 2.9 μm. For 5 mm/step and 10 mm/step, theoretical values are higher than measured data. The ratio between measured and theoretical value is 0.9-1.

Trial N°3 surface profile measurement is shown in Figure 5.2.

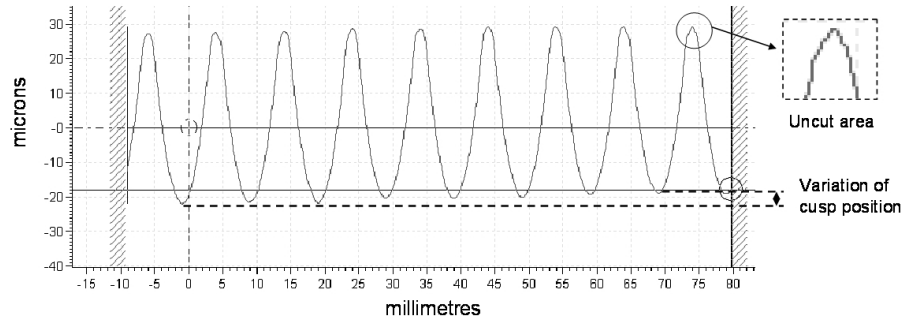

Figure 5.2: Parameter screening - Surface Profile measurement example (Zerodur - Trial N°3)

This example illustrates the contribution of the cusp height to the surface profile P_t value. The difference between the theoretical and measured P_t is the variation of cusp heights as shown.
For this particular trial, an "uncut" region remains visible on top of each cusping peak. The actual measured value is 10 μm lower than the calculated surface profile height.

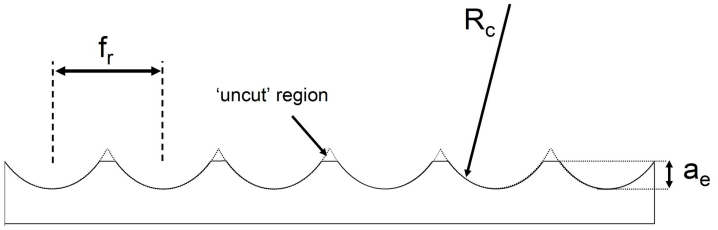

Figure 5.3: "uncut" region example - Zerodur

The feedrate is higher than the maximum contact length between the grinding wheel and the ground part (See Figure 5.3). For a given combination of grinding wheel radius of curvature and feedrate, a minimum depth of cut is required. The grinding process feedrate level is limited by equation 5.1.1.

$$f_r < 2 \times \sqrt{a_e \times (a_e + 2 \times R_c)} \tag{5.1.1}$$

In Trial N°3, for a_e = 50 μm, the maximum feedrate is 8.5 mm/step . For depths of cut of 100 μm and 250 μm, those maximum feedrates are 12 mm/step and 19 mm/step respectively.

The surface roughness responses, R_a versus material removal rate (MMR) and R_a versus R_a along X* are shown in Figure 5.4.

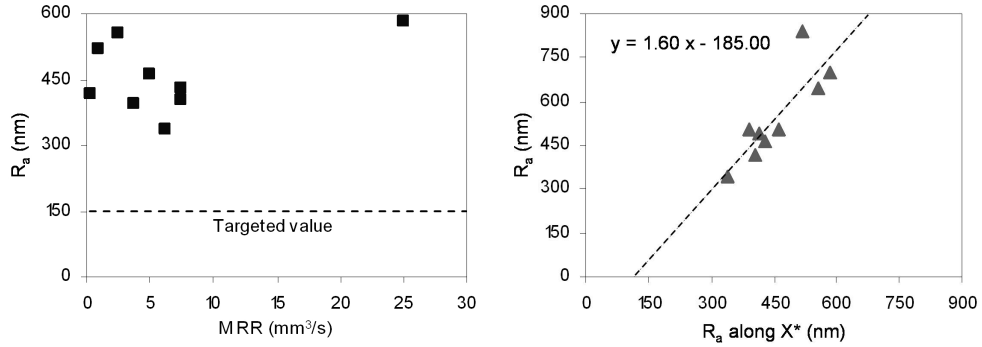

(a) Surface roughness (R_a)

(b) R_a versus R_a along X*

Figure 5.4: Parameter screening - Surface roughness results - Zerodur

Figure 5.4(a) shows the surface roughness (R_a) varies between 338 nm and 584 nm. The targeted surface roughness of R_a <150 nm is not reached. A 46 μm grit size is not adequate for Zerodur. A smaller grit size, 25 μm, was used for the finish step of the grinding process development.

Figure 5.4(b) shows the difference between the surface roughness along Y* and along X*. A linear trend line fits those values. The surface roughness along X* is higher than the surface roughness along Y*. This difference becomes more important for a spiral tool path. The surface roughness along the work speed direction (Y*) would be rendered difficult to measure.

5.1.2 Subsurface damage responses

The subsurface damage (SSD) evaluation technique used is described in section 3.4.2. The number of cracks per mm^2 against the depth beneath ground surfaces were plotted. An example, corresponding to Trial N°1, is shown in Figure 5.5.

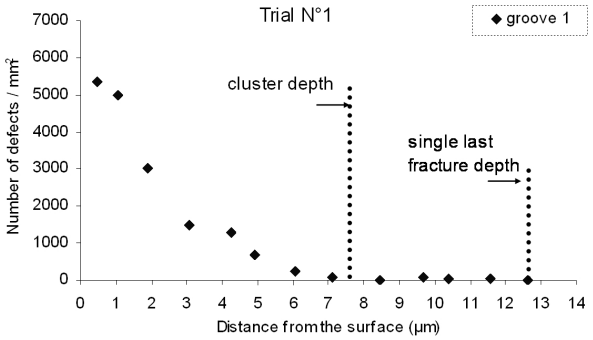

Figure 5.5: Number of cracks per mm^2 against the depth beneath the surface - Trial N°1

As described in section 2.10.4, the subsurface damage depth can be divided into cluster

depth and single last fracture depth. The choice of cluster depth value is explained in details in the subsurface damage damage distribution chapter in section 8.1. The cluster depth correponds to the fracture feature caused during the grinding operation. The single last fracture depth is the distance beneath the ground surface where the last median crack is observed.

The subsurface damage responses, cluster and single last fracture depths, are shown in Table 5.3.

	Depth of cut	Subsurface damage responses		
	a_e	Cluster depth	Single last fracture depth	Ratio
Trial N°	μm	μm	μm	Sing./Clus.
1	50	8	12.6	1.6
2	50	10	13.7	1.4
3	50	6.5	9	1.4
4	100	10.5	14.2	1.4
5	100	8	10.8	1.4
6	100	9	12.2	1.4
7	250	8	11	1.4
8	250	5	7.7	1.5
9	250	10	13.3	1.3

Table 5.3: Parameter screening - Subsurface damage responses - Zerodur

By definition, the cluster depth is lower than the single last fracture depth. The single last fracture depth varies from 7.7 μm to 14.2 μm. The cluster depth ranges between 5 μm and 10.5 μm. The lowest subsurface damage depth is obtained for Trial N°8 despite a bigger depth of cut. The deepest crack occurs in Trial N°4.
The ratio between the single last fracture depth and the cluster depth was calculated. The values obtained are ranging from 1.3 to 1.6 with six levels showing a similar value 1.4. Different ratios are highlighted in section 2.10.4. This relation is discussed in more details in section 8.1.

The cluster depth and single last fracture depth are shown in Figure 5.6.

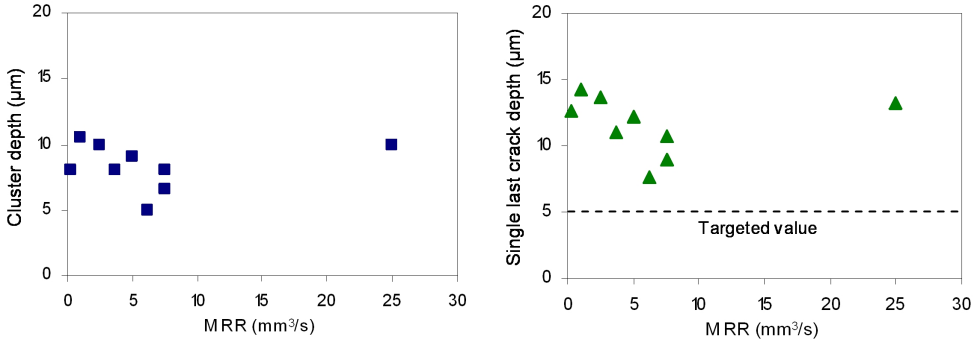

(a) Cluster depth (b) Single last fracture depth

Figure 5.6: Parameter screening - Subsurface damage results - Zerodur

The single last fracture depths are higher than 7.5 μm. The targeted 5 μm subsurface damage depth is not reached. The cluster depths are also above the targeted value. Studies showed that lower grit sizes induce lower subsurface damage (Lambropoulos, 2000). For the Edgetek based test programme, a D25 grinding wheel is employed to reduce the surface roughness response and to improve the subsurface damage depth during finish grinding.
Interestingly, a general trend shows a decrease of cluster and single last fracture depths with material removal rate except for the highest value. This suggests that other factors, not evaluated, have an influence.

5.1.3 Process responses

The process responses recorded are the normal grinding forces, tangential grinding forces, total spindle power and grinding spindle power. The normal and tangential grinding forces responses are shown in Figure 5.7.

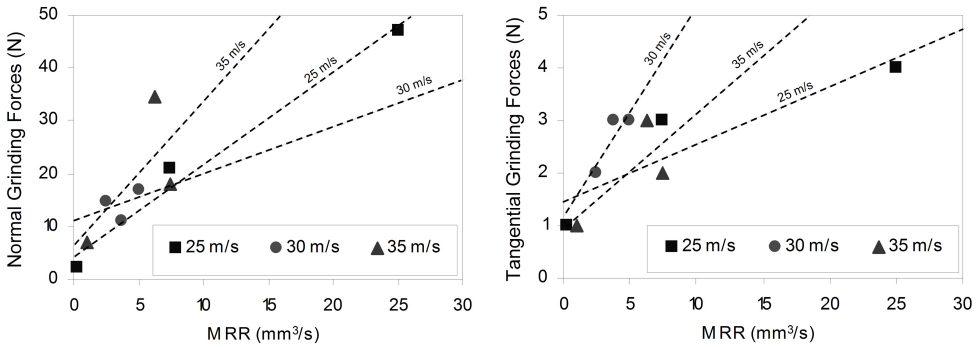

(a) Normal grinding forces (b) Tangential grinding forces

Figure 5.7: Parameter screening - Grinding forces results

Higher material removal rates lead to larger normal grinding forces. For a given grinding wheel speed, the normal grinding force increases with the material removal rate. For a material removal rate reaching 25 mm^3/s, the normal grinding force reaches 48 N. This remains below the maximum targeted value of 100 N based on the 100 N/μm theoretical BoX Z axis stiffness as explained in section 3.3.1. The grinding wheel speed contributes to the level of normal grinding forces.
The tangential grinding forces are as much as 10 times lower than normal grinding forces (Note scale difference in Figure 5.7). For a given material removal rate, the tangential grinding forces increase with decreasing grinding wheel speed.

The total and grinding powers responses are shown in Figure 5.8.

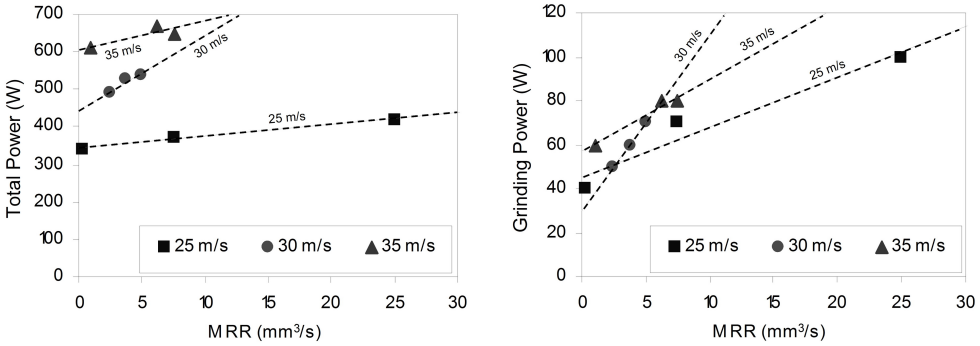

(a) Total grinding power (b) Grinding power

Figure 5.8: Parameter screening - Grinding powers results - Zerodur

As described in section 2.8.6, the total power corresponds to a combination of grinding power, coolant power, idle power and other loss power. For a given grinding wheel speed, the total power increases with the material removal rate. The highest total power value is reached for 6.25 mm^3/s for 35 m/s. The maximum removal rate of 25 mm^3/s gives a total power of 420 W. For a given material removal rate, an increase of grinding wheel speed results in higher total spindle powers and higher grinding powers.
The grinding power increases with a power function with the material removal rate for any grinding wheel speed. The ratio difference between total power and grinding power is between 4.2 and 10.2. The maximum removal rate generates 100 W of grinding power.

The recorded and calculated grinding powers are shown in Figure 5.9.

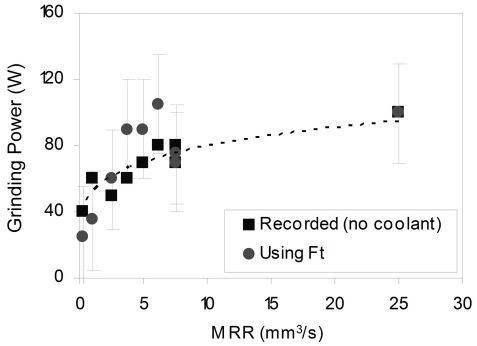

Figure 5.9: Parameter screening - Recorded and calculated grinding power results - Zerodur

The grinding power was calculated using equation 2.8.25 described is section 2.8.6. The grinding power is calculated by multiplying the grinding wheel speed by the tangential grinding force. The variation between calculated and recorded grinding powers is $\pm$ 30 W. This corresponds to an error of $\pm$1 N for a grinding wheel speed of 30 m/s. The averaging value taken from Kistler platform and spindle power signals contribute largely towards that error. The tangential grinding forces were used to estimate the grinding power during Edgetek and BoX based test programme experiments.

5.1.4 Summary

The screening experiments showed that a finer grit size grinding wheel was required to achieve lower surface roughness and subsurface damage depth. The D46 grinding wheel is proven to work over a large range of material removal rate. On Zerodur, the process responses are promising for finish grinding cuts.

5.2 Edgetek based test programme

5.2.1 Surface profile and roughness

As SiC was expected to be harder to grind than Zerodur (2.8.7), a grinding wheel with coarser grit size, 76 μm was employed for rough cut grinding experiments.

- **Finish cuts**

The surface roughness (R_a) and surface profile (P_t) measurements for the "finish" cuts are shown in Figure 5.10.

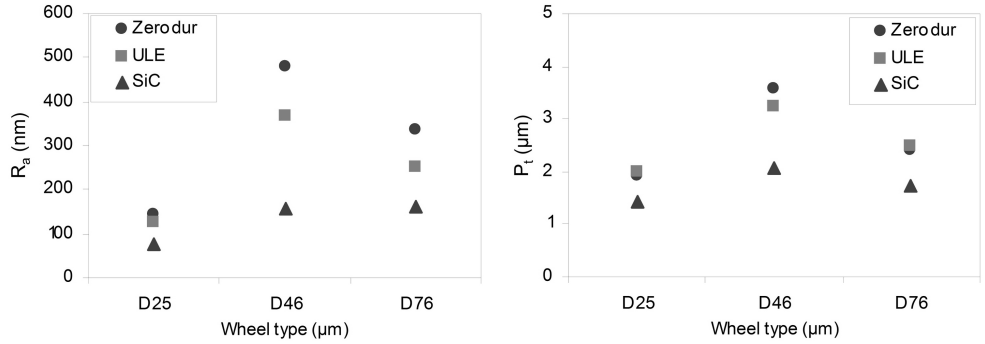

(a) Surface roughness (R_a) (b) Surface profile (P_t)

Figure 5.10: Surface responses for "finish" cuts - a_e = 50 μm, f_r = 1.5 mm/rev, v_w = 25 mm/s, Q_w = 1.87 mm^3/s

The lowest surface roughness is achieved using D25 grinding wheel. The surface roughness is 78 nm, 124 nm and 145 nm for SiC, ULE and Zerodur respectively. R_a increases using 25 μm and 46 μm grit size. For SiC, the surface roughness (R_a) increases with larger grit size, the measured values remains below 160 nm for each grinding wheel. Interestingly, 76 μm grit size gives less surface roughness than 46 μm grit size and more than 25 μm grit size. For each grinding wheel, the surface roughness in ULE is lower than in Zerodur.

Using equation 2.9.3, the calculated surface profile value is 1.54 μm for the D25 and D46 grinding wheels. It is 1.16 μm for the D76 grinding wheel as the cutting radius is larger.
The lowest surface profile is obtained with the D25 grinding wheel. The values increases with a larger grit size, 46 μm, while using a similar abrasive layer radius. The surface profile obtained using a larger grinding wheel, D76, illustrates the influence of a larger grinding wheel cutting radius. Moreover, the surface profile is influenced by the material ground for a similar grinding wheel. In fact, ULE and Zerodur have higher surface profile than SiC. However, those lower surface profile values remain higher than the calculated values. The screening experiments showed that difference in Zerodur. This behaviour is observed in SiC as shown in Figure 5.11.

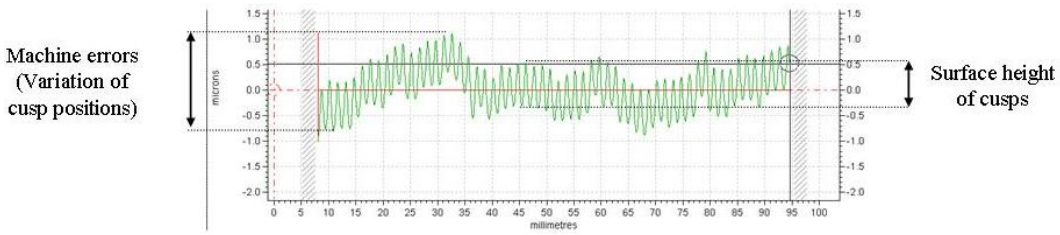

Figure 5.11: Form Talysurf profile of cusps (SiC - Finish cut)

The measurement corresponds to the surface profile of a finish cut (D46) in SiC. This particular example is representative of the surface profiles observed through ULE, Zerodur and SiC. The material properties of those three materials have a limited influence on the measured cusp height values. For the finish ground surfaces, the SiC material has a lower cusp height value.
A closer look at a Form Talysurf profile (Figure 5.11) shows that the ground cusps are distributed around the average surface line by approximately ± 1 μm. This result highlights a possible repositioning error of the Edgetek grinding machine due to positioning accuracy and thermal stability. This variation ranges between 0.4 μm and 2 μm over all three materials.

- **Semi Finish cuts**

The surface roughness (R_a) and surface profile (P_t) measurements for the semi finish cuts are shown in Figure 5.12.

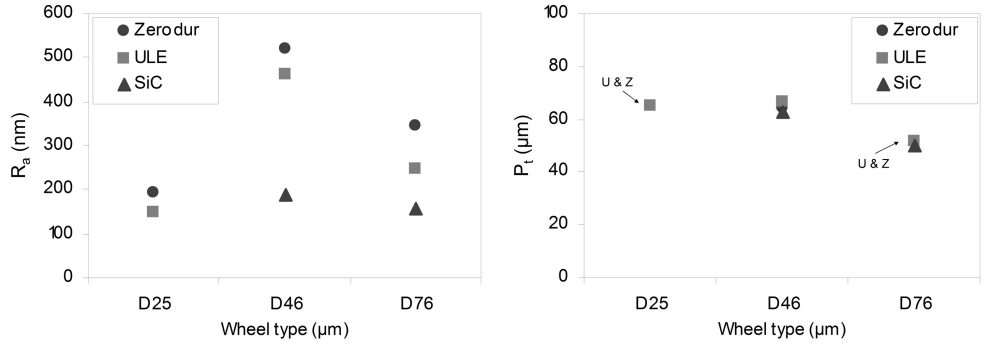

(a) Surface roughness (R_a)

(b) Surface profile (P_t)

Figure 5.12: Surface responses for semi finish cuts - a_e = 200 μm, f_r = 10 mm/rev, v_w = 20 mm/s, Q_w = 40 mm^3/s

As explained in section 3.3.3, no experiment was done with the D25 grinding wheel on SiC for semi finish cut. The lowest surface roughness is obtained on SiC using the D76 grinding wheel. The surface roughness is higher on Zerodur than ULE. The difference between Zerodur and ULE is lower.
For SiC, the surface roughness increases with larger grit size. For ULE and Zerodur, this effect is seen using the D25 and D46 grinding wheels. Interestingly, as observed during finish cut, the 76 μm grit size induces lower surface roughness than 46 μm. This can be explained as the number of active grits contributing to removing material increases due to the D76 grinding wheel larger surface contact area.

The surface profile measured is lower than the calculated surface profile. Those varia-

tions are between 2 μm and 5.5 μm for the D25 and D46 grinding wheels respectively. An error of up to 1.7 μm is observed for the D76 grinding wheel.

- **Rough cuts**

The surface roughness (R_a) and surface profile (P_t) measurements for the rough cuts are shown in Figure 5.13.

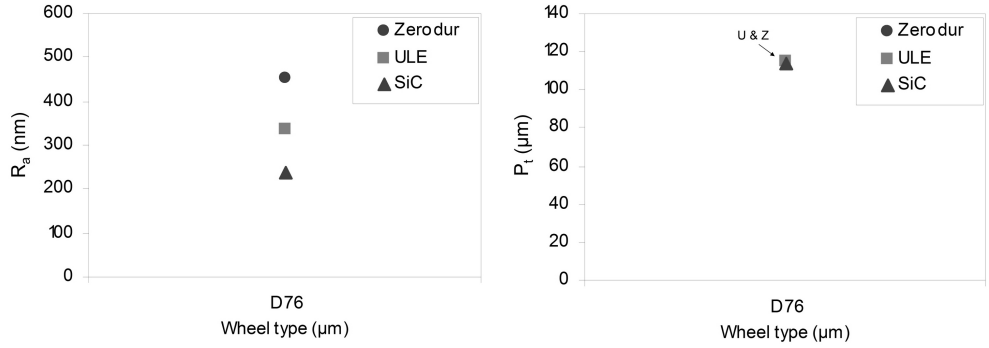

(a) Surface roughness (R_a) (b) Surface profile (P_t)

Figure 5.13: Surface responses for rough cuts - a_e = 500 μm, f_r = 15 mm/rev, v_w = 25 mm/s, Q_w = 187.5 mm^3/s

The surface roughness is lower on SiC than ULE. The highest surface roughness is obtained on Zerodur.

During rough grinding, the surface profile achieved on each material is similar. The surface profile measured is 1-2 μm lower than the calculated value across each material.

- **Surface profile and roughness ratios**

The surface roughness (R_a) and the surface roughness along X* are shown in Table 5.4.

Grinding Conditions	Surface Roughness					
	R_a *(nm)*			Ratio Y*/X*		
	ULE	Zerodur	SiC	ULE	Zerodur	SiC
Finish cut (D25)	124	137	78	0.8	1.1	1.0
Finish cut (D46)	368	648	155	0.8	0.7	1.6
Finish cut (D76)	249	386	159	0.7	0.9	1.5
Semi Finish cut (D25)	147	147	-	1.4	1.3	-
Semi Finish cut (D46)	462	707	187	0.6	0.7	1.3
Semi Finish cut (D76)	245	366	156	1.0	0.9	1.0
Rough cut (D76)	335	487	237	0.9	0.9	1.3

Table 5.4: Surface roughness results - Edgetek

As observed during screening experiments, the surface roughness values differ with the measurement direction. For ULE and Zerodur, the surface roughness measured along the surface speed direction (Y*) is lower than the one along the surface profile (X*). An exception is seen for the semi finish cut (D25) on ULE and Zerodur and for the finish cut (D25) on Zerodur.
For SiC, the surface roughness along Y* is higher than the surface roughness along X*.

The theoretical and measured surface profile (P_t) are shown in Table 5.5.

Grinding Conditions	Surface Profile					
	P_t (μm)			Ratio Meas./Theo.		
	ULE	Zerodur	SiC	ULE	Zerodur	SiC
Finish cut (D25)	2.0	1.9	1.4	1.3	1.2	0.9
Finish cut (D46)	3.2	3.6	2.1	2.1	2.3	1.3
Finish cut (D76)	2.5	2.4	1.7	2.1	2.1	1.5
Semi Finish cut (D25)	64.9	65.1	-	0.9	1.0	-
Semi Finish cut (D46)	66.5	64.2	62.7	1.0	1.0	0.9
Semi Finish cut (D76)	51.3	51.7	50.0	1.0	1.0	1.0
Rough cut (D76)	115.0	114.7	114.2	1.0	1.0	1.0

Table 5.5: Surface profile results - Edgetek

The ratio between measured surface profile and theoretical surface profile is calculated. This ratio decreases with higher feedrate. This behaviour was seen during the screening experiments responses. Higher grit sizes show an increase in ratio except the finish cut (D46) in Zerodur. This can be explained by the increase of grinding forces. Those grinding forces increase the deflection between the grinding wheel and the part. This is shown for Zerodur for the screening experiments in section 5.1.2, Figure 5.5.

Interestingly, ULE and Zerodur surface profile responses are very close. SiC shows similar trend with a lower ratio difference. The surface generated has height fluctuation as described in more details in Figure 5.11.

For smaller surface profile values, the grit size contributes due to a variation of the grinding wheel radius of curvature. For higher surface profile values during semi finish and rough grinding conditions, the difference becomes very small for each material.

5.2.2 Subsurface damage

For each grinding condition, on ULE and Zerodur, the subsurface damage cracks were observed using an optical microscope. The experimental procedure details are described in section 3.4.2.

The subsurface damage cracks observed in ULE are shown in Figure 5.14.

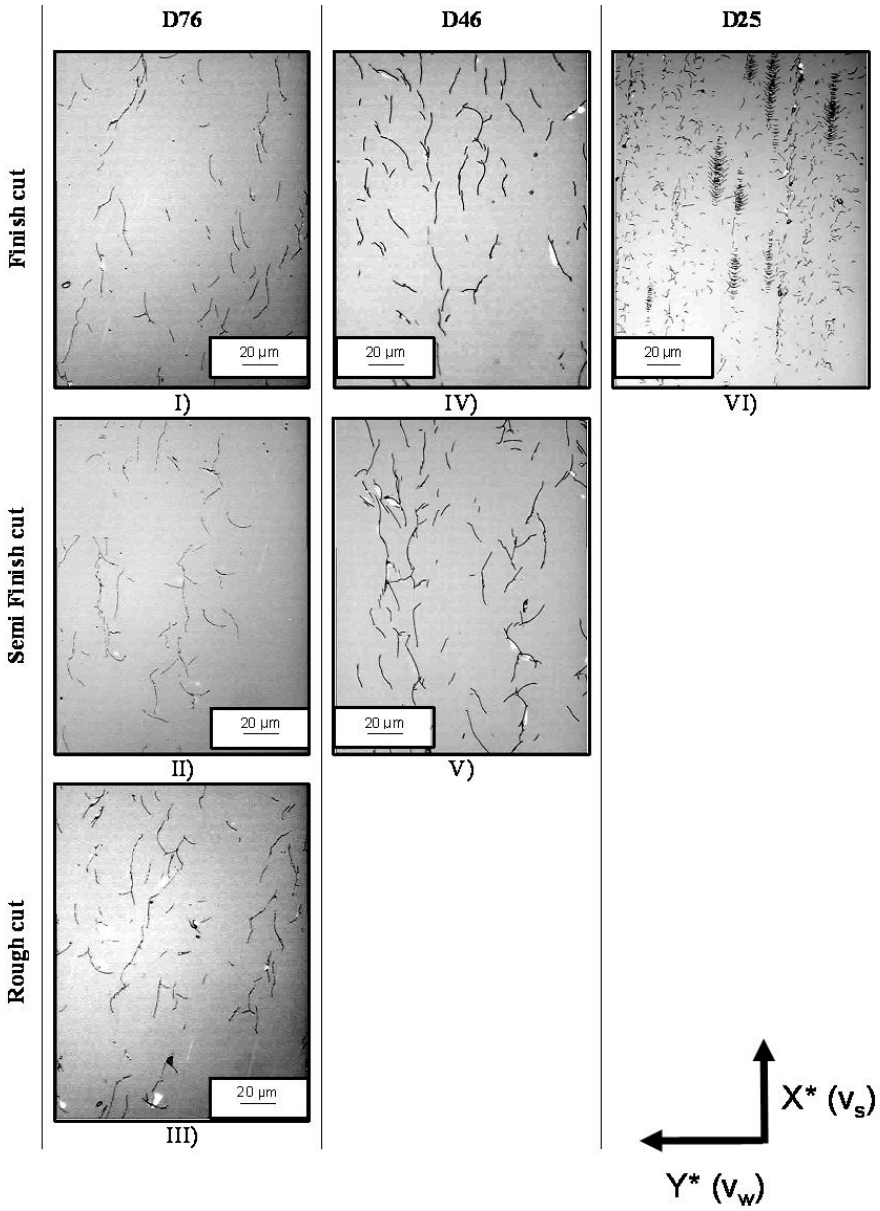

Figure 5.14: Subsurface damage - ULE

The cracks are thin and long for each grinding condition except for the finish cut (D25). The micrograph shows high concentration of small cracks for the final finishing condition. Each subsurface damage crack is distinctive for finish cut using 25 μm grit size. For finish cuts, using D46 and D76 grinding wheels, the long cracks are a combination

of smaller cracks. Each crack is long enough to join an adjacent crack to end up with a large quantity of "fork" type damage. Counting the number of cracks becomes difficult in those particular cases. However, the amount of damage decreases quickly leaving lower cracks number. This enables an efficient manual observation and counting.

The subsurface damage cracks observed in Zerodur are shown in Figure 5.15.

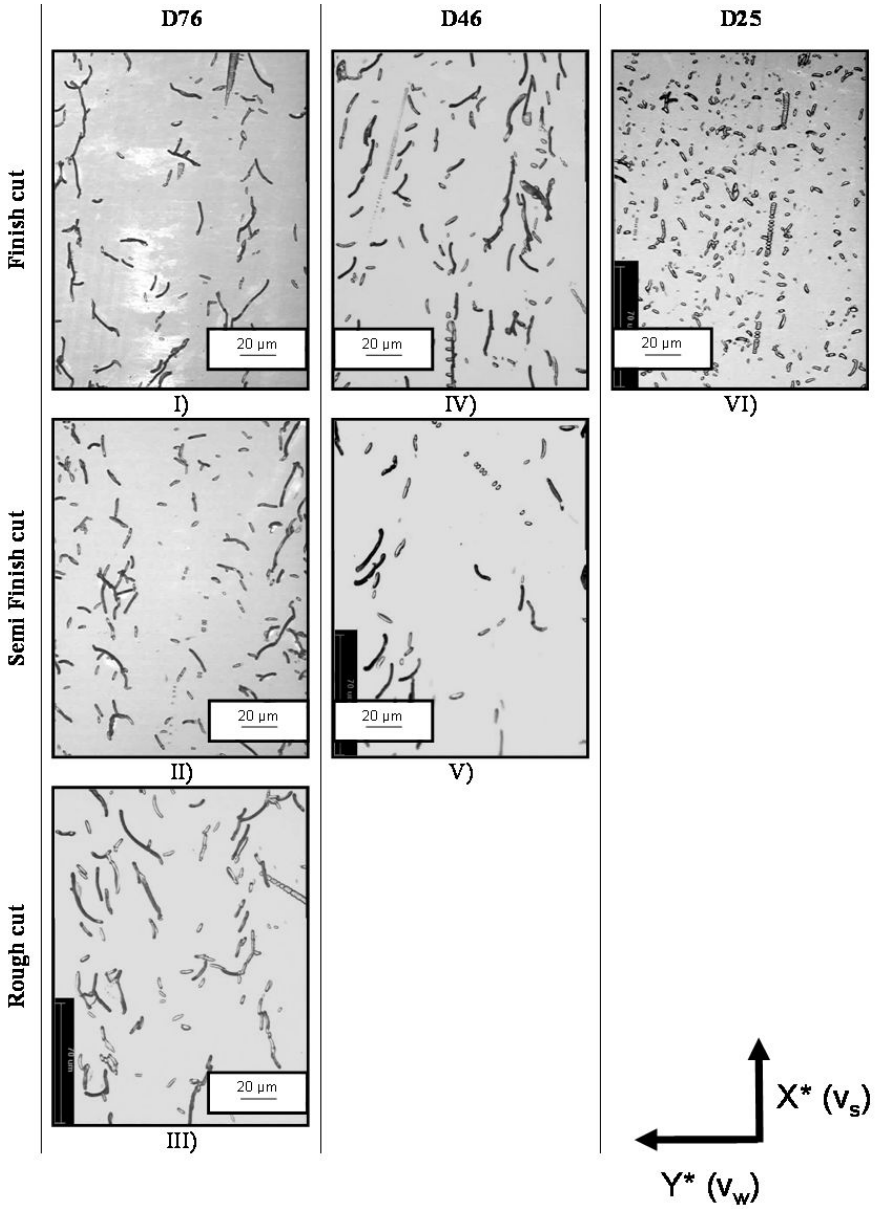

Figure 5.15: Subsurface damage - Zerodur

For Zerodur, the length and width of the cracks are similar using D46 and D76 grinding wheels. Using the D25 grinding wheel, the cracks generated are significantly smaller. Using the 76 μm grit size, cracks have "fork" type shape while with smaller grit size this

type decreases. The 46 μm grit size wheel leaves less interlinked cracks under similar grinding conditions. The finish cut, using 25 μm grit size, leaves very small concentrated cracks.
The cracks are wider and shorter in Zerodur than ULE under similar grinding conditions. A direct comparison of the cracks width has to be done carefully (Menapace et al., 2005*b*). As the etching solution used for both materials is not the same, the crack opening rate and etching rate are not comparable. While both materials show analogous trend for different grit size used, the number of joined cracks decreases with grit size.

The subsurface damage evaluation technique employed is described in section 3.4.2. The number of cracks per mm^2 against the depth beneath ground surfaces can be plotted as shown in Figure 5.16.

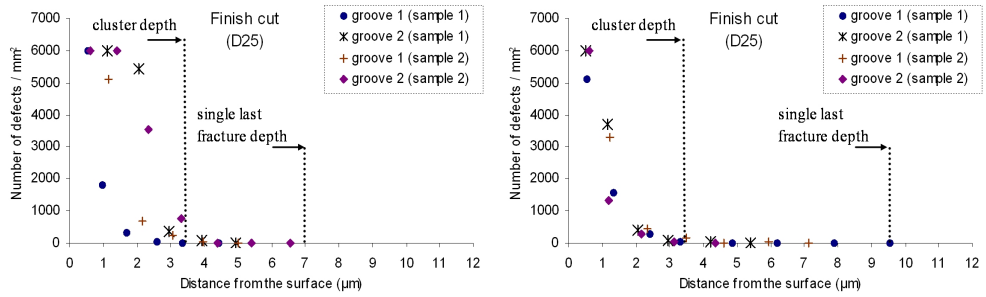

(a) ULE (b) Zerodur

Figure 5.16: Number of cracks per mm^2 against the depth beneath ground surfaces

The subsurface damage depths are divided in two levels. The cluster depth and the single last fracture depth have been measured. Those two values have been identified as significant in the literature review 2.10.3. For each grinding condition, the number of cracks per millimetre square was plotted versus the depth beneath ground surface in micrometres. Those graphs are compiled in Appendix C.2.

The results obtained during the process development using the Edgetek grinding machine are detailed in Table 5.6.

Grinding Conditions	Cluster depth (μm)		Single last fracture depth (μm)	
	ULE	Zerodur	ULE	Zerodur
Finish cut (D25)	3.5	3.5	6.6	9.5
Finish cut (D46)	10.5	8	14.6	11.5
Finish cut (D76)	15	10.5	23.5	18
Semi Finish cut (D46)	11	8.5	17.4	15.6
Semi Finish cut (D76)	17	12.5	23	16.5
Rough cut (D76)	12	11	14.7	12.2

Table 5.6: Subsurface damage results - Edgetek

Lower cluster depths are induced in Zerodur than ULE for all grinding conditions. The single last fracture depths follow the same trend. An exception is seen for the finish cut using the finer D25 grinding wheel. Under given grinding conditions, cluster and single last fracture depths increase when coarser grinding wheels are employed in both materials. When increasing the material removal rate, the subsurface damage depth increases using 46 μm grit size and decreases using 76 μm grit size.
Interestingly, the subsurface depth observed for the rough grinding cut (D76) is lower than the semi finish (D46 & D76) and finish (D76) grinding cuts.

The cluster and single last fracture depths for finish cuts are detailed in Figure 5.17.

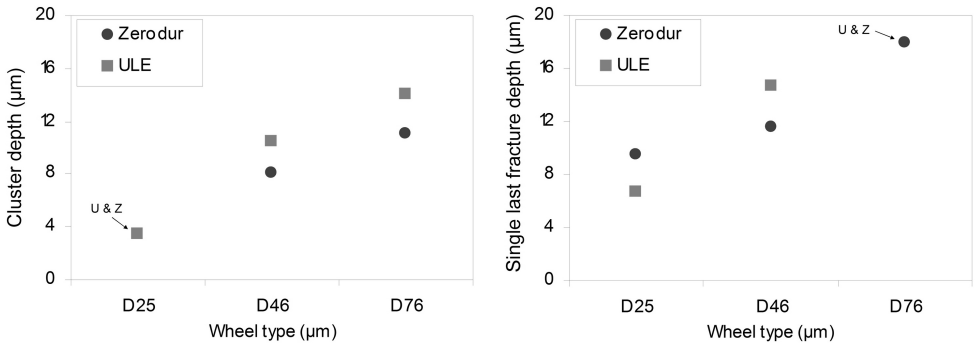

(a) Cluster depth (b) Single last fracture depth

Figure 5.17: Subsurface damage for finish cuts - a_e = 50 μm, f_r = 1.5 mm/rev, v_w = 25 mm/s, Q_w = 1.87 mm^3/s

The cluster depth for the finer grit size, 25 μm, is kept below 5 μm. The increased level of cluster depth SSD with increasing grain size is lower for Zerodur than ULE.
However, the single last fracture depth is 6.6 μm in ULE and 9.5 μm in Zerodur. For

ULE and Zerodur, the subsurface damage depth target is not achieved. Based on the results obtained during the screening experiments on Zerodur using a D46 grinding wheel, lower subsurface damage was expected by using a D25 grinding wheel. This behaviour is confirmed in Figure 5.17.

5.2.3 Normal and tangential grinding forces

- **Finish cuts**

The normal and tangential grinding forces recorded during the finish cuts are shown in Figure 5.18 for ULE, SiC and Zerodur.

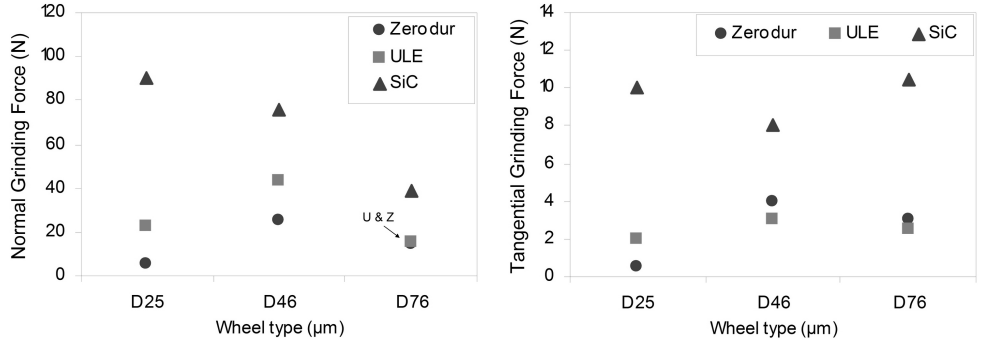

(a) Normal grinding forces (b) Tangential grinding forces

Figure 5.18: Grinding forces for finish cuts - a_e = 50 μm, f_r = 1.5 mm/rev, v_w = 25 mm/s, Q_w = 1.87 mm^3/s

The normal grinding forces are four and sixteen times higher using the D25 grinding wheel on SiC than on Zerodur and ULE respectively. They remain significantly higher using the D46 and D76 grinding wheels. The normal grinding forces decrease with increase in grit size for SiC. This decrease is larger between 46 μm and 76 μm grit sizes.
For ULE and Zerodur, a similar trend is observed. Between the D25 and D46 grinding wheels, the normal grinding forces increase. In Zerodur, normal grinding forces are half the level found when grinding ULE for 25 μm and 46 μm grit sizes. For 76 μm grit size, no difference is recorded between both materials.
These results demonstrate that a larger grit size in ULE and SiC and smaller grit size in Zerodur limits the maximum normal grinding forces. For a given grinding machine stiffness, reduced normal grinding force is preferable at it achieves a reduced form error.

The same observations can be made for the tangential grinding forces. The normal and tangential grinding forces follow similar trends for each material. Exception is made for SiC using the D76 grinding wheel. The tangential grinding forces are higher than using the D25 and D46 grinding wheels.

- **Semi Finish cuts**

The normal and tangential grinding forces recorded during the semi finish cuts are shown in Figure 5.19.

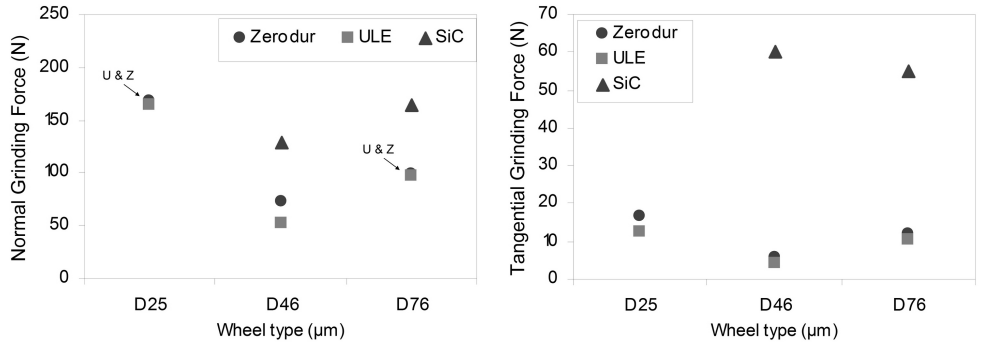

(a) Normal grinding forces (b) Tangential grinding forces

Figure 5.19: Grinding forces for semi finish cuts - a_e = 200 μm, f_r = 10 mm/rev, v_w = 20 mm/s, Q_w = 40 mm^3/s

Normal and tangential grinding forces recorded are higher than found during the finish cut trials. Due to those high grinding forces, the D25 grinding wheel was not used on SiC.
There is a decrease in normal grinding forces in Zerodur and ULE between D25 and D46 grinding wheels. This is in opposition to the trend observed during the finish cuts. Similar differences are present for the tangential grinding forces.
For each material, the normal grinding forces are higher for the D76 grinding wheel than the D46 grinding wheel. The trend is opposite to the finish grinding operations.

- **Rough cuts**

The normal and tangential grinding forces recorded during the rough cuts are shown in Figure 5.20.

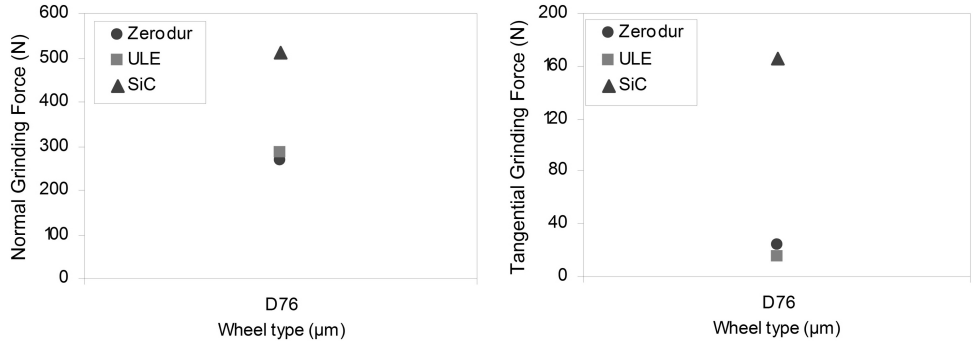

(a) Normal grinding forces (b) Tangential grinding forces

Figure 5.20: Grinding forces for rough cuts - a_e = 500 μm, f_r = 15 mm/rev, v_w = 25 mm/s, Q_w = 187.5 mm^3/s

The rough cut is used to remove large amount of material. Only the D76 grinding wheel was used for rough grinding. The highest normal and tangential grinding forces are recorded in SiC. The normal and tangential grinding forces are higher and lower in ULE than Zerodur respectively.

5.2.4 Total and grinding power

The total spindle power was recorded during each grinding experiment. The grinding power was calculated by removing, from the total power recorded, the spindle power recorded during a spark out cut for each grinding condition employed. The idle power and the coolant power effect are removed with those spark out runs.
The grinding power was also calculated using tangential grinding forces recorded based on equation 2.8.25. The recorded and calculated grinding power are compiled in Table 5.7.

Grinding Conditions	Grinding Power (W)					
	Recorded			Calculated		
	ULE	Zerodur	SiC	ULE	Zerodur	SiC
Finish cut (D25)	40	75	340	60	15	300
Finish cut (D46)	40	25	190	90	120	240
Finish cut (D76)	55	100	300	75	90	315
Semi Finish cut (D25)	450	560	-	375	495	-
Semi Finish cut (D46)	160	160	1100	120	165	1800
Semi Finish cut (D76)	340	370	1620	315	360	1650
Rough cut (D76)	780	820	4600	450	720	4950

Table 5.7: Recorded and calculated Edgetek grinding power results

The grinding power recorded and grinding power calculated were compared. For Zerodur and ULE, the grinding power differences vary with the grinding conditions.
For SiC, the grinding power recorded is lower than the grinding power calculated under any grinding conditions except the finish cut (D25). For the semi finish cut (D46), the calculated grinding power is 700 W larger than the measured grinding power. The tangential grinding force is believed to be unstable for that particular experiment as the total power is also lower than the calculated grinding power.
The difference for each material during the finish and semi finish cuts is within $\pm$ 90 W. This corresponds to an error of $\pm$ 3 N on the tangential grinding forces recorded. During rough grinding conditions, the grinding power difference is $\pm$ 350 W, corresponding to an tangential grinding force variation of 12 N.
The variation is due to the mean value used from the tangential grinding forces and spindle power recorded signals. The grinding wheel wear is another potential contribution to this variation as shown in section 5.3. Overall, the tangential grinding force can be used to monitor the grinding power for different ground materials under different grinding conditions.

- **Finish cuts**

The total and grinding power measurements for the finish cuts are shown in Figure 5.21.

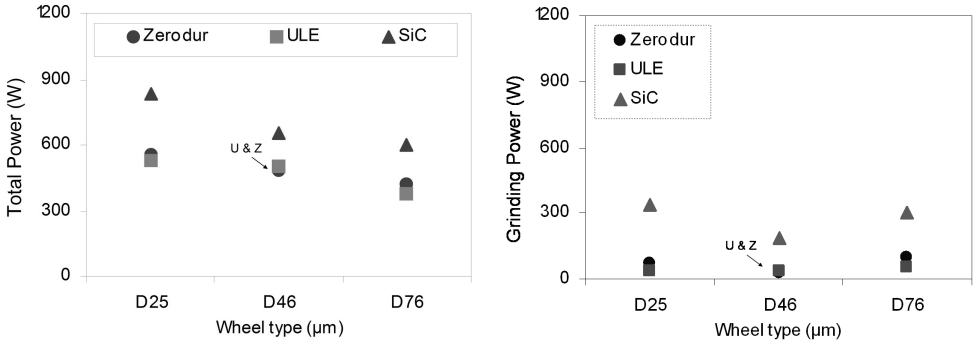

(a) Total spindle power (b) Grinding spindle power

Figure 5.21: Spindle power for finish cuts - a_e = 50 μm, f_r = 1.5 mm/rev, v_w = 25 mm/s, Q_w = 1.87 mm^3/s

The total spindle power recorded is the largest for SiC. For ULE and Zerodur, total power levels are similar. Interestingly, the total spindle power decreases with an increase in grit size for each material in finish grinding conditions.
The grinding power changes with the grit size. Under similar grinding conditions, SiC requires higher grinding power than ULE and Zerodur. The smallest grinding power is generated using the D46 grinding wheel for each material with 40 W, 25 W and 190 W for ULE, Zerodur and SiC respectively.

- **Semi Finish Cuts**

The total and grinding power measurements for the semi finish cuts are shown in Figure 5.22.

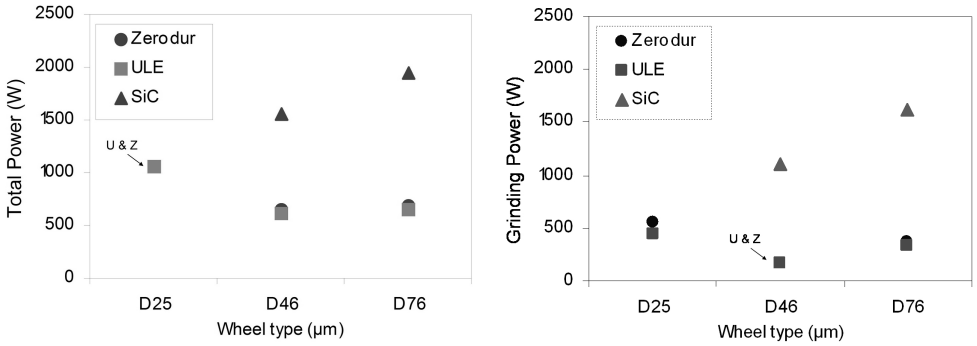

(a) Total spindle power (b) Grinding spindle power

Figure 5.22: Spindle power for semi finish cuts - a_e = 200 μm, f_r = 10 mm/rev, v_w = 20 mm/s, Q_w = 40 mm^3/s

For ULE and Zerodur, the finer grit size, 25 μm, requires the highest total spindle power. The difference between total spindle power and grinding power remains constant. The

amount of power lost during the semi finish grinding is close to the finish grinding losses. The D76 grinding wheel generates more grinding power than the D46 grinding wheel. This can be explained as the D76 grinding wheel is larger than the D46 grinding wheel increasing the surface contact zone between the grinding wheel and the ground part. For SiC grinding, the required grinding power increases quickly with the use of larger grit size. The total power and grinding power follow the same behaviour for each ground material.

- **Rough cuts**

The total and grinding power measurements for the rough cuts are shown in Figure 5.23.

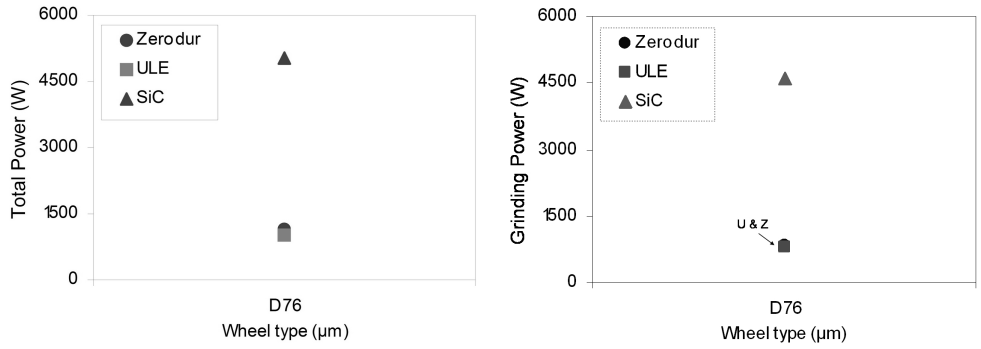

(a) Total spindle power (b) Grinding spindle power

Figure 5.23: Spindle power for rough cuts - a_e = 500 μm, f_r = 15 mm/rev, v_w = 25 mm/s, Q_w = 187.5 mm^3/s

The use of a large depth of 500 μm generates larger total spindle power and grinding power. For ULE and Zerodur, the maximum spindle power used is 1020 W and 1160 W respectively. The grinding powers are 780 W and 820 W.
SiC requires larger spindle power of 5500 W and grinding power of 4600 W.
The maximum removal rate of 187.5 mm^3/s is achievable using the specified total spindle power defined for the BoX grinding machine. However, the maximum spindle power has to take into account the grinding wheel wear influence as discussed in section 5.3.2.

5.2.5 Specific grinding energy

The specific grinding energy is calculated using equation 2.8.26 described in section 2.8.7. The grinding power recorded is divided by the material removal rate. The specific grinding energy results are shown in Table 5.8.

Grinding Conditions	SiC *(J/mm^3)*	ULE *(J/mm^3)*	Zerodur *(J/mm^3)*
Finish cut (D25)	181	21	40
Finish cut (D46)	101	21	13
Finish cut (D76)	160	29	53
Semi Finish cut (D25)	-	11	14
Semi Finish cut (D46)	28	4	4
Semi Finish cut (D76)	41	9	9
Rough cut (D76)	25	4	4

Table 5.8: Specific grinding energy results - Edgetek

The specific grinding energy decreases with the increase of material removal rate. This energy is material dependant. The specific energies for SiC are the highest for all grinding conditions. For the finish cuts (D25/D76) and semi finish cut (D25), the specific energy for Zerodur is higher than ULE. For the finish cut (D46), the specific grinding energy is lower for Zerodur than ULE. No difference is observed for the other grinding conditions between ULE and Zerodur.
Using the same grinding wheel, the specific energy decreases with an increase of material removal rate for ULE, SiC and Zerodur. For SiC, the specific grinding energy is larger for the finish cut (D25) than the finish cut (D76).

These results show that the specific grinding energy used to specify the maximum grinding spindle requirement on the BoX grinding machine is adequate. As explained in section 3.3.1, the selected value was 30 J/mm^3 for a material removal rate of 200 mm^3/s. For a material removal rate of 187.5 mm^3/s, the specific grinding energy is 25 J/mm^3 for SiC using the D76 grinding wheel. Based on the results above, this value is expected to decrease for a higher removal rate with the same grinding wheel.

5.3 Grinding wheel wear experiments

The experimental procedure employed to measure the grinding wheel wear is described in section 3.4.3. An imprint for the grinding wheel was done using graphite blocks. Those blocks were measured using the Taylor Hobson 120L profilometer. The surface profile was collected at regular interval during the grinding process. Each profile was plotted on the same graph as shown in Figure 5.24.

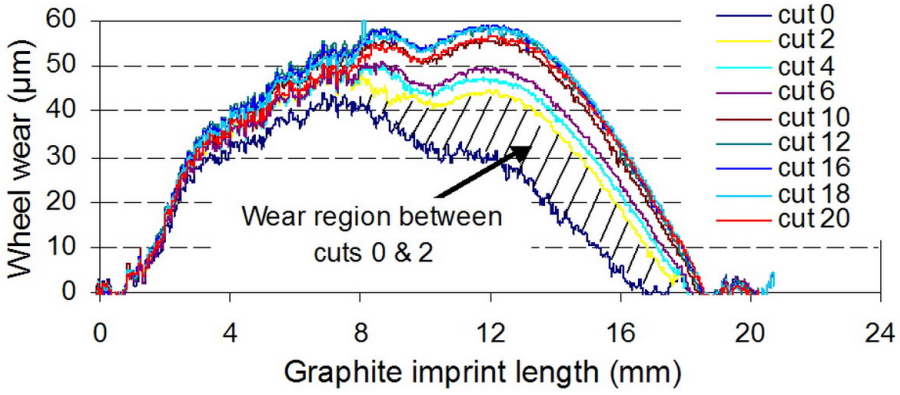

Figure 5.24: Wheel wear measurement - Finish cut (D46) - SiC

The grinding wheel wears rapidly during the first two cuts. Thereafter, the amount of material worn out is significantly reduced. The contact zone that worn out is 10 mm. The cumulative grinding wheel wear was calculated with the same manner for each grinding condition employed.

5.3.1 Cumulative grinding wheel wear and G ratio

The cumulative grinding wheel wear for a given cumulative material removed is plotted. The ratio between those two parameters is called G ratio. This ratio was also plotted. Those experiments were done on SiC and Zerodur. On Zerodur, they were repeated once for finish and semi finish cuts. The grinding conditions tested are the finish (D46), semi finish (D46) and rough (D76) cuts. Those grinding conditions are representative to the expected final grinding process sequence employed for grinding large parts.

- **Finish cuts**

The cumulative grinding wheel wear and G ratio during finish cuts using a D46 grinding wheel on SiC and Zerodur are shown in Figure 5.25.

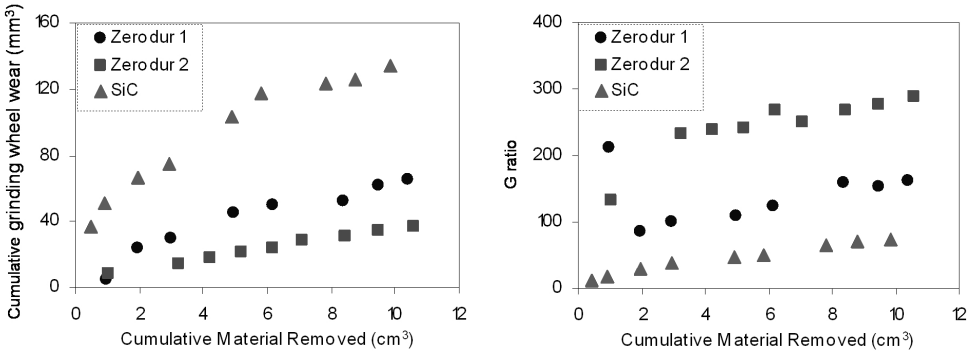

(a) Cumulative grinding wheel wear (b) G ratio

Figure 5.25: Cumulative grinding wheel wear and G ratio during finish cuts (D46)

The cumulative grinding wheel wear is lower on Zerodur than SiC. Two distinct stages are present. An important wear occurs until 3 cm^3 of material is removed. It is followed by a linear increase. An error compensation of the grinding wheel wear is possible.
For the finish cut, the amount of material worn from the wheel is 37 mm^3 to 65 mm^3 for Zerodur and 133 mm^3 for SiC. The wheel wear is assumed to be constant on the whole wheel abrasive layer grinding surface. The wheel radius modification is 40 μm when grinding SiC and 11-20 μm when grinding Zerodur.
The G ratio is 100-230 for Zerodur and 40 for SiC after removing 3 cm^3 of material. The maximum G ratio value reached is 160-288 for Zerodur and 74 for SiC. The difference between two repetitive grinding cuts is 15 mm^3 and 30 mm^3 for 3 cm^3 and 10.5 cm^3 of Zerodur removed respectively. The corresponding G ratio varies between 160 and 290. This difference highlights the limitation on the final error compensation achievable.

- **Semi Finish cuts**

The cumulative grinding wheel wear and G ratio during the semi finish cuts using a D46 grinding wheel on SiC and Zerodur are shown in Figure 5.26.

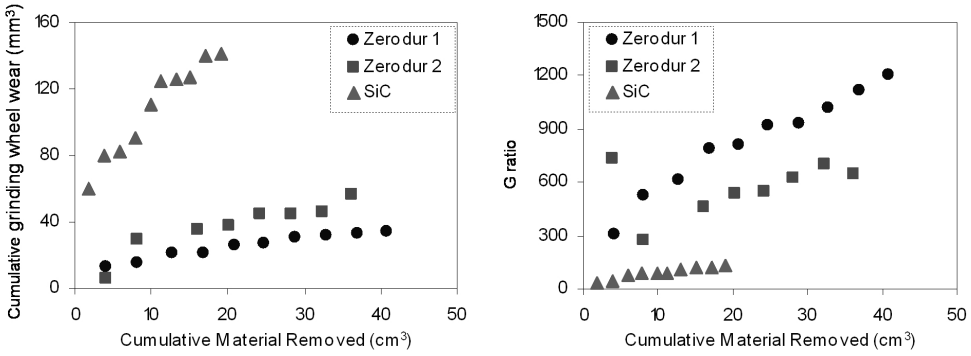

(a) Cumulative grinding wheel wear (b) G ratio

Figure 5.26: Cumulative grinding wheel wear and G ratio during semi finish cuts (D46)

The cumulative grinding wheel wear is higher on SiC. For SiC, three stages are identified at 4 cm^3, 11 cm^3 and thereafter. Each stage corresponds to a lower increase rate of the grinding wheel wear. The corresponding G ratios are 50, 90 and 135.
For Zerodur, two stages are present. The linear grinding wheel wear is reached after 8 cm^3 of Zerodur is removed. From that stage, the difference between two repetitive grinding cuts is 15 mm^3 for "Zerodur2" cut. At 4 cm^3 of Zerodur removed, the difference is 7 mm^3 for "Zerodur1" cut. The corresponding G ratios are 305-730 at 4 cm^3 and 650-1120 at 36 cm^3 of material removed.
For Zerodur and SiC, the G ratio increases and is not constant. This increase appears to be linear. While for SiC this increase is moderate, it is more significant for Zerodur. Therefore, the use of G ratio to estimate the cumulative grinding wheel wear is limited.

- **Rough cuts**

The cumulative grinding wheel wear and G ratio during rough cuts using a D76 grinding wheel on SiC and Zerodur are shown in Figure 5.27.

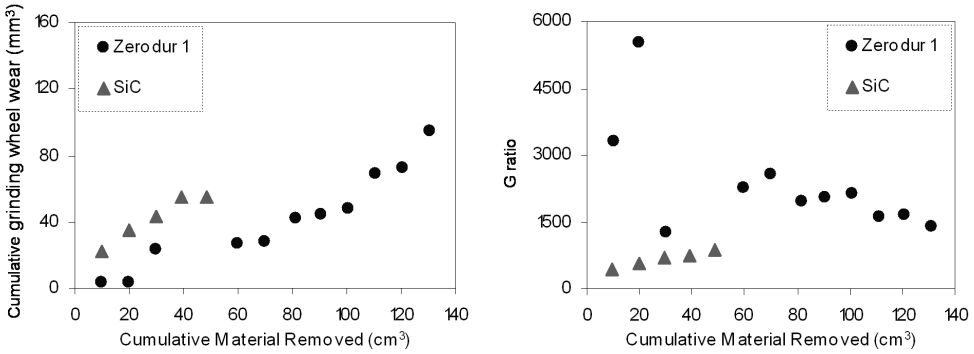

(a) Cumulative grinding wheel wear (b) G ratio

Figure 5.27: Cumulative grinding wheel wear and G ratio during rough cuts (D76)

The cumulative grinding wheel wear is more important on SiC. For both ground materials, the grinding wheel wear difference is less important than for finish and semi finish cuts. The amount of wear and G ratio increase linearly for SiC. For Zerodur, the grinding wheels wear increases by steps. After 35 cm^3 of Zerodur is removed, the grinding wheel is worn out significantly. The amount of wear increases after each step, the G ratio shows this behaviour. In fact, the G ratio after increasing up to 2545 decreases by steps after 70 cm^3 to 2000 down to 1600.
The D76 grinding wheel is adequate for grinding large amount of SiC.

The grinding ratio, G, values, for each grinding conditions are compiled in Table 5.9.

Grinding Conditions	Cumulative material removed (cm^3)	Zerodur G ratio	SiC G ratio
Rough cut (D76)	48 (20)	2000 (1280)	880 (560)
Semi Finish cut (D46)	19 (34)	540/800 (700/1020)	135
Finish cut (D46)	9.5	160/288	74

Table 5.9: Grinding ratio

As discussed previously, the G ratio for the finish cut estimates the amount of material removed from the grinding wheel. However, for the semi finish and rough cuts, this ratio increases with time. Its usage is limited to help for comparison of different grinding wheel.

For SiC, the G ratio increases with the grinding conditions employed. Using the same grinding wheel, D46, the G ratio after removing 9.5 cm^3, is 74 and 90 for the finish cut and semi finish cut respectively. For Zerodur, G ratio increases approximately from 160/288 to 300/550 under same conditions. The grinding ratio increases with material removal rate.
After removing 20 cm^3 of SiC, the G ratio increases from 135 to 560 using higher removal rate and coarser grinding wheel. For the same amount of Zerodur, removed the G ratio increases from 540/800 to 1280. The use of a coarser grinding wheel is more important for SiC than Zerodur. SiC is considered harder to grind and requires larger grit size to minimise the amount of grinding wheel wear.

5.3.2 Normal grinding forces and grinding power

- **Finish cuts**

The normal grinding forces and grinding power for finish cuts are shown in Figure 5.28.

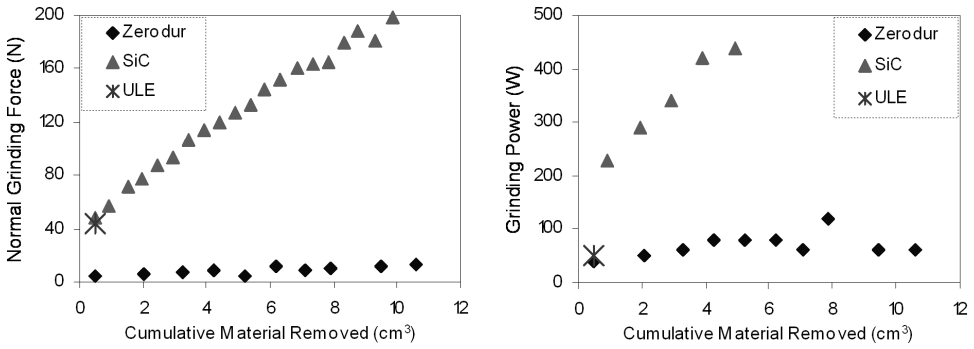

(a) Normal grinding forces (b) Grinding power

Figure 5.28: Normal grinding forces and grinding power for finish cuts (D46)

The measured normal grinding forces increases differently between SiC and Zerodur. For Zerodur, the normal grinding force stays below 12 N after removing 10 cm^3 from the ground surface. For SiC, after removing only 3 cm^3 of material, the normal grinding force reaches 100 N. Based on the expected stiffness of 100 N/μm, after removing 10 cm^3, the grinding wheel deflection has reached 2 μm. The grinding wheel needs to be dressed after 2.9 cm^3 which corresponds to 26.5 minutes.
The grinding power increases from 230 W to 440 W after removing 10 cm^3 of SiC. For the same amount of Zerodur removed, the grinding power increases from 40 W to 120 W.

- **Semi Finish cuts**

The normal grinding forces and grinding power for semi finish cuts are shown in Figure 5.29.

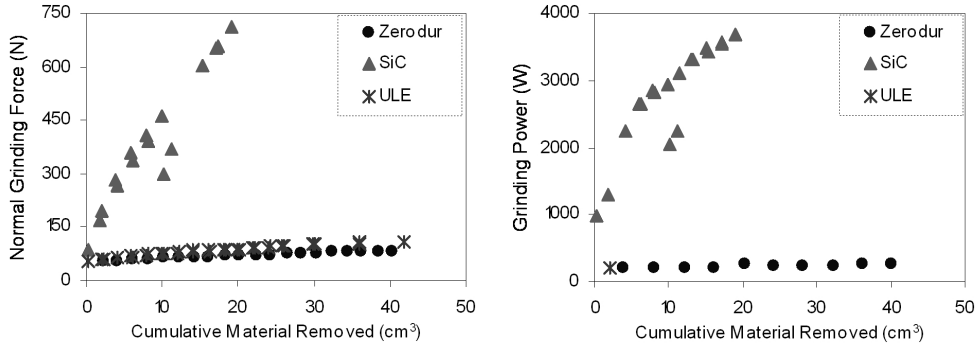

(a) Normal grinding forces (b) Grinding power

Figure 5.29: Normal grinding forces and grinding power for semi finish cuts (D46)

After removing 20 cm^3, the normal grinding forces has increased by 40 N, 20 N and 630 N for ULE, Zerodur and SiC respectively. The increasing factors are 1.8, 1.4 and 8.4 for ULE, Zerodur and SiC. The normal grinding forces increases steadily to 110 N and 85 N for ULE and Zerodur after removing 40 cm^3.
After removing 40 cm^3, the grinding power reaches 255 W for Zerodur. For SiC, the grinding power increases from 980 W to 3700 W after removing 20 cm^3. While dressing is not required, monitoring of the total spindle power when grinding SiC is necessary during the semi finish cuts.

- **Rough cuts**

The normal grinding forces and grinding power for rough cuts are shown in Figure 5.30.

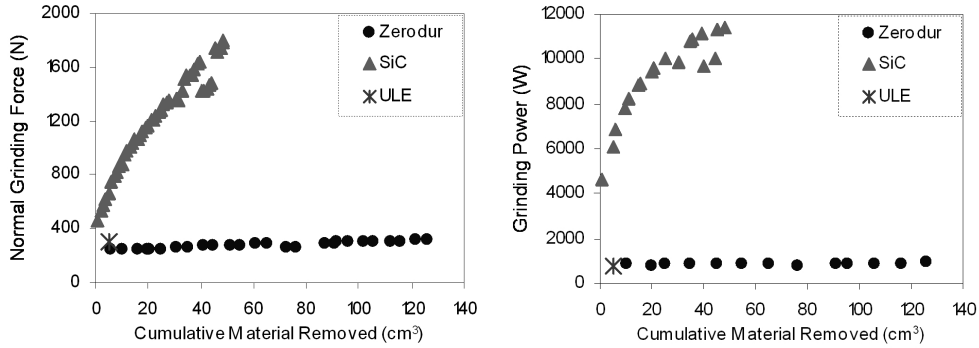

(a) Normal grinding forces (b) Grinding power

Figure 5.30: Normal grinding forces and grinding power for rough cuts (D76)

Normal grinding forces and grinding power values recorded show that large amount of material can be removed with high removal rate in ULE, Zerodur and SiC. The material removal rate used is 187.5 mm^3/s.
For Zerodur, the normal grinding force increases by 80 N after 125 cm^3 has been ground.

After removing 50 cm^3 on SiC, the normal grinding force has reached 1800 N.
For Zerodur, 910 W of grinding power is used after removing 125 cm^3. However, after removing 50 cm^3 of SiC, the grinding power reaches 11400 W. The BoX maximum grinding power was specified at 10000 W. The grinding wheel needs to be dressed after 20 cm^3 are removed during rough grinding. This corresponds to a dressing each 2 minutes. The grinding wheel shows no sign of bond burn after removing 50 cm^3.
During SiC rough grinding, the grinding wheel wear to grinding force increase is less than for the semi finish and finish cuts. This highlights the importance of using larger grit size and lower concentration. Interestingly, no dressing is required during rough grinding of Zerodur.

5.4 Summary

On each material, the maximum removal rate of 187.5 mm^3/s was achieved using a 76 μm grit size grinding wheel. The grinding process developed can remove 1 mm over a metre in less than 10 hours.

On Zerodur, the screening experiments responses showed that the targeted form accuracy of $P_t < 1$ μm is achievable. The "static" form accuracy is controlled by the grinding wheel cutting radius and feedrate per revolution. A "dynamic" effect increases the final form accuracy due to non repeatability of depth between successive "cusps". It is believed to be due to the grinding machine dynamics such as grinding stiffness and thermal response. The process development experiments on ULE, Zerodur and SiC confirmed those observations. The best form accuracy achieved was $P_t = \pm 1$ μm over 100 mm. Such cusp height variation will be reduced using the BoX grinding machine having a higher positioning accuracy, with good thermal stability.

During the screening experiments, using a D46 grinding wheel, the Zerodur surface roughness (R_a) obtained was over 340 nm. A finer grit size, 25 μm, was used for the process development. For each material, the finish cut (D25), surface roughness (R_a), was reduced below 150 nm achieving the targeted value.

The subsurface damage depths obtained on Zerodur were between 7.7 μm and 14.2 μm for the screening experiments. Using a D25 grinding wheel, the lowest subsurface depths were obtained. The single last fracture depths were 6.6 μm and 9.5 μm for ULE and Zerodur respectively. The subsurface damage depth target is not achieved. Based on the project assumption, that the machine stiffness is an important factor influencing on the subsurface damage depth, the BoX grinding machine should help to obtain less than 5 μm subsurface damage.

The normal grinding forces are kept below 100 N for each material during the finish cut using three different grit sizes. In ULE and Zerodur, the normal grinding forces increase with the grinding wheel wear and remain below 100 N. In SiC, the grinding wheel requires to be dressed each 26.5 minutes to maintain such a normal grinding force level. As the expected BoX grinding stiffness is 100 N/μm, the targeted normal grinding force is 100 N to keep the deflection below 1 μm.

The total spindle powers recorded are kept below 6000 W for any grinding cut on each material. For ULE and Zerodur, the spindle power increases with grinding wheel wear. During rough cut (D76), the maximum spindle power stays below 1000 W. For SiC rough cut, the grinding wheel wear experiment showed that after 2 minutes, the grinding power reaches 10 000 W. Special attention is required to achieve the maximum removal rate on SiC. The total spindle power recorded fits the BoX grinding machine spindle power capability when grinding 100 mm parts.

6. BoX BASED EXPERIMENTAL RESULTS

In this chapter, the grinding results using the BoX grinding machine are presented. Three specific sets of experiments are detailed: BoX based test programme and large scale surface experiments. The experimental responses evaluated were: surface roughness (R_a), surface profile (P_t), subsurface damage, grinding forces and specific grinding energy.

6.1 BoX based test programme

6.1.1 Surface profile and roughness

The surface profile measurements, for the finish (D25) and semi finish (D76) grinding conditions on SiC, are shown in Figure 6.1.

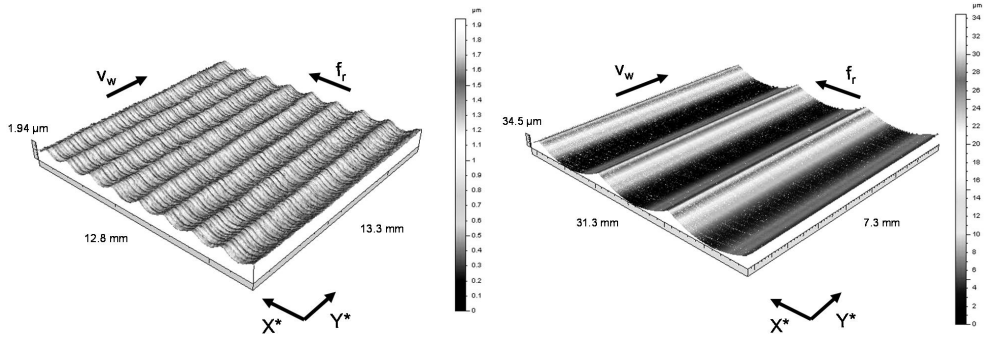

(a) "Finish" cut (D25) (b) "Semi-Finish" cut (D76)

Figure 6.1: SiC surface responses - CCI measurements examples (2.5X lens)

Figure 6.1(a) shows the "cusping" generated during a finish cut by a given feedrate, f_r. Those "cuspings" represent the final surface profile accuracy, P_t along X*. The perpendicular lines to X* direction corresponds to the grinding wheel rotation speed, v_s versus surface speed, v_w. Those lines represent the surface roughness, R_a, measured along Y*.

The "cusping" height can be calculated using equation 2.9.3, described in section 2.9.2. The theoretical and measured surface profile (P_t) are shown in Table 6.1.

Grinding Conditions	Surface Profile						
	P_t (μm)				Ratio Meas./Theo.		
	ULE	Zerodur	SiC	Theoretical	ULE	Zerodur	SiC
Finish cut (D25)	1.6	1.8	2.7	0.7	2.3	2.5	3.7
Finish cut (D46)	2.4	1.9	1.7	0.7	3.3	2.6	2.3
Finish cut (D76)	1.4	2.7	2.2	0.7	2.0	3.8	3.1
Semi Finish cut (D25)	31.2	32.1	-	32.1	1.0	1.0	-
Semi Finish cut (D46)	32.5	32.5	-	32.1	1.0	1.0	-
Semi Finish cut (D76)	33.6	33.6	32.9	32.1	1.0	1.0	1.0
SiC Rough cut (D76)	-	-	70.2	72.1	-	-	1.0
Rough cut (D76)	73.1	72.2	-	72.1	1.0	1.0	-

Table 6.1: Surface profile results - BoX

The surface profile is higher than the theoretical value of 0.7 μm. The expected surface profile is 1/2 to 1/4 times smaller than the measured surface profile (P_t). During the finish cuts, the machine dynamics, such as stiffness and thermal errors, influence the surface profile. It is also due to the grinding wheel shape error induced during truing.

During the semi finish and rough cuts, the surface profiles calculated and measured are very similar. The surface profile varies with the grinding wheel grit sizes. This variation differs with the grinding conditions and ground material.

- **Finish cuts**

The surface roughness (R_a) and surface profile (P_t) measurements for the finish cuts are shown in Figure 6.2.

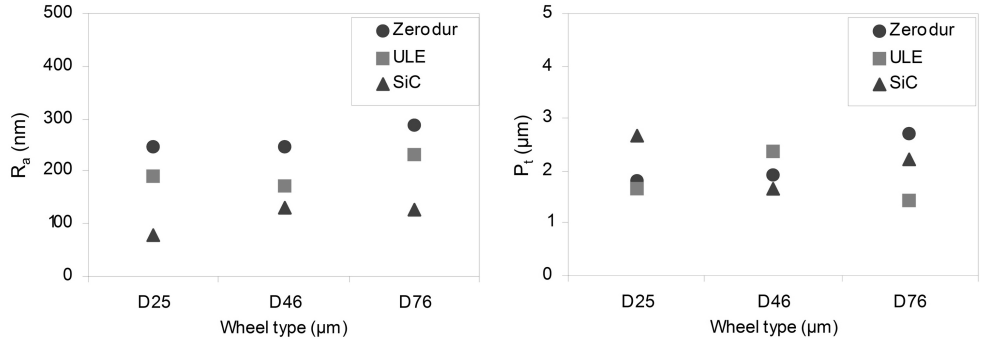

(a) Surface roughness (R_a) (b) Surface profile (P_t)

Figure 6.2: Surface responses for finish cuts - a_e = 50 μm, f_r = 1.5 mm/rev, v_w = 25 mm/s, Q_w = 1.87 mm^3/s

For the surface roughness, the use of a smaller grit size on SiC leaves a better surface finish. The surface roughness is similar between 46 μm and 76 μm grit size. A similar trend is seen for ULE and Zerodur except 46 μm grit size leaves lower value than 25 μm in ULE.
Interestingly, ULE has a surface roughness better than Zerodur for a similar grit size. The targeted surface roughness (R_a) value of 150 nm is achieved in SiC using the D25 grinding wheel. The lowest surface roughness value in ULE is 172 nm using the D46 grinding wheel. In Zerodur, using the D25 grinding wheel, R_a = 247 nm.
For the finish grinding conditions, the surface profile error in Zerodur increases with the grit size employed. However, SiC and ULE materials behave differently. For ULE, the finish cut with the D76 grinding wheel gives the better form accuracy. The D46 grinding wheel is more adequate for SiC. The targeted surface profile accuracy is not achieved.

- **Semi Finish cuts**

The surface roughness (R_a) and surface profile (P_t) measurements for the semi finish cuts are shown in Figure 6.3.

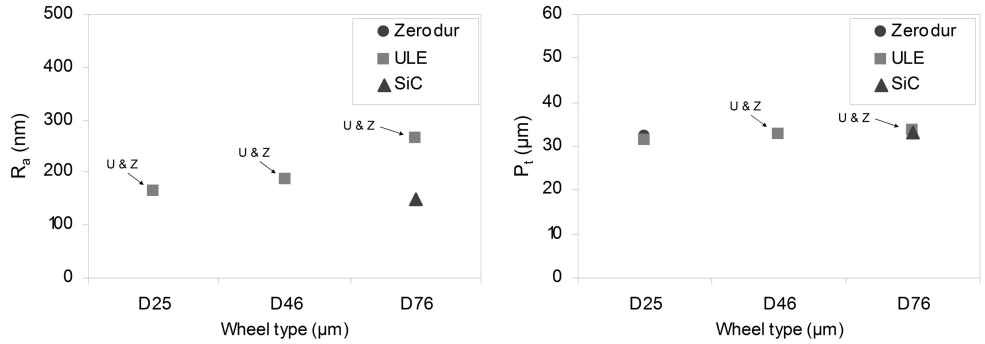

(a) Surface roughness (R_a) (b) Surface profile (P_t)

Figure 6.3: Surface responses for semi finish cuts - a_e = 200 μm, f_r = 10 mm/rev, v_w = 20mm/s, Q_w = 40 mm^3/s

The surface roughness value is below 200 nm for the D25 and D46 grinding wheels, on ULE and Zerodur. The increase in grit size leaves a worse surface quality. The achieved surface roughness is better in SiC. Only the D76 grinding wheel was used and it generated a surface roughness of 149 nm. Interestingly, the surface roughness is lower in Zerodur during a semi finish cut than a finish cut. The minimum surface roughness value is 165 nm using the D25 grinding wheel.
The surface profile achieved is similar for each ground material. The measured and theoretical profile accuracy varies less than 2 μm for a final value of 32 μm. The profile error does not increase using coarser grinding wheels.

- **Rough cuts**

The surface roughness (R_a) and surface profile (P_t) measurements for the rough cuts are shown in Figure 6.4.

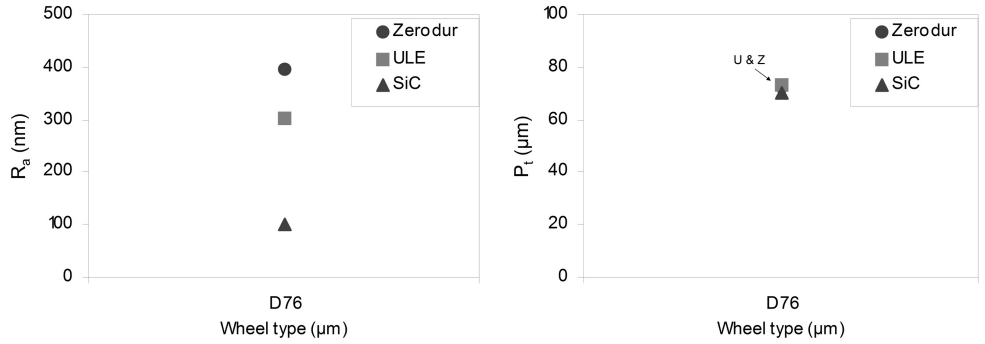

(a) Surface roughness (R_a)

(b) Surface profile (P_t)

Figure 6.4: Surface responses for rough cuts - a_e = 500 μm ($a_{e(SiC)}$ = 300 μm), f_r = 15 mm/rev, v_w = 25 mm/s, Q_w = 187.5 mm^3/s (SiC - 112.5 mm^3/s)

The surface roughnesses are 303 nm and 394 nm in ULE and Zerodur respectively. Interestingly, the rough cut leaves the lowest surface roughness of 100 nm in SiC.
The surface profile obtained is similar for ULE and Zerodur. The error between calculated and measured grinding profile values is less than 1 μm. In SiC, this error reaches nearly 2 μm.

Under different grinding conditions and material ground, few trends are highlighted. A better surface roughness is achieved in SiC. The measured values are better for ULE than Zerodur. The profile error remains similar at 2 μm. The repeatability, between two "cuspings", is not directly related to the grinding forces applied or material removal rate used. For a finish cut, the surface roughness targeted is achieved for SiC. It remains 22 nm and 100 nm higher for ULE and Zerodur respectively. Interestingly, during the semi finish cuts (D25 & D46) of Zerodur, a lower surface roughness of 165 nm is achieved.
For each ground material, the surface profile is less than 2 μm over 95 mm. The targeted surface profile, P_t, is not reached.

6.1.2 Subsurface damage

For each grinding condition investigated, the subsurface damage cracks were observed using an optical microscope. The experimental procedure details are described in section 3.4.2.

The subsurface damage cracks observed in ULE are shown in Figure 6.5.

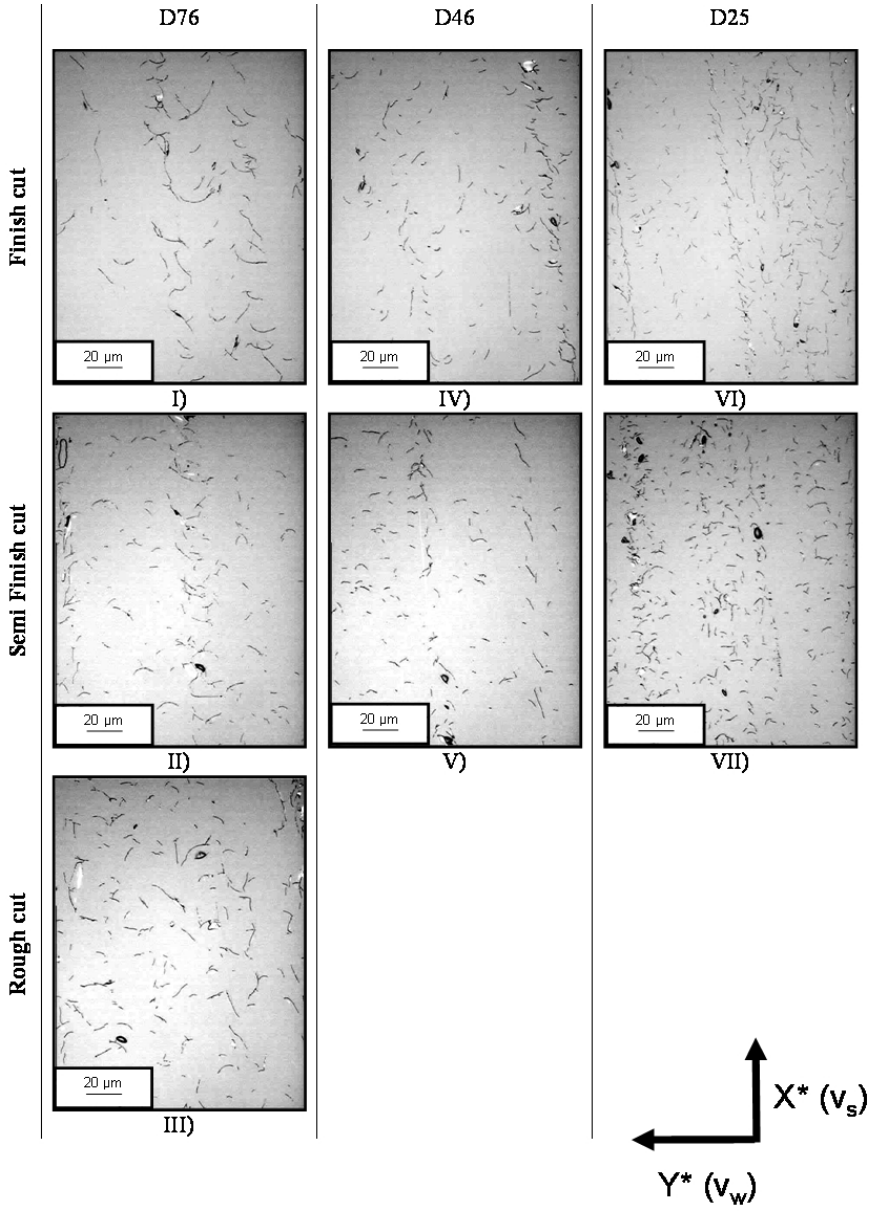

Figure 6.5: Subsurface damage - ULE

The cracks length increases with coarser grinding wheel grit size. No significant difference can be observed between grinding conditions for a given grinding wheel. A direction in the cracks distribution can be observed along X*. This orientation corresponds to the

grinding wheel rotation direction.

The subsurface damage cracks observed in Zerodur are shown in Figure 6.6.

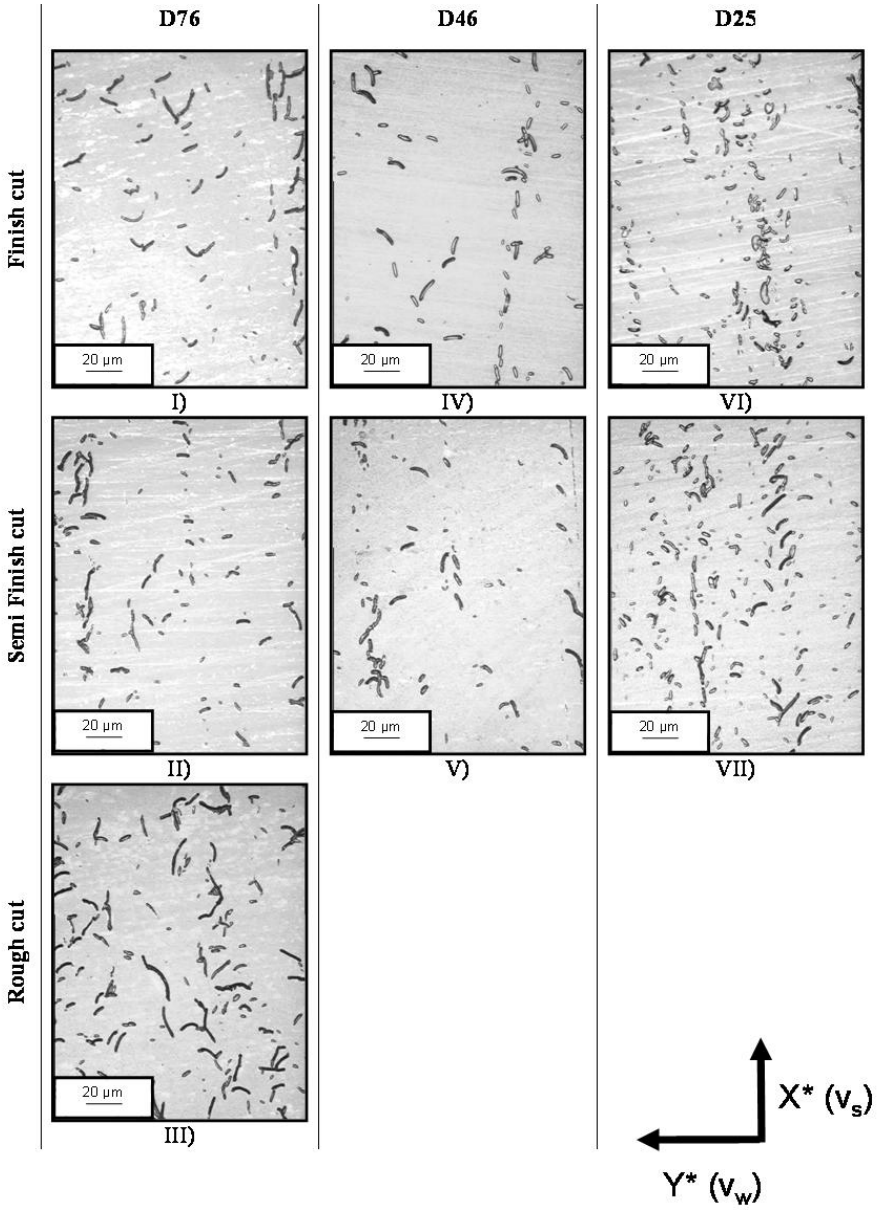

Figure 6.6: Subsurface damage - Zerodur

No significance in crack size can be seen between each grinding condition for a given grinding wheel. The crack length increases with grinding wheel grit size. The repartition of the cracks follows a pattern with an orientation that corresponds to the grinding wheel rotation direction in both materials.
The crack width is wider on Zerodur. However, the etching solution employed is different. Therefore, no particular conclusion can be drawn here.

The subsurface damage evaluation technique employed is described in section 3.4.2. The number of cracks per mm^2 against the depth beneath ground surfaces can be plotted as shown in Figure 6.7.

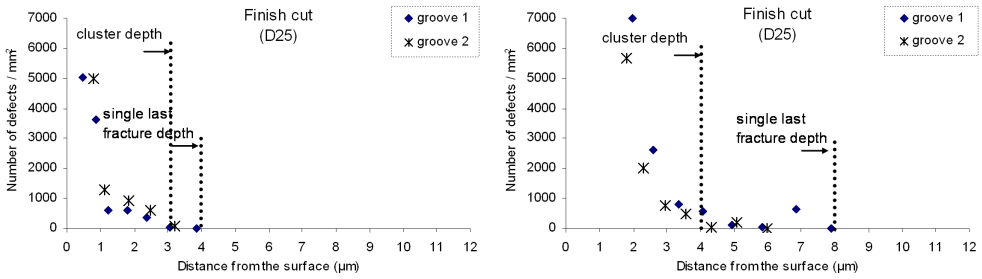

(a) ULE (b) Zerodur

Figure 6.7: Number of cracks per mm^2 against the depth beneath ground surfaces

The subsurface damage depths are divided in two levels. The cluster depth and the single last fracture depth have been measured. Those two values have been identified as significant in the literature review 2.10.3. For each grinding condition, the number of cracks per millimetre square was plotted versus the depth beneath ground surface in micrometres. Those graphs are compiled in Appendix C.3.

The cluster and single last fracture depths for the finish cuts in ULE and Zerodur are shown in Figure 6.8.

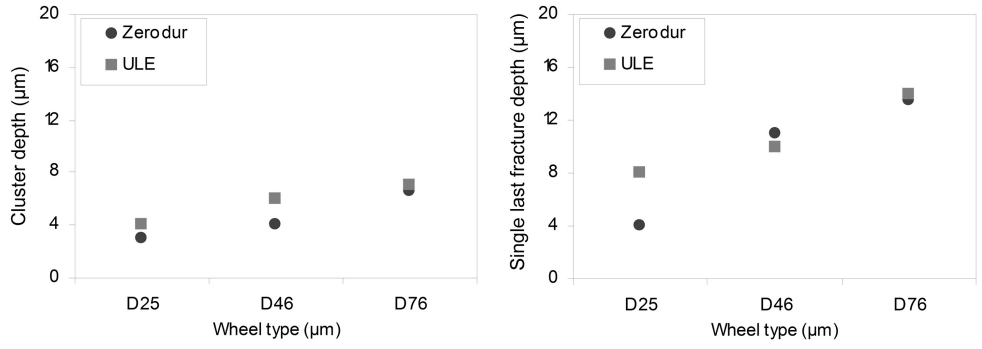

(a) Cluster depth (b) Single last fracture depth

Figure 6.8: Subsurface damage for finish cuts - a_e = 50 μm, f_r = 1.5 mm/rev, v_w = 25 mm/s, Q_w = 1.87 mm^3/s

For finish grinding conditions, cluster and single last crack depths are increasing with larger grit size. For the finish cut (D25), the single last crack depth is measured at 8 μm and 4 μm for ULE and Zerodur respectively. The lowest subsurface damage is achieved

using those grinding conditions. The project targeted subsurface damage depth of under 5 μm is achieved for Zerodur. The damage depth increases faster in Zerodur than ULE for an increase of grit size.

The cluster and single last fracture depths measured for the BoX based test programme are detailed in Table 6.2.

Grinding Conditions	Cluster depth (μm)		Single last fracture depth (μm)	
	ULE	Zerodur	ULE	Zerodur
Finish cut (D25)	4	3	8	4
Finish cut (D46)	6	4	10	11
Finish cut (D76)	7	6.5	14	13.5
Semi Finish cut (D25)	5	7	11.5	10
Semi Finish cut (D46)	4.5	4	9	7.5
Semi Finish cut (D76)	6	5	11	12
Rough cut (D76)	8.5	5	18.5	8

Table 6.2: Subsurface damage results - BoX

The lowest cluster depth is measured for the finish cut (D25) in ULE and Zerodur. In ULE, a coarser grinding wheel induces deeper cluster depth for a given grinding condition except for the semi finish cut (D46). A similar influence of the grit size on the cluster depth is observed for Zerodur except the semi finish cut (D25). The cluster depths are deeper in ULE than Zerodur except for the semi finish cut (D25).
The lowest single last fracture depth is measured for the finish cut (D25) in ULE and Zerodur. For a finish cut, in ULE and Zerodur, a coarser grinding wheel generates deeper single last fracture. For a semi finish cut, the lowest single last fracture depth is obtained using the D46 grinding wheel on both materials. Interestingly, in Zerodur, the rough cut (D76) is shallower than semi finish and finish cuts using a similar grinding wheel. The single last crack depths are deeper in ULE than Zerodur except for the finish cut (D46) and semi finish cut (D76).

6.1.3 Normal and tangential grinding forces

- **Finish cuts**

The normal and tangential grinding forces measurements for the finish cuts are shown in Figure 6.9.

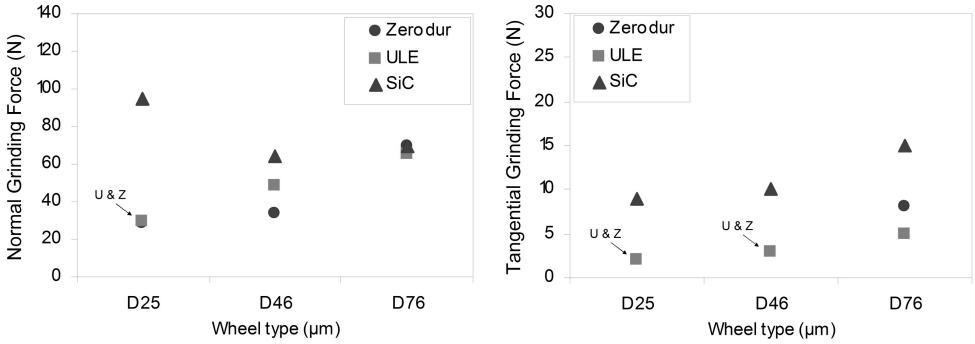

(a) Normal grinding forces (b) Tangential grinding forces

Figure 6.9: Grinding forces for finish cuts - a_e = 50 μm, f_r = 1.5 mm/rev, v_w = 25 mm/s, Q_w = 1.87 mm^3/s

The normal and tangential grinding forces are highest in SiC. The normal grinding forces are higher in ULE while the tangential grinding forces are higher in Zerodur. The normal grinding forces decrease with an increase in grit size in SiC. They increase with the grit size for ULE and Zerodur. The tangential grinding forces increase at different rates when using coarser grinding wheels. The targeted normal grinding force, below 100 N, is achieved using all grinding wheels for each ground material.

- **Semi Finish cuts**

The normal and tangential grinding forces measurements for the semi finish cuts are shown in Figure 6.10.

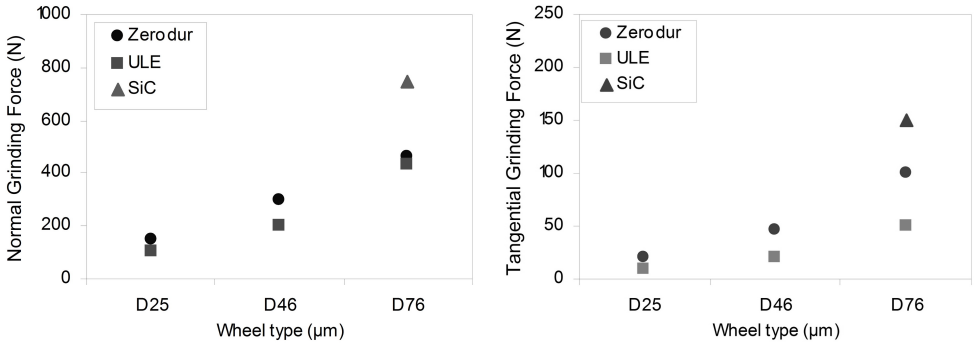

(a) Normal grinding forces (b) Tangential grinding forces

Figure 6.10: Grinding forces for semi finish cuts - a_e = 200 μm, f_r = 10 mm/rev, v_w = 20 mm/s, Q_w = 40 mm^3/s

The normal and tangential grinding forces are increasing with the grit size. The normal and tangential grinding forces remain highest for SiC. Lower grinding forces are obtained when grinding ULE than Zerodur.

- **Rough cuts**

The normal and tangential grinding forces measurements for the rough cuts are shown in Figure 6.11.

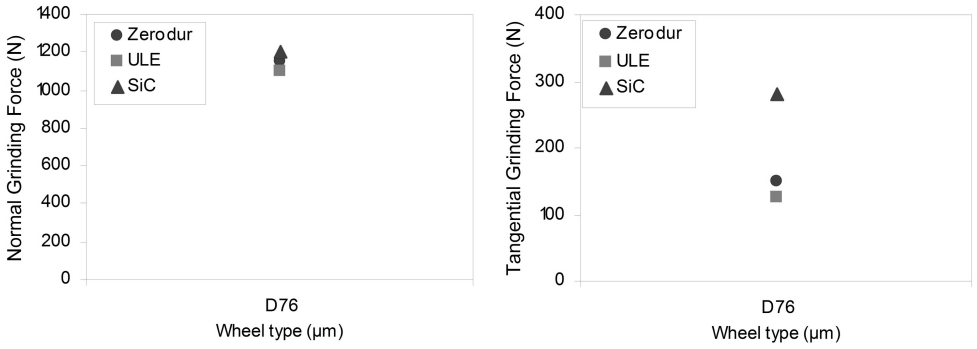

(a) Normal grinding forces (b) Tangential grinding forces

Figure 6.11: Grinding forces for rough cuts - a_e = 500 μm ($a_{e(SiC)}$ = 300 μm), f_r = 15 mm/rev, v_w = 25 mm/s, Q_w = 187.5 mm^3/s (SiC - 112.5 mm^3/s)

The grinding forces are the highest for SiC for depth of cut of 300 μm only. The grinding forces remain lower for ULE than Zerodur. The normal grinding forces are higher than 1000 N for each ground material.

The targeted normal grinding force is achieved using any grinding wheel for each ground material. For ULE and Zerodur, the normal and tangential grinding forces increase with coarser grinding wheels. Grinding ULE generates less grinding force than Zerodur except normal grinding forces for the finish cuts (D25 & D46). SiC induces the highest normal and tangential grinding forces except for the semi finish cut using 76 μm grit size.

6.1.4 Grinding power

The grinding power is calculated using equation 2.8.25. The tangential grinding force recorded is multiplied by the grinding wheel speed.

- **Finish and Semi Finish cuts**

The calculated grinding power for the finish and semi finish cuts is shown in Figure 6.12.

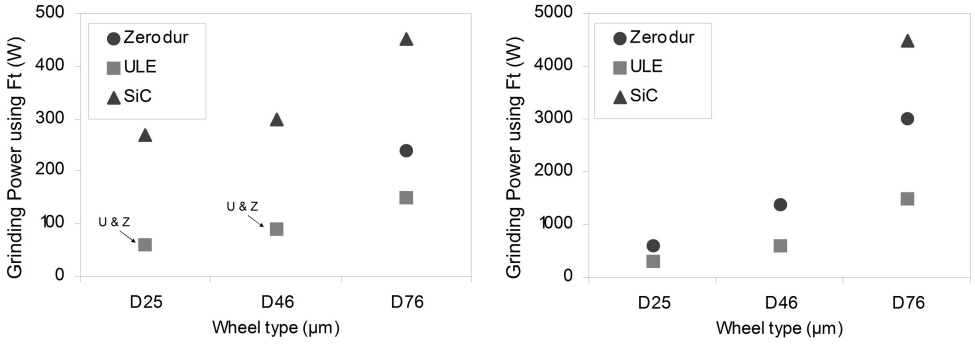

(a) Finish cuts - a_e = 50 μm, f_r = 1.5 mm/rev, v_w = 25 mm/s, Q_w = 1.87 mm^3/s

(b) Semi finish cuts - a_e = 200 μm, f_r = 10 mm/rev, v_w = 20 mm/s, Q_w = 40 mm^3/s

Figure 6.12: Grinding power for finish and semi finish cuts

The grinding power is the largest for SiC. Grinding of Zerodur requires more grinding power than ULE. For the finish cuts using the D25 and D46 grinding wheels, this grinding power is similar. The necessary grinding power increases with material removal rate. For a given grinding condition, a coarser grinding wheel generates more grinding power. For a finish cut, less than 500 W are used for SiC while less than 300 W are required for ULE and Zerodur. During the semi finish cut (D76), the required power is 1500 W and 3000 W for ULE and Zerodur respectively. For SiC, the grinding power used is 4500 W. The use of a 46 μm grit size reduce the power demands down to 600 W and 1400 W for ULE and Zerodur.

- **Rough cuts**

The calculated grinding power for the rough cuts is shown in Figure 6.13.

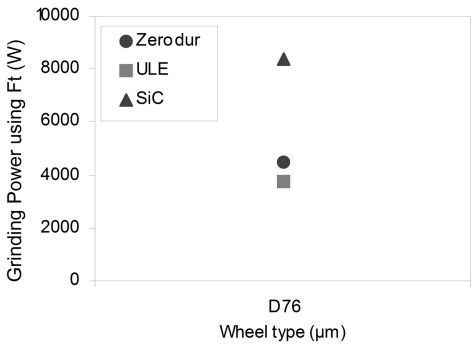

Figure 6.13: Grinding power for rough cuts - a_e = 500 μm ($a_{e(SiC)}$ = 300 μm), f_r = 15 mm/rev, v_w = 25 mm/s, Q_w = 187.5 mm^3/s (SiC - 112.5 mm^3/s)

The calculated grinding power used for SiC reaches 8400 W for a material removal rate of 112.5 mm^3/s. This comes close to the maximum available grinding power of BoX

grinding machine. Therefore, the SiC maximum depth of cut was limited to 300 μm. The targeted value of 200 mm^3/s can not be reached using a D76 grinding wheel using those grinding conditions. A material removal rate of 187.5 mm^3/s, induces a calculated grinding power of 3750 W and 4500 W for ULE and Zerodur respectively. The maximum removal rate targeted can be achieved on those two materials. The chosen grinding wheel is adequate.

6.1.5 Specific grinding energy

The specific grinding energy was calculated using equation 2.8.26 described in section 2.8.7. The measured tangential grinding forces were multiplied by the grinding wheel speed. This calculated grinding power was divided by the material removal rate. The specific grinding energy results are shown in Table 6.3.

Grinding Conditions	SiC *(J/mm^3)*	ULE *(J/mm^3)*	Zerodur *(J/mm^3)*
Finish cut (D25)	144	32	32
Finish cut (D46)	160	48	48
Finish cut (D76)	240	80	128
Semi Finish cut (D25)	-	8	15
Semi Finish cut (D46)	-	15	35
Semi Finish cut (D76)	113	38	75
SiC Rough cut (D76)	75	-	-
Rough cut (D76)	-	20	24

Table 6.3: Specific grinding energy results - BoX

The specific grinding energy increases with a larger grit size for a given grinding condition. With an increase in material removal rate for a given grinding wheel, the specific grinding energy decreases. The ground material has an influence as the grinding of SiC induces the largest values. The grinding of Zerodur requires larger specific grinding energy than ULE except during a finish cut (D25) as the specific grinding energies are similar.

6.2 BoX large scale surface experiments

The grinding process, developed on 100 mm square parts, was replicated on larger parts. The grinding process scalability was validated for each ground material type.
The sample sizes were: 400 mm across corner hexagonal SiC part, 400 mm square ULE part and 1000 mm across corner hexagonal Zerodur blank. A sphere was ground in each sample.

The SiC part had a radius of curvature of 3180 mm. Both ULE and Zerodur parts had a 3000 mm radius of curvature. Those radii of curvature were chosen to match the lapping tool size and the optical tower measuring capabilities.

6.2.1 400 mm SiC part

The grinding process validation on SiC was performed on a hexagonal part of 400 mm across corners. This part was 25 mm thick and non-weight relieved monolith. A 3180 mm radius of curvature sphere was ground. This part is shown in Figure 6.14.

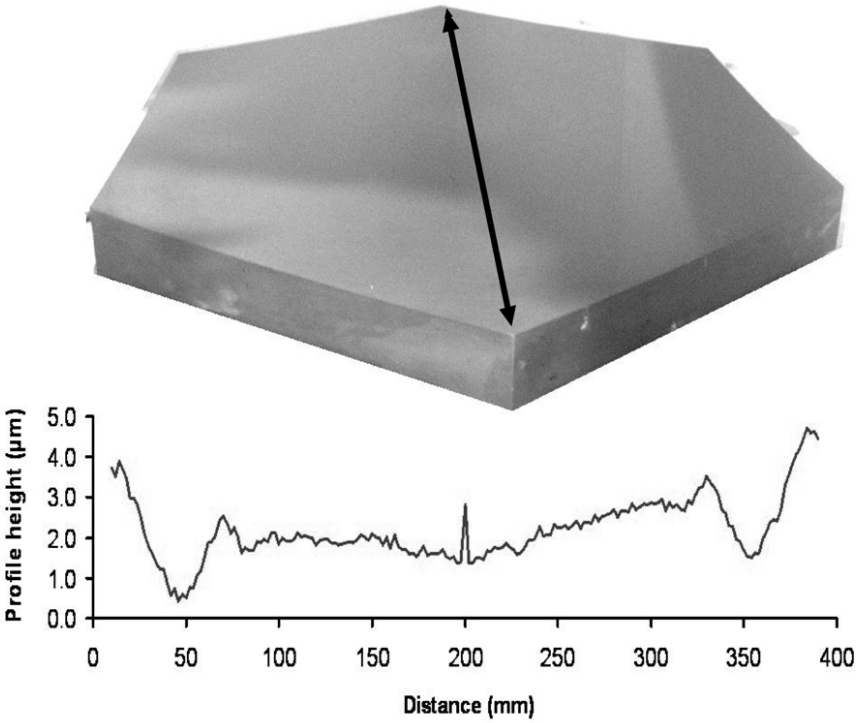

Figure 6.14: 400 mm across corner hexagonal SiC part

In order to reduce the grinding requirements, the part was ordered with a 3000 mm radius of curvature sphere. The radius accuracy was specified to be $\pm$ 12 mm. The surface profile error was 0.4 mm. The part was ground into the final sphere using a D46 grinding wheel. The final finish cut removed 50 μm. To improve the surface profile on the 400 mm part, the feed rate (f_r) was reduced from 1.5 mm/rev to 0.5 mm/rev. The material removal rate was 0.6 mm^3/s.

The surface profile was measured using a Leitz PMM-F co-ordinate measuring machine (see section 3.2.5). This surface profile was fitted to a best fit radius of curvature sphere. The surface profile (P_t) is $\pm$ 2.5 μm over 380 mm. A non symmetric profile error is observed reaching a value of 1 μm. The centre region has a surface profile of P_t = 1 μm.

The maximum error was shown within 50 mm of the edge.
This ground part was also measured using a Form Talysurf (see section 3.2.5). Two surface profiles were obtained from corner to centre of the part as shown in Figure 6.15.

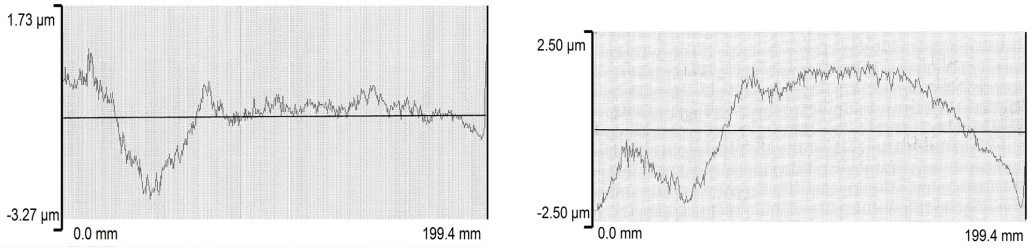

(a) RoC = Best fit (b) RoC = 3180 mm

Figure 6.15: 400mm SiC part - Profile measurements

Figure 6.15(a) shows results similar to the measurements done using the Leitz CMM. For a best fit RoC, the surface peak to valley (P_t) value is 3.5 μm over 200 mm. A form error is shown at 50 mm from the edge corner.

The surface profile fitted to the targeted 3180 mm radius of curvature is shown in Figure 6.15(b). The surface profile measured is 4.05 μm over 200 mm. The part shape is different from the CMM measurement. This profile illustrates some of the anticipated grinding effects. At the edge of the part, the grinding wheel deflects. A second deflection is seen when the grinding wheel starts to cut over the whole surface at 141 mm from the centre. From that point, the deflection is due to the grinding machine stiffness. The grinding wheel wear increases the normal grinding forces. The surface speed is held constant until reaching a distance of 30 mm from the part centre, where the maximum rotation speed of the grinding table is reached. This causes a decrease in normal grinding forces inducing a grinding wheel deflection. This effect is seen at around 20 mm from the part centre. The "centre peak" corresponds to a misalignment of the truing wheel compared to the centre of the grinding table.

The surface profiles using the D46 grinding wheel for 400 mm across corner hexagonal part and 100 mm parts can be compared. The surface profile (P_t) measurement on small parts was 1.66 μm over 95 mm using a feed rate of 1.5 mm/rev. By reducing the feed rate to 0.5 mm/rev, the height between each groove is reduced, as illustrated over small regions of the 400 mm part. On the 400 mm part, over 32 mm, the surface profile was 0.23 μm. For each part, the final surface profile accuracy is influenced by the repeatability between each groove generated.

The targeted surface profile accuracy is not obtained without subsequent error compensa-

tion. The surface roughness (R_a) measurement was 129 nm using a D46 grinding wheel on 100 mm part. The value obtained on the 400 mm part is R_a = 138 nm using the same grinding wheel.

6.2.2 400 mm ULE part

For ULE, a 400 mm square part with 20 mm thickness was ground. It is shown in Figure 6.16.

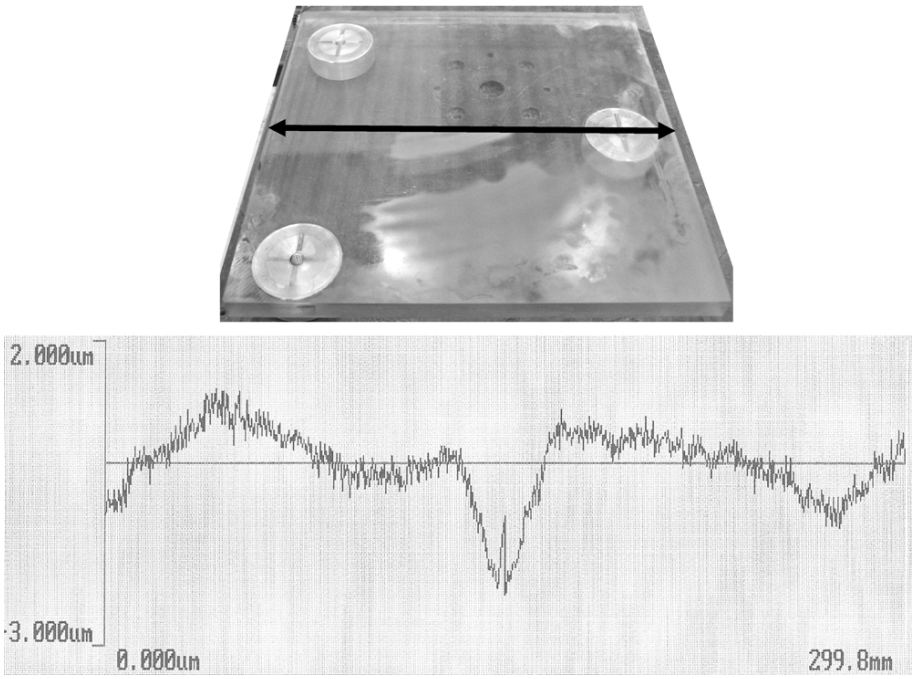

Figure 6.16: 400mm square ULE part

The part was ground from a flat into a sphere. A 3000 mm radius of curvature sphere was generated. The measurement showed, in Figure 6.16, corresponds to a best fitted radius of curvature. A form Talysurf profilometer was used to measure 300 mm symmetrically over the part centre across the flat (see section 3.2.5). The capacity of the equipment (350 mm) did not allow measurement of the part across corners.

For a radius of curvature of 2999.95 mm, the surface profile peak to valley (P_t) is 3.4 μm over 300 mm. This measurement shows an astigmatism of the final form that is not due to a grinding error but to the distortion of the part due to its relative thin thickness. As on 400 mm SiC part, the centre defect and "centre peak" contribute to the surface profile error significantly more than the cusping repeatability error. The centre defect and centre peak are 20 mm and 1.5 mm from the centre respectively. The surface speed is held constant until reaching a distance of 30 mm from the part centre. The targeted surface profile

is not achieved using a feed rate (f_r) of 1.5 mm/rev.

The targeted surface roughness (R_a) is achieved. The surface roughness measured, using a 120L Talysurf surface profilometer, was 152 nm. No intermediate dressing was performed during the finish cut which led to worn grits. During the process development, the surface roughness on 100 mm sample, was over 200 nm for similar grinding conditions.

6.2.3 1 m Zerodur part

A one metre across corners hexagonal Zerodur part was ground. This one metre hexagonal Zerodur part was ground from a flat to a 3000 mm radius of curvature sphere. The targeted full size part was ground. Figure 6.17 shows some ground surface finish examples.

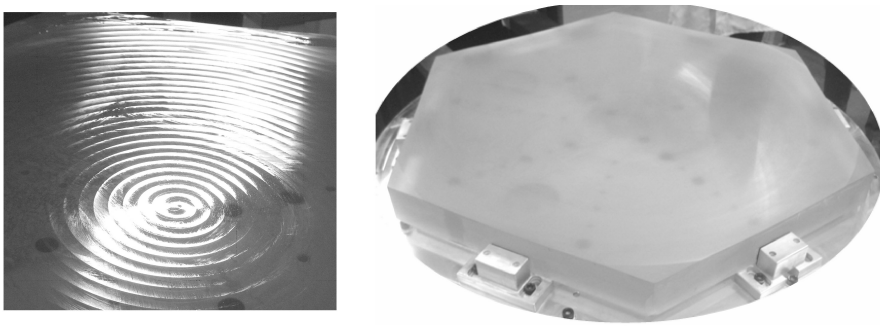

a) Rough grinding cut b) Finish grinding cut

Figure 6.17: Ground surface finish examples

Figure 6.17a shows a surface generated using a rough cut used to removed a large amount of material. As much as 32 mm saggitta was removed. The final 0.5 mm was removed in less than 10 hours. This shows the efficiency of the grinding process developed. Figure 6.17b shows the finish ground surface. A spiral tool path was employed.

The final ground surface was measured using the Leitz PMM-F co-ordinate measuring machine. A surface profile measurement across corners was performed as illustrated in Figure 6.18.

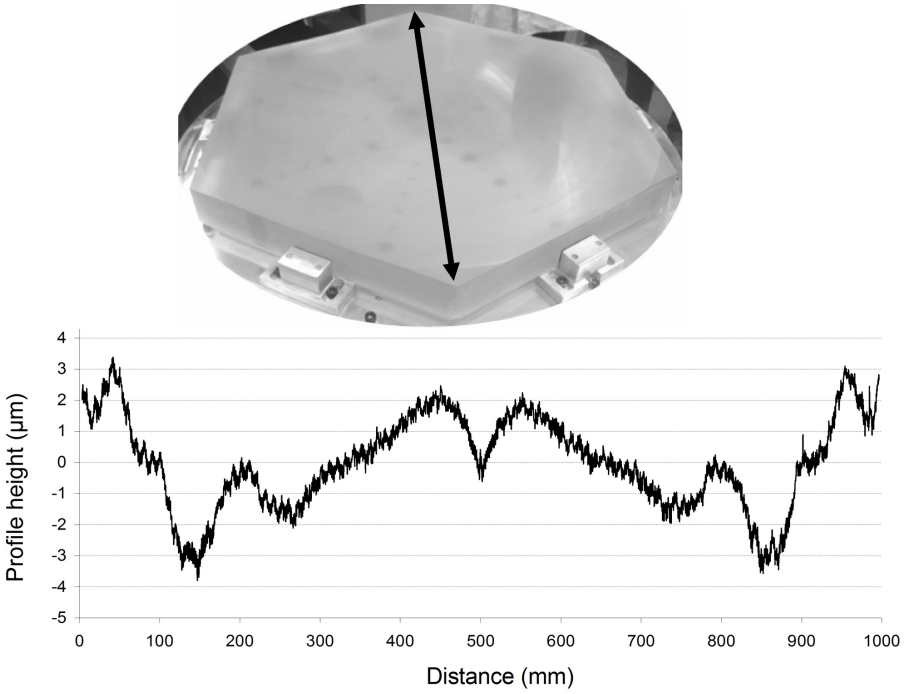

Figure 6.18: 1m across corner hexagonal Zerodur part

The form error observed corresponds to a best fit radius of curvature. The surface profile is symmetrical with no apparent astigmatism. The surface profile form accuracy obtained is $P_t < 7$ μm.

An intermittent grinding is done over six corners until a radius of 354 mm from the centre. The largest error amplitude is observed over that distance. From that point, the grinding wheel cuts over the whole surface. At 250 mm from the edges, the form error increases steadily until about 80 mm from the centre. Over 300 mm of each side of the centre, the surface profile error is below 4 microns. A centre defect and "centre peak" are presents. This error shape is comparable to the SiC and ULE parts. The centre defect starts at 50 mm from the centre. The height is 2.5 μm. The grinding surface speed is kept constant until reaching a distance of 30 mm from the part centre.

The maximum removal rate is achieved. A one metre part can be ground in less than 10 hours using the grinding process developed using the BoX grinding machine. The grinding process was proven reliable and efficient. Successive grinding runs were done to remove 32 mm sagitta. The targeted form accuracy is not achieved over one metre without subsequent error compensation.

Observation was done on the edges obtained. The grinding cuts did not induce visible chipping even with no chamfer. No damage was done on the sample corners. Chamfering

can be kept to a minimum.

6.3 Summary

The BoX test programme was performed on 100 mm x 100 mm x 20 mm samples. The surface results showed that not every target was met for each ground material.
The project surface roughness target was achieved on SiC for the finish cut (D25). For the finish cut (D25), the subsurface damage depth target was achieved for Zerodur. During the finish cuts, the surface profile qualities achieved were 1.4 μm, 1.8 μm and 1.7 μm for ULE, Zerodur and SiC respectively. The targeted surface profile (P_t) of 1 μm was not achieved.

The grinding process developed can remove 0.5 mm over a metre in less than 10 hours. A maximum material removal rate of 187.5 mm^3/s was achieved on ULE and Zerodur and 112.5 mm^3/s on SiC. The limitation for the SiC rough cut (D76) was due to the BoX maximum available grinding power. The normal grinding force recorded met the targeted value below 100 N for finish cut. Therefore, for the targeted profile error with an expected machine grinding stiffness of 100 N/μm, the final form accuracy was achievable.

The developed process was validated on larger ground parts. On ULE, the grinding process was successfully replicated on a 400 mm square part. The form accuracy achieved was 3.4 μm over 300 mm. On SiC, the grinding process was used on a 400 mm across corners hexagonal part. The form accuracy achieved was $\pm$ 2.5 μm. On Zerodur, the grinding process was achieved on a 1 m across corners hexagonal part. The form accuracy obtained was $\pm$ 3.5 μm.

The final form accuracy target was not achieved on any material. The overall profile error observed was symmetric. The centre defects were similar across material as well as some edge effect over 50 mm. Therefore, the use of an error compensation strategy would be necessary to improve the final form accuracy.

The stability of the BoX grinding machine was proven as no visible chipping of the edges or corners was observed. The grinding process was showed to be repeatable as 32 mm of sagitta were ground on 1 m Zerodur part.

7. GRINDING PROCESSES COMPARISON

This chapter discusses the grinding process results achieved on the Edgetek and BoX grinding machines. The ground surface qualities and process responses are compared against the project targets.

7.1 Surface profile results

The differences between the measured surface profile (P_t) and the calculated surface profile using equation 2.9.3, are shown in Figure 7.1.

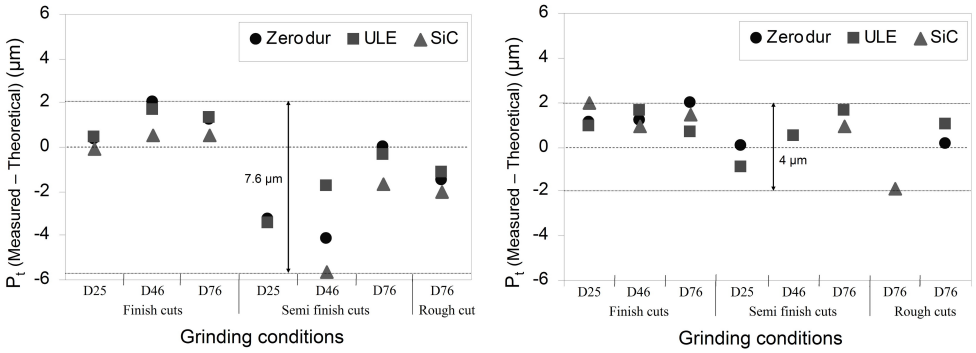

(a) Edgetek (b) BoX

Figure 7.1: Difference between measured and theoretical profiles

The charts show the general capability of the two grinding machines. The amplitude difference between the calculated and measured surface profile (P_t) are 7.6 μm and 4 μm on the Edgetek and BoX grinding machines respectively. On the two grinding machines, the results are comparable for the finish cuts. The repeatability between each "cusping" generated, as described in the results chapters, leads to errors below 2 μm. This grinding machine repeatability has to be accounted when calculating the expected surface profile (P_t).

Using the BoX grinding machine, the semi finish and rough cuts give lower results than the Edgetek grinding machine. The grinding machine stiffness is significant on the error generated as the grinding forces increase with higher material removal rates (semi finish and rough cuts) and higher substrate material hardness (SiC).

Another factor is the difference between the estimated and measured grinding wheel radius of curvature due to local flattening of the grinding wheel profile (Rowe et al., 1993) with high normal grinding forces and grinding wheel wear. This geometric effect becomes more important with an increase in feedrate per revolution (equation 2.9.3).

7.2 Surface roughness results

Using the BoX grinding machine, the SiC surface roughness (R_a) levels are lower when compared with the Edgetek grinding machine, for all grinding conditions. The surface roughness is lower than on ULE and Zerodur as higher material hardness induces high normal grinding forces that lead to flattening of the grinding wheel profile (Rowe et al., 1993).

The comparison of surface roughness (R_a) between the grinding machines, on ULE and Zerodur, is provided in Figure 7.2.

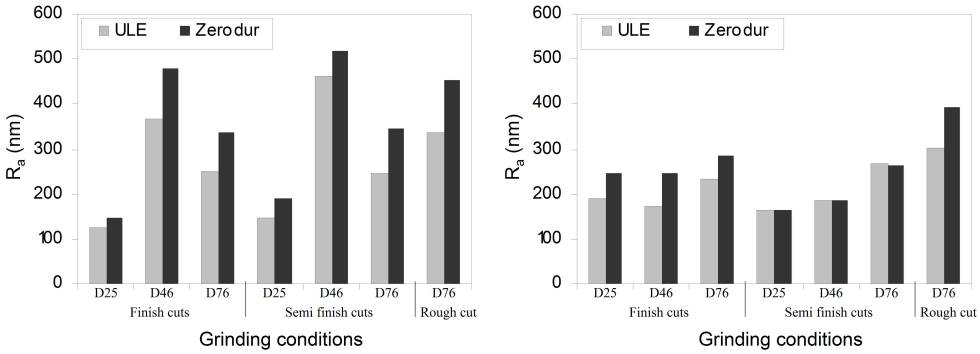

(a) Edgetek (b) BoX

Figure 7.2: Surface roughnesses (R_a) (Edgetek & BoX)

Generally, the surface roughness (R_a) levels are better on the BoX grinding machine. Such tendency is suggested by the contact area and number of grits differences obtained in Table 7.1.

For the two grinding machines, the contact area and estimated number of grits, for each grinding condition, are shown in Table 7.1.

Grinding Conditions	Contact area (mm^2)		Number of grits (#)	
	Edgetek	BoX	Edgetek	BoX
Finish cut (D25)	18	27	1620	2430
Finish cut (D46)	18	27	756	1134
Finish cut (D76)	21	27	504	648
Semi Finish cut (D25)	86	107	7740	9630
Semi Finish cut (D46)	86	107	3612	4494
Semi Finish cut (D76)	86	107	2064	2568
SiC Rough cut (D76)	-	161	-	3864
Rough cut (D76)	211	268	5064	6432

Table 7.1: Grinding wheel contact area and number of grits

Larger contact areas are obtained using the BoX grinding wheels. On the BoX grinding machine, the number of grits is 50% more for finish cuts and 25% more for semi finish and rough cuts than the Edgetek grinding machine.

7.3 Subsurface damage results

Subsurface damage in the form of cluster and single last fracture depths are shown in Figure 7.3 and 7.4 respectively.

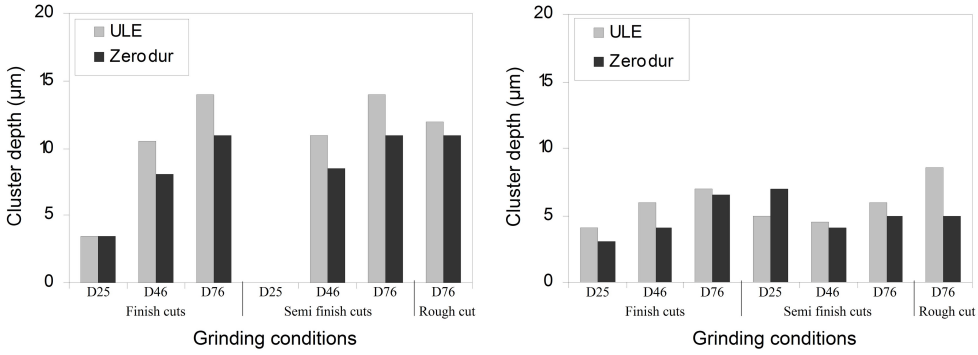

(a) Edgetek (b) BoX

Figure 7.3: Cluster depths (Edgetek & BoX)

Generally, the subsurface damage in terms of cluster depths are smaller for the BoX grinding machine when compared with the Edgetek grinding machine. The lowest cluster depths in both materials are achieved during the finish cut (D25).

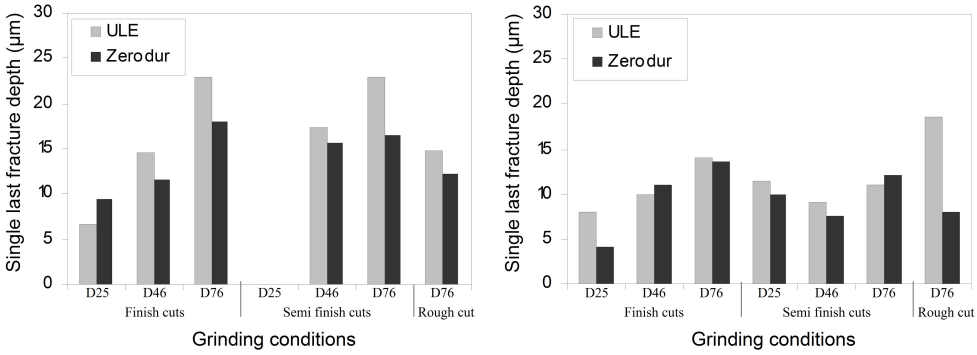

(a) Edgetek (b) BoX

Figure 7.4: Single last fracture depths (Edgetek & BoX)

Generally, the single last fracture depths are smaller for the BoX grinding machine when compared with the Edgetek grinding machine. The lower single last fracture depths in both materials are achieved during the finish cut (D25) on both grinding machines. For a given grinding condition, in general, an increase in grit size induces deeper single last fractures.

7.4 Specific normal and tangential grinding forces

The specific grinding forces and the tangential grinding forces are shown in Figure 7.5 and 7.6 respectively.

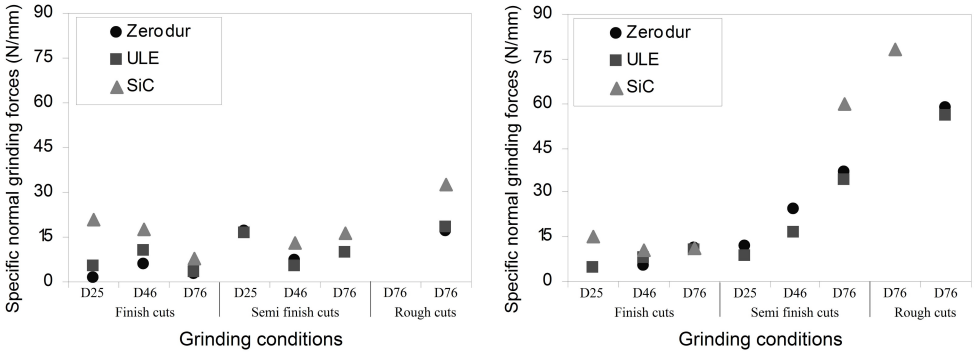

(a) Edgetek (b) BoX

Figure 7.5: Specific normal grinding forces (Edgetek & BoX)

On the two grinding machines, the specific normal grinding forces (F'$_n$) are similar. During the semi finish (D76) and rough grinding (D76) cuts, the BoX grinding machine generates larger values than the Edgetek grinding machine. Those differences can be explained by larger contact areas as shown in Table 7.1 and a higher "actual" depth of cut due to higher grinding stiffness on the BoX grinding machine.

The material ground also affects the specific normal grinding forces. In general, F'$_n$ values are highest in SiC, the harder material (Wager and Saini, 1986, Saini and Wager, 1985). The specific normal grinding forces are slightly higher in ULE compared to Zerodur during the finish cuts but for the semi finish and rough cuts, grinding of Zerodur is more demanding than ULE. This outcome suggests that fracture toughness and elastic modulus influence the specific normal grinding forces as reported by Huang and Liu (2003) based on equation 2.8.21 in section 2.8.5.

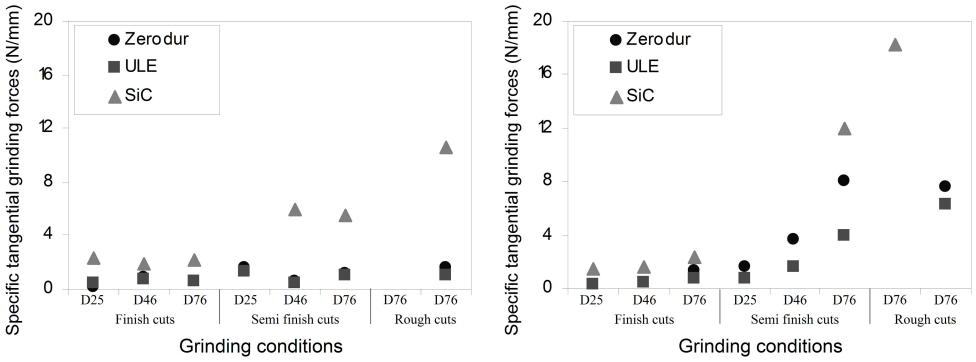

(a) Edgetek (b) BoX

Figure 7.6: Specific tangential grinding forces (Edgetek & BoX)

The same observation can be made on the tangential grinding forces (F'$_t$) when compared to the normal grinding forces. Higher F'$_t$ values obtained using the BoX grinding machine for the semi finish (D76) and rough (D76) cuts.

The tangential grinding forces versus normal grinding forces (friction coefficient) are shown in Figure 7.7.

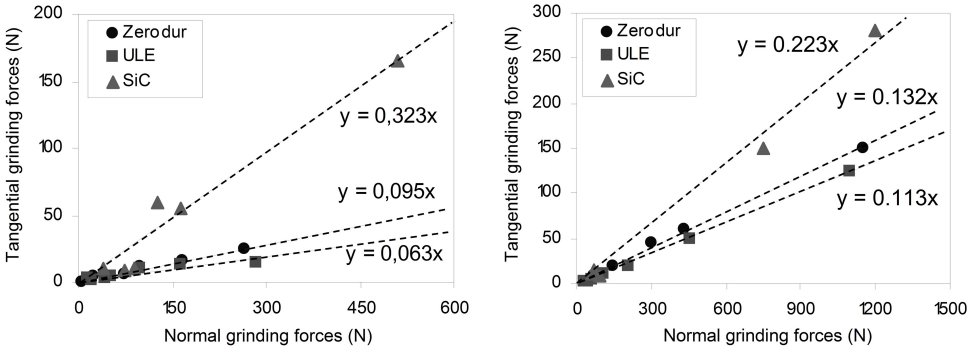

(a) Edgetek (b) BoX

Figure 7.7: Friction coefficients calculated (Edgetek & BoX)

Using the two grinding machines, the highest friction coefficient is obtained for SiC. This can be explained by the hardness of SiC leading to larger normal grinding forces. The grinding wheel wear affects the cutting efficiency as shown during the grinding wheel wear experiments on the Edgetek grinding machine.

Compared to the Edgetek grinding machine, the BoX grinding machine results show higher friction for ULE and Zerodur and lower by 0.1 on SiC. For a given ground material, this friction coefficient is proportional to the grit size, grain shape and coolant viscosity (Section 2.8.5). Higher contact area between the grinding wheel and workpiece can also explain this effect. The difference observed for SiC means that further testing is required.

7.5 Grinding power and energy

The calculated grinding powers are shown in Figure 7.8. An error bar of $\pm$ 30 W was added, corresponding to a 1 Newton measurement uncertainty level as recorded tangential grinding forces observed in the results chapters.

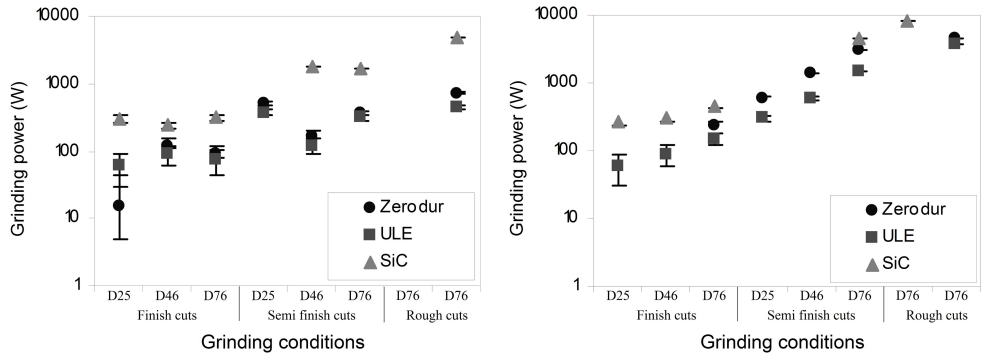

(a) Edgetek (b) BoX

Figure 7.8: Grinding power (Edgetek & BoX)

The grinding power was calculated by multiplying the tangential grinding forces recorded by the grinding wheel speed. As the grinding wheel speed was kept constant at 30 m/s, the effect of the grinding machine on the tangential grinding forces and on the grinding powers were the same. The BoX machine maximum power availability of 10 kW meant the largest depth of cut possible when rough grinding SiC was 0.3 mm equating to a 112.5 mm^3/s removal rate. The Edgetek grinding machine with a 27 kW power availability achieves 187.5 mm^3/s.

The specific grinding energy values, calculated by dividing the grinding power by the material removal rate, are shown in Figure 7.9.

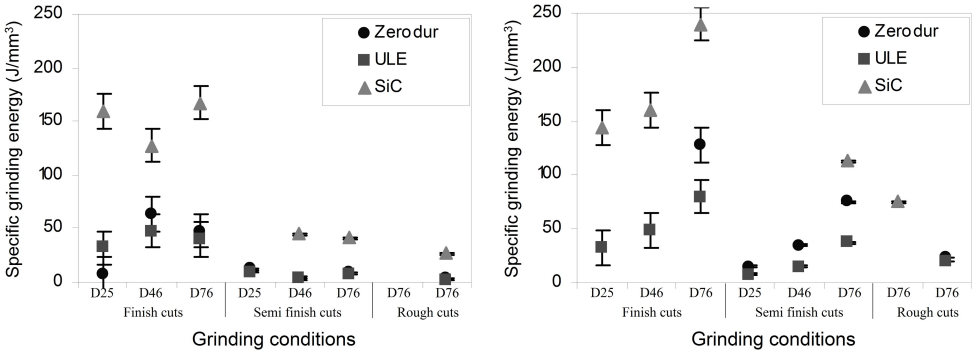

(a) Edgetek (b) BoX

Figure 7.9: Specific grinding energy (Edgetek & BoX)

On the Edgetek grinding machine, the maximum specific grinding energy for a rough cut (D76) confirm the expected 30 J/mm^3 obtained in the literature (Hwang and Malkin, 1999). However, in general, the specific grinding energy values are higher using the BoX grinding machine. Those differences are partially explained by higher friction coefficients and the BoX seven times higher stiffness. Further work is required especially on SiC as the Box spindle power limitation restricted the maximum removal rate to 112.5 mm^3/s.

7.6 Preston coefficient

The Preston coefficient (C_p) values, calculated using equation 2.8.30, are shown in Figure 7.10. As the Preston coefficients are similar in ULE and Zerodur (Z), ULE values are not included.

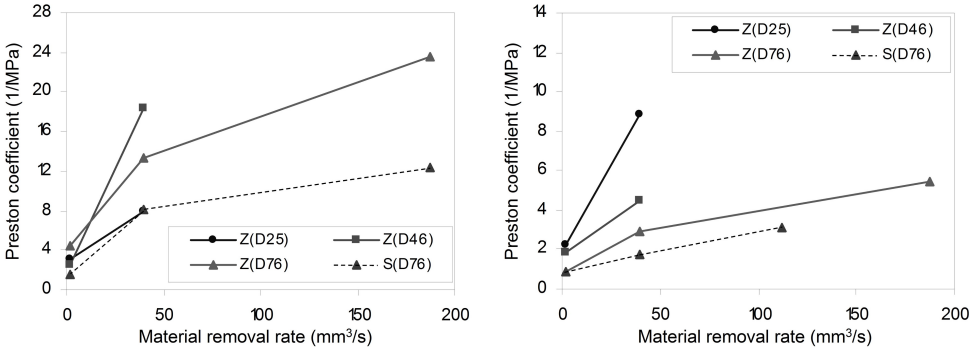

(a) Edgetek (b) BoX

Figure 7.10: Preston coefficients (Edgetek & BoX)

On the Edgetek grinding machine, the largest grit size induces generally the highest Preston coefficient values. This trend highlights the need to use large grit size for rough cuts to limit the amount of normal grinding forces generated. On the BoX grinding machine,

the Preston coefficients are lower than on the Edgetek grinding machine. The difference of coefficient is partially affected by the grinding machine stiffness as previously explained in 7.4. The grinding wheel cutting efficiency is reduced for Zerodur and SiC (S) using the BoX grinding machine as shown using the specific grinding energy values. The lower Preston coefficient is suggesting that lower grit sizes can be used to grind Zerodur on the BoX grinding machine.

7.7 Equivalent and maximum undeformed chip thicknesses

The size effect of the grinding processes is compared using the equivalent chip thickness (section 2.8.4) and the maximum undeformed chip thickness (section 2.8.3). Equation 2.8.12 and equation 2.8.9 are used respectively. The equivalent chip thicknesses versus the specific normal grinding force are shown in Figure 7.11.

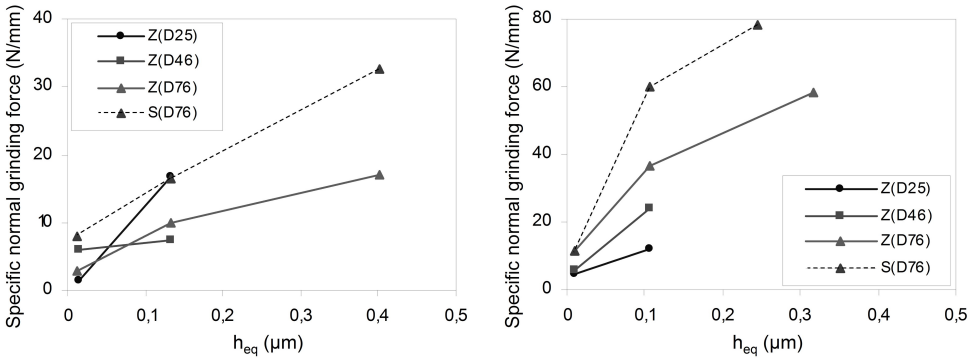

(a) Edgetek (b) BoX

Figure 7.11: Equivalent chip thickness versus specific normal grinding force (Edgetek & BoX)

On the two grinding machines, specific normal grinding force (F'$_n$) increases with higher equivalent chip thickness values.
On the Edgetek grinding machine, the D25 grinding wheel induces as much F'$_n$ on Zerodur as the D76 grinding wheel on SiC (S) for higher equivalent chip thickness. No significant fluctuation of specific normal grinding force (F'$_n$) is seen for an increase in equivalent chip thickness using the D46 grinding wheel, for Zerodur (Z).

On the BoX grinding machine, the effect of the grinding wheel is clearly illustrated. The specific normal grinding forces are increasing with larger equivalent chip thickness proportionally with the grinding wheel grit size. The effect of the ground material is highlighted as Zerodur shows lower F'$_n$ values for a given h$_{eq}$ compared to SiC.

The equivalent chip thicknesses versus the specific grinding energy are shown in Figure 7.12.

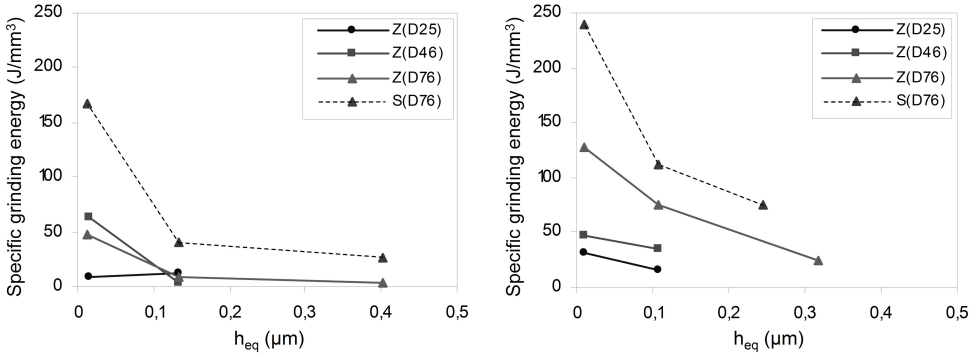

(a) Edgetek (b) BoX

Figure 7.12: Equivalent chip thickness versus specific grinding energy (Edgetek & BoX)

On both grinding machines, a "size effect" is observed for specific grinding energy versus equivalent chip thickness.
On the Edgetek grinding machine, specific grinding energies are similar for $h_{eq} > 0.1$ μm except for the D76 grinding wheel on SiC. In Zerodur, for a variation of h_{eq} between 0.1 μm to 0.01 μm, the specific grinding energies increase from 3-12 J/mm^3 to 32-48 J/mm^3. An exception is seen for finish cut (D25) in Zerodur, where the specific energy decreases from 12 J/mm^3 to 8 J/mm^3.

On the BoX grinding machine, larger grit size and a decrease of h_{eq} generate larger specific grinding energy values. For a given grinding wheel, Zerodur requires lower specific grinding energy than SiC. For the D76 grinding wheel, a convergence in specific energy at 20-24 J/mm^3 on Zerodur is observed for an equivalent chip thickness of 0.4 μm.

The maximum undeformed chip thicknesses versus the specific grinding energy are shown in Figure 7.13.

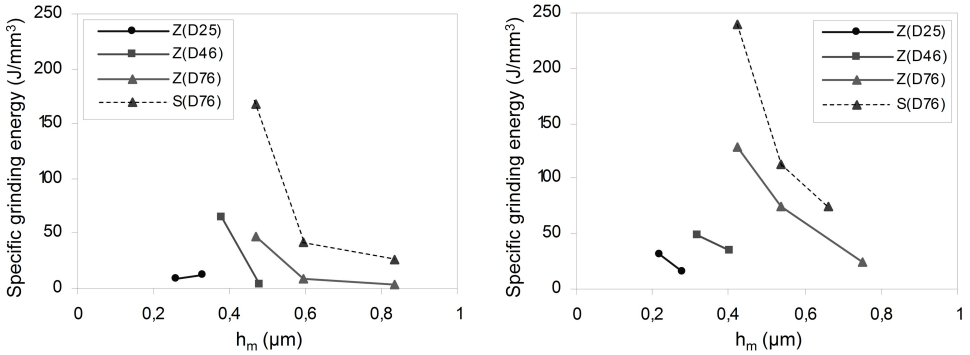

(a) Edgetek (b) BoX

Figure 7.13: Maximum undeformed chip thickness versus specific grinding energy (Edgetek & BoX)

In comparison with the equivalent chip thickness, the influence of the grinding wheel parameters on the specific grinding energy are considered. On both grinding machines, a "size effect" is observed for specific grinding energy versus maximum chip thickness. An increase of h_{max} generates lower specific grinding energy. This effect follows literature as showed in section 2.8.7 and is reported to correspond to an increase of sliding and ploughing power proportions (Rowe and Chen, 1997).

7.8 Summary

In general, the BoX grinding machine generates lower surface roughnesses (R_a) and lower subsurface damage depths. The surface profile, normal and tangential grinding forces levels are similar on the two grinding machines. The maximum material removal rate, 187.5 mm^3/s, is achieved on ULE and Zerodur.

The specific grinding energy is lower than expected and suggested in the literature for semi finish (D46 & D76) and rough (D76) grinding conditions using the Edgetek grinding machine. For SiC, the maximum material removal rate is limited to 112.5 mm^3/s due to the maximum grinding power available on the BoX grinding machine. In fact, the measured specific grinding energy on SiC, 70 J/mm^3, is higher than the value of 30 J/mm^3 reported in the literature.

8. SUBSURFACE DAMAGE DISTRIBUTION

Measured subsurface damage distributions in ULE and Zerodur using Edgetek and BoX grinding machines are discussed within this chapter. The influence of the grinding process and grinding machine dynamics on the subsurface damage distribution is analysed.

8.1 Edgetek grinding machine results

The number of cracks per mm^2 against the depth beneath the ground surfaces was plotted for each grinding condition (see Appendix C.2). The subsurface damage depths measured are detailed in the result chapter in section 5.2.2.
The subsurface damage observed was split into two proposed damage regions/zones, namely, "process" related (Zone 1) and "machine dynamics" related (Zone 2). The number of cracks per mm^2 decreases rapidly until a defined cluster depth is reached. The deeper cracks observed, below the cluster depth, are fewer. The deepest crack propagation depth (the maximum subsurface damage depth) has been named as the single last fracture depth.

In Figure 8.1(a), the number of cracks beneath the ground surface decreases exponentially with the depth beneath the surface. In order to identify the point of inflection of the curve corresponding to the cluster depth, the logarithm function properties was used. A logarithmic scale was used to plot the number of cracks per mm^2 versus the depth beneath the surface (see Figure 8.1(b)). A linear trend is obtained over the "process" related zone until the cluster depth is reached. A different trend is observed over the "machine dynamics" related zone. For each measurement, the cluster depth ($sd_{process}$) was found to be at a level of 100-300 cracks per mm^2.

For all grinding conditions, "process" related and "machine dynamics" related regions were established. Four measurements are shown in this chapter, that correspond to the finish cuts in ULE and Zerodur. The numbers of defects per mm^2 against the depth beneath the ground surfaces are given in Figure 8.1, for the finish cut (D25) in Zerodur.

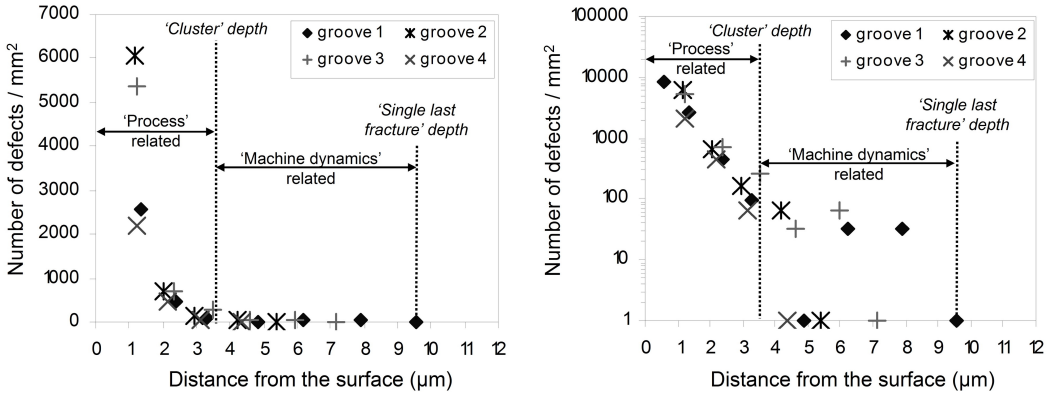

(a) "Normal" scale (b) Logarithm scale

Figure 8.1: "Process" related and "machine dynamics" related zones - Edgetek - Zerodur - Finish cut (D25)

Two distinctive zones are identified for the finish cut (D25) on Zerodur. The number of defects decreases rapidly (Zone 1) then it follows another distinct trend (Zone 2). Zone 1 is the "process" related region and Zone 2 is the "machine dynamics" related region. The transition point between these two zones has been defined as $\text{sd}_{process}$ (cluster depth). The length of the lateral crack (cluster depth) was identified to be specific to a given grinding process (Suratwala et al., 2006). The $\text{sd}_{process}$ depth is 3.5 μm and the Zone 2 depth is 9.5 μm.

The numbers of defects per mm^2 against the depth beneath the ground surfaces are shown in Figure 8.2 for the finish cut (D25) in ULE.

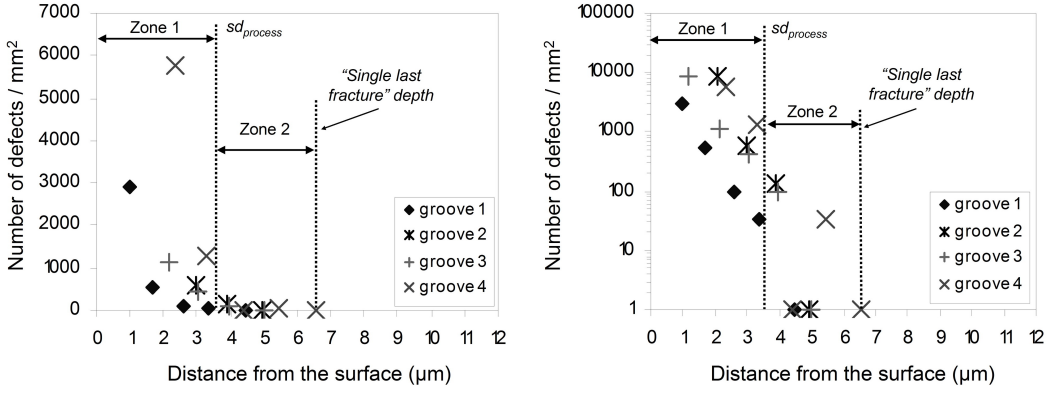

(a) "Normal" scale (b) Logarithm scale

Figure 8.2: "Process" related and "machine dynamics" related zones - Edgetek - ULE - Finish cut (D25)

In ULE, the distribution of subsurface damage cracks is in two distinctive zones, as observed in Zerodur. For the finish cut (D25), ULE is less responsive to the machine dy-

namics than Zerodur due to longer cracks resulting from easier propagation in ULE, as discussed in section 6.1.2. Figure 8.2(a) shows the transition point depth, $sd_{process}$, at 4 μm. This value is the same as on Zerodur using the same grinding wheel with same grinding condition. The single last fracture depth occurs 3 μm deeper beneath the surface than in Zerodur.

The numbers of defects per mm^2 against the depth beneath the ground surfaces are shown in Figure 8.3 for the finish cut (D46) in ULE and in Zerodur.

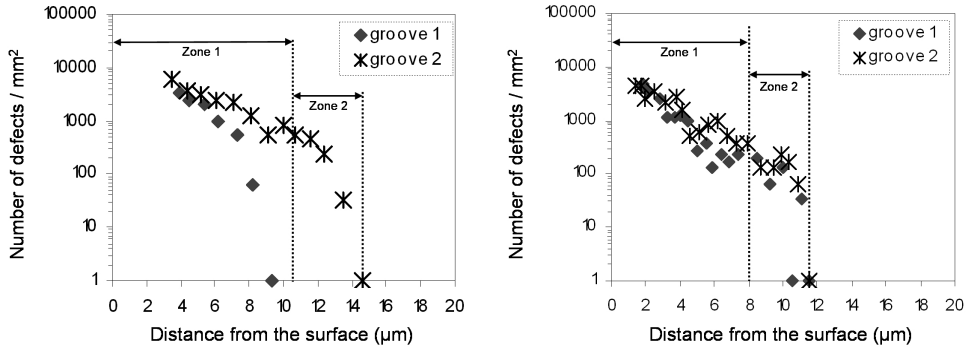

(a) ULE (b) Zerodur

Figure 8.3: "Process" related and "machine dynamics" related zones - Edgetek - Finish cut (D46)

As for the finish cut (D25), the cluster depth is deeper in ULE than in Zerodur. The $sd_{process}$ values are 10.5 μm and 8 μm for ULE and Zerodur respectively. A clear transition point is observed using the normal scale as shown in Appendix C.2. Zone 1 is deeper than the finish cut (D25) so it is influenced by an increase of the grinding wheel grit size for both materials. Zone 2 is 4 μm deep for ULE and Zerodur.
For all grinding conditions tested on Edgetek, Zone 1 and Zone 2 were found.

8.2 BoX grinding machine results

The same subsurface damage plots were obtained on the samples processed using the BoX grinding machine (Appendix C.2). The subsurface damage depths measured are shown in section 6.1.2. The cluster depths ($sd_{process}$) were obtained using a logarithmic scale as described for the Edgetek grinding machine.

The results obtained on the BoX grinding machine for the finish cut (D25) for Zerodur are shown in Figure 8.4.

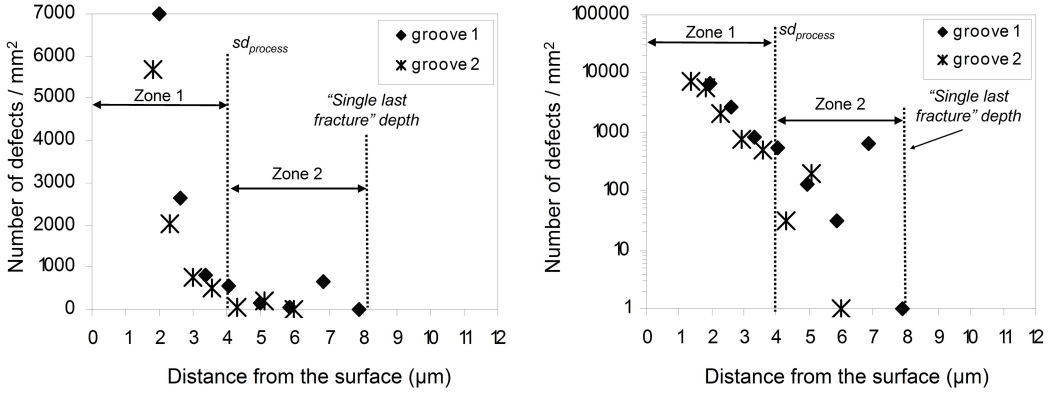

(a) "Normal" scale (b) Logarithm scale

Figure 8.4: "Process" related and "machine dynamics" related zones - BoX - Zerodur - Finish cut (D25)

Two distinctive zones are identified. The same assumptions remain as Zone 1 is "process" related and Zone 2 is "machine dynamics" related. The transition point, $sd_{process}$, is 4 μm deep from the ground surface. Zone 2 extends over a depth of 4 μm.

The results obtained on the BoX grinding machine for the finish cut (D25) for ULE are shown in Figure 8.5.

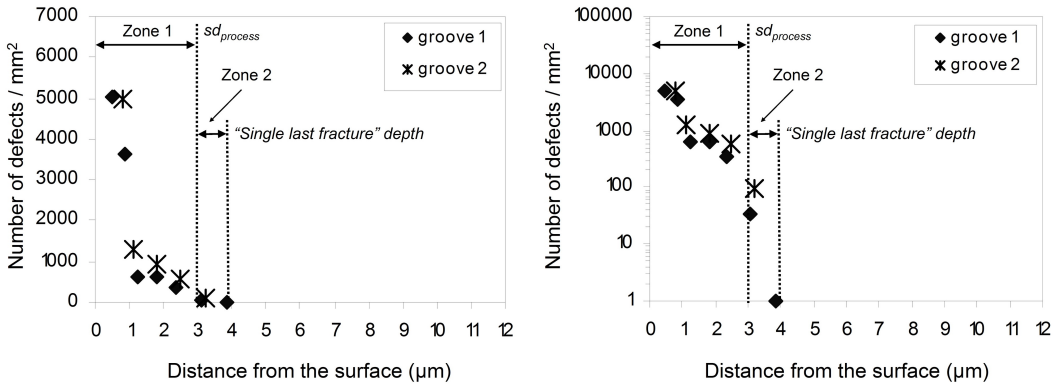

(a) "Normal" scale (b) Logarithm scale

Figure 8.5: "Process" related and "machine dynamics" related zones - BoX - ULE - Finish cut (D25)

The subsurface damage distribution in two distinctive zones, Zone 1 and 2, is shown in Figure 8.5(a). The cluster depth is 3 μm. The cluster depth in Zerodur is deeper than in ULE. Zone 2 extends to 1 μm depth.

The results obtained on BoX grinding machine for the finish cut (D46) for ULE and Zerodur are shown in Figure 8.6.

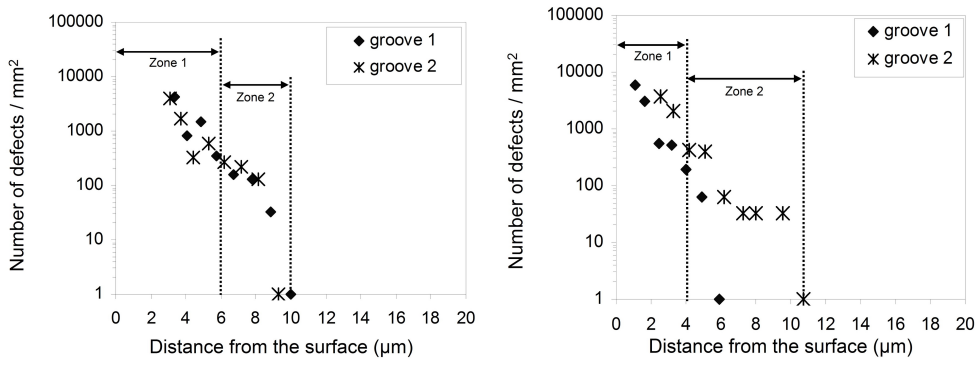

(a) ULE (b) Zerodur

Figure 8.6: "Process" related and "machine dynamics" related zones - BoX - Finish cut (D46)

In Zerodur, Zone 2 is deeper than using the D25 grinding wheel with a value of 7 μm. In comparison, $sd_{process}$ increases by 1 μm when using the D46 grinding wheel instead of the D25 grinding wheel. The increase of Zone 1 with larger grit size, due to the grinding process, is observed in ULE. Zone 2 is constant at a depth of 4 μm using both grinding wheels.
A similar distribution into Zone 1 and Zone 2 were found for all grinding conditions tested on BoX.

8.3 Relations between machine tool and subsurface damage distribution

Different depths of subsurface damage beneath the surface were identified for both grinding machines as shown in Figure 8.7.

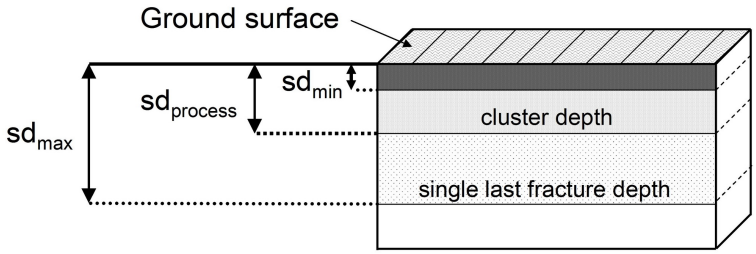

Figure 8.7: Distribution of subsurface damage depths

As explained in section 3.4.2, the number of cracks beneath the surface were counted once a depth (sd_{min}) was reached. This corresponds to a concentration of 5000-7000 cracks per mm^2. For each grinding conditions on both grinding machines, the value obtained is 2 μm except for the finish cut (D25) where it is 0.5 μm.

For the BoX grinding machine, during the finish cut (D25), $sd_{process}$ values are 3 μm and 4 μm for ULE and Zerodur respectively. For the Edgetek grinding machine, $sd_{process}$ values are 3.5 μm for both materials. This confirms that the cluster depth is "process" related.

In the two previous sections, the single last fracture depth (sd_{max}) has been proven to be a combination of cluster depth ($sd_{process}$) and "machine dynamic" related depth. The distribution of the number of defects per mm^2 can be summarized in Figure 8.8.

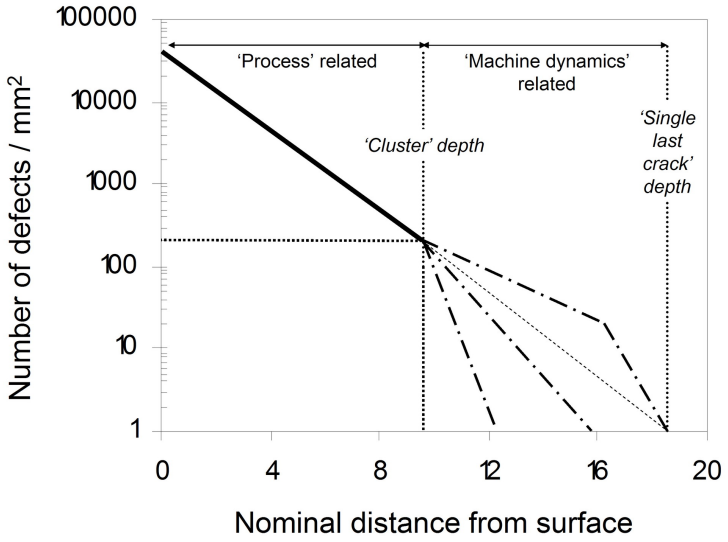

Figure 8.8: Distribution profile of subsurface damage

The number of cracks per mm^2 decreases rapidly following an exponential curve until cluster depth. This trend is observed for all grinding conditions and on the two grinding machines. A second exponential curve trend corresponds to the number of cracks per mm^2 decreasing until the single last fracture depth. This trend is different for all the grinding conditions.

The subsurface damage depths for the two grinding machines are shown in Figure 8.9 and Figure 8.10 for ULE and Zerodur respectively.

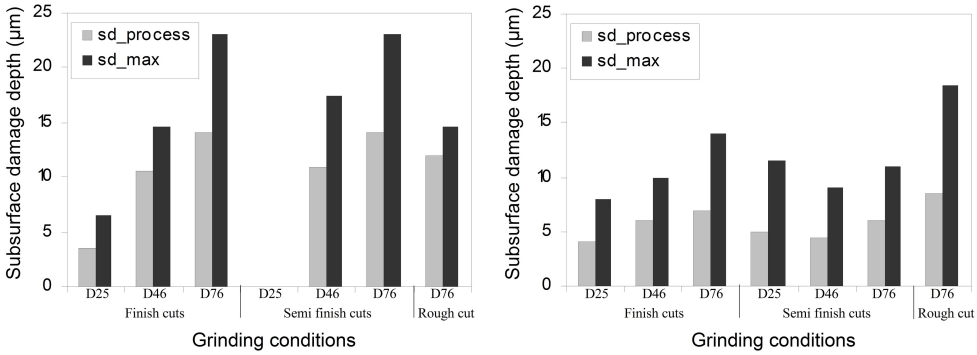

(a) Edgetek (b) BoX

Figure 8.9: Subsurface damage depths - ULE

The results showed that $sd_{process}$ and sd_{max} in ULE are both influenced by the grinding machine employed. The BoX grinding machine with a higher grinding stiffness and smoother motions, leads to more uniform $sd_{process}$ value in ULE than using the Edgetek grinding machine.

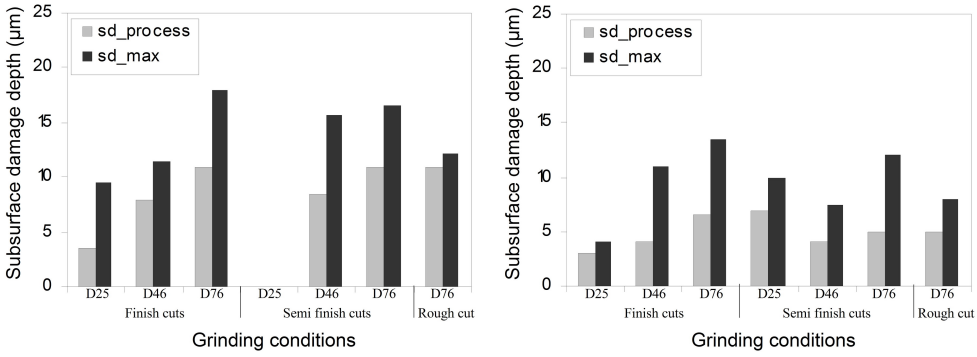

(a) Edgetek (b) BoX

Figure 8.10: Subsurface damage depths - Zerodur

Similar grinding machine influences on $sd_{process}$ and sd_{max} is observed in Zerodur. The Edgetek grinding machine in general leaves the highest $sd_{process}$ and sd_{max} values in both materials. The BoX grinding machine with a controlled grinding process leads to significant contribution of the grinding machine dynamics on cluster depth and single last fracture depth measured.

8.4 *Relations between grinding process and subsurface damage distribution*

Previous work indicated that the surface roughness is an important parameter to evaluate the subsurface damage depth. Those include different lapping processes but also bounded grinding processes (Hed and Edwards, 1987*b*, LLE, 1997, Suratwala et al., 2006, Shafrir et al., 2007). The values obtained were reported with details in the literature review in section 2.4.1. The surface roughness parameter, generally employed in these models, is the surface roughness peak to valley (R_t). The RMS surface roughness and R_a previously showed good correlations in those works.

In this work, surface roughnesses (R_a) and (R_t) were plotted versus the measured value of cluster depth ($sd_{process}$) in Figure 8.11.

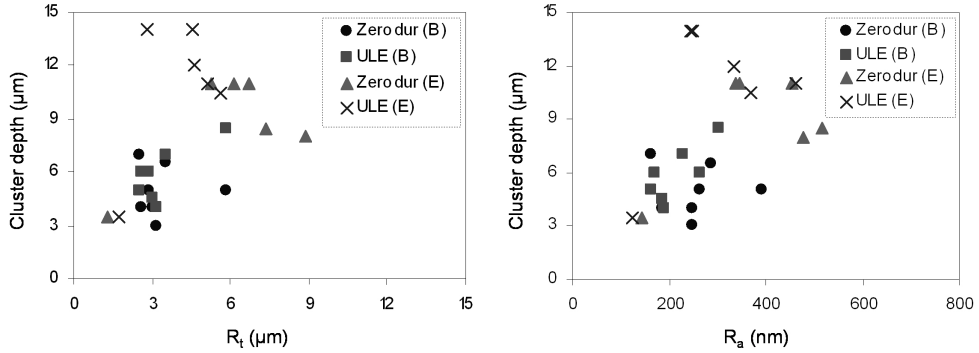

(a) Surface measurement - R_t (b) Surface measurement - R_a

Figure 8.11: Surface roughnesses versus subsurface damage (B - BoX & E - Edgetek)

There was poor correlation irrespective of grinding wheel type or grinding machine. This follows observations by Miller et al. (2005).

The normal grinding force per grit (f_{gn}) was calculated using the number of grits per mm^2 and grinding wheel contact area in Table 7.1, see Figure 8.12.

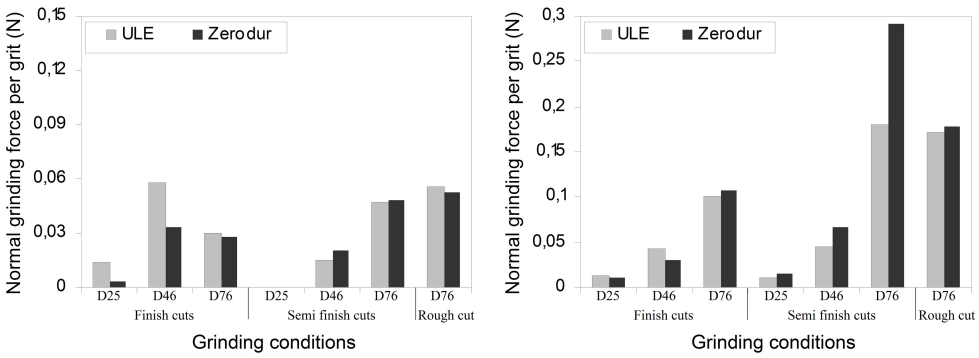

(a) Edgetek (b) BoX

Figure 8.12: Comparison of the normal grinding force per grit (f_{gn})

The normal grinding forces per grit are lower in the Edgetek grinding machine compared to the BoX grinding machine. While the number of grits per mm^2 and grinding wheel contact area are larger for a given grinding condition using the BoX grinding machine, the total grinding forces are higher especially for the D76 grinding wheel as discussed in section 7.4.

Previous work related the subsurface damage depth to the substrate material and the indentation load. The indentation load (P) is replaced by the normal grinding force per grit (f_{gn}) in equation 2.10.2 and equation 2.10.3. For a given substrate material and a fixed indentation angle, equation 8.4.1 and equation 8.4.2 are resulting.

$$b \propto f_{gn}^{1/2} \tag{8.4.1}$$

$$c_m \propto f_{gn}^{2/3} \tag{8.4.2}$$

with b, the lateral crack depth and c_m, the median crack depth.

The relation between the lateral crack depth and the cluster depth was investigated. Cluster depths were plotted versus $f_{gn}^{1/2}$ as shown in Figure 8.13.

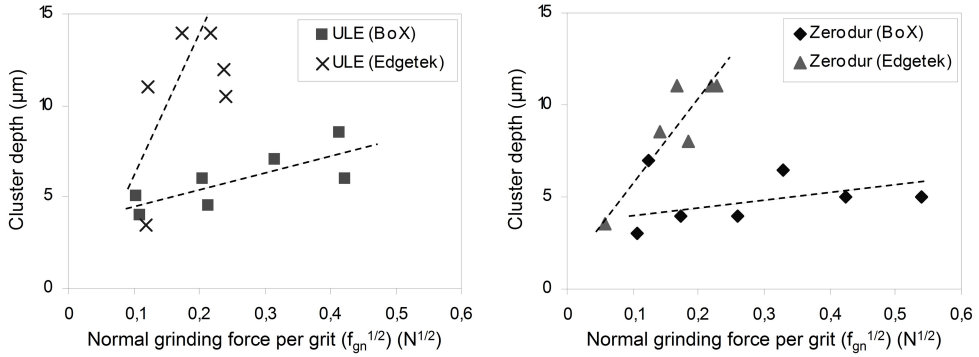

(a) ULE (b) Zerodur

Figure 8.13: Comparison between $f_{gn}^{1/2}$ and cluster depths

The results show that the cluster depth is proportional to $f_{gn}^{1/2}$. For our grinding process, the cluster depth is proportional to the lateral crack depth. The BoX grinding machine with higher $f_{gn}^{1/2}$ values induces shallower cluster depth in ULE and Zerodur. On BoX grinding machine, the straight line data fit would indicate a minimum cluster depth of 3.5 μm under low loading. On the two grinding machines, the cluster depth induced in ULE are deeper for a similar level of $f_{gn}^{1/2}$.

The influence of the median crack on the single last fracture depth was also investigated. Single last fracture depths were plotted versus $f_{gn}^{2/3}$ as shown in Figure 8.14.

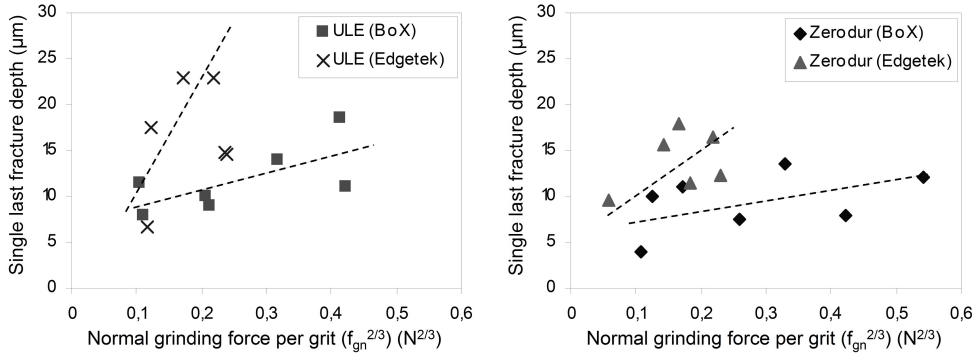

(a) ULE (b) Zerodur

Figure 8.14: Comparison between $f_{gn}^{2/3}$ and single last fracture depths

The linear trends observed in Figure 8.14(b) confirm the effect of $f_{gn}^{2/3}$ on the last fracture depth measured. On the two grinding machines, the single last fracture depth induced in ULE are deeper for a similar level of $f_{gn}^{2/3}$. The single last fracture depths are proportional to $f_{gn}^{2/3}$ relating to median cracks ("sharp" indenter) or Hertzian cracks ("blunt" indenter).

The BoX grinding machine with higher $f_{gn}^{1/2}$ and $f_{gn}^{2/3}$ values induces shallower cluster and single last fracture depths in ULE and Zerodur respectively, compare to the Edgetek grinding machine. The impact indentation load generated during the grinding process influenced the "static" indentation load and degrades the material strength (Wiederhorn and Lawn, 1977, 1979). The smoothness of the BoX grinding machine reduced the impact load effect of the diamond grit on the substrate.

As the actual indentation is not static, "trailing" cracks can be observed due to friction during grinding (Miller et al., 2005). This friction effect is calculated using equation 8.4.3.

$$P' = P(1 + \mu^2)^{1/2} \tag{8.4.3}$$

This sliding load P' replaces P in radial and Hertzian equations. The highest friction coefficient for our grinding process is μ = 0.13 for grinding Zerodur using the BoX grinding machine. Therefore, the maximum value obtained for relation (1+ μ^2)$^{1/2}$ is 1.01 which was considered negligible for our grinding process.

8.5 Summary

The results show that the number of defects apparent at different depths beneath the surface is a function of "process" related and "machine dynamics" related damage. Those distributions are observed for ULE and Zerodur on both grinding machines.

The BoX grinding machine with higher stiffness and smoother motions than the Edgetek grinding machine, is proven to reduce the "process" related depth (cluster depth) and single last fracture depth. The ratio between single last fracture depth and "process" related damage are increasing with an increase of the grinding machine stiffness.

The cluster depth is recognized to be proportional to lateral crack depth and the single last fracture depth is function of the median or Hertzian cracks. Those observations were based on fracture mechanisms, described in particular in Lawn's work, detailed in section 2.10.1, using the normal grinding force per grit as an indentation load.

For a given grinding force per grit, the Edgetek grinding machine induced larger subsurface damage depths. The smoothness of the grinding machine reduced the impact effect (Wiederhorn and Lawn, 1977) of the diamond grit on the substrate.
The "trailing" cracks effect for a moving indentation, leading to deeper subsurface damage, was shown to be negligible within this research.

The material brittleness gives further understanding of the distribution of the numbers

of defects beneath the surface. A low brittleness value gives longer cracks that combine with machine dynamics related cracks. More aggressive grinding parameters, in particular coarser grit sizes, leave deeper cracks which reduce the importance of the machine dynamics related damage in rough grinding.

These results disprove the relation between the cluster depth and the surface roughness (R_a & R_t) proposed by other authors (Hed and Edwards, 1987*a*, Lambropoulos et al., 1999, Randi et al., 2005). They also disprove the results reported by Yang et al. (2001) that the subsurface damage depth reduces with a decrease in grinding machine stiffness.

9. OVERALL DISCUSSION

This chapter discusses the approach taken in order to investigate the research hypothesis. The research objectives achieved to establish the required capability for large optics fabrication (UPS project) and the results obtained during this research are examined.

9.1 Summary overview

The research postulation was that a stiff large scale machine, BoX, would provide an effective means to rapidly produce accurate large scale (1 m) optical surfaces. In this respect, the hypothesis was that the depth of subsurface damage was associated with the machine performance in terms of machine stiffness and motion dynamics.

The research objectives, based on the production demands from the UPS project, were 1 mm depth removal in 10 hours on one metre scale optics achieving a form accuracy of 1 μm, surface roughness of 150 nm R_a and subsurface damage below 5 μm.

The UPS project production demand was broken down into grinding process parameter levels. The viability of parameter levels were initially considered through a comprehensive literature review and subsequently by small scale experiments performed on an available high quality production grinding machine (Edgetek).

The results of the so-called Edgetek based screening experiments provided an indication of achievability of the overall UPS project production demand. These screening trials helped in the initial definition of a three stage grinding process, which was considered as able to meet the overall project objective.

Subsequently proposed rough, semi finish and finish processing levels were tested on small scale samples using the Edgetek grinding machine. At this time the BoX machine was still under finalisation. These tests generally provided good confidence in regard to the overall project demand on small scale surfaces. Base line data regarding surface qualities and subsurface damage levels associated with each of the three process stages was produced and examined. Confidence level of the performance of the selected grinding wheels was gained through specific grinding wheel wear trials.

Reproduced (replica) trials on the BoX machine, the so-called BoX grinding test programme, showed the influence of each grinding parameter with respect to the project targets again in regards of surface qualities, sub-surface damage and processing time. Test data was used and examined to support the research hypothesis that the level of induced subsurface damage is associated with machine tool stiffness and smoothness of motions.

The BoX large scale experiments validated the three stage process on large optical parts (400-1000 mm). This process achieved the processing time objective (< 10 hours). The form accuracy, surface roughness and subsurface damage measurements provided good confidence that further optimisation work of the BoX grinding machine would ensure the overall UPS project production objective is met.

9.2 Edgetek based test programme

Key findings of the Edgetek based test programme were:

The surface roughness (R_a), for the given grinding condition, decreased with use of smaller grit size. This followed previous observations (Inasaki, 1987, Namba and Abe, 1993, Mayer Jr. and Fang, 1994, Zhang and Howes, 1995). The surface roughness R_a values were also influenced by substrate material properties. Under similar grinding conditions, lowest R_a values were obtained in the harder and tougher SiC. The surface roughness was lower in ULE than Zerodur. These results confirmed that the surface roughness decreased with an increase of the substrate elastic modulus (Hed et al., 1988). The proposed effect of an increase of substrate fracture toughness leading to a decrease of the surface roughness (Zhao et al., 2007) was disproved.

The target surface profile (< 1 μm P_t) was achievable. The developed grinding mode induced a surface profile (P_t) dependant on the grinding wheel shape and the feed per step. The surface profile obtained was a function of a "static" geometric relationship of wheel and feed (based on equation 2.9.3) and a "dynamic" aspect based on the machine tool repositioning and repeatability. For higher material removal rates (semi finish and rough cuts), the surface profile "dynamic" aspects were of 5.5 μm amplitude. This followed observations that the machine dynamics were important to control the surface profile generated (Franse, 1991, Shore, 1995).

The subsurface damage depths were shown to be shallower using smaller grit size which validated previous observations (Inasaki, 1987, Namba and Abe, 1993). In Zerodur, the subsurface damage depths were lower than ULE as the fracture toughness was higher in

Zerodur (Lawn and Evans, 1977). The direction of the lateral cracks was shown to be along the grinding wheel velocity direction.

The normal and tangential grinding forces generally increased with material removal rate for a given grinding wheel. It was reported that in SiC, the specific normal grinding forces increased with depth of cut (Inasaki, 1987) and decreased with higher grinding wheel speed (Ramesh, Yeo, Gowri and Zhou, 2001). In general, the grinding forces recorded showed a decrease with increase in grit size. The same effect was previously reported (Namba et al., 1997).

The grinding energy levels obtained during rough grinding on SiC, confirmed that the chosen value (30 J/mm^3) to specify the BoX grinding spindle was adequate. The specific energies required for grinding ULE and Zerodur are comparably less. Hwang and Malkin (1999) reported using a resin bond diamond grinding wheel, specific energies of 10-40 J/mm^3 and 5-10 J/mm^3 for SiC and soda lime respectively. The specific energy levels, in this research, were 25 J/mm^3 for SiC and 4 J/mm^3 for ULE and Zerodur for the rough grinding conditions.

The wheel wear tests results showed that the normal grinding forces and grinding power increase with the quantity of material removed. This increase was particularly important in SiC and required a dressing after 26.5 minutes to keep the normal grinding force below 100 N during finish cut (D46). Also during rough cut (D76) on SiC, in order to maintain a grinding power below 10 kW, the grinding wheel needed to be dressed every two minutes to maintain the 187.5 mm^3/s removal rate.

The G ratios obtained for the tested grinding wheels showed that the proposed resin bond type were adequate for grinding ULE and Zerodur. In SiC, the G ratio measured were of the same order of magnitude as reported in SiC by Inasaki (1987) for D46 and D126 resin bonded diamond grinding wheels.

The proposed three stage grinding process was supported as being adequate to achieve project demands. The normal grinding forces and spindle power during the rough cut were reduced using a larger grit size. The surface roughness, subsurface damage and form accuracy, induced by the rough cut, were within the depth of cut of the semi finish cut. Similar observations were made between the semi finish cut and the finish cut. For the finish grinding conditions, the surface roughness and subsurface damage depth were improved using a smaller grit size. The surface roughness values met the target (< 150 nm R_a) for the three materials. The surface profile (P_t) amplitudes were 2 μm on the three materials and the subsurface damage depths were below 10 μm for Zerodur and ULE.

9.3 BoX based test programme

The surface roughness (R_a) results showed generally lower values than the Edgetek grinding machine. A higher number of active grits within the larger contact area contributed towards the improved surface roughness values.

The subsurface damage depths, cluster and single last fracture depths were shallower using the BoX grinding machine. The subsurface depth target (< 5 μm) was achieved in Zerodur using the D25 grinding wheel. The single last fracture depth was shallower in Zerodur than in ULE. In general the cluster depth was lower for the BoX grinding machine than the Edgetek grinding machine. For the case of the finer grit grinding wheel D25, ULE seemed to be less responsive to the machine dynamics. A similar effect was observed for the rough grinding conditions in ULE. Those two particular cases are explained in detail in section 9.5.

The surface profile (P_t) amplitude was 2 μm for the finish grinding conditions. The repeatability between the "cusping" was due to machine "dynamic" errors (Franse, 1991, Shore, 1995). This effect led to surface profile values higher than the 1 μm P_t target. For the semi finish and rough cuts, the surface profile amplitude was 4 μm from the calculated surface profile. This difference was also due to the machine "dynamic" errors. Another source of error was the divergence between the expected and actual grinding wheel radius of curvature values used to calculate the surface profile.

The grinding forces for higher material removal rates showed an increase compared to the Edgetek grinding machine. These higher forces were attributed principally to the grinding machine stiffness as high "actual" depth of cut was maintained using a stiff machine (Corbett et al., 2002, Yang et al., 2001). Larger friction coefficients were observed compared to the Edgetek grinding machine. A larger number of grits and higher grinding machine stiffness partly explained those results. The cutting efficiency of the grinding wheel and the grinding wheel wear leading to dull grits and pulled out grits increased the friction coefficient (Inasaki, 1989).

The grinding power levels on ULE, Zerodur and SiC were adequate for semi finish and finish cuts. When grinding SiC using the BoX grinding machine, the rough cut was however limited to 112.5 mm^3/s. The maximum depth of cut achievable on SiC for the rough grinding conditions was 300 μm.

The grinding energies obtained on ULE and Zerodur were relatively lower than SiC and compare well with Hwang and Malkin (1999) work. For SiC, higher specific grinding

energies were obtained than found using the Edgetek grinding machine. The reason for a higher specific grinding energy was partially due to the actual depth of cut, the cutting efficiency of the grinding wheel and the grinding wheel wear effect.

The proposed three stage process was validated on the BoX grinding machine. The surface roughness and subsurface damage obtained for the three stage grinding process were improved using the BoX grinding machine. The surface profile (P_t) remained similar for the finish grinding condition. The surface roughness target was obtained on ULE and SiC. The subsurface damage target was achieved in Zerodur. The experiments showed that each stage provided an adequate input quality for the subsequent finer stage. The processing target time of 10 hours was confirmed as being credible.

9.4 BoX large scale surface experiments

A depth of 1 mm of material was removed in less than 10 hours over a 1 m Zerodur across corner hexagonal part. This was achieved using a maximum material removal rate of 187.5 mm^3/s, approximately 6.5 times and 37 times higher than the reported levels for LOG and OAGM machine tools respectively (Parks et al., 1985, Leadbeater et al., 1989). This maximum material removal rate (Q_w) was also achieved on the 400 mm ULE square part. On SiC, the semi finish (Q_w = 40 mm^3/s) and finish cuts (Q_w = 1.87 mm^3/s) using the D46 grinding wheel were obtained on the 400 mm across corner hexagonal part.

The resin bonded diamond grinding wheels selected were adequate for this grinding process. No intermediate dressing was used during any grinding cut and no bond burning was observed. The maximum amount of material removed between dresses was 20 cm^3, 80 cm^3, 325 cm^3 for SiC, ULE and Zerodur respectively.

The surface roughness measured on SiC and ULE, achieved the project target with R_a below 152 nm. No edge damage was observed even on non chamfered edges during the grinding process for the three materials. This highlights the importance of a grinding machine with smooth contactless motions.

The form accuracy obtained on the large scale surfaces were of the same order of magnitude as the levels reported for the LOG and OAGM machine tools (Parks et al., 1985, Shore and Walker, 2004). Interestingly, this form accuracy was achieved without error compensation strategy as used on the OAGM machine tool. Some form errors observed on the three large scale parts were due to the holding fixture, the substrate thickness and the grinding machine. As measured during the Edgetek test part programme, the grinding wheel wears linearly and contributes to the large scale surface form error. Those results

showed the use of the in situ separate metrology frame was required (Wills-Moren and Wilson, 1989, Donaldson and Patterson, 1983). The implementation of error compensations strategies would be necessary (Ferreira and Liu, 1986, Weck et al., 1995, Sartori and Zhang, 1995) to obtain the form (P_t) accuracy target of 1 μm (P-V).

9.5 Subsurface distribution and machine performance influence

The hypothesis behind this research was that the levels of subsurface damage were highly associated with the machine tool stiffness and the motion dynamics. A main contribution of this work has been to show that the machine tool stiffness has indeed an effect on the level of induced subsurface damage. The subsurface damage depths were lower using the stiffer and smoother motion BoX grinding machine.

The distribution of the subsurface damage showed two distinct subsurface damage zones identified as cluster depth and last fracture depth (Hed and Edwards, 1987*a*). The number of cracks per mm^2 decreased rapidly until a depth identified as $sd_{process}$ or cluster depth. An exponential curve was followed for all grinding conditions and on the two grinding machines. The number of cracks per mm^2 decreased until the maximum subsurface damage depth. This area corresponded to the machine dynamics related zone. A second exponential curve trend was obtained which was different for all the grinding conditions.

The cluster depths were shallower using the BoX grinding machine. The grinding machine motion smoothness influenced the lateral cracks. The cluster depth was shown to be process related and was influenced by the increase of the grinding wheel grit size (Inasaki, 1987, Namba and Abe, 1993) for both materials. The cluster depth was made of lateral cracks as described in Lawn's work (Lawn and Wilshaw, 1975). Those lateral cracks lengths were generated along the grinding wheel velocity direction.

The single last fracture depths were in general shallower using the BoX grinding machine. The single last fracture depth corresponded to Hertzian crack (blunt grain) or median crack (sharp grain) length (Lawn et al., 1975, 1980). For the case of the rough cut (D76), ULE seemed to be less responsive to the machine dynamics. This is believed to be due to longer cracks, resulting from an easier propagation in ULE due to the fracture toughness (Lawn and Evans, 1977).

The results confirmed that the difference of subsurface damage development between different materials can be described using the brittleness and fracture toughness characteristics. The subsurface damage depths are deeper in ULE than Zerodur. A material with low brittleness value (ULE) requires a higher initial load to generate subsurface damage.

The fracture toughness controls the subsurface damage depth after an initial crack is obtained. A material with higher fracture toughness value (ULE) has deeper damage depth for a given load (Lawn and Evans, 1977).

Interactions between the normal grinding force per grit and the subsurface damage depths were observed. The static indentation load was proportional to the lateral crack depth and median cracks as shown in equations described by Lawn and Wilshaw (1975). For a given grinding force per grit, the Edgetek grinding machine induced larger subsurface damage depths. The smoothness of the grinding machine reduced the impact effect (Wiederhorn and Lawn, 1977) of the diamond grit on the substrate.

The results, in particular the rough cut (D76) in ULE, showed that for larger grit sizes, the median cracks are less responsive to the grinding machine stiffness. This effect was not seen for Zerodur, an interaction between the grit size and the substrate ground was highlighted.

The absolute value of the indentation load has to be treated carefully. The normal grinding force per grit calculated is lower than the minimum initial load, 2.37 N, required to develop an initial crack of 6.74 μm, based on equation 2.10.7 from Lawn and Evans (1977). Those equations were using dimensionless constant factors relative to the grain geometry. The number of grits per mm^2 involved in the subsurface damage loading were based on an even distribution leading to different absolute grain loading as previously observed, for example, by Miller et al. (2005).

An interaction between the grinding wheel wear on the cluster depth would be expected as dull grits and pulled out grits would lead to higher grinding force per grit. The effect of the sliding motion between the diamond grits and the substrate were investigated. The penetration angle of the diamond grit variation leads to deeper subsurface damage cracks. The "trailing" effect due to the grinding friction coefficient was calculated to be negligible for this research.

The finish cut (D25) in ULE showed shallow subsurface damage depth less responsive to the grinding machine stiffness. Previous works showed that the grinding machine stiffness was important to obtain a controlled process (Wills-Moren et al., 1990, Ball et al., 1991). Other important parameters were controlled to obtain a minimal subsurface ductile grinding mode (Bifano et al., 1991). Small grain sizes with a controlled minimum depth of cut generated ductile grinding mode. This grinding mode was showed to be substrate material related (Shore et al., 1995).

10. CONCLUSIONS AND SUGGESTIONS FOR FURTHER WORKS

Conclusions and contributions to knowledge from this research are drawn in this chapter. Recommendations for further works are also proposed.

10.1 Summary of conclusions

This research established a significant advance in precision grinding of large freeform optics. The grinding process was optimized through a series of small scale grinding experiments. Screening experiments validated expected grinding process parameters influence on surface responses reported in the literature. The Edgetek based test programme showed that a proposed three stage grinding process, rough, semi finish and finish cuts, achieves a high material removal rate with low form error. The grinding wheel wear experiments showed that resin bonded diamond grinding wheels are adequate for grinding a large quantity of material. The BoX based test programme validated the grinding process developed. Improvement of the surface responses quality and subsurface damage depths was demonstrated using a grinding machine with higher static stiffness and smoother dynamics motions. Large scale part experiments on 400 mm to 1 m optical parts, showed scalability of the grinding process on large spherical parts.

10.2 Summary of contributions

The contributions to knowledge of this research are:

1. A stiff grinding machine, BoX, with smooth axis motions, induced lower cluster depths and shallower single last fracture depths in glass (ULE) and glass ceramics (Zerodur) confirming the research hypothesis. The results disproved that lower grinding machine stiffness led to lower subsurface damage as the normal grinding force per grit decreased as described by Yang et al. (2001). More aggressive grinding parameters, in particular coarser grit size in ULE, left deeper cracks which reduced the importance of the machine dynamics related damage in rough grinding.

2. The cluster depth was related to the grinding machine stiffness. Based on Lawn's fracture mechanisms equations, using the normal grinding force per grit, the cluster

depth was identified to be related to the lateral crack depth. Lateral cracks were observed to be shortened with a smaller grit size. Those cracks were generated along the grinding wheel velocity direction. These results disproved the relation between the cluster depth and the surface roughness (R_a & R_t) (Hed and Edwards, 1987*a*, Lambropoulos et al., 1999, Randi et al., 2005).

3. The subsurface damage was identified to be proportional to Hertzian crack for dull grits. The single last fracture depth was associated with the grinding machine stiffness. Subsurface damage in ULE was less susceptible to crack due to the material low brittleness. The last fracture depths measured were shallower in Zerodur than in ULE due to a higher fracture toughness impeding crack damage propagation.

4. A wedge polishing technique was developed to observe the subsurface damage beneath the surface without inducing significant surface damage. This technique observed subsurface damage depths for material removal rate between 0.3 mm^3/s and 187.5 mm^3/s. This technique required only one polishing operation to measure as deep as 70 μm below the ground surface. Etching was required to reveal subsurface damage cracks. Counting the number of defects was proven to give important results in understanding the subsurface damage distribution and a good alternative to the obscuration observation method (Menapace et al., 2005*a*).

5. Resin bonded grinding wheels were used successfully for an effective grinding of ULE and Zerodur without intermediate dressing. A limited increase in grinding forces and a linear wheel wear trend were obtained on a 1 m scale surface. For SiC, resin bonded grinding wheels had to be carefully used especially at high material removal rates (112.5 mm^3/s). The increase in grinding forces and grinding power showed that intermediate dressing would be required when grinding large optical parts.

6. The surface profile (P_t) generated by the selected grinding mode is controlled by the grinding wheel radius of curvature and the feed rate per revolution. The surface profile can be estimated using an equation employed in diamond turning. For low feed rate, the grinding machine repeatability and the grinding process stability govern the surface profile.

7. An efficient three step grinding process was developed for ULE, Zerodur and SiC. The grinding of a one metre part in 10 hours to remove 1 mm of material was achieved on Zerodur and would be obtainable for ULE. For SiC, a lower amount of material was removed in such grinding process time due to the BoX grinding spindle power limit.

10.3 Further works suggestions

Further works proposed based on conclusions drawn from this project are:

1. The development of an effective subsurface damage assessment technique for SiC would be beneficial. The contribution of grinding process and grinding machine properties on the induced cluster and single last fracture depth ought to be studied. The correlation with the observation made for ULE and Zerodur would be significant in understanding interactions between machine and workpiece material properties.

2. The development of an automatic large surface etching and observation technique would be beneficial for finding the single last fracture depth for large laser fusion optics. This development would correspond to an improvement of the subsurface damage assessment technique over the relatively small samples within this research. In this research, the assessment area relied on a repetitive and stable grinding process.

3. The development of an analytical model correlating the results of this research in respect of the grinding machine stiffness, the cluster depth and the single last fracture depth should be undertaken. Dedicated experiments would be required for deeper understanding of the interaction between the cluster depth and the single last fracture depth.

4. To obtain the final surface profile form accuracy (1 μm P-V), finalisation of the work to establish the in-situ metrology frame on the BoX grinding machine would be needed. It was not commissioned at the time of this research. Error compensation techniques for the grinding machine errors and grinding wheel wear based on that capability ought to be carried out.

5. This research highlighted interactions between the grinding wheel grit sizes and the grinding machines that influenced the grinding process responses. Dedicated experiments would be required for deeper understanding of those interactions on the grinding forces and friction coefficient.

REFERENCES

Agarwal, S. and Venkateswara Rao, P. (2005), 'A probabilistic approach to predict surface roughness in ceramic grinding', *International Journal of Machine Tools & Manufacture* **45**(6), 609–616.

Agarwal, S. and Venkateswara Rao, P. (2008), 'Experimental investigation of surface/subsurface damage formation and material removal mechanisms in SiC grinding', *International Journal of Machine Tools & Manufacture* **48**(6), 698–710.

Ali, Y. M. and Zhang, L. C. (1999), 'Surface roughness prediction of ground components using a fuzzy logic approach', *Journal of Materials Processing Technology* **89-90**, 561–568.

AMEC Dynamic Structures Ltd. (2002), Design development of a 20 m segmented mirror with lightweighted silicon carbide segments, Technical report, Herzberg Institute for Astrophysics.

Andersen, T., Ardeberg, A. and Owner-Petersen, M. (2003), Euro50: Design study of a 50 m adaptive optics telescope, Technical report, Lund University, Sweden.

Argon, A. S. (1959), 'Distribution of cracks on glass surfaces', *Royal Society of London Proceedings Series A* **250**, 482–492.

Arrasmith, S. R., Jacobs, S. D., Lambropoulos, J. C., Maltsev, A., Golini, D. and Kordonski, W. I. (2001), The use of Magnetorheological Finishing (MRF) to relieve residual stress and subsurface damage on lapped semiconductor silicon wafers, *in* 'Proceedings of the SPIE', Vol. 4451, pp. 286–294.

Ball, M. J., Murphy, N. A. and Shore, P. (1991), Electrolytically assisted "ductile" mode diamond grinding of BK7 and SF10 optical glasses, *in* 'Proceedings of the SPIE', Vol. 1573, pp. 30–38.

Belforte, G., Bona, G., Canuto, E., Donati, F., Ferraris, F., Gorini, I., Morei, S., Peisino, M. and Sartori, S. (1987), 'Coordinate measuring machines and machine tools self-calibration and error correction', *CIRP annals* **36**(1), 359–364.

Bibeau, C., Wegner, P. J., Moses, E. I. . and Warner, B. E. (2006), 'Generating powerful ultraviolet beams with the world´s largest laser', *Laser Focus World* **42**(6), 113–117.

Bifano, T. G., Dow, T. A. and Scattergood, R. O. (1991), 'Ductile-regime grinding : a new technology for machining brittle materials', *Journal of Engineering for Industry* **113**(2), 184–189.

Boland, R. J. (1999), Computer control and process monitoring of electrolytic in-process dressing of metal bond fine diamond wheels for NIF optics, *in* 'Proceedings of the SPIE', Vol. 3782, pp. 61–71.

Bougoin, M. and Deny, P. (2004), The SiC technology is ready for the next generation of extremely large telescopes, *in* 'Proceedings of the SPIE', Vol. 5494, pp. 9–18.

Brinksmeier, E. (1989), 'State-of-the-art of non-destructive measurement of sub-surface material properties and damages', *Precision Engineering* **11**(4), 211–224.

Brinksmeier, E., Heinzel, C. and Wittmann, M. (1999), 'Friction, cooling and lubrication in grinding', *CIRP annals* **48**(2), 581–598.

Brinksmeier, E. and Minke, E. (1993), 'High-Performance Surface Grinding - The influence of coolant on the abrasive process', *CIRP annals* **42**(1), 367–370.

Bryan, J. (1979), 'Design and construction of an 84 inches diamond turning machine', *Precision Engineering* **1**(1), 13–17.

Bryan, J. (1990), 'International status of thermal error research', *CIRP annals* **39**(1), 645–656.

Bryan, J. B. (1984), The power of deterministic thinking in machine tool accuracy, *in* 'First International Machine Tool Engineers Conference, Tokyo, Japan', pp. 1–16.

Bryant, J. (1998), 'Which diamond grinding wheel ?', *Manufacturing Engineering* **120**(3), 3.

Campbell, J. H., Hawley-Fedder, R. A., Stolz, C. J., Menapace, J. A., Borden, M. R., Whitman, P. K., Yu, J., Runkel, M. J., Riley, M. O., Feit, M. D. and Hackel, R. P. (2004), NIF optical materials and fabrication technologies: an overview, *in* 'Proceedings of the SPIE', Vol. 5341, pp. 84–101.

CEA (2007), 'http://www-lmj.cea.fr - Accessed 11/07'.
URL: *http://www-lmj.cea.fr*

Chen, W. K., Huang, H. and Yin, L. (2005), 'Loose abrasive truing and dressing of resin bond diamond cup wheels for grinding fibre optic connectors', *Journal of Materials Processing Technology* **159**(2), 229–239.

Chen, X. and Rowe, W. B. (1996), 'Analysis and simulation of the grinding process. Part I : Generation of the grinding wheel surface', *International Journal of Machine Tools & Manufacture* **36**(8), 871–882.

Cheung, C. F. and Lee, W. B. (2000), 'Modelling and simulation of surface topography in ultra-Precision Diamond Turning', *Proceedings of the I MECH E Part B Journal of Engineering Manufacture* **214**(6), 463–480.

CIRP (1978), 'A proposal for defining and specifying the dimensional Uncertainty of Multi-Axis Measuring Machines', *CIRP annals* **27**(2), 623–630.

Cook, R. F. and Pharr, G. M. (1990), 'Direct observation and analysis of indentation cracking in glasses and ceramics', *Journal of the American Ceramic Society* **73**(4), 787–817.

Corbett, J., McKeown, P. A., Peggs, G. N. and Whatmore, R. (2000), 'Nanotechnology: International developments and emerging products', *CIRP annals* **49**(2), 523–545.

Corbett, J., Morantz, P., Stephenson, D. J. and Read, R. F. (2002), 'An advanced ultra-precision face grinding machine', *International Journal of Advanced Manufacturing Technology* **20**, 639–648.

Court, T. and Von Rohr, M. (1929), 'A history of the development of the telescope from about 1675 to 1830 based on documents in the court collection', *Transactions of the Optical Society* **30**(5), 207–260.

Crabtree, D., Roberts, S., Carlberg, R. and Halliday, D. (2003), Canadian efforts towards a future large telescope, *in* 'Proceedings of the IAU meeting', Vol. 8.

Cranfield Precision Engineering Centre (2005), Precision engineering, *in* 'Industrial short course at Cranfield University'.

Dai, Y., Ohmori, H., Watanabe, Y., Eto, H., Lin, W. and Suzuki, T. (2004), 'Subsurface properties of ceramics for lightweight mirrors after ELID grinding', *Jsme International Journal Series C* **47**, 66–71.

Derkx, J., Hoogstrate, A., Saurwalt, J. and Karpuschewski, B. (2008), 'Form crush dressing of diamond grinding wheels', *CIRP annals* **57**(1), 349–352.

Dierickx, P. (2000), Optical fabrication in the large, *in* 'Proceedings of the SPIE', Vol. 5382, pp. 224–236.

Dierickx, P., Brunetto, E. T., Comeron, F., Gilmozzi, R., Gonté, F. Y. J., Koch, F., le Louarn, M., Monnet, G. J., Spyromilio, J., Surdej, I., Verinaud, C. and Yaitskova, N. (2004), OWL phase - A status report, *in* 'Proceedings of the SPIE', Vol. 5489, pp. 391–406.

Donaldson, R. R. (1980), 'Error budgets', *Technology of Machine Tools* **5**, 1–14.

Donaldson, R. R. and Patterson, S. R. (1983), Design and construction of a large, vertical-axis diamond turning machine, *in* 'Proceedings of the SPIE', Vol. 433, pp. 62–67.

Donmez, A., Blomquist, D. S., Hocken, R. J., Liu, C. R. and Barash, M. M. (1986), 'A general methodology for machine tool accuracy enhancement by error compensation', *Precision Engineering* **8**(4), 187–196.

Ealcy, M. A. (2003), Large optics in the 21st century: a transition from discrete manufacturing to highly integrated techniques, *in* 'Proceedings of IEEE Aerospace Conference', Vol. 4, pp. 1705–1716.

Eman, K. F., Wu, B. T. and DeVries, M. F. (1987), 'A generalized geometric error model for multi-axis machines', *CIRP annals* **36**(1), 253–256.

Enard, D., Noethe, L., Alvarez, P., Atad, E., Andersen, T., Castro, J., Goncharov, A., Iye, M., Korhonen, T., Lemaitre, G., Salinari, P., Brunetto, E., Delabre, B., Dierickx, P., Dimmler, M., Koch, F., Schneerman, M., Spyromilio, J., Swat, A. and Tamai, R. (2006), ELT Telescope design working group report - Issue 3, Technical report, Working Group on telescope design (WG4).

Enard, D. and Swings, J. P. (1983), 'The Very Large Telescope project', *Messenger* **34**, 1–3.

Estler, W. T. (1985), 'Calibration and use of optical straightedges in the metrology of precision machines', *Optical Engineering* **24**(3), 372–379.

Evans, B. M., Miller, A. C. and Egert, C. M. (1997), Comparison of materials for use in the precision grinding of optical components, *in* 'Proceedings of the SPIE', Vol. 3134, pp. 190–197.

Fan, K. C., Lee, M. Z. and Mou, J. I. (2002), 'On-line non-contact system for grinding wheel wear measurement', *International Journal of Advanced Manufacturing Technology* **19**, 14–22.

Fay, B. (2002), 'Advanced optical lithography development, from UV to EUV', *Microelectronic Engineering* **61-62**, 11–24.

Feinberg, L. D. (2005), NASA capabilities roadmap: advanced telescopes and observatories, *in* 'Proceedings of the SPIE', Vol. 5899, p. 589906.

Ferreira, P. and Liu, C.R.and Merchant, E. (1986), 'A contribution to the analysis and compensation of the geometric error of a machining center', *CIRP annals* **35**(1), 259–262.

Foss, C. A. J. (2005), CVC Silicon carbide optical properties and systems, *in* 'Proceedings of the SPIE', Vol. 5868, pp. 42–50.

Franse, J. (1990), 'Manufacturing techniques for complex shapes with submicron accuracy', *Reports on Progress in Physics* **53**(8), 1049–1094.

Franse, J. (1991), Aspects of precision grinding, PhD thesis, Technische Universiteit Eindhoven.

Franse, J., Roblee, W. and Modemann, K. (1991), 'Dynamic characteristics of the Lawrence Livermore National Laboratory Precision Engineering Research Lathe', *Precision Engineering* **13**(3), 196–202.

Furutani, K., Nguyen, T. H., Ohguro, N. and Nakamura, T. (2003), 'Automatic compensation for grinding wheel wear by pressure based in-process measurement in wet grinding', *Precision Engineering* **27**(1), 9–13.

Galen, E. (2001), 'Superabrasive grinding: why bond selection matters', *Manufacturing Engineering* **126**(2), 1–5.

Gashi, B. and Shore, P. (2006), Thermal analysis of joint interfaces in machine tools, *in* '6th Euspen International Conference', Vol. 1, pp. 269–272.

Geyl, R. and Cayrel, M. (1999), REOSC contribution to VLT and Gemini, *in* 'Proceedings of the SPIE', Vol. 3739, pp. 40–46.

Gilmozzi, R. (2004), Science and technology drivers for future giant telescopes, *in* 'Proceedings of the SPIE', Vol. 5489, pp. 1–10.

Gilmozzi, R. and Dierickx, P. (2000), 'OWL concept study', *ESO Messenger* **100**, 1–10.

Gilmozzi, R. and Spyromilio, J. (2007), 'The European Extremely Large Telescope (E-ELT)', *ESO Messenger* **127**, 11–19.

Goch, G., Schmitz, B., Karpuschewski, B., Geerkens, J., Reigl, M., Sprongl, P. and Ritter, R. (1999), 'Review of non-destructive measuring methods for the assessment of surface integrity: a survey of new measuring methods for coatings, layered structures and processed surfaces', *Precision Engineering* **23**(1), 9–33.

Gopal, A. V. and Rao, P. V. (2004), 'A new chip-thickness model for performance assessment of silicon carbide grinding', *International Journal of Advanced Manufacturing Technology* **24**(11-12), 816–820.

Guss, G. M., Bass, I. L., Hackel, R. P., Mailhiot, C. and Demos, S. G. (2008), 'In situ monitoring of surface postprocessing in large aperture fused silica optics with optical coherence tomography', *Applied optics* **47**(25), 4569–4573.

Hale, L. C. (1999), Principles and techniques for design of precision machines, PhD thesis, Massachusetts Institute of Technology.

Hamilton, C. T., Hrdina, K. and Kenney, S. (2004), CTE in ULE glass, *in* '2nd International Workshop on EUV Lithography', pp. 1–14.

Hassui, A., Diniz, A., Oliveira, J., Felipe, J. and Gomes, J. (1998), 'Experimental evaluation on grinding wheel wear through vibration and acoustic emission', *Wear* **217**, 7–14.

Hed, P. P. and Edwards, D. F. (1987*a*), 'Optical glass fabrication technology 2: Relationship between surface roughness and subsurface damage', *Applied optics* **26**(21), 4677–4680.

Hed, P. P. and Edwards, D. F. (1987*b*), 'Relationship between subsurface damage depth and surface roughness during grinding of optical glass with diamond tools', *Applied optics* **26**(13), 2491–2491.

Hed, P. P., Edwards, D. F. and Davis, J. B. (1988), Subsurface damage in optical materials: origin, measurement and removal (summary), *in* 'Proceedings of the SPIE', pp. 99–125.

Heinzel, C., Grimme, D. and Moisan, A. (2006), 'Modeling of surface generation in contour grinding of optical molds', *CIRP annals* **55**(1), 581–584.

Hill, J. M. and Salinari, P. (1998), The Large Binocular Telescope project, *in* 'Proceedings of the SPIE', Vol. 3352, pp. 23–33.

Hocken, R., Simpson, J., Borchardt, B., Lazar, J. and Stein, P. (1977), 'Three dimensional metrology', *CIRP annals* **26**(1), 403–408.

Hosokawa, A., Ueda, T. and Yunoki, T. (2006), 'Laser dressing of metal bonded diamond wheel', *CIRP annals* **55**(1), 329–332.

Huang, H. and Liu, Y. C. (2003), 'Experimental investigations of machining characteristics and removal mechanisms of advanced ceramics in high speed deep grinding', *International Journal of Machine Tools & Manufacture* **43**(8), 811–823.

Huang, H., Yin, L. and Zhou, L. (2003), 'High speed grinding of silicon nitride with resin bond diamond wheels', *Journal of Materials Processing Technology* **141**(3), 329–336.

Hwang, T. W., Evans, C. J. and Malkin, S. (1999), 'Size effect for specific energy in grinding of silicon nitride', *Wear* **225**, 862–867.

Hwang, T. W. and Malkin, S. (1999), 'Upper bound analysis for specific energy in grinding of ceramics', *Wear* **231**(2), 161–171.

Inasaki, I. (1987), 'Grinding of hard and brittle materials', *CIRP annals* **36**(2), 463–471.

Inasaki, I. (1988), 'Speed stroke grinding of advanced ceramics', *CIRP annals* **37**(1), 299–302.

Inasaki, I. (1989), 'Dressing of resinoid bonded diamond grinding wheels', *CIRP annals* **38**(1), 315–318.

Inasaki, I. and Nakayama, K. (1986), 'High-efficiency grinding of advanced ceramics', *CIRP annals* **35**(1), 211–214.

Irani, R., Bauer, R. and Warkentin, A. (2005), 'A review of cutting fluid application in the grinding process', *International Journal of Machine Tools & Manufacture* **45**(15), 1696–1705.

ISO 4287:2000 (2000), *Geometrical product specification (GPS) – Surface texture: Profile method – Terms, definitions and surface texture parameters*, ISO, Geneva, Switzerland.

ISO 4288:1998 (1998), *Geometrical product specifications (GPS) – Surface texture – Profile method: Rules and procedures for the assessment of surface texture*, ISO, Geneva, Switzerland.

ISO 6104:2005 (2005), *Superabrasive products – General survey, designation and multilingual nomenclature*, ISO, Geneva, Switzerland.

ISO 6106:2005 (2005), *Abrasive products – Checking the grit size of superabrasives*, ISO, Geneva, Switzerland.

Itoh, N., Katoh, T. and Ohmori, H. (2004), 'Eco-friendly ELID grinding using metal-free electro-conductive resinoid bonded wheel', *Jsme International Journal Series C* **47**(1), 72–78.

Jackson, M. J. (2004), 'Fracture dominated wear of sharp abrasive grains and grinding wheels', *Proceedings of the I MECH E Part J Journal of Engineering Tribology* **218**(3), 225–235.

Jackson, M., Khangar, A., Chen, X., Robinson, G., Venkatesh, V. and Dahotre, N. (2007), 'Laser cleaning and dressing of vitrified grinding wheels', *Journal of Materials Processing Technology* **185**(1-3), 17–23.

Kanematsu, W. (2006), 'Visualization of subsurface damage in silicon nitride from grinding by a plasma etching and dye impregnation method', *Journal of the American Ceramic Society* **89**(8), 2564–2570.

Kemp, K. and Wurm, S. (2006), 'EUV lithography', *Comptes Rendus Physique* **7**, 875–886.

Kitajima, K., Cai, G. Q., Kumagai, N., Tanaka, Y. and Zheng, H. W. (1992), 'Study on mechanism of ceramics grinding', *CIRP annals* **41**(1), 367–371.

Klocke, F., Baus, A. and Beck, T. (2000), 'Coolant induced forces in CBN high speed grinding with shoe nozzles', *CIRP annals* **49**(1), 241–244.

Koenigsberger, F. and Tlusty, J. (1971), *Structure of Machine Tools*, Pergamon Press.

Kompella, S., Farris, T. N. and Chandrasekar, S. (2001), 'Techniques for rapid characterization of grinding wheel-workpiece combinations', *Proceedings of the I MECH E Part B. Journal of engineering manufacture* **215**(10), 1385–1395.

Krodel, M. R. (2006), Cesic for extremely large telescopes, *in* 'Proceedings of the SPIE', Vol. 6273, p. 627303.

Kuriyagawa, T., Syoji, K. and Zhou, L. (1993), 'Precision form truing and dressing for aspheric ceramics mirror grinding', *NIST Special Publication* **847**(6), 325–331.

Kuriyagawa, T., Zahmaty, M. S. S. and Syoji, K. (1996), 'A new grinding method for aspheric ceramic mirrors', *Journal of Materials Processing Technology* **62**(4), 387–392.

Lambropoulos, J. C. (2000), 'From abrasive size to subsurface damage in grinding', *Optical Fabrication & Testing, OSA Technical Digest* **8**, 17–18.

Lambropoulos, J. C., Li, Y., Funkenbusch, P. D. and Ruckman, J. L. (1999), Non contact estimate of grinding-induced subsurface damage, *in* 'Proceedings of the SPIE', Vol. 3782, pp. 41–50.

Lambropoulos, J. C., Xu, S., Fang, T. and Golini, D. (1996), 'Twyman effect mechanics in grinding and microgrinding', *Applied optics* **35**(28), 5704–5713.

Lawn, B. R. (1985), *Indentation: deformation and fracture processes*, Plenum, New York, chapter Strength of inorganic glass, pp. 67–86.

Lawn, B. R. and Evans, A. G. (1977), 'A model for crack initiation in elastic/plastic indentation fields', *Journal of Materials Science* **12**, 2195–2199.

Lawn, B. R., Evans, A. G. and Marshall, D. B. (1980), 'Elastic / plastic indentation damage in ceramics: the median / radial crack system', *Journal of the American Ceramic Society* **63**(9-10), 574–581.

Lawn, B. R., Fuller, E. R. and Wiederhorn, S. M. (1976), 'Strength degradation of brittle surfaces: Sharp indenters', *Journal of the American Ceramic Society* **58**(5-6), 193–197.

Lawn, B. R., Wiederhorn, S. M. and Johnson, H. H. (1975), 'Strength degradation of brittle surfaces: Blunt indenters', *Journal of the American Ceramic Society* **58**(9-10), 428–432.

Lawn, B. R., Wiederhorn, S. M. and Roberts, D. E. (1984), 'Effect of sliding friction forces on the strength of brittle materials', *Journal of the Materials Science* **19**, 2561–2569.

Lawn, B. R. and Wilshaw, T. R. (1975), *Fracture of brittle solids*, Cambridge university press.

Leadbeater, P. B., Clarke, M., Wills-Moren, W. J. and Wilson, T. J. (1989), 'A unique machine for grinding large off-axis optical components: the OAGM 2500', *Precision Engineering* **11**(4), 191–196.

Löfken, J. O. (2008), 'Pushing the limits with Extreme Ultraviolet Light', *Innovation* **20**, 30–33.

Li, K. and Liao, T. W. (1996), 'Surface/subsurface damage and the fracture strength of ground ceramics', *Journal of Materials Processing Technology* **57**(3-4), 207–220.

Li, K. and Liao, T. W. (1997), 'Modelling of ceramic grinding processes Part I. Number of cutting points and grinding forces per grit', *Journal of Materials Processing Technology* **65**(1-3), 1–10.

Li, S., Wang, Z. and Wu, Y. (2008), 'Relationship between subsurface damage and surface roughness of optical materials in grinding and lapping processes', *Journal of Materials Processing Technology* **205**, 34–41.

Li, Y., Funkenbusch, P. D., Gracewski, S. M. and Ruckman, J. (2004), 'Tool wear and profile development in contour grinding of optical components', *International Journal of Machine Tools & Manufacture* **44**(4), 427–438.

Liang, S. X. and Devereux, O. F. (1993), Grinding of ceramic materials: a model for energy consumption and force transformation, *in* 'Proceedings of Machining of Advanced Materials', pp. 21–32.

Lin, S. Y., Fang, Y. C. and Huang, C. W. (2008), 'Improvement strategy for machine tool vibration induced from the movement of a counterweight during machining process', *International Journal of Machine Tools & Manufacture* **48**(7-8), 870–877.

Lindsay, R. P. (1983), 'The effect of wheel wear rate on the grinding performance of three wheel grades', *CIRP annals* **32**(1), 247–249.

LLE (1997), 'Subsurface damage in microgrinding optical glasses', *Laboratory for Laser Energetics Review* **73**, 45–49.

Lodha, G. S., Yamashita, K., Kunieda, H., Tawara, Y., Jin, Y., Namba, Y. and Bennett, J. M. (1998), 'Effect of surface roughness and subsurface damage on grazing-incidence x-ray scattering and specular reflectance', *Applied optics* **37**(22), 5239–5252.

Lucca, D. A., Brinksmeier, E. and Goch, G. (1998), 'Progress in assessing surface and subsurface integrity', *CIRP annals* **47**(2), 669–693.

Maksoud, T. M. A., Mokbel, A. A. and Morgan, J. E. (1999), 'Evaluation of surface and sub-surface cracks of ground ceramic', *Journal of Materials Processing Technology* **88**, 222–243.

Malkin, S. (1968), The attritious and fracture wear of grinding wheels, Scd thesis, Massachusetts Institute of Technology.

Malkin, S. (1989), *Grinding Technology: Theory and Application of Machining with Abrasives*, Reprinted by SME.

Malkin, S. and Hwang, T. W. (1996), 'Grinding mechanisms for ceramics', *CIRP annals* **45**(2), 569–580.

Marinescu, I. D., Rowe, B. W., Dimitrov, B. and Inasaki, I. (2004*a*), *Tribology of abrasive machining processes*, William Andrew, Inc., chapter Fluid Delivery, pp. 265–296.

Marinescu, I. D., Rowe, B. W., Dimitrov, B. and Inasaki, I. (2004*b*), *Tribology of abrasive machining processes*, William Andrew, Inc., chapter Forces, Friction and Energy, pp. 130–132.

Marshall, D. B., Lawn, B. R. and Evans, A. G. (1982), 'Elastic plastic indentation damage in ceramics the lateral crack system', *Journal of the American Ceramic Society* **65**(11), 561–566.

Martin, H. M., Allen, R. G., Burge, J. H., Dettmann, L. R., Ketelsen, D. A., Miller, III, S. M. and Sasian, J. M. (2003), Fabrication of mirrors for the Magellan Telescopes and the Large Binocular Telescope, *in* 'Proceedings of the SPIE', Vol. 4837, pp. 609–618.

Materials (2007), 'http://astron.berkeley.edu/ jrg/MATERIALS/ - Accessed 11/07'.
URL: *http://astron.berkeley.edu/ jrg/MATERIALS/*

Matson, L. (2003), CTE tailored materials for hybrid mirror systems, *in* 'SOMTC Technology days', Presented at the SOMTC Technology days.

Matsuo, T., Toyoura, S., Oshima, E. and Ohbuchi, Y. (1989), 'Effect of grain shape on cutting force in superabrasive single-grit tests', *CIRP annals* **38**(1), 323–326.

Mayer Jr., J. E. and Fang, G. P. (1994), 'Effect of grit depth of cut on strength of ground ceramics', *CIRP annals* **43**(1), 309–312.

Mayer Jr., J. E. and Fang, G. P. (1995), 'Effect of grinding parameters on surface finish of ground ceramics', *CIRP annals* **44**(1), 279–282.

McKeown, P. A. and Morgan, G. H. (1979), 'Epoxy granite: a structural material for precision machines', *Precision Engineering* **1**(4), 227–229.

Meiling, H., Banine, V., Kuerz, P. and Harned, N. (2004), Progress in the ASML EUV program, *in* 'Proceedings of the SPIE', Vol. 5374, pp. 31–42.

Menapace, J. A., Davis, P. J., Steele, W. A., Wong, L. L., Suratwala, T. I. and Miller, P. E. (2005*a*), MRF applications : measurement of process-dependent subsurface damage in optical materials using the MRF wedge technique, *in* 'Proceedings of the SPIE', Vol. 5991, pp. 599103.1–599103.11.

Menapace, J. A., Davis, P. J., Steele, W. A., Wong, L. L., Suratwala, T. I. and Miller, P. E. (2005*b*), Utilization of magnetorheological finishing as a diagnostic tool for investigating the three-dimensional structure of fractures in fused silica, *in* 'Proceedings of the SPIE', Vol. 5991, pp. 599102.1–599102.13.

Meneghello, R., Concheri, G., Savio, G. and Comelli, D. (2006), 'Surface and geometry error modeling in brittle mode grinding of ophthalmic lenses moulds', *International Journal of Machine Tools & Manufacture* **46**(12-13), 1662–1670.

Meyer, H. R. and Klocke, F. (2000), *Handbook of Ceramics Grinding and Polishing*, Noyes Publications, chapter Grinding tools, pp. 205–236.

Miller, P. E., Suratwala, T. I., Wong, L. L., Feit, M. D., Menapace, J. A., Davis, P. J. and Steele, R. A. (2005), The distribution of subsurface damage in fused silica (Invited Paper), *in* 'Proceedings of the SPIE', Vol. 5991, pp. 599101.1–599101.25.

Moore, G. E. (1965), 'Cramming more components onto integrated circuits', *Electronics* **38**, 114–117.

Morantz, P., Shore, P., Luo, X. and Baird, I. (2006), Control strategy of the Big Optix grinding machine, *in* 'Proceedings of the 6th Euspen International Conference'.

Mountain, M., Kurz, R. and Oschmann, J. (1994), Gemini 8m Telescopes project, *in* 'Proceedings of the SPIE', Vol. 2199, pp. 41–55.

Nakao, M. and Hatamura, Y. (1996), 'Development of an intelligent face grinding machine to fabricate ultraflat surfaces on thin, brittle substrates', *CIRP annals* **45**(1), 397–400.

Namba, Y. and Abe, M. (1993), 'Ultraprecision grinding of optical glasses to produce super smooth surfaces', *CIRP annals* **42**(1), 417–420.

Namba, Y., Shiokawa, M., Yu, J. and Ikawa, N. (1997), 'Surface roughness generation mechanism of ultraprecision grinding of optical materials with a cup-type resinoid-bonded diamond wheel', *CIRP annals* **46**(1), 253–256.

Namba, Y., Wada, R., Unno, K., Tsuboi, A. and Okamura, K. (1989), 'Ultra-precision surface grinder having a glass-ceramic spindle of zero-thermal expansion', *CIRP annals* **38**(1), 331–334.

Nelson, J. E. (2000), Design concepts for the California Extremely Large Telescope (CELT), *in* 'Proceedings of the SPIE', Vol. 4004, pp. 282–289.

Ohara (2008), 'Ultra-low expansion glass-ceramics clearceram-z', Booklet, www.oharacorp.com/pdf/CCZ.pdf.

Ohmori, H., Lin, W., Moriyasu, S. and Yamagata, Y. (2001), 'Microspherical lens fabrication by cup grinding wheels applying ELID grinding', *RIKEN Review - Advances on Micro-mechanical Fabrication Techniques* **34**, 3–5.

Ohmori, H. and Nakagawa, T. (1995), 'Analysis of mirror surface generation of hard and brittle materials by ELID (electronic in-process dressing) grinding with superfine grain metallic bond wheels', *CIRP annals* **44**(1), 287–290.

Onaka, T., Kaneda, H., Okuda, H., Murakami, H., Kohno, T., Miura, S., Yamashiro, R. and Sugiyama, Y. (1999), Development of lightweight silicon carbide mirror at cryogenic temperatures for infrared imaging surveyor, *in* 'Proceedings of Ultra lightweight space optics challenge workshop', Vol. 6666, pp. 666601–07.

Pannhorst, W. (2002), 'Low expansion glass ceramics - current developments', *Glastechn. Ber. Glass Sci. Technol.* **75**, 78–85.

Paret, V., Boher, P., Geyl, R., Vidal, B., Putero-Vuaroqueaux, M., Quesnel, E. and Robic, J. Y. (2002), 'Characterization of optics and masks for the EUV lithography', *Microelectronic Engineering* **61-62**, 145–155.

Parks, R. E. (2004), Two approaches to generating free-form optics, *in* 'Proceedings of ASPE 2004 Winter Topical Meeting', pp. 88–93.

Parks, R. E., Lam, P. and Kuhn, W. (1985), The Large Optical Generator - a progress report, *in* 'Proceedings of the SPIE', Vol. 542, p. 28.

Pfeiffer, W. and Hollstein, T. (1997), 'Influence of grinding parameters on strength-dominating near-surface characteristics of silicon nitride ceramics', *Journal of the European Society* **17**, 487–494.

Pileri, D. and Krabbendam, V. L. (1995), Hobby-Eberly primary mirror fabrication, *in* 'Proceedings of the SPIE', Vol. 2536, pp. 344–349.

Preston, F. W. (1922), 'The structure of abraded glass surfaces', *Transactions of the Optical Society* **23**(3), 141–164.

Preston, F. W. (1927), 'The theory and design of plate glass polishing machines', *Journal of the Society of Glass Technology* **11**, 214–256.

Puttick, K. E., Jeynes, C., Whitmore, L., Rudman, M. R., Yamasaka, M., Shore, P. and Gee, A. E. (1992), Surface damage in nanoground silicon, *in* 'Proceeding of IMECH - Tribology in metal cutting and grinding', pp. 49–51.

Ramesh, R., Mannan, M. A. and Poo, A. N. (2000), 'Error compensation in machine tools - a review Part I: geometric, cutting-force induced and fixture dependent errors', *International Journal of Machine Tools & Manufacture* **40**(9), 1235–1256.

Ramesh, R., Yeo, S. H., Gowri, S. and Zhou, L. (2001), 'Experimental evaluation of super high-speed grinding of advanced ceramics', *International Journal of Advanced Manufacturing Technology* **17**(2), 87–92.

Ramesh, R., Yeo, S. H., Zhong, Z. W. and Sim, K. C. (2001), 'Coolant shoe development for high efficiency grinding', *Journal of Materials Processing Technology* **114**, 240–245.

Randi, J. A., Lambropoulos, J. C. and Jacobs, S. D. (2005), 'Subsurface damage in some single crystalline optical materials', *Applied optics* **44**(12), 2241–2249.

Roberts, S. (2001), Primary mirror substrate materials for the XLT telescope: a comparison of various options including silicon carbide, Technical report, National Research Council, Herzberg Institute of Astrophysics.

Ronse, K. (2006), 'Optical lithography - a historical perspective', *C. R. Physique* **7**, 844–857.

Roth, P. and Tonshoff, H. K. (1993), Influence of microstructure on grindability of alumina ceramics, *in* 'Machining of Advanced Materials', pp. 247–261.

Rowe, W. B. and Chen, X. (1997), 'Characterization of the size effect in grinding and the sliced bread analogy', *International Journal of Production Research* **35**(3), 887–899.

Rowe, W. B., Morgan, M. N., Qi, H. S. and Zheng, H. W. (1993), 'The effect of deformation on the contact area in grinding', *CIRP annals* **42**(1), 409–412.

Saini, D. (1990), 'Wheel hardness and local elastic deflections in grinding', *International Journal of Machine Tools & Manufacture* **30**(4), 637–649.

Saini, D. and Wager, J. (1985), 'Local contact deflections and forces in grinding', *CIRP annals* **34**(1), 281–285.

Saito, T. T., Wasley, R. J., Stowers, I. F., Donaldson, R. R. and Thompson, D. C. (1994), Precision and manufacturing at the Lawrence Livermore National Laboratory, *in* 'NASA, Washington, Technology 2003: The Fourth National Technology Transfer Conference and Exposition', Vol. 1, pp. 81–89.

Sartori, S. and Zhang, G. X. (1995), 'Geometric error measurement and compensation of machines', *CIRP annals* **44**(2), 599–610.

Sata, T., Li, M., Takata, S., Hiraoka, H., Li, C. Q., Xing, X. Z. and Xiao, X. G. (1985), 'Analysis of surface roughness generation in turning operation and its applications', *CIRP annals* **34**(1), 473–476.

Sazedur Rahman, M., Saleh, T., Lim, H., Son, S. and Rahman, M. (2008), 'Development of an on-machine profile measurement system in ELID grinding for machining aspheric surface with software compensation', *International Journal of Machine Tools & Manufacture* **48**(7-8), 887–895.

Schellekens, P., Rosielle, N., Vermeulen, H., Vermeulen, M., Wetzels, S. and Pril, W. (1998), 'Design for precision: Current status and trends', *CIRP annals* **47**(2), 557–586.

Schlesinger, G. (1978), *Testing Machine Tools: For the Use of Machine Tool Makers, Users, Inspectors and Plant Engineers - 8th Revised edition*, Elsevier.

Schultschik, R. (1981), 'Possibilities and limits of error feedback in automatic machining', *CIRP annals* **30**(1), 467–471.

Shafrir, S. N., Lambropoulos, J. C. and Jacobs, S. D. (2007), 'Subsurface damage and microstructure development in precision microground hard ceramics using magnetorheological finishing spots', *Applied optics* **46**(22), 5500–5515.

Shaohui, Y., Morita, S., Ohmori, H., Uehara, Y., Lin, W., Liu, Q., Maihara, T., Iwamuro, F. and Mochida, D. (2005), 'ELID precision grinding of large special schmidt plate for fibre multi-object spectrograph for 8.2 m subaru telescope', *International Journal of Machine Tools & Manufacture* **45**(14), 1598–1604.

Shore, P. (1995), Machining of optical surfaces in brittle materials using an ultra-precision machine tool, PhD thesis, Cranfield University.

Shore, P. and May-Miller, R. (2003), Production challenge of the optical segments for Extra Large Telescopes, *in* 'Proceedings of the International Workshop on Extreme Optics and Sensors', Vol. 40, pp. 25–30.

Shore, P., McKeown, P., Impey, S. and Stephenson, D. (1995), Surface and near surface conditions of "ductile" mode ground Zerodur, *in* 'Proceedings of 8th International Precision Engineering Seminar', pp. 365–368.

Shore, P. and Parr-Burman, P. (2003), Large Optics Manufacturing study (LOMS), Technical report, Cranfield University.

Shore, P. and Walker, D. (2004), Manufacture of segments for extremely large telescopes: a new perspective, *in* 'Proceedings of the SPIE', Vol. 5382, pp. 277–284.

Slocum, A. (1992), *Precision machine design*, Prentice Hall, New Jersey.

Snoeys, R., Peters, J. and Decneut, A. (1974), 'The significance of chip thickness in grinding', *CIRP annals* **23**(2), 227–237.

Stahl, H. P. and Feinberg, L. D. (2007), Summary of NASA advanced telescope and observatory capability roadmap, *in* 'Proceedings of the IEEE Aerospace Conference', pp. 1–11.

Stepp, L. M. and Strom, S. E. (2004), The Thirty-Meter Telescope project design and development phase, *in* 'Proceedings of the SPIE', Vol. 5382, pp. 67–75.

Stowers, I. F., Komanduri, R. and Baird, E. D. (1998), Review of precision surface generating processes and their potential application to the fabrication of large optical components, *in* 'Proceedings of the SPIE', Vol. 966, pp. 62–73.

Strom, S. E., Stepp, L. M. and Gregory, B. (2003), Giant segmented mirror telescope: a point design based on science drivers, *in* 'Proceedings of the SPIE', Vol. 4840, pp. 116–128.

Stulen, R. H. (1999), 'Progress in the development of extreme ultraviolet lithography exposure systems', *Microelectronic Engineering* **46**, 19–22.

Sun, X., Stephenson, D. J., Ohnishi, O. and Baldwin, A. (2006), 'An investigation into parallel and cross grinding of BK7 glass', *Precision Engineering* **30**(2), 145–153.

Suratwala, T., Wong, L., Miller, P., Feit, M. D., Menapace, J., Steele, R., Davis, P. and Walmer, D. (2006), 'Sub-surface mechanical damage distributions during grinding of fused silica', *Journal of Non-Crystalline Solids* **352**, 5601–5617.

Szeged (2007), 'http://astro.u-szeged.hu/ismeret/orias/Osszehas.gif - Accessed 11/07'.
URL: *http://astro.u-szeged.hu/ismeret/orias/Osszehas.gif*

Takasu, S., Masuda, M. and Nishiguchi, T. (1985), 'Influence of study vibration with small amplitude upon surface roughness in diamond machining', *CIRP annals* **34**(1), 463–467.

Tamaki, J. and Kitagawa, T. (1995), 'Evaluation of surface topography of metal-bonded diamond wheel utilizing three-dimensional profilometry', *International Journal of Machine Tools & Manufacture* **35**(10), 1339–1351.

Taylor-Hobson (2009), 'http://www.taylor-hobson.com/en/precision-inductive-range - Accessed 04/09'.
URL: *http://www.taylor-hobson.com/en/precision-inductive-range*

Taylor, J. S., Sommargren, G. E., Sweeney, D. W. and Hudyma, R. M. (1998), The fabrication and testing of optics for EUV projection lithography, *in* 'Proceedings of the SPIE', Vol. 3331, pp. 580–590.

Thompson, D. C. (1988), COP Gage error budget, *in* 'Certification of process gage design review meeting', pp. 1–37.

Thompson, D. C. and McKeown, P. A. (1989), 'The design of an ultra-precision CNC measuring machine', *CIRP annals* **38**(1), 501–504.

Tönshoff, H. K., Peters, J., Inasaki, I. and Paul, T. (1992), 'Modelling and simulation of grinding processes', *CIRP annals* **41**(2), 677–688.

Tong, S., Gracewski, S. M. and Funkenbusch, P. D. (2006), 'Measurement of the Preston coefficient of resin and bronze bond tools for deterministic microgrinding of glass', *Precision Engineering* **30**(2), 115–122.

Tonnellier, X., Morantz, P., Shore, P., Baldwin, A., Evans, R. and Walker, D. (2007), 'Subsurface damage in precision ground ULE and Zerodur surfaces', *Optics Express* **15**(19), 12197–12205.

VanBrocklin, R. R., Hobbs, T. W. and Edwards, M. J. (2004), Corning's approach to segment blank manufacturing for an extremely large telescope, *in* 'Proceedings of the SPIE', Vol. 5494, pp. 1–8.

Verma, Y., Chang, A. K., Berrett, J. W., Futtere, K., Gardopee, G. J., Kelley, J., Kyler, T., Lee, J., Lyford, N., Proscia, D. and Sommer, P. R. (2006), Rapid damage-free shaping of silicon carbide using reactive atom plasma (RAP) processing, *in* 'Proceedings of the SPIE', Vol. 6273, p. 62730B.

Viens, M. (1990), Fracture toughness and crack growth of Zerodur, Nasa technical memorandum - 4185, National Aeronautics and Space Administration.

Wager, J. and Saini, D. (1986), 'Local contact deflections in grinding - Groups of grains and single grains', *CIRP annals* **35**(1), 245–248.

Walker, D. D., Doel, A. P., Bingham, R. G., Brooks, D., King, A. M., Peggs, G., Hughes, B., Oldfield, S., Dorn, C., McAndrews, H., Dando, G. and Riley, D. (2002), Design study report: the primary and secondary mirrors for the proposed Euro50 telescope, Technical report, Lund Observatory.

Walton, I. (2008), A real time method for determining temperature in the high performance grinding process, *in* 'Proceedings of CMC'. CD, paper N°107.

Webster, J. A., Cui, C. and Mindek Jr, R. B. (1995), 'Grinding fluid application system design', *CIRP annals* **44**(1), 333–338.

Webster, J. and Tricard, M. (2004), 'Innovations in abrasive products for precision grinding', *CIRP annals* **53**(2), 597–617.

Weck, M., McKeown, P., Bonse, R. and Herbst, U. (1995), 'Reduction and compensation of thermal errors in machine tools', *CIRP annals* **44**(2), 589–598.

Wiederhorn, S. M. and Lawn, B. R. (1977), 'Strength degradation of glass resulting from impact with spheres', *Journal of the American Ceramic Society* **60**(9-10), 451–458.

Wiederhorn, S. M. and Lawn, B. R. (1979), 'Strength degradation of glass impacted with sharp particles: I, Annealed surfaces', *Journal of the American Ceramic Society* **62**(1-2), 66–70.

Wills-Moren, W. J., Carlisle, K., McKeown, P. A. and Shore, P. (1990), Ductile regime grinding of glass and other brittle materials by the use of ultra-stiff machine tools, *in* 'Proceedings of the SPIE', Vol. 1333, pp. 126–135.

Wills-Moren, W. J., Modjarrad, H., Read, R. F. J. and McKeown, P. A. (1982), 'Some aspects of the design and development of a large high precision CNC diamond turning', *CIRP annals* **31**(1), 409–414.

Wills-Moren, W. J. and Wilson, T. (1989), 'The design and manufacture of a large CNC grinding machine for off-axis mirror segments', *CIRP annals* **38**(1), 529–532.

Wu, S. M. and Ni, J. (1989), 'Precision machining without precise machinery', *CIRP annals* **38**(1), 533–536.

Wuttig, A., Steinert, J., Duparre, A. and Truckenbrodt, H. (1999), Surface roughness and subsurface damage characterization of fused silica substrates, *in* 'Proceedings of the SPIE', Vol. 3739, pp. 369–376.

Xie, X. Z., Chen, G. Y. and Li, L. J. (2004), 'Dressing of resin-bonded superabrasive grinding wheels by means of acousto-optic Q-switched pulsed Nd:YAG laser', *Optics & Laser Technology* **36**, 409–419.

Xu, H. H. K. and Jahanmir, S. (1994), 'Simple technique for observing subsurface damage in machining of ceramics', *Journal of the American Ceramic Society* **7**(5), 1388–1390.

Xu, H. H. K., Jahanmir, S. and Ives, L. K. (1997), 'Effect of grinding on strength of tetragonal zirconia and zirconia toughened alumina', *Machining Science and Technology* **1**(1), 49–66.

Yang, F., Zhang, B., Wang, J., Zhu, Z. and Monahan, R. (2001), 'The effect of grinding machine stiffness on surface integrity of silicon nitride', *Journal of Manufacturing Science and Engineering* **123**(4), 591–600.

Yin, L., Huang, H., Ramesh, K. and Huang, T. (2005), 'High speed versus conventional grinding in high removal rate machining of alumina and alumina-titania', *International Journal of Machine Tools & Manufacture* **45**(7-8), 897–907.

Yoshihara, N., Kuriyagawa, T. and Ono, H. (2004), Development of fluctuation-free ultra-precision aspherical grinding method for extreme precise optical parts, *in* 'The 7th International Conference on Monitoring and Automatic Supervision in Manufacturing'. CD-ROM.

Zhang, B. and Howes, T. D. (1995), 'Subsurface evaluation of ground ceramics', *CIRP annals* **44**(1), 263–266.

Zhang, B., Wang, J., Yang, F. and Zhu, Z. (1999), 'The effect of machine stiffness on grinding of silicon nitride', *International Journal of Machine Tools & Manufacture* **39**(8), 1263–1283.

Zhao, Q., Liang, Y., Stephenson, D. and Corbett, J. (2007), 'Surface and subsurface integrity in diamond grinding of optical glasses on Tetraform C', *International Journal of Machine Tools & Manufacture* **47**(14), 2091–2097.

Zhao, Q., Wang, B., Dong, S., Stephenson, D. and Corbett, J. (2006), Subsurface damage mechanisms in diamond grinding of BK7 on Tetraform C, *in* 'Proceedings of the SPIE', Vol. 6149, p. 61490L.

Zhong, Z. and Nakagawa, T. (1996), 'Grinding of aspherical SiC mirrors', *Journal of Materials Processing Technology* **56**, 37–44.

Zhong, Z. and Nakayama, T. (1992), 'New grinding methods for aspheric mirrors with large curvature radii', *CIRP annals* **41**(1), 335–338.

Zhou, X. and Xi, F. (2002), 'Modeling and predicting surface roughness of the grinding process', *International Journal of Machine Tools & Manufacture* **42**(8), 969–977.

Zhou, Y., Funkenbusch, P. D., Quesnel, D. J., Golini, D. and Lindquist, A. (1994), 'Effect of etching and imaging mode on the measurement of subsurface damage in microground optical glasses', *Journal of the American Ceramic Society* **77**(12), 3277–3280.

APPENDICES

A. LOAD CELL CALIBRATION

The load cell calibration plotted is shown in Figure A.1.

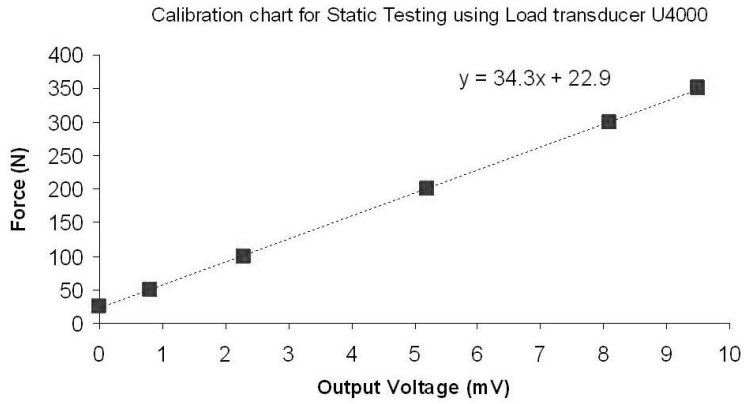

Figure A.1: Load cell calibration

B. MATERIAL ETCHING RATES

B.1 Fused silica

The etching rate obtained for Fused silica, using a solution of Hydrofluoric acid, is shown in Figure B.1.

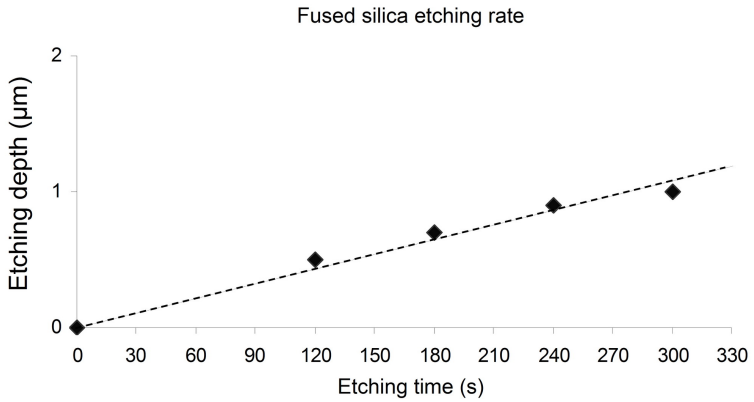

Figure B.1: Etching rate - Fused silica

B.2 ULE

The etching rate obtained for ULE, using a solution of Ammonium bifluoride, is shown in Figure B.2.

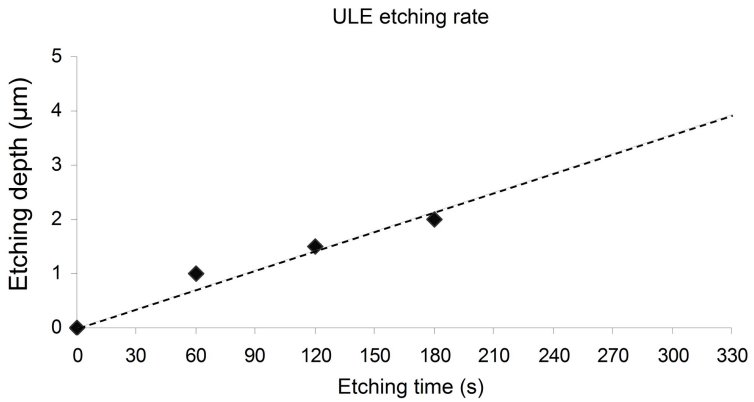

Figure B.2: Etching rate - ULE

B.3 Zerodur

The etching rate obtained for Zerodur, using a solution of Hydrofluoric and Hydrochloric acids, is shown in Figure B.3 .

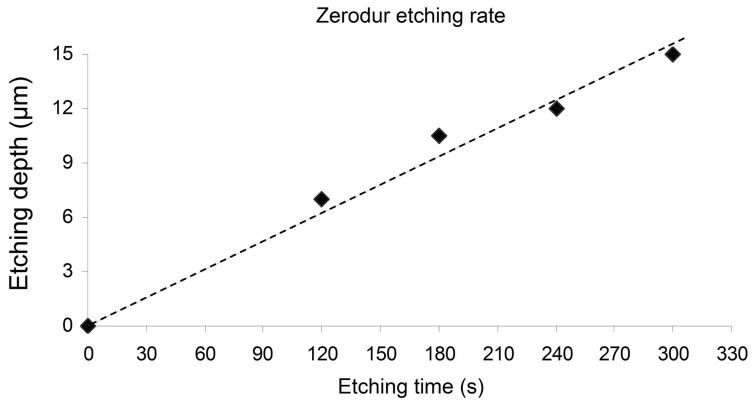

Figure B.3: Etching rate - Zerodur

C. SUBSURFACE DAMAGE GRAPHS

C.1 Parameters screening

The subsurface damage results on Zerodur are shown in Figure C.1.

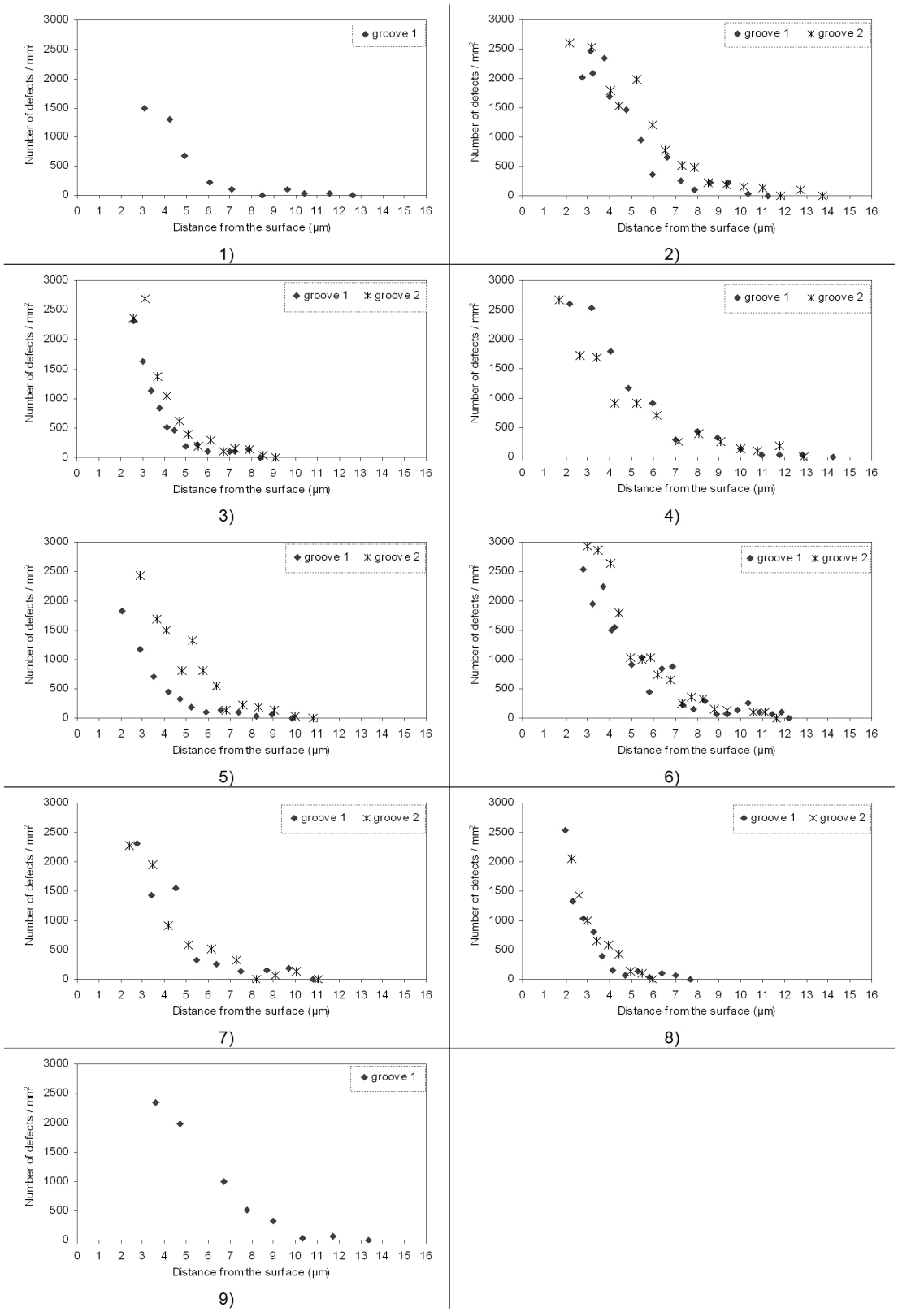

Figure C.1: Parameters screening - Subsurface damage results

C.2 Edgetek based test programme

The subsurface damage results on ULE are shown in Figure C.2.

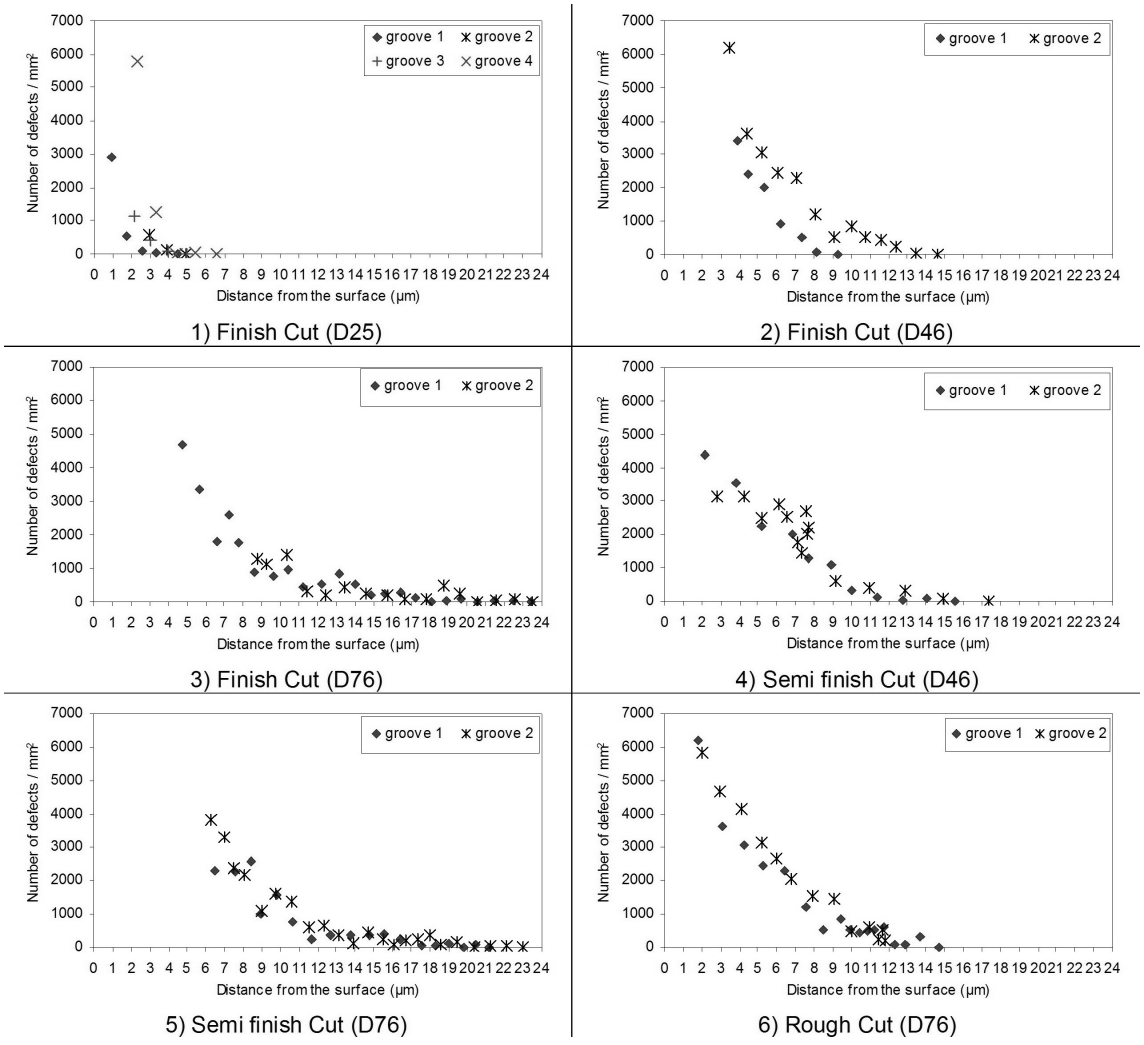

Figure C.2: Subsurface damage results - ULE - Edgetek

The subsurface damage results on Zerodur are shown in Figure C.3.

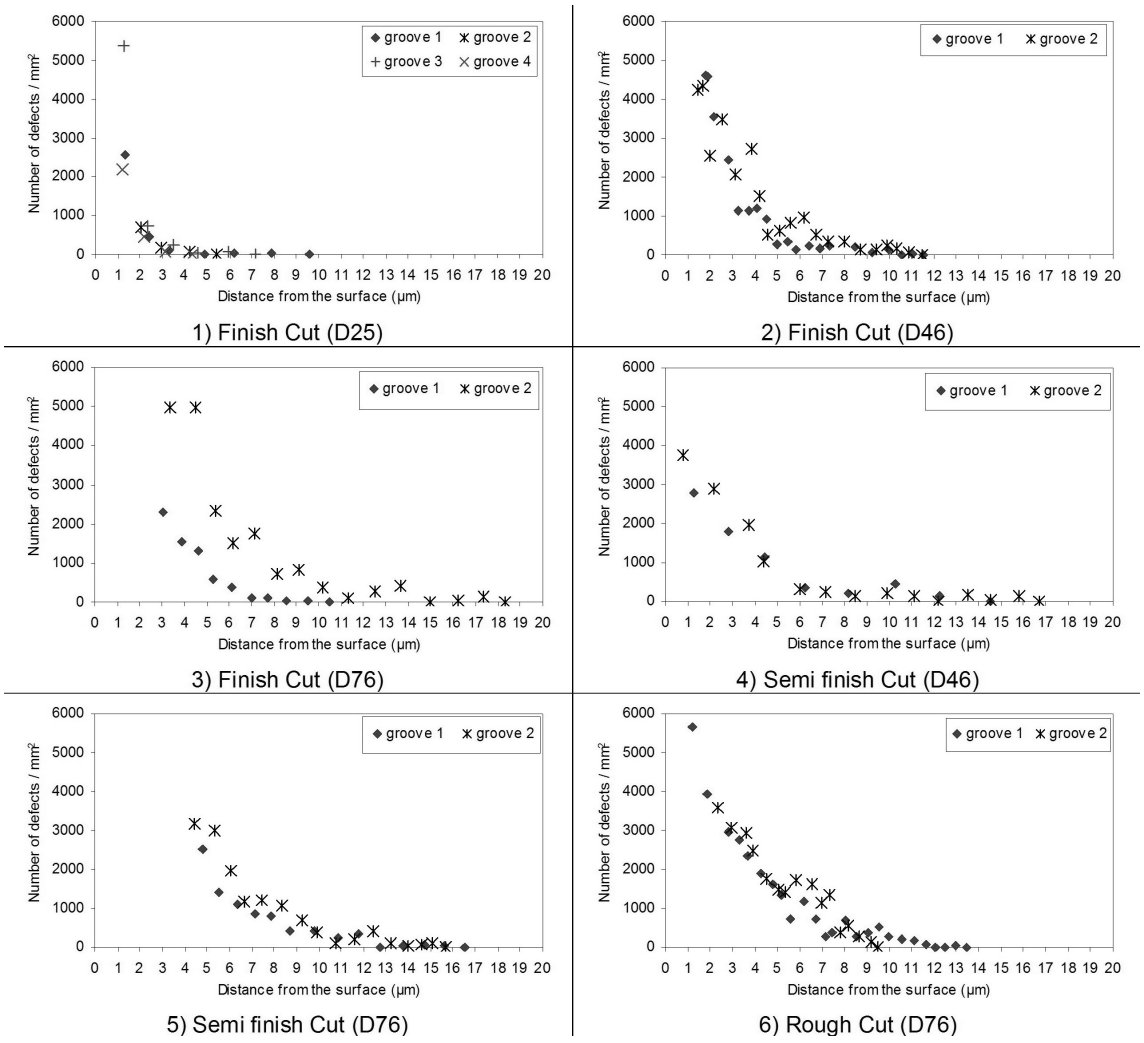

Figure C.3: Subsurface damage results - Zerodur - Edgetek

C.3 BoX based test programme

The subsurface damage results on ULE are shown in Figure C.4.

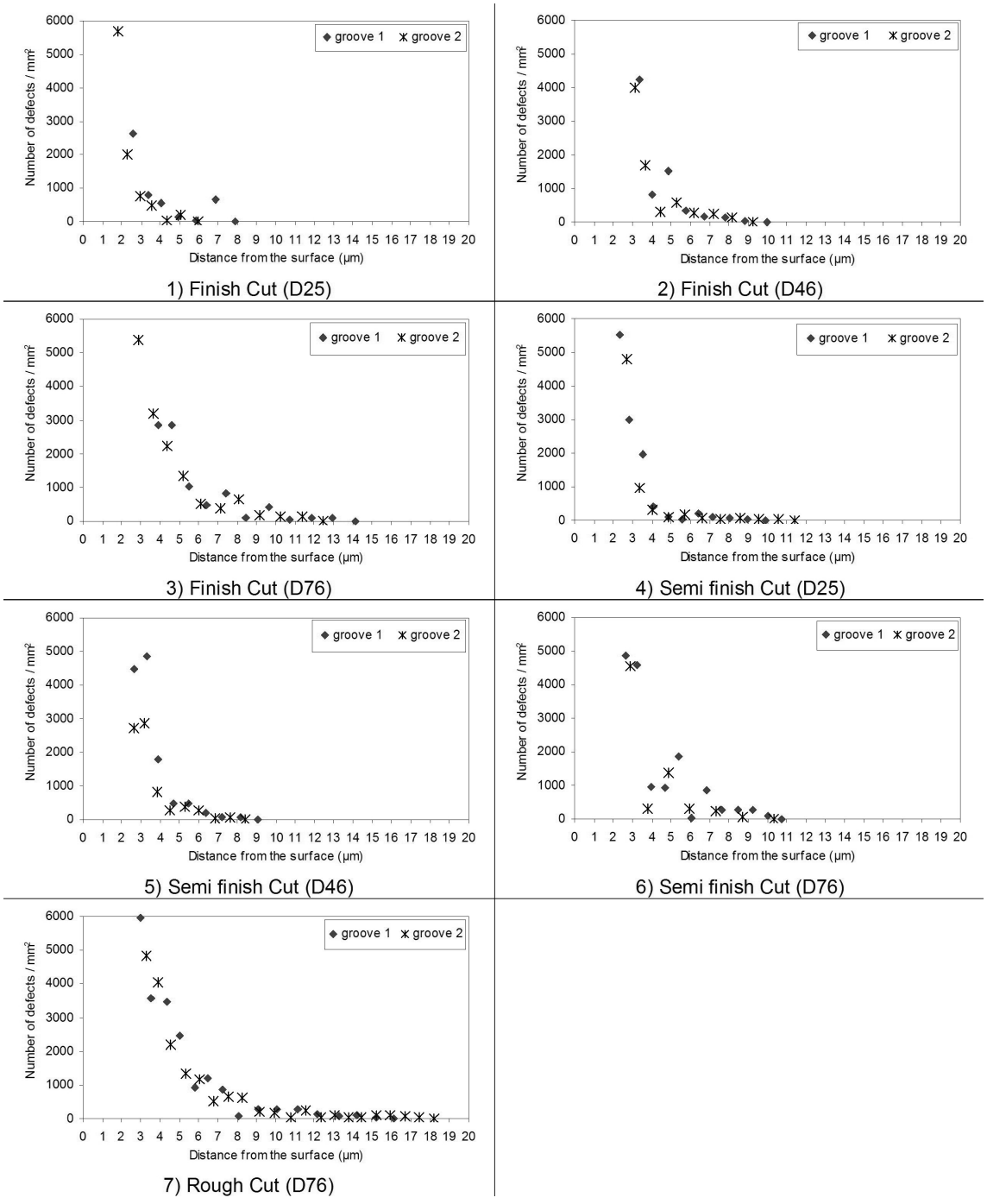

Figure C.4: Subsurface damage results - ULE - BoX

The subsurface damage results on Zerodur are shown in Figure C.5.

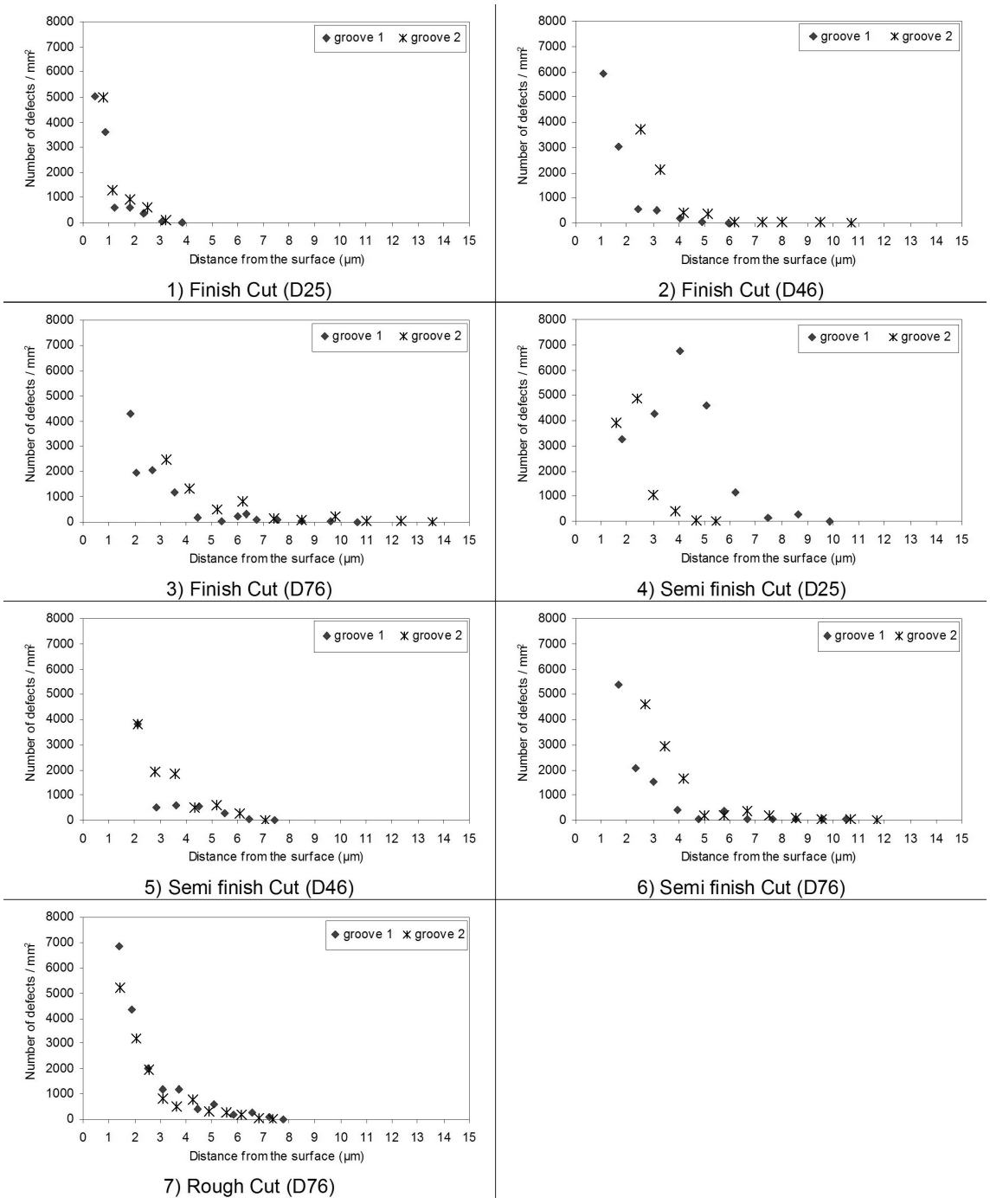

Figure C.5: Subsurface damage results - Zerodur - BoX